Downloaded from orbit.dtu.dk on: May 05, 2023

DTU Library

Chemical Production of Graphene Catalysts for Electrochemical Energy Conversion

Seselj, Nedjeljko

Publication date:
2017

Document Version
Publisher's PDF, also known as Version of record

Link back to DTU Orbit

Citation (APA):
Seselj, N. (2017). *Chemical Production of Graphene Catalysts for Electrochemical Energy Conversion*. DTU Chemistry.

General rights
Copyright and moral rights for the publications made accessible in the public portal are retained by the authors and/or other copyright owners and it is a condition of accessing publications that users recognise and abide by the legal requirements associated with these rights.

- Users may download and print one copy of any publication from the public portal for the purpose of private study or research.
- You may not further distribute the material or use it for any profit-making activity or commercial gain
- You may freely distribute the URL identifying the publication in the public portal

If you believe that this document breaches copyright please contact us providing details, and we will remove access to the work immediately and investigate your claim.

Technical University of Denmark

Chemical Production of Graphene Catalysts for Electrochemical Energy Conversion

Nedjeljko Seselj

Ph.D. Thesis

June 2017

Chemical Production of Graphene Catalysts for Electrochemical Energy Conversion

Ph.D. Thesis

June 14th, 2017

Nedjeljko Šešelj

nese@kemi.dtu.dk

Supervisor

Prof. Jingdong Zhang

Co-supervisor

Prof. Jens Ulstrup

NanoChemistry group

Department of Chemistry

Technical University of Denmark

"Chemistry without catalysis would have a sword without a handle, a light without brilliance, a bell without sound."

Alwin Mittasch, 1948.

Preface and Acknowledgments

The thesis is submitted as application for the Ph.D. degree in chemistry from the Technical University of Denmark (DTU). The work was carried out at the NanoChemistry group, Department of Chemistry, DTU, under the supervision of Prof. Jingdong Zhang and Prof. Jens Ulstrup. The Ph.D. project "Chemical Production of Graphene Catalysts for Electrochemical Energy Conversion" was a part of a FTP project. It involved cooperation with the company Danish Power Systems (DPS) led by Hans Aage Hjuler, Prof. Yi Ding at the Institute for New Energy Materials and Low-Carbon Technologies at Tianjin University of Technology (TJUT), and Assoc. Prof. Pengchao Si at Shandong University (SU). International network project "Three Dimensional Porous Nanoelectrodes for Efficient Energy Conversion" and EU-Project "Electronanomat" are acknowledged for my external stay in State Key Laboratory of Physical Chemistry of Solid Surfaces, Xiamen University (XU) and TJUT.

First and foremost, I would like to thank my supervisor Prof. Jingdong Zhang for all the help and motivation during the last three years. She helped me grow as a scientist and a person. Prof. Jens Ulstrup has been such an inspiration, a consistent source of stimulating scientific discussions and valuable advice. Assoc. Prof. Qijin Chi gave me good input and guidance during my study. I am thankful to Assoc. Prof. Jiawei Yan and Prof. Bingwei Mao for making my stay in Xiamen so pleasant and productive. I would like to thank Prof. Yi Ding for the help he has given me during my stay in Tianjin. You are truly a wonderful person, a good friend and a brilliant scientist.

Thank you Lars Nilausen Cleemann and Larissa Seerup at the Department of Energy Conversion and Storage (DTU) for the help in fuel cell station assembly and TGA measurements. I would like to thank Jette Berg Nestén for an endlessly up-lifting spirit. Mette Hansen has made every paperwork and administrative issue much easier. My gratitude goes to Bo Sørensen and his IT team for always being so efficient. Maria Bundgaard, my friend, has made me laugh many times.

Dr. Ramendra Sundar Dey and I had many good scientific discussions. Dr. Michal Wagner, helped me with scientific contributions, moreover, with all the laughter and good spirit. Dr. Arnab Halder, Dr. Gunnar Olsen and Dr. Minwei Zhang have been such a wonderful family to me. Long working days felt like a minute. Dr. Christian Engelbrekt has taught me so much, about science and life, about Denmark and Danes. His calming and good-natured disposition was always much appreciated.

Last, but not the least, I wish to thank my friends and family in Croatia. They have been my constant support and source of perpetual joy. Thanks to my sisters, Lara and Josipa, for tolerating me all these years.
Thanks to my parents for giving me everything. Everything I am, everything I own. Then, they gave me more.

June 2017, Kgs. Lyngby

Nedjeljko Seselj

Abstract

Recently developed FC technology is among many approaches aiming at solving the global energy challenges. FCs are electrochemical devices that convert chemical energy from fuel molecules into electrical energy via electrochemical reactions. FCs are, however, limited by the scarce and expensive platinum (Pt) electrocatalysts. Approach in this Ph.D. thesis is, therefore, in reducing Pt content to ultra-low loadings in the electrocatalysts and optimizing their electronic structures to efficiently utilize Pt. Syntheses of small Pt nanoparticles (NPs) were performed in order to increase the specific area of Pt. Syntheses of core-shell Au-Pt (Au@Pt) NPs, with atomically-thin Pt shells on Au NP cores were performed. The Au@Pt NPs were further chemically immobilized on a highly conductive graphene support to ensure efficient electronic structure of the catalyst. Graphene possesses unique properties, such as high charge carrier mobility, high conductivity, mechanical strength (130 GPa), and high surface area (2600 m^2g^{-1}).[1] Chemical inertness of graphene in polymer electrolyte membrane FC (PEMFC) operating conditions resulted in enhanced electrocatalyst stability. Chemical anchoring of Pt and Au@Pt NPs was achieved via L-cysteine linker molecules that provided pathways for fast electron transfers during the electrocatalytic reactions. Electrochemical properties of self-assembled L-cysteine monolayers immobilized on single-crystal Au(111) surfaces were studied in ionic liquids and their structures imaged by scanning tunneling microscopy (STM), to investigate the nature of L-cysteine bonds on Au.

Synthesized electrocatalysts were characterized by spectroscopic, microscopic and electrochemical techniques. Electrocatalysis was examined by electrochemical oxidation of formic acid, methanol and ethanol, and oxygen reduction reaction experiments, for both anode and cathode catalyst applications respectively. Finally, the main goal was to investigate the electrocatalytic performance within the PEMFC systems. Direct formic acid, methanol and ethanol PEMFC station was established. As-synthesized graphene-immobilized Au@Pt NPs exhibited high electrocatalytic performance and long stability in direct formic acid, methanol and ethanol PEMFCs.

Motivation and project objectives

Motivation

Depleting non-renewable energy resources, along with rapidly growing human population has had detrimental effect on environmental sustainability. High-energy demands of modern-day society have been largely based on exploiting fossil fuels. Driving forces of chemical reactions in oil processing heavily rely on hazardous chemicals and/or reaction conditions. Electrocatalysis, however, provides a reaction-driving force in a sense of potential difference between two electrodes. Therefore, electrocatalysts within electrochemical energy devices offer a new and environmentally benign solution to the snowballing energy crisis. Electrochemical energy conversion and storage devices can be divided into four main groups:

1. capacitors,
2. supercapacitors,
3. batteries,
4. fuel cells.

Depending on the application and energy requirements, combination of, or a specific power device can be used. Ragone plot represents these technologies according to their respective power and energy densities, Fig. 1.

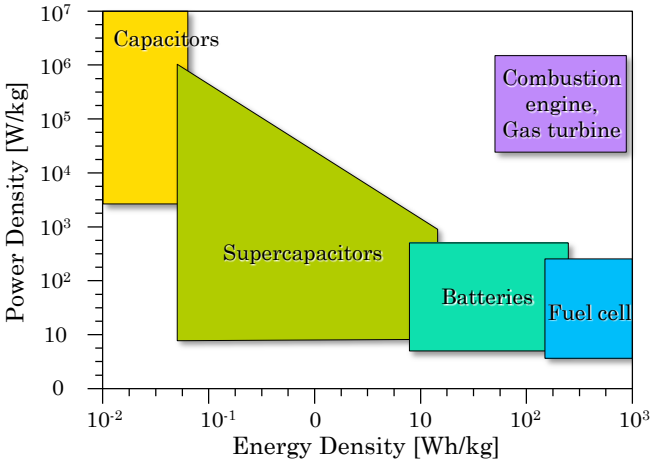

Figure 1. Power density versus energy density, a Ragone plot, for energy storage and conversion devices.[2]

Although the mass-production industry standard of today are battery-powered devices, fuel cell (FC) technology is a new and environmentally benign approach offering high energy density. Focus here is on polymer electrolyte membrane fuel cells (PEMFCs) employing bio-fuels and oxygen to produce electrical energy. Although PEMFCs offer high specific energy density (volumetric and gravimetric), the technology is not widely available, primarily due to the expensive catalyst employed in their operation. Highly active catalysts, like Pt, are required since the mild operating conditions (up to 100 °C) do not significantly contribute to elevating the reaction-driving forces. Pt is a growingly expensive metal with fluctuating price (201 300.0 DKK/kg in June 2017). Scientific research is constantly developing novel electrocatalysts based on less Pt and even Pt-free approaches. However, they still cannot compete with the expensive noble metal. Furthermore, stability is one of the PEMFC challenges. NP migration and aggregation is often due to insufficient immobilization forces to support materials. Carbon-based supports are commonly used in PEMFC technology, like carbon black or graphitized carbon. These types of supports can be oxidized at acidic/basic operating conditions. Graphene is a recently discovered carbon-based material, possessing unique properties and high chemical resistance in harsh FC operating conditions. Based on optimized bimetallic nanostructures immobilized on graphene support, this Ph.D. thesis offers new approaches to PEMFC technology.

Project objectives

Our approach to develop PEMFC technology by synthesizing electrocatalysts with reduced Pt content and optimized electronic structures. Furthermore, electrocatalysts will be studied by spectroscopic, microscopic and electrochemical techniques to investigate the morphology and their electrochemical properties. Small and uniform NPs or NP structures must be firmly immobilized on support materials to ensure fast electron transfer rates during the electrocatalytic reactions. Highly conductive and chemically inert supports must be utilized in PEMFCs, due to usually very acidic/basic operating conditions. Graphene is, therefore, used as a good support material, due to its distinctive properties, specifically high conductivity, mechanical strength and high surface area (2600 m^2g^{-1}).[1] Furthermore, graphene is chemically inert in PEMFC operating conditions. Electrocatalytic performance is examined by electrochemical oxidation and oxygen reduction reaction experiments, which emulate conditions at the anode and the cathode of a PEMFC, respectively. Finally, the main goal of the project is to examine the electrocatalytic performance of the as-synthesized electrocatalysts within the direct formic acid, methanol and ethanol PEMFC systems. The PEMFC station is assembled and tested with the commercially available catalysts to obtain benchmark values.

Electrocatalytic performance and stability of the as-synthesized catalysts are compared with the commercially available catalyst, currently used in industry.

Outline

The thesis is structured in six chapters. The general descriptions of each of the chapters is presented here.

- **Chapter 1** is a general introduction to fuel cell technology, graphene and platinum electrocatalysts. It introduces concepts and theory necessary for the discussion in the following chapters.
- **Chapter 2** summarizes methodology and techniques used for characterization of electrocatalysts. It describes principles and focus points of employed methods.
- **Chapter 3** focuses on syntheses, characterization and electrocatalysis of graphene-supported platinum catalysts. It highlights the focus points in syntheses optimization of electrocatalysts. The chapter emphasizes the importance of strong nanoparticle immobilization on supports by chemical linkers, L-cysteine molecules. The electrocatalytic performance of as-synthesized graphene-platinum nanocatalysts was compared to commercially available catalyst, platinum nanoparticles immobilized on graphitized carbon.
- **Chapter 4** further improves the syntheses of nanocatalysts, conducted in previous chapter, by formation of core-shell nanoparticle catalysts. The gold nanoparticle cores are strongly attracted and chemically immobilized on graphene by L-cysteine molecular anchors, followed by formation of atomically-thin platinum shells. By replacing the platinum nanoparticle cores by gold, synergetic effects are achieved between the two metals, benefitting the resistance towards catalytic poisoning and enhancing electrocatalysis. The performance of graphene-supported core-shell nanocatalysts was compared to the commercial catalyst.
- **Chapter 5** describes the fuel cell technology in detail. It shows the entire process of fuel cell station assembly, electrode membrane assembly, software design, focus points during fuel cell testing, and finally, electrocatalytic performance of graphene-supported core-shell nanocatalysts in direct formic acid, methanol and ethanol fuel cells. The electrocatalysis on graphene-supported core-shell nanocatalysts was compared to the commercial catalyst used in industry.
- **Chapter 6** focuses on fundamental study of the nature of L-cysteine molecules on Au. The self-assembled L-cysteine monolayers on Au(111) single-crystal electrodes were investigated by electrochemical methods and scanning tunneling microscopy.
- **Chapter 7** gives summary conclusion for the entire Ph.D. thesis.

Acronyms and instructional notes

ADC: Analog-to-digital converter
AFC: Alkaline fuel cell
AFM: Atomic force microscopy
Au@Pt: Au_{core}-Pt_{shell} nanoparticles
Au_{ox}: Gold oxide
BFC: Biofuel cell
$BMIPF_6$: 1-n-butyl-3-methylimidazolium
BPG: Basal-plane pyrolytic graphite electrodes
BMPTFSI: 1-Butyl-1-Methylpyrrolidinium-bis
CA: Chronoamperometry
CE: Counter electrode
CO_{ads}: Adsorbed CO
C-Pt: Commercial catalyst, 20 wt.% Pt NPs (< 5 nm) on graphitized carbon
CV: Cyclic voltammetry
CVD: Chemical vapor deposition
Cys: L-cysteine
DAC: Digital-to-analog converter
DAQ: Data acquisition
DEFC: Direct ethanol fuel cell
DFAFC: Direct formic acid fuel cell
DMFC: Direct methanol fuel cell
DTA: Differential thermal analysis
DTU: Technical University of Denmark
EC: Electrochemistry/Electrochemical
ECSA: Electrochemical surface area
EDC: N-(3-Dimethylaminopropyl)-N'-ethylcarbodiimide hydrochloride
EDX: Energy-dispersive X-ray spectroscopy
E_{HW}: Half-wave potential
EMITFSI: 1-ethyl-3-methylimidazolium bis(trifluoromethylsulfonyl)imide
(trifluoromethylsulfonyl)imide
E_p: Peak potential
EOR: Ethanol oxidation reaction
EPG: Edge-plane pyrolytic graphite electrodes
EtOH: Ethanol
FA: Formic acid
FAOR: Formic acid oxidation reaction
FC: Fuel cell
FE-SEM: Field Emission Scanning Electron Microscopy
FET: Field-effect transistor
FTIR: Fourier transform infrared spectroscopy
G: Graphene
GCE: Glassy carbon electrode
G-Cys: graphene functionalized by L-cysteine molecules
G-Cys-Au: Au nanoparticles immobilized on L-cysteine functionalized graphene
G-Cys-Au@Pt: Au@Pt nanoparticles immobilized on L-cysteine functionalized graphene
G-Cys-Pt: Pt nanoparticles immobilized on L-cysteine functionalized graphene
GF: Graphene foam
GO: Graphene oxide
HPLC: High-performance liquid chromatography
HR: High resolution
H-UPD: Hydrogen underpotential deposition region
I_D: Disk current
IP: Internet Protocol
I_R: Ring current
LSV: Linear sweep voltammetry
MB: Mass controller bandwidth
MbFC: Microbial fuel cells
MCFC: Molten carbonate fuel cell
MEA: Membrane electrode assembly
MeOH: Methanol
MES: 2-(N-morpholino)ethanesulfonic acid
MFC: Mass flow controller
MOR: Methanol oxidation reaction
MOR: Methanol oxidation reaction
n: Electron number

NHS: N-Hydroxysuccinimide
N-G: Nitrogen-doped graphene
NP: Nanoparticle
OCV: Open circuit voltage
OMIPF$_6$: 1-methyl-3-octylimidazolium hexafluorophosphate
ORR: Oxygen reduction reaction
PAFC: Phosphoric acid fuel cell
PEI: Polyethylenimine
PEM: Plymer electrolyte membrane
PEMFC: Polymer electrolyte membrane fuel cell
PID: Proportional-integral-derivative controller
ppm: Parts per million
ppt: Parts per thousand
Pt$_{ox}$: Platinum oxide
PVP: Polyvinylpyrrolidone
RDE: Rotating disk electrode
RE: Reference electrode
RHE: Reversible hydrogen electrode
RRDE: Rotating ring disk electrode
RSF: Relative sensitivity factor
r.t.: Room temperature
SAM: Self-assembled monolayer
SAMENS: Saccharide-based approach to metal nanostructure synthesis
SCE: Saturated calomel electrode
SEM: Scanning electron microscopy
SHE: Standard hydrogen electrode
SOFC: Solid oxide fuel cell
SPR: Surface plasmon resonance
SPM: Scanning probe microscopy
STEM: Scanning transmission electron microscopy
STM: Scanning tunneling microscopy
SU: Shandong University
TEM: Transmission electron microscopy
TGA: Thermogravimetric analysis
THF: Tetrahydrofuran
TJUT: Tianjin University of Technology
UI: User interface
UV-Vis: Ultraviolet–visible spectroscopy
WCR: Wet chemical reduction
WE: Working electrode
XPS: X-ray photoelectron spectroscopy
XU: Xiamen University

Instructional notes

Acronyms of terms ending in -microscopy, -chemistry, -voltammetry or -spectroscopy, refer to -microscope, -chemical, -voltammogram and –spectrum/spectra, as well. Abbreviations are used in plural form by adding “s”. Figures are abbreviated to “Fig.” in the text.

Table of Contents

Chapter 1

Fuel cells, Graphene and Pt-based catalysts

1.1 Introduction to fuel cell technology

Due to depleting fossil fuel resources accompanied with drastic climate changes, the need to explore new renewable and sustainable energy sources is imminent. Fuel cell (FC) technology is among many approaches recently developed aiming at solving the global energy challenges. FCs are electrochemical devices that convert chemical energy stored in fuel molecules into electric energy via electrochemical reactions.[3] Basic elements in a fuel cell are cathode, anode and electrolyte. Commonly used fuels are dihydrogen, methanol, ethanol, formic acid, etc.[4] Reactions that provide energy occur at both electrodes. As an example, reactions for a formic acid fuel cells [5] are:

$$\text{Anode:} \quad HCOOH \rightarrow CO_2 + 2\,H^+ + 2\,e^- \tag{1.1}$$

$$\text{Cathode:} \quad 1/2\,O_2 + 2\,H^+ + 2\,e^- \rightarrow H_2O \tag{1.2}$$

$$\text{Net reaction:} \quad HCOOH + 1/2\,O_2 \rightarrow CO_2 + H_2O \tag{1.3}$$

FCs provide clean energy with low pollution. Several different types of fuel cells exist, categorized by the fuel and electrolyte. Important technologies include hydrogen FCs such as alkaline fuel cells (AFCs), polymer electrolyte membrane fuel cells (PEMFCs), phosphoric acid fuel cells (PAFCs), solid oxide fuel cells (SOFCs) and molten-carbonate fuel cells (MCFCs). FCs use liquid organic fuels are often denoted as direct or indirect FCs depending on whether the fuel directly participates in the reaction or is first split into H_2 which then reacts at the anode. Direct FCs are robust devices that allow usage of different fuels. Representative setups are the direct methanol fuel cell (DMFC), the direct ethanol fuel cell (DEFC) and the direct formic acid fuel cell (DFAFC).[6][7][8] Different FC technologies with potential application are summarized in Figure 1.1. We focus on direct FCs, in which liquid hydrocarbons are fuel molecules and a polymer electrolyte membrane (PEM, primarily Nafion®) the electrolyte. The PEM simultaneously acts as a separator between anode and cathode, as well as the proton conductor.

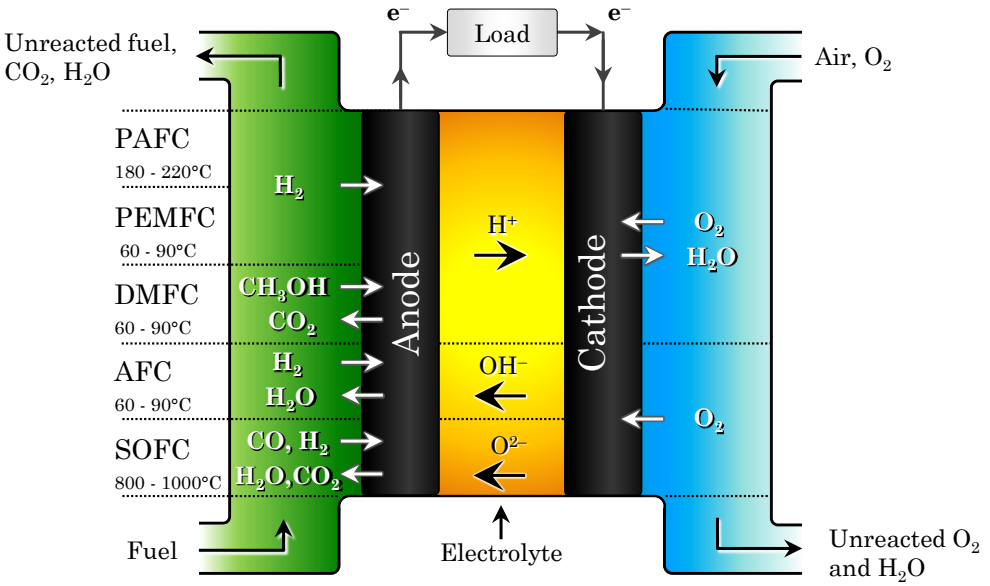

Figure 1.1 Scheme of representative FC systems: AFC, PEMFC, DMFC, PAFC, and SOFC. The fuel oxidation occurs at the anode while oxygen is reduced to water at the cathode. Ionic species involved in the reactions of different FC technologies is noted as the electrolyte.

Pt-based materials are most commonly used as catalysts with appealing properties such as low operating temperatures, high power densities and relatively easy scale-up. On the other hand, Pt is both an increasingly expensive material and as a catalyst, easily poisoned.[9] Only a few parts per billion of CO_2 or CO can leave large parts of the catalytic surface inactive for H_2 dissociation.[10] It is a challenge to overcome such issues, therefore prodigious effort are invested in reducing Pt usage in FCs.

1.2 Graphene

Graphene is a two-dimensional single sheet of sp^2 carbon in a hexagonal structure arrangement, Fig. 1.2.[11] Graphene possesses unique properties, such as high charge carrier mobility (up to 105 $cm^2 \cdot V^{-1} \cdot s^{-1}$), high conductivity, ambipolar electric field effect, quantum Hall effects at room temperature, high mechanical strength (130 GPa) and high surface area (2600 $m^2 g^{-1}$).[1] Graphene can be chemically synthesized from graphite and used as 3D foam or paper. These properties make graphene perfect as electrode support for catalysts in electrochemical energy systems.[12]

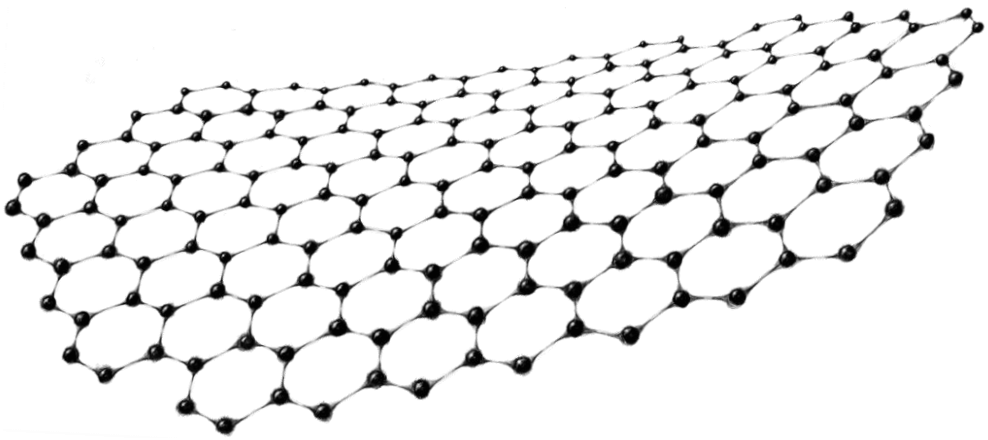

Figure 1.2 Scheme of a single graphene nanosheet.

3D porous graphene has exhibited remarkable properties for electrochemical power systems. Porous materials are classified by their pore size: macroporous (> 50 nm), mesoporous (2 – 50 nm) and microporous (< 2 nm).[13] Synthesizing 3D graphene with precise control of shape and pore size is required. Metallic nanoparticles (NPs) can interact strongly with functional groups on graphene, e.g. hydroxyl, epoxide, carbonyl and carboxylate making exact engineering of graphene functionalization vital.[14] However, this compromises the high electronic conductivity of graphene. Usually, graphene production is divided into "wet" and "dry" approaches.[15][16] The latter is based on building graphene sheets from simple carbon molecules, usually methane and ethanol.[17] Wet approaches include chemical syntheses of graphene in solutions, from graphite via formation of graphene oxide (GO).[15] A summary of GO reducing agents in reported procedures and their corresponding properties is shown in Table 1.1. For FC applications porous 3D graphene structures can be created.[12] Porous graphene networks are in rapid development with the most important ones (1) graphene nanomesh and (2) graphene foam. Graphene nanomesh is graphene structure with high-density nanoscale pores located on top of conjugated carbon surfaces.[12] Its synthesis includes polymer building blocks, photo, electron- and plasma-etching, template methods and chemical etching methods.[18] Graphene foam (GF) is a macroscopic 3D graphene made by stacking graphene nanosheets into a strongly connected network. GFs are ultralight, mechanically strong, compressible materials with multidimensional electron pathways which ensure excellent electrochemical performance. However, GF surface area is generally limited to below 1000 m^2/g so the resulting GFs are denoted as "defective". They are usually prepared by hydrothermal methods, chemical reduction methods, or template directed chemical vapor deposition (CVD) methods. In hydrothermal methods, GO is used as a

precursor to create cross-linking sites followed by freeze drying to form a 3D framework due to the expansion of ice and evaporation of water.

Table 1.1. A summary of GO reducing agents and reacting conditions in accordance to well-supported and proposed mechanisms.

Reducing agents	**T (°C)** [A]	**κ (S·m^{-1})** [B]	**C/O ratio**	**Ref**
$NaBH_4$	80	82	4.8 [C]	[19]
NH_4BH_4	66 (THF)	20 300	9.8 [C]	[20]
HI	100	29 800	12 [C]	[21]
Hydrazine		2 420	10.3 [D]	[22]
Ethanol		$1.8 \cdot 10^{-4}$	6 [D]	[23]
Urea/NH_3	95	43	4.5 [C]	[24]
L-Ascorbic acid/NH_3		7 700	12.5 [C]	[25]
$NaHSO_3$		6 500	7.9 [D]	[26]
Zn-H_2SO_4	RT	3 416	21.2 [C]	[27]
L-Cysteine		$1.2 \cdot 10^{-1}$	-	[28]
Green tea	90	53		[29]
Leaf extract	RT	4 006	7.1 [D]	[30]

[A] Reduced in aqueous solution unless stated otherwise. B Conductivity of synthesized un-annealed graphene. [C] XPS. [D] Elemental analysis.

These procedures can be modified by introducing different precursors, such as pyrrole, amine, thiourea, ammonia boron trifluoride, etc.[31] In order to create in situ polymerized polypyrrole-graphene foam, e.g. Qu et al. electrodeposited polypyrrole on hydrothermally treated GF.[32] GFs have been combined with transition metal oxides, hydroxides and sulfides for applications as energy storage devices.[33] The advantage of chemical methods is that not only is GO reduced to graphene, but crosslinking sites are provided, leading to a chemically bonded GF framework. Worsley et al. cross-linked GO in aqueous solution with resorcinol-formaldehyde by reducing it in a sol-gel procedure using $NaCO_3$ as a catalyst, followed by supercritical CO_2 drying and pyrolysis (1050 °C) under N_2 atmosphere.[34] The final product obtained showed high specific surface area (1200 m^2g^{-1}). In template methods, graphene is deposited by chemical vapor deposition on an existing template material. Representative work was done by CH_4 deposition at 1000 °C on porous Ni foam template.[35] The final product had more wrinkles and ripples as a result of different thermal expansion coefficients of graphene and Ni, which increased the specific surface area and improved the mechanical interlocking with polymer chains for composite

materials. Structures like GF-poly(dimethyl siloxane) could be bent, stretched and twisted without breaking.
Current graphene-based research is focused on enhancing the mechanical strength of 3D graphene structures for practical application. The diameter of GF pores has not yet been fully optimized and ranges from macroporous structures to pores of a few hundred micrometers. Networks of nanometer-sized pores are needed to develop optimized fuel cell system.

1.3 Platinum in fuel cells and electrochemical oxygen reduction

Pt was discovered as a valuable material in 1780s and is one of the most widely used catalysts for chemical reactions.[35] The main drawback is the high price of platinum-based catalysts. Pt is a scarce element in the Earth's crust, with a relative abundance of approximately 0.01 ppm.[36] Some nickel and copper ores contain Pt and are located mostly in South Africa (80% of the world Pt production). Only a few hundred tones are produced annually. It is overall used as a catalytic converter (35-40%), jewelry (up to 35%), petroleum and glass production (18%).[37] For these reasons, extensive studies have been undertaken to synthesize specific Pt nanocrystals to maximize and optimize the catalytic surface area, while minimizing material consumption. Research has been undertaken to optimize shape, size and facet distribution of the NPs, leading to improved activity and selectivity. Syntheses through wet chemical reduction (WCR) enable nanoscale design by controlling synthetic parameters to tune shape and size of the NPs.[38] Formation of Pt nanoparticles (Pt NPs) in solution includes reduction, nucleation, growth and ligand capping, Fig. 1.3.[39] Representative examples of synthesis procedures are given in Table 1.2. In electrochemical sense, platinum is primarily utilized as a catalyst for oxygen reduction reaction (ORR), a limiting step in the performance of a FC system.[39][40] ORR is a multi-electron reaction which includes a number of elementary steps with different reaction intermediates.[41]
Wroblowa et al. proposed a reaction scheme elucidating the complexity of O_2 reduction at metal surfaces (1976), which has been repeatedly supported by various experimental and computational studies.[42][43] O_2 can be electrochemically reduced directly to H_2O ("direct", $4e^-$ reduction) or through intermediate formation of adsorbed H_2O_2 ("series", $2e^-$ reduction). Adsorbed $H_2O_{2,ad}$ can be electrochemically reduced into H_2O ("series", $4e^-$ pathway), decomposed at the metal surface or desorb into the solution. Marković et al. has experimentally established an interpretation of Pt catalyst reaction based on ORR through a "series" pathway via $H_2O_{2,ad}$ intermediate,[41] concluding that negligible O-O bond splitting occurs prior to peroxide formation. $H_2O_{2,ad}$ may or may not be reduced to

water but in both cases, the addition of the first electron to O_2 appears to be the rate determining step in the ORR. The rate expression is:

$$i = nFKc_{O_2}\left(1-\theta_{ad}\right)^{x}\exp\left(-\frac{\beta FE}{RT}\right)\cdot\frac{\exp\left(-\gamma r\,\theta_{ad}\right)}{RT} \tag{1.4}$$

where i is the observed current, n the number of electrons, K the chemical rate constant, c_{O_2} the concentration of O_2 in the solution, θ_{ad} the total surface coverage by all adsorbed species, x = (1 or 2) depending on the site requirements of the adsorbates, E the applied potential, β and γ are symmetry factors (assumed 1/2) and $r\theta_{ad}$ parameter characterizing the rate of change of the apparent standard free energy of adsorption with the surface coverage by adsorbing species.

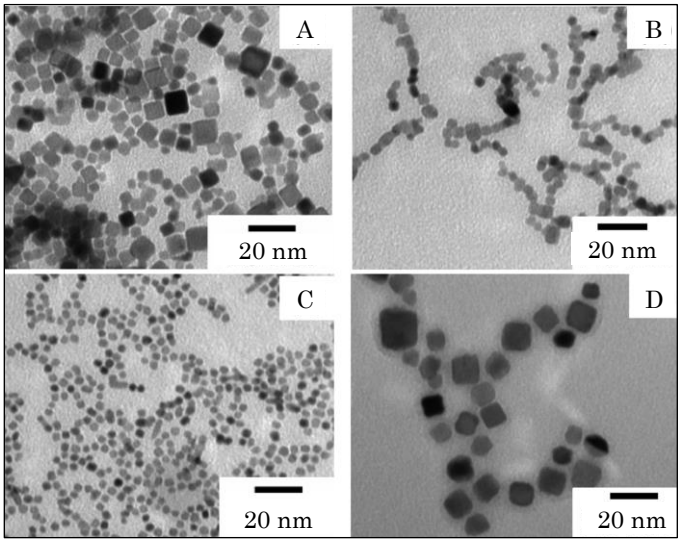

Figure 1.3 TEM images of Pt cubes: (A) without time control of NaI addition during the synthesis, (B) with time control, (C) prepared in dimethylformamide (DMF)/H_2O = 3:1 with time control of NaI addition, and (D) with time and pH control. Adapted with permission from ref.[44]. Copyright © (2010), American Chemical Society.

This rate expression, in combination with the reaction pathway mechanism, is used to analyze the effects of different factors on the kinetics of the ORR regarding Pt(hkl) surfaces. Catalyst development has to rely on fundamental understanding of the platinum-electrolyte interfacial reactions, as well as optimization of platinum surfaces, Fig. 1.4. Most promising catalyst must include both optimizing the catalyst surface area and modifying the intrinsic activity of Pt by introducing bimetallic nanostructures. Changing the local bonding environment, the distribution of active sites and intrinsic

electronic properties allow for tailor-made catalysts with enhanced electrocatalysis and ultra-low Pt loadings.

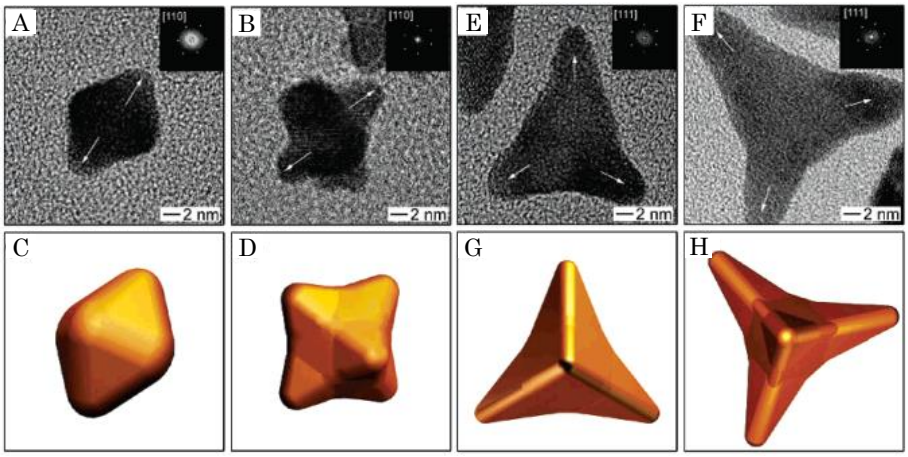

Figure 1.4 High-resolution transmission electron microscope (HR-TEM) images of Pt NPs obtained with molar ratios between $NaNO_3$ and H_2PtCl_6 of (A, E) 5.5 and (B, F) 11.0, respectively. The insets show fast Fourier transform (FFT) patterns used to determine the crystallographic directions marked in the insets. (C, D, G, H) Models showing that the growth of Pt NP was substantially enhanced at ridges and corners to form both octapods and tetrapods. (Adapted with permission from ref.[45]. Copyright © 2010, American Chemical Society.)

The relationship between surface area and electrochemical reactivity has been termed "structural sensitivity" and establishes a relationship between the kinetics of electrochemical reactions and Pt single crystal surface structures.[46] Correlations between the kinetics of the ORR and the surface coverage of chemisorbed oxygen-containing species on both polycrystalline and single-crystal electrodes have been reported.[47] Chemisorbed oxygen-containing species are present on the Pt surfaces in a reversible form (denoted as OH_{ad}) and an irreversible form (denoted as "oxide"). Experiments demonstrated that the order of activity of Pt(hkl) in 0.1 M KOH, under combined kinetic-diffusion control (potential range of O_2 reduction E > 0.75V) is (100) < (110) < (111).[48]

Table 1.2 Pt nanoparticle green syntheses

Precurs.	Reducing agent	Solv.	Stabilizing agent	NP size (nm)	Ref
H_2PtCl_6	Voltage	Water	PEI	20-800	[49]
	H_2, citric acid		Citrate	40-50	[50]
	Ascorbic acid		Block copolymer [A]	~ 6	[51]
	Glucose		Starch	1.7	[52]
	Starch			2-4	[53]
	H_2, ethanol	Ethanol	-	< 3	[54]
	$NaBH_4$	THF	2-phenylethanethiol	~ 1	[55]
	Ethylene glycol		PVP	> 30	[45]
$Pt(acac)_2$	200 °C [B]	Oleylamine		8	[56]

[A] Pluronic F127 block copolymer, [B] Synthesis performed in autoclave.

However, reversible adsorption of hydroxyl ions (OH_{rv}) on Pt(hkl) suppresses the kinetics of the ORR, but does not change the pathway of the reaction. As observed by rotating (Pt) ring disk electrode (RRDE) experiments, the "oxide" form, irreversibly adsorbed on the Pt(hkl) surface, does change the pathway of the reaction, since peroxide is experimentally detected on the ring electrode, when there is a significant amount of adsorbed peroxide on the electrode surface.[48] Furthermore, trace amounts of chloride can significantly change the activity and the reaction pathway of the ORR on Pt catalysts. In PEM fuel cells, chloride impurities can be present at the ppm level arising from the membrane electrode assembly (MEA) preparation process or from contamination of humidified feed streams. Even a 4 ppm chloride impurity can result in a voltage loss of 50 mV and equally affect the open circuit cell voltage.[41] MEA preparation and humidified feed streams therefore require highly clean conditions. In addition, extensive H_2O_2 production can damage the perfluorinated membranes and ionomers in the catalyst layer.[57]

1.4 Graphene-Pt catalysts

Hybrid graphene-platinum (G-Pt) materials can be traced back to 1999 and have developed fast during the past decade.[58] G-Pt syntheses can be broadly divided into three strategies: (1) "One-pot synthesis" where both precursors, GO and Pt salt, are reduced simultaneously,[59] (2) "Stepwise syntheses" involving already reduced GO (graphene) interacting with Pt salt which is subsequently reduced to Pt NPs, or (3) "Separate

reduction" where reduced GO (graphene) is mixed with already prepared Pt NPs which are then incorporated in the graphene network.[60] G-Pt with specific structural features including nanotubes [61], nano-spheres [62], nanofibers [63], and nanocages [64] have been synthesized using different reduction methods, such as chemical reduction, electrochemical reduction, thermally assisted methods, microwave assisted methods and combined reduction methods. Honma et al. synthesized graphene nanosheets decorated by Pt clusters with a range of sizes (from subnano Pt clusters of 0.5 to 1.5 nm).[65] The Pt NPs obtained exhibited a greatly enhanced specific surface area in comparison with Pt on graphite support material (Vulcan XC-72R) and improved activity for the methanol oxidation reaction (MOR).

A general approach to the preparation of graphene-metal NPs in water-ethylene-glycol systems using GO as a precursor and metal NPs (Au, Pt and Pd) as building blocks has been proposed.[66] In this method, metal NPs were adsorbed on the GO surface, which was not only beneficial for the subsequent reduction of GO by ethylene glycol, but also prevented restacking of reduced graphene sheets and resulted in formation of stable G-NP composites. Kou et al. synthesized a G-Pt hybrid material with strong Pt NP bonding, average size of 2 nm, and greatly enhanced durability.[67] The properties of both G-Pt and commercial catalyst were investigated with cyclic voltammetry (CV) during 5000 cycles in N_2-saturated 0.5 M H_2SO_4. The initial electrochemical surface area (ECSA) of G-Pt and commercial catalyst (E-TEK) were 108 m^2g^{-1} and 75 m^2g^{-1}, respectively. The retained ECSA after the 5000 cycle degradation for both G-Pt and E-TEK had decreased to 62.4% (67.6 m^2g^{-1}) and 40%, respectively. ORR activities decreased similarly to 49.8% for the G-Pt, while the commercial catalyst kept only 33.6% of its original activity. Li et al. prepared G-Pt via chemical reduction of GO and H_2PtCl_6 by $NaBH_4$.[68] The peak current density of Pt at the potential of 0.652 V (vs. Ag/AgCl) showed that the composite had superior catalytic performance towards methanol oxidation, almost twice higher than the commercial Pt-Vulcan catalyst (199.6 mA/mg Pt and 101.2 mA/mg Pt, respectively). The Pt NPs in this setup were in the size range of 5 to 6 nm. The catalytic stabilities of the G-Pt and Pt-Vulcan in 0.5 M CH_3OH and 0.5 M H_2SO_4 solution at a fixed potential of 0.60 V were examined by chronoamperometry. Initially catalysts showed rapid current decay due to the formation of intermediate species, such as CO_{ads} and CHO_{ads}, during methanol oxidation. Gradually, the current stabilized and a pseudo-steady state was achieved. It appeared that the current density of the G-Pt was higher than that of Pt-Vulcan catalyst electrodes during the whole testing duration which indicated superior electrocatalytic stability of the G-Pt catalyst. Pt loadings up to 80 wt.% were achieved on surface-functionalized graphene nanosheets, with particle diameters less than 3 nm, resulting in current densities of methanol electrooxidation at least twice than the conventional Pt on carbon support.[69] Furthermore, these catalysts maintained high activities without noticeable NP aggregation even at increased catalyst loadings ranging from 0.2 to 2.0

mg_{Pt}/cm^2. Highly controllable deposition of uniform Pt NPs assembled on graphene and functionalized with poly(diallyldimethylammonium chloride) via a $NaHB_4$ reduction process has also been established.[70] Loadings ranging from 18 to 78 wt.% of approximately 4.6 nm Pt NPs with predominantly Pt(111) facets was achieved. An overview of representative electrocatalysts employed in PEMFC systems and relevant properties is given in Table 5.1, Chapter 5.

Bimetallic NPs enhance the catalytic properties and resistance to catalyst poisoning compared to monometallic NPs.[71][72][73] G-Pt/Ru catalyst exerted higher electrocatalytic activity for both methanol and ethanol oxidation than monometallic G-Pt catalyst.[74] Similar works report the achievement of graphene supported Pt, Pt_3Co, Pt_3Cr and G-Pt/Pd alloy NPs.[75][76] These alloyed electrocatalysts generally show enhanced properties towards ORR or fuel oxidation reactions (e.g. methanol oxidation reaction, MOR), high electrocatalytic activities and low overpotentials, due to the properties of the individual nanoparticle and synergetic effects. However, they still consist of expensive, noble metals and exert limited stability to intermediate species and anode fuel crossover. Reports on bi- and trimetallic Pt-based catalysts are summarized in Table 5.2, Chapter 5.

Defective GF as a support for Pt NPs provides a large specific surface area and small pore sizes.[77] Loading of Pt NPs increased from 20 wt.% (for more pristine GF, carbon black, commercially available graphene) to 33 wt.% on defective GF. Relative durability was also tested by recording the retention of ECSA over 60 000 cycles via accelerated start/stop tests. GF-Pt lost all of the activity after only 30 000 cycles, which was attributed to facile oxidation of GF support (high content of oxygen groups). In membrane assemblies, GF showed better performance than carbon black, but significantly poorer performance in the mass diffusion region. Ajayan et al. recently presented promising data for methanol oxidation catalysis using Pt on functionalized graphene 3D structures, Fig. 1.5.[78] Pt-decorated 3D architectures were synthesized from graphitic carbon and nitride nanosheets by means of a facile, cost-effective co-assembly approach. Interconnecting 3D structures with much higher nitrogen content in the graphene sample than previously reported (29.4 at% compared to less than 10 at.%) enhanced the Pt NP adhesion, effectively avoiding aggregation. The NPs were uniformly dispersed, closely packed, 3.4 nm in size and had Pt(111) faceting. Moreover, a strong metal-support link (induced by N) resulted in reduced accumulation of CO_{ads} on Pt, increasing the catalyst poison tolerance. Stability of the catalyst was investigated by chronoamperometry at 0.5 V for 2000 seconds. The prepared catalyst showed the lowest current decay and retained the highest oxidation current over time, which was also confirmed by cyclic voltammetry. After 100 cycles initial forward peak current density decreased by 38.9%, compared to 71.2% for Pt-C catalyst.

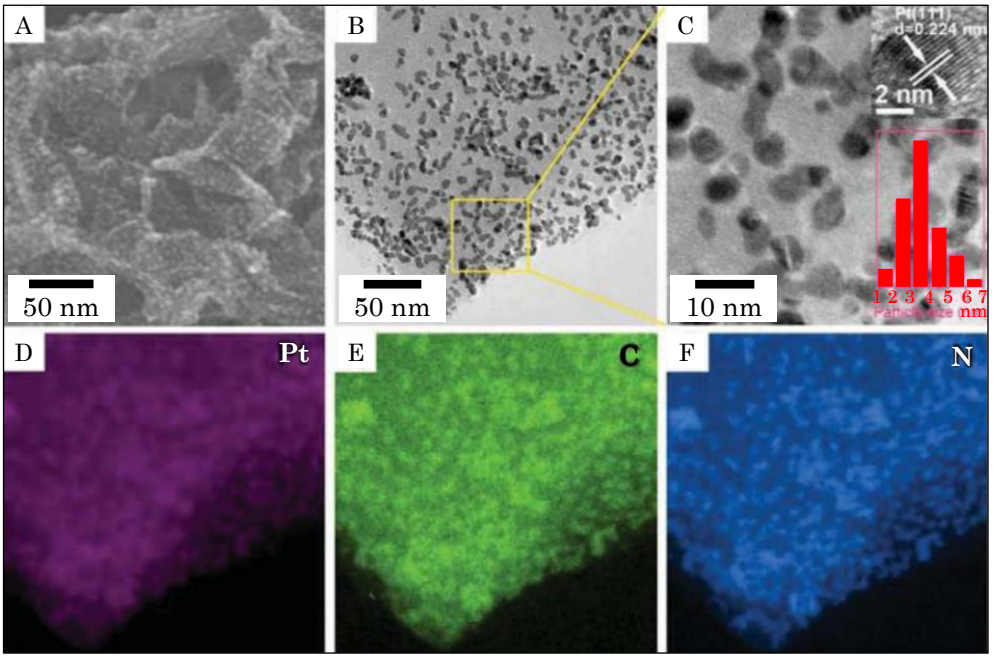

Figure 1.5 Morphological and structural analysis of 3D G-Pt architectures (A-C). FE-SEM image (A) and TEM images (B-C) of 3D G-Pt reveal well-dispersed Pt NPs on a 3D porous interconnected 3D framework. Insets in (C) is HR-TEM image and Pt NP size distribution. Elemental mapping images for detection of (D) platinum, (E) carbon, and (F) nitrogen.

Scanning electron microscopy (SEM) and tunneling electron microscopy (TEM) images were recorded after the durability measurements, showing clearly integrated, well-preserved and highly dispersed Pt NP assembly on the surface of the functionalized graphene structure.

New methods are continuously introduced to prepare graphene with higher specific surface area, more stable, inert and good anchor sites for Pt NPs. Bimetallic and trimetallic crystals, alloys and different nano-structures are being pursued in order to increase activity, decrease catalyst poisoning, improve adhesion to the support and overall stability. Still, there are challenges to be overcome, such as combining the two materials through a scalable synthesis process, which should also be environmentally friendly. Research is extensively turning to DMFC, DEFC and DFAFC setups as environmentally most benign with high throughput at low-cost.[8][79][80] Pt as a catalytic material should be recyclable in these systems, since its price is still one of the major challenges for commercialization.

1.5 Electrocatalysis

Electrocatalysis is the change of rate and selectivity of catalyzed electrochemical reactions on the electrode surface [81] and is studied using electrochemical techniques including cyclic voltammetry (CV), electrochemical impedance spectroscopy (EIS), chronoamperometry (CA), chronopotentiometry (CP), rotating disk electrode (RDE) and rotating ring disc electrode (RRDE) methods.[82][83] These methods provide information on the thermodynamics of redox processes, adsorption processes, kinetics of electron transfer reactions, reaction mechanisms, dielectric properties of a medium over a range of frequencies, capacitive properties of the material and quantitative determination of electroactive species adsorbed on the electrode. The RRDE provides information about specific products formed during catalytic reactions at the disk electrode based on the current measured at the surrounding ring electrode. Electrochemical dioxygen reduction is one of the key reactions for the conversion of chemical energy into electrical energy.[84] Voltammetry under RRDE hydrodynamic conditions are basis for evaluation of the selectivity of the ORR on a target catalyst and for understanding electron transfer pathways and formation of intermediates. Although valuable information can be obtained employing these methods, they were developed for flat surfaces and do not ideally fit to porous electrodes.[85] In these types of electrodes, the ORR products do not travel perpendicularly to the films due to the rotation, but stay in pores and channels inside the catalyst. Prolongation of the time that products spend in contact with the catalyst layer may lead to secondary reactions and the number of transferred electrons can be strongly affected. Research in FC catalytic material development is, however still primarily focused on RDE and RRDE methods for catalyst characterization, even when working with porous structures. In order to characterize catalytic material more efficiently, in situ methods i.e., electrochemical methods combined with other techniques, are employed.

Scanning electrochemical microscopy (SECM) is a microscopy based electrochemical approach providing laterally resolved characterization of electrode surfaces.[86] The SECM tip is positioned in close proximity to the sample surface acting as a local sensor for detection of reaction products generated at the surface of the catalyst. Spatial distribution of selective domains of electrocatalyst surfaces can be obtained with submicrometer resolution.[87]

Selectivity of electrocatalysis can be identified using a combination of electrochemical and chromatographic techniques, such as gas chromatography, ion chromatography, and high-performance liquid chromatography (HPLC).[88][89][90] Santasalo-Aarnio et al. investigated the selectivity of Pt and Pd during oxidation of methanol and ethanol, respectively, in alkaline solutions.[91] It was demonstrated that the electrochemical oxidation of methanol on Pt leads to the formation of two side products, formaldehyde and formate. In the case of Pd, only formate was obtained. Electrochemical ethanol oxidation

produced acetaldehyde and acetate on Pt, while it was more selectively oxidized to acetate on Pd.

Differential electrochemical mass spectroscopy (DEMS) technique can be applied to investigate the selectivity of Pt-based catalysts during methanol, ethanol and formic acid electrooxidation.[92] Electrochemical measurements are here combined with mass spectroscopy (MS) in order to detect reaction products.

Scanning differential electrochemical mass spectroscopy (SDEMS) was employed to efficiently evaluate the "integral" selectivity of electrocatalysts and spatially map the catalyst selectivity.[93] An array of electrodeposited Pt and Pt-Ru catalysts was tested for their selectivity in methanol electrooxidation. Pure Pt exhibited extremely high conversion efficiency of methanol to CO_2, reaching up to 90%. The addition of Ru of 6 at.% led to the highest current densities in case of both bimetallic Pt-Ru and pure Pt catalysts. Increased Ru content led to a decrease in the amount of formic acid produced during methanol electrooxidation. At Ru contents above 50 wt.%, formic acid was not detectable and formaldehyde was the only side product. DEMS is suitable for volatile reaction products capable of passing through the separating membrane between the electrochemical cell and the MS detector.

Detection of products of electrocatalytic reactions can be achieved by electrospray ionization mass spectrometry (ESI-MS).[94] Limited fragmentation occurs during ionization which minimizes interference among different mass fragments. ESI-MS was used to simultaneously detect volatile and non-volatile side products of methanol electrooxidation on Pt-based catalysts.[95]

A number of spectroscopic techniques have been combined with electrochemical techniques. Infrared absorption/reflection spectroscopy (IRS) [96], surface-enhanced infrared absorption spectroscopy (ATR-SEIRAS) [97], electron plasmon resonance (EPR) [98], fast Fourier transform infrared spectroscopy (FTIRS) [99], attenuated total reflection – Fourier transform infrared spectroscopy (ATR-FTIRS) [100] and Raman spectroscopy [101] are spectroscopic techniques used for in situ probing of electrochemical systems. FTIRS and Raman spectroscopy are techniques mostly combined with electrochemical methods to determine the selectivity of electrocatalysts. In-situ FTIRS elucidates mechanistic and kinetic behavior in respect to organic fuels used in FCs (methanol, ethanol, formic acid). Using ATR-SEIRAS method, the triple path mechanism in electrooxidation of formic acid on Pt catalyst in acidic media was discovered.[102] The adsorption–desorption equilibrium of adsorbed formate is quickly established and a part of the adsorbed formate is decomposed to CO_2 and H^+ ions. Adsorbed formate is an important intermediate in the electro-oxidation of methanol.

Testing of catalysts towards activity, durability and stability in FC systems is fundamental. Durability of an electrocatalyst must be tested at its development stage to evaluate the long-term performance. Potentiostatic and galvanostatic polarization

techniques are the most commonly used electrochemical techniques to estimate catalyst stability.[103] Electrochemical impedance spectroscopy (EIS) is used to monitor electrocatalyst degradation on the electrode-electrolyte interface.[104][105] CV provides simple means to obtain information about degradation at certain potential values. Electrochemical quartz crystal microbalance (EQCM) technique monitors degradation of metallic catalyst by mass measurements.[106][107] Inductively coupled mass spectrometer (ICP-MS) equipped with an electrochemical scanning flow cell offers in-depth investigation for studying degradation of electrocatalysts.[108] ICP-MS enables on-line downstream elemental surveillance of electrocatalyst product degradation at different electrode potentials.

Ex-situ methods include microscopic and spectroscopic techniques. Morphology, spatial distribution and size of the particles are imaged prior and after the durability tests. TEM, HR-TEM, identical location TEM (IL-TEM) [109], identical location scanning electron microscopy (IL-SEM) [110], atomic force microscopy (AFM) and electron energy loss spectroscopy (EELS) are advanced techniques that monitor ex-situ degradation of catalyst particles. An overview of techniques used to characterize PEMFC components is given in Table 1.3. Surface-sensitive spectroscopic techniques provide information on the degradation phenomena based on crystallographic structures, elemental states and distribution. Techniques primarily used include X-ray photoelectron spectroscopy (XPS) to analyze the spectrum of elements and binding energies, powder X-ray diffraction (XRD) to examine durability of particles, size and faceting [111], X-ray adsorption spectroscopy (XAS) to investigate atomic local structure and electronic states, Raman spectroscopy which identifies molecules by their vibrational and rotational frequencies, and IR spectroscopy which can determine functional groups in molecules. Applied techniques depend on the type of the required information.

Table 1.3 Techniques used to characterize different components of FC systems.

Technique	Subject of investigation	Advantages	Disadvantages	Ref
Electrochemical (CV, RDE, RRDE)	Kinetic characterization	Significant kinetic insight	Sensitive to artefacts and roughness	[112]
In-situ FTIR	Products and adsorbed species	Detection of volatiles, identification of adsorbates	Sensitive to roughness and reflectivity in liquid electrolytes; IR-drop	[113]
On-line FTIR	Volatiles formed in FCs	Detection of volatiles	No commercial setup available	[114]
FTIR Diffuse Reflection	Volatiles and FC adsorbates	In-situ FC studies	No detection of non-volatiles	[115]
DEMS	Volatiles at technical electrodes	Detection of volatiles by galvanostatic and potentiostatic methods	Only liquid electrolytes, No detection for non-volatile products	[116]
X-ray methods (XRD, XPS, XAS)	Particle size, facets, and bond strength	Qualitative/ quantitative analysis of catalyst and support surface composition, bonding state of elements determined	Quantitative analysis needs careful calibration	[117]
Microscopy (SEM, TEM, AFM, EELS)	Morphology characterization	Determination of particle size and shape	Sensitive to el.-stat. charge, not for all types of carbon	[118]
EIS	Characterization of FC electrodes	Structure and kinetic studies	Equilibrium required, artefacts	[119]
Multi-Purpose Electrochemical Mass Spectrometry (MPEMS)	Volatiles at FC electrodes	In-situ FC studies	Mass signals overlapping	[120]
NMR-spectroscopy	Polymer electrolytes	Reactions in polymer matrix, thermal stability studies	Sample preparation critical, expensive instrumentation	[121]
Thermogravimetric Analysis (TGA, DTA)	Polymer electrolytes	Thermal stability studies	Long term stability predictions	[122]

1.6 Future perspectives: Pt-free catalysts

Recently, Pt-free catalysts have been developed. These are, e.g. non-precious metals (Fe, Co, Mn), metal oxides (Fe_2O_3, Fe_3O_4, Co_3O_4), doped graphene, and biomaterials (bacteria and enzymes).[123][124][125][126][127][128] Metal and metal-oxide catalysts often suffer from dissolution, sintering and aggregation in working conditions of a FC system. This results in catalyst degradation and strongly diminished electrical conductivity. Electron transfer

is then hampered during the ORR process. Based primarily on high electrochemical surface area (ECSA) and possibility of heteroatom-doping (N, B and S), graphene nanomaterials were found to give good electrochemical response and reactivity. Therefore, graphene-based materials are regarded as promising candidates in replacing noble elements as electrocatalysts towards ORR.[14] Nitrogen-doped graphene (N-G) exhibited high electrocatalytic activity with long durability as well as CO tolerance compared to conventional Pt catalysts. Biofuel cells operate using biological molecular systems as catalysts in order to achieve redox reactions. Biological systems are either enzymes or whole organisms, such as bacteria. Biofuel cells (BFC) are promising green energy sources able to harvest electricity from various organic materials. Key advantages of BFCs, over conventional energy sources, are abundancy of catalysts and environmental sustainability. Most critical issues are short lifetime and low power density. These limitations are related to enzyme/bacteria stability, low electron transfer rates and catalyst loadings.[129][130] Microbial catalysts are whole living organisms that catalyze reactions in FCs. Generally, these are robust systems able to operate on a variety of fuels, and are usually capable of oxidizing the substrate completely to CO_2 and water. An example is direct electrochemical communication of *Shewanella putrefaciens* bacteria with an anode by membrane cytochromes, Fig. 1.6: [129]

$$\text{Lactate} \xrightarrow[\textit{putrefaciens}]{\textit{Shewanella}} \text{Waste} + \text{Cyt}^-$$

$$\text{Cyt}^- \xrightarrow{\text{Anode}} \text{Cyt} + e^-$$

In order to increase the catalyst loading, graphene was employed as electrode material in BFCs.[131] Reports on highly porous 3D interfaces made from crumpled, strutted and graphene foam 3D structures are considered for future BFC fabrications. It has been reported that bacteria provide higher anodic biocatalytic current densities once graphene is part of the electrode interface.[132] Bahartan et al. prepared recombinant *Saccharomyces cerevisiae*, wrapped by GO sheets. After the microbes reduced GO to graphene, glucose oxidase was immobilized on the surface of graphene-wrapped *Saccharomyces cerevisiae*.[133] Longer stability and direct electron transfer occurred only in the setup with graphene sheets, in contrast to a reference experiment without graphene present.

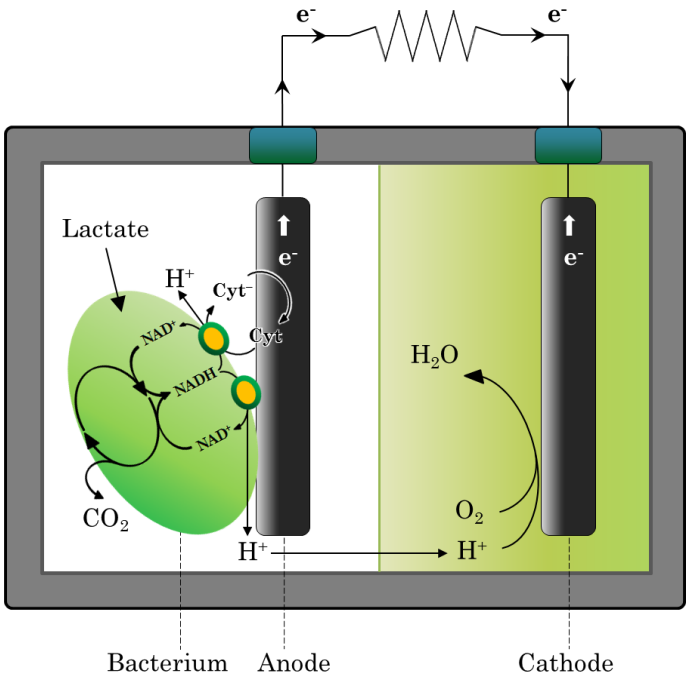

Figure 1.6 Schematic principle of a microbial fuel cell (MbFC). A microorganism serves as a catalyst.

Complex optimization addressing the influence of the electrolyte, electrode arrangement, compartment volumes, etc. has been scarcely covered in graphene-based microbial FCs (MbFCs), although these parameters were key features for remarkable BFC power outputs in the past.[134] This indicates that graphene properties are still not fully utilized. The most intriguing achievement so far has been fabrication of bioanodes and biocathodes by self-assembling bacteria with graphene, in a single-step process.[135] However, this effective and sustainable approach needs optimization of operational and constructional features in order to develop cutting edge, high performance BFCs.

Chapter 2

Methodology

This chapter is the overview of methods and techniques used for characterization of synthesized electrocatalysts. Fundamental principles and focus points of employed methods are described in order to support the discussions in following chapters. Methodology is, therefore, divided into three main segments: (1) spectroscopic, (2) microscopic, and (3) electrochemical techniques. The exceptions are thermogravimetric analysis and differential thermal analysis, which are described separately.

2.1 Thermogravimetric analysis

Thermogravimetric analysis (TGA) is a method to weigh the material as a function of increasing temperature or time.[136] TGA gives information about physical properties of the material such as phase transitions, vaporization, absorption, desorption and sublimation. Chemical information such as chemisorption, desolvation, oxidative degradation and solid-gas reaction can also be obtained from TGA measurements.[136] TGA can be used for reaction kinetics and degradation mechanism studies, materials characterization by analysis of specific decomposition profiles, determination of organic/inorganic content in a sample (useful for verifying predicted material compositions), and in polymer material science as a versatile characterization tool. TGA measurements are defined by high-precision instruments required to monitor mass change during temperature change. The basic instrumental requisites for TGA are a high accuracy balance with a crucible holder for the sample, and a programmable furnace (either constant heating rate, or for heating to achieve constant mass loss by time). The operating principle is generally the same: a precise amount of the sample is placed in a small crucible and inserted in an electrically heated furnace. In order to accurately conduct the measurements, the furnace is equipped with a thermocouple.[136] The voltage output of the thermocouple is compared to the voltage vs. temperature table stored in the computer's memory. The sample chamber can be purged with an inert gas to prevent oxidation or side-reactions.

In the Ph.D. project, the TGA measurements were employed to investigate the NP loading in the graphene-supported catalysts.

2.1.1 Differential thermal analysis

Differential thermal analysis (DTA) is a thermoanalytic technique, similar to TGA, where the material under study and an inert reference material experience identical thermal cycles, while the temperature difference between them is recorded.[137] The differential temperature (sample to reference) is plotted against time or temperature and expressed as a DTA curve, or thermogram. The DTA curve exhibits data on the experienced transformations in the sample, such as: glass transitions, fusion, crystallization, melting and sublimation.[137] The DTA setup contains sample holders, thermocouple joints between the sample and reference containers, a programmable furnace for regulating the temperature, and a recording system. The two thermocouple units are connected to a voltmeter where the first thermocouple is placed in an inert material (usually Al_2O_3), the second one in the analyzed sample. A deflection of the voltmeter is recorded with the increase of the temperature. The input of heat increases the temperature of the reference material, but is incorporated as latent heat in the sample. In this way, sample phase transitions can be obtained.[138]

2.2 Spectroscopic techniques

2.2.1 Ultraviolet–visible spectroscopy

Ultraviolet–visible spectroscopy or ultraviolet-visible spectrophotometry (UV-Vis) is a spectroscopy technique in which light absorption is measured in the visible and adjacent (near-UV and near-infrared) electromagnetic spectrum.[139] A spectrophotometer is used for measuring transmitted light signal through solutions, transparent solids and even gaseous samples. Depending on the the monochromator, the sample can be scanned at a fixed wavelength (λ) or the entire spectrum of visible light. The UV-Vis spectrophotometer compares the light intensity before (I_0) and after (I) has passed through the sample, usually expressed as a percentage (%). Transmittance is the ratio between the two signals (I/I_0) and absorbance is related to transmittance through the Beer-Lambert's law[140]:

$$A = -\log\left(\frac{I}{I_0}\right) = \varepsilon \cdot l \cdot c \qquad (2.1)$$

where ε is the molar absorptivity [M^{-1} cm^{-1}], l is the light path length (dimension of a cuvette containing the sample) in cm and c is the analyte concentration in mol/L (Fig. 2.1).[140] When the analyte is excited by a light source, specific wavelengths are absorbed while the rest are transmitted and recorded by the detector. Transmittance is then

converted to absorbance through equation 2.1 and often presented as a diagram of absorbance vs. wavelength. The UV-vis diagram exhibits sets of peaks, specific to the analyzed species, distinguishing different chemicals according to the absorbed wavelengths of the emitted light. Assuming the chemical composition of the sample and the light path length are well defined (ε and l), and the absorbance (A) experimentally obtained, the analyte concentration can be determined from the linearity of equation 2.1. However, the linear relation of the Beer-Lambert's law has its limitations: (1) at high concentrations, deviation of molar absorptivity coefficient causes nonlinearity due to electrostatic interactions of molecules in close proximity; (2) the refractive index change or shift in the chemical equilibrium can occur at high concentrations; (3) sample pollution might induce light scattering; (4) non-monochromatic radiation and stray light produce serious measurement errors.[141] To avoid these limitations, measurements require clean environment, proper sample dilution, optimized equipment, and calibration.

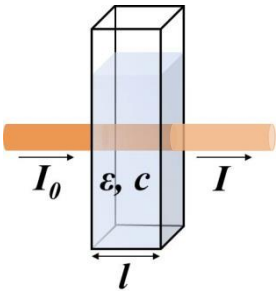

Figure 2.1 Scheme of UV-Vis absorption measurement principle.

Nature of light has a wave-particle duality and is described as a segment of electromagnetic radiation spectrum with synchronized oscillations of electric and magnetic fields, propagating at the speed of light.[142] As a particle, light is a stream of photons, while as a wave it possesses velocity, wavelength and frequency. Every photon has an energy associated to wave frequency according to Planck's equation[142]:

$$E = h\nu \tag{2.2}$$

where E is photon energy [eV], Planck's constant h = $6.626 \cdot 10^{-34}$ J s and ν is wave frequency in hertz = 1/s [Hz]. If photon frequency matches the natural frequency of free electrons at the nanoparticle surface, the atom is excited and electron energy levels elevated inducing resonant oscillation. This event is described as surface plasmon resonance (SPR).[143] Exciting a thin, continuous metal film, resonance spreads along its surface and is defined as a propagating surface plasmon resonance (PSPR). Since metallic NPs have defined size and shape, resonant oscillation is limited to the NP surface and defined as localized surface plasmon resonance (LSPR).[143] Due to this phenomenon,

optical surface-dependent nanoparticle properties like size, shape and composition can be measured by the UV-Vis method.[144] LSPR is characteristic to noble metals, especially gold, and it significantly enhances light absorbance.

The spherical gold nanoparticles (d = 7.9 ± 0.7 nm) show single LSPR peak at 520 nm in the absorption spectrum, while e.g. gold nanorods (width = 10 ± 2 nm, length = 50 ± 6 nm) exhibit a set of peaks at 520 nm for transverse orientation and shifting peak from 650 to 1050 nm for the longitudinal orientation.[145][146]

Platinum precursor ($H_2PtCl_6 \cdot xH_2O$) generates Pt(IV) in the reaction solution which exhibits a peak at 258 nm, while formed Pt NPs in the size range from 0.8 to 7.7 nm show no distinguishable peak in the absorption spectrum.[147] Pt nanospheres larger than 70 nm in diameter absorb light around 390 nm with a red shift peak progression as the NP size increases.[148] Since Pt NPs synthesized in this work are 1.2 ± 0.8 nm in diameter, no observable absorption peaks within the visible light range is observed. The distinguishable features of the precursor and Pt NPs formed, observed by UV-vis, are useful in monitoring Pt nanoparticle formation progress during the synthesis.

Gold-platinum core-shell NP (Au@Pt) synthesis is performed as a two-step reaction: (1) Au core synthesis followed by (2) Pt shell formation in the saccharide-based approach to metal nanostructure synthesis (SAMENS).[149] The ratio between the two metals in Au@Pt NPs was 5:2 which corresponded to atomically thin Pt shells on Au core for 8 ± 2 nm nanoparticles.[150] Formation of Pt shell structure on Au core can be monitored from the changes of the Au LSPR peak in the absorption spectrum. The extinction of both prominent peaks, Au at 520 nm and Pt(IV) at 258 nm, is an indication of a drastic change in the Au nanoparticle surface structure and complete reduction of Pt(IV) to Pt^0, i.e. successful Au surface coverage by Pt atoms. [150][151][152]

Graphene was used as a support material for synthesized nanoparticles. Its precursor, graphene oxide (GO) shows two distinguishable absorption peaks, the main at 230 nm, originating from π-π* bonds in sp^2 hybrid regions, and a peak at 303 nm due to σ-π* bonds from sp^3 hybridized orbitals.[153] Upon GO reduction, graphene exhibits observable changes in the absorption spectrum with a red-shifted, single peak at 270 nm.[154]

The graphene-nanoparticle hybrid materials keep most of their inherent properties, with slight peak shifts due to chemical interactions.[155] Graphene-Au material shows two distinct peaks at 270 nm from graphene, and a 530 nm red-shifted Au peak due to the coupling effect.[156][157] Graphene-Pt exhibits a single peak at 270 nm, originating from the graphene support. Graphene-Au@Pt catalyst holds the same peak positions as graphene-Au with a clear Au LSPR peak extinction, indicating core-shell structure.

UV-Vis spectroscopy is a suitable technique for characterization of compounds in solution. Absorption spectra of Au, Pt, Au@Pt, GO, graphene and graphene-NPs materials were recorded in this Ph.D. project.

2.2.2 Fourier transform infrared spectroscopy

Fourier transform infrared spectroscopy (FTIR) is a technique in which infrared (IR) radiation is passed through a solid, liquid or gas sample and an absorption or emission IR spectrum is recorded.[158] A mathematical process (Fourier transform algorithm) converts the raw data into the spectrum. Fourier transform spectroscopy shines a beam containing a spectrum of light frequencies, measuring how much of the beam is absorbed in the sample. This is followed by modification of the beam with combinations of frequencies. It is performed through a defined configuration of mirrors in the Michelson interferometer.[158] As one of the mirror moves, each wavelength of light in the beam is intermittently blocked and transmitted by the interferometer (Fig. 2.2). The signal of different wavelengths is recorded at different rates obtaining a broad spectral range. The process is repeated multiple times. Finally, a computer calculates all the accumulated data of the light absorption for each mirror position for a specific wavelength.[158] The raw data is called an "interferogram", whereas obtained spectrum is presented as transmittance vs. wavenumber.

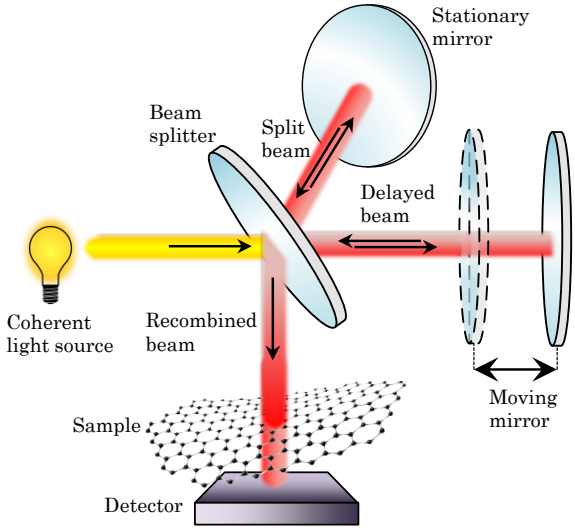

Figure 2.2 Scheme of FTIR spectrometer measurement principle.

GO FTIR spectrum discloses various configurations of oxygen groups and their vibrational modes, Table 2.1. Depending on the nature of group vibrational frequencies, the mid-infrared FTIR spectrum (400 – 4000 cm-1) can be divided into four regions: (1) the fingerprint region (600 – 1500 cm-1), (2) the double-bond region (1500 – 2000 cm-1), (3) the triple-bond region (2000 – 2500 cm-1) and the X–H stretching region (2500 – 4000 cm-1).[159]

Table 2.1 Infrared (IR) absorptions table for GO functional groups

Functional group		Absorption (cm^{-1})	Ref
Epoxide	C-O-C	1230 – 1320	[160]
sp^2 hybridized C	C=C	1500 – 1650	
Carboxyl group	COOH	1650 – 1750	
Carboxylic C–OH	C–OH	1080, 3530	
Hydroxyl group (phenol)	C–OH	3050 – 3800	
Ketone group	C=O	1600 – 1650, 1750 – 1850	

Functionalization of GO can be precisely characterized since nitrogen- and sulfur-containing compounds have specific stretching band values and can be differentiated from the groups mentioned.[161][162][163][164] Complementary to UV-Vis, FTIR is an effective tool in detecting the shape and size of optically active nanoparticles. It is extensively used for NP surface absorbents studies as well as NP shell characterization.[165] The advantage of FTIR is that a variety of spectra can be obtained in a short time not only from a solution, but also solid samples such as graphene paper with immobilized NPs. FTIR is a valuable characterization technique for graphene and functionalized graphene-based materials.

2.2.3 X-ray photoelectron spectroscopy

X-ray photoelectron spectroscopy (XPS) is a quantitative, surface-sensitive spectroscopic technique in which elemental compositions, empirical formula, and electronic states of the elements can be measured.[166] XPS records surface composition at depth of 0 to 10 nm. XPS spectra are acquired in high vacuum conditions by exciting the sample with an X-ray beam while measuring the kinetic energy and number of electrons that escape the material being analyzed. Generally, XPS is able to detect all elements with the detection limits in the range of parts per thousand (ppt). Parts per million (ppm) detection limits are possible with requirements to concentration of the analyte at top surface or long exposure time. XPS is often used to analyze elements, metal alloys, inorganic compounds, semiconductors, polymers, glasses, ceramics, inks, teeth, bones, medical implants, bio-materials, ion-modified materials and many other samples.[167][168][169] A representative XPS spectrum is a plot of the number of electrons versus the corresponding binding energy.[169] Each of the elements produces a fingerprint XPS signal where individual binding energy values identify the specific element in the sample. These spectral peaks correspond to the electron configurations each of the atoms. The number of detected electrons correlates with the amount of a certain element in the XPS sampling volume.[169] The raw XPS signal is corrected by dividing its signal intensity with a relative sensitivity

factor (RSF), and normalized over all of the elements detected.[169] These atomic percentages exclude hydrogen.
In the Ph.D. study, XPS is employed to corroborate elemental composition and functionalization of catalytic material since valuable information about binding energies can be obtained.

2.2.4 Energy-dispersive X-ray spectroscopy

Energy-dispersive X-ray spectroscopy (EDS, EDX, or XEDS) is an analytical technique for elemental and chemical characterization of a sample.[170] EDS is routinely used for chemical analysis of small volumes down to micro, nano and even atomic levels. EDX microanalysis can identify the characteristic X-rays produced by each element after bombarding the sample with high-energy electrons within an electron microscope. Generated X-rays from the sample are detected with an energy-dispersive spectrometer which distinguishes element-specific X-ray energies. Generally, the EDX detector is assembled of a semiconductor in a field-effect transistor (FET) preamplifier, a main amplifier, and a digital pulse processor.[170] When the sample emits X-rays, a charge pulse is generated on the detector, which converts it into a voltage pulse with an amplitude correlated to the detected X-ray energy. The voltage pulse is then converted into a digital signal, producing a typical X-ray spectrum. EDX is particularly useful in elemental concentration determination. The amount of X-rays emitted by each element in the sample depends on the concentration of the element as a mass or atomic fraction.[170] This is the basis of concentration assessment of different chemicals within the sample from a final X-ray spectrum. Finally, the information about the local elemental composition can be obtained through a process of X-ray mapping,[171] which is a combination of computer-assisted imaging and X-ray spectroscopy, resulting in a full qualitative and quantitative analysis of a studied sample. In the Ph.D. study, EDX technique was used within a TEM in order to identify and quantify elemental composition of the samples. However, the complexity of X-ray interactions with a sample may result in undesired events that require caution when analyzing the EDX spectrum. Elemental peak overlap, background signal noise and impurity contributions (mainly from the TEM sample grid) demand experimental and procedural exclusion in order to improve the data quality. Large contributions of Cu within the EDX spectrum of analyzed samples come, for example, from the TEM grid.

2.3 Microscopic techniques

2.3.1 Scanning electron microscope

A scanning electron microscope (SEM) is an electron microscope that scans the sample with a focused electron beam and generates images. The electrons interacting with sample atoms emit signals with information about the topography and composition. Depending on the instrument, the resolution of SEM can range between 1 nm and 20 nm. A wide range of magnifications is possible, from about 10 times (about equivalent to that of a powerful hand-lens) to more than 500,000 times, about 250 times the magnification limit of the best light microscopes. Samples for SEM can be solid, bulk specimens of any size that will fit within the specimen chamber. For conventional imaging in the SEM, specimens must be electrically conductive, at least at the surface, and electrically grounded to prevent the accumulation of electrostatic charge. Nonconductive specimens tend to charge when scanned by the electron beam, and especially in secondary electron imaging mode, this causes scanning faults and other image artifacts. Non-conducting materials are usually coated with an ultrathin coating of electrically conducting material, deposited on the sample either by low-vacuum sputter coating or by high-vacuum evaporation. Samples can be observed in high vacuum, or wet conditions (environmental SEM) and at a wide range of temperatures.

The detection of secondary electrons emitted by sample atoms when excited by the electron beam is the most common SEM mode. The number of detected electrons is closely related to the sample topography. By scanning the sample and collecting the electron signal, the topography image of the surface is, therefore, created. The signals result from interactions of the electron beam with atoms at various depths within the sample. In the most common or standard detection mode, the secondary electrons are emitted from the specimen surface. Consequently, SEM can produce very highly resolved images of a sample surface, disclosing details less than 1 nm in size. Back scattered electron images can provide information about the distribution of different elements in the sample. Characteristic X-rays are emitted when the electron beam removes an inner shell electron from the sample, causing a higher-energy electron to fill the shell and release energy. These characteristic X-rays are used to identify the composition and measure the abundance of elements in the sample.

Due to the very narrow electron beam, SEM micrographs have a large depth of field yielding a characteristic three-dimensional appearance useful for understanding the surface structure of a sample. In a typical SEM, an electron beam is thermionically emitted from an electron gun fitted with a tungsten filament cathode. Tungsten is normally used in thermionic electron guns because it has the highest melting point and lowest vapor pressure of all metals, thereby allowing it to be electrically heated

for electron emission, and because of its low cost. Other types of electron emitters include lanthanum hexaboride (LaB_6) cathodes or zirconium oxide emitters.

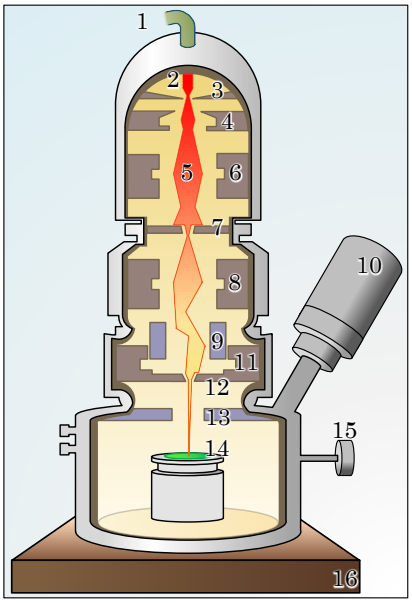

1. High voltage
2. Electron gun
3. Suppressor
4. Extractor
5. Electron beam
6. Electrostatic lens 1
7. Spray aperture
8. Stigmator
9. Deflection coils
10. X-ray detector
11. Electrostatic lens 2
12. Deflector aperture
13. Backscatter electron detector
14. Sample
15. Secondary electron detector
16. Vacuum pump

Figure 2.3 Schematic representation of SEM.

The electron beam, with energy ranging from 0.2 keV to 40 keV, is focused by one or two condenser lenses to a spot about 0.4 nm to 5 nm in diameter. The beam passes through pairs of scanning coils or pairs of deflector plates in the electron column, typically in the final lens, which deflect the beam in the x and y directions so that it scans in a raster fashion over a rectangular area of the sample surface. When the primary electron beam interacts with the sample, the electrons lose energy by repeated random scattering and absorption within a drop-shaped volume of the specimen known as the interaction volume, which extends from less than 100 nm to approximately 5 µm into the surface. Unlike optical and transmission electron microscopes, image magnification in an SEM is not a function of the power of the objective lens. SEMs may have condenser and objective lenses, but their function is to focus the beam to a spot, and not to image the specimen. Magnification is therefore controlled by the current supplied to the x, y scanning coils, or the voltage supplied to the x, y deflector plates, and not by objective lens power.
Depending on the instrument, the resolution can be between less than 1 nm and 20 nm. As of 2009, The world's highest resolution conventional (<30 kV) SEM can reach a point resolution of 0.4 nm using a secondary electron detector.[172]

2.3.2 Transmission electron microscope

After the development of electron lenses, Ruska and Knoll built a first transmission electron microscope (TEM) in the 1930s (Fig. 2.5A) for which Ruska was awarded the Nobel Prize in physics (1986). In TEM, a high energy electron beam (E_0 = 500 eV to 1 MeV) is transmitted through a thin sample (up to 100 nm), transmitted electrons are magnified and focused using electromagnetic and electrostatic lenses. The electrons are then imaged with a digital camera obtaining atomic resolution (~50 pm in latest setups).[173] Highly accelerated electrons pose wavelengths smaller than that of light (200 kV electrons have 0.025Å wavelength). This theoretically high resolution of an electron microscope is limited by aberrations in electromagnetic lenses. The implementation of aberration correction system can lead to an electron probe smaller than 1 Å.

Basic components of TEM include an electron beam generator (W, LaB_6 or field-emission gun), vacuum system, a series of electromagnetic lenses, electrostatic plates, sample stage and digital cameras used to image transmitted electrons. The usual electron source is W in the form of a hairpin-style or a spike-shaped filament. By connecting this gun to a high voltage source (~100 to 300 kV) it emits electrons to the vacuum by thermionic or field electron emission. The interaction of electrons with a magnetic field is utilized in manipulating the electron beam, Fig. 2.5B. Created magnetic field allows for the formation of a magnetic lens with adjustable focusing power. Deflection of electrons through a constant angle is further achieved with electrostatic fields. The electron beam is then focused in the objective configuration of a TEM. The vacuum system in TEM consists of several levels. A diaphragm pump achieves a sufficiently low pressure to allow the operation of a diffusion pump, providing the high vacuum level necessary for operations. Ultra-high vacuum (10^{-7} to 10^{-9} Pa) is required for high-voltage operation. This prevents generation of an electrical arc, especially important for the TEM cathode. Poor vacuum causes several major issues - a deposition of gas to the sample, or in more severe cases damage to the cathode caused by electrical discharge.[175] Sample sublimation issues are limited by the cold trap which adsorbs sublimated gases in the vicinity of the specimen. TEM sample stage is designed with airlocks, allowing the insertion of the sample holder into the vacuum with minimal increase of pressure in other microscope compartments.

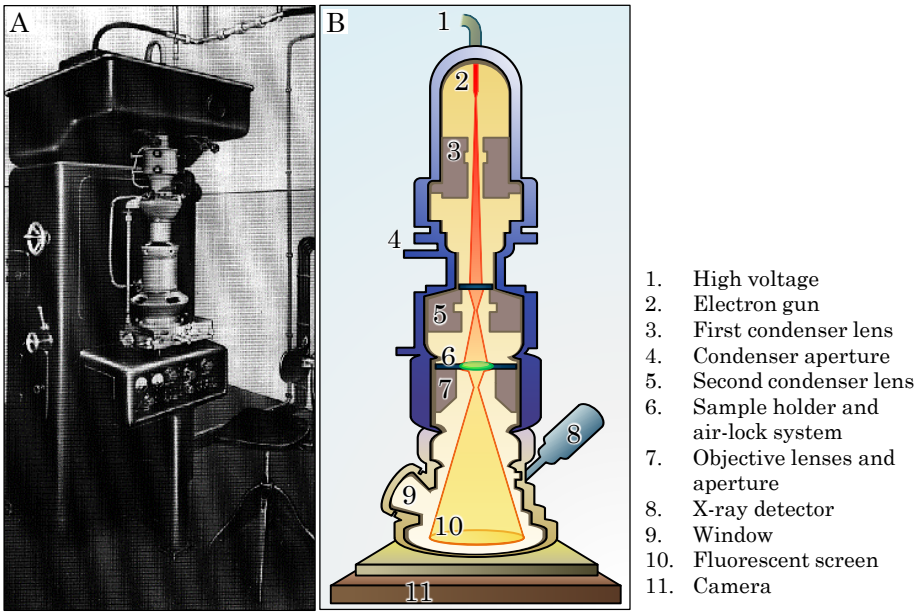

Figure 2.5 (A) The first commercially available TEM (produced by Siemens).[174] (B) Cross-sectional scheme of a TEM.

The sample holders support standard size of a TEM grid (3.05 mm diameter ring, few 100 μm thickness). Modern stages provide the ability for two orthogonal rotation angles of movement in double-tilt sample holders. The design criteria of TEM stages are complex and have many unique implementations depending on the experimental design and requirements.

2.3.3 State-of-the-art TEM

One of the fundamental limits of the resolution is determined by the quality of the objective lens and the wavelength (λ) of the electrons which form the image. This limit is called the point resolution limit and can be described by the equation[176]:

$$d_{min} = 0.43 \cdot C_s^{1/4} \lambda^{3/4} \quad (2.3)$$

C_s is the coefficient of spherical aberration and is the main factor that determines the lens quality. Rays passing a spherically aberrated lens at a high angle to the optical axis are focused closer to the lens than the rays passing along or at a small angle to the optical axis, Fig. 2.6A-B.

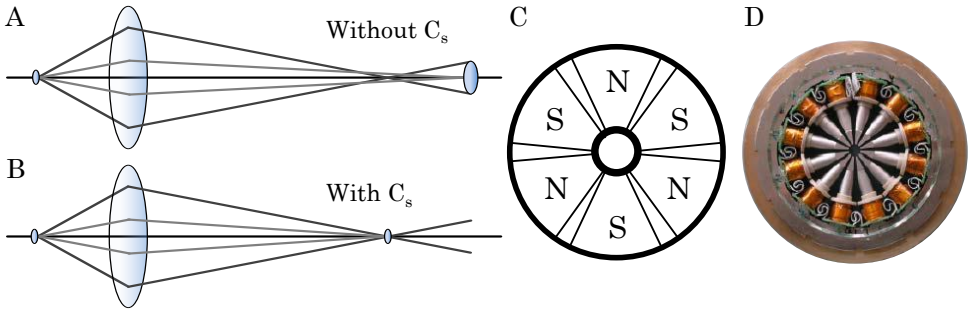

Figure 2.6 A) Standard electron lens with spherical aberration: rays at different angles to the optic axis are brought to a focus at different points. (B) Correction of the spherical aberration focusing all the rays in the same point. The small blue area on the right of the lens represents the aberration disc. (C) C_s corrector scheme with "N" and "S" representing magnetic polarity. (D) Actual C_s corrector.[177]

These incorrectly focused, high-angle rays produce a smearing of the image. Rays scattered at high angle carry information about the small spacings in the object. If they are blocked by inserting a suitable aperture in the back focal plane of the lens, the image is formed only by the small angle rays. In this image, spacings of the object are seen down to the point resolution. The major objective over the past decades has been the development of aberration correctors to compensate the spherical aberration, improving the resolution. Correction of electron optical lens aberrations is achievable through application of corrector hardware (Fig. 2.6C-D) for either imaging (TEM) or probe forming (STEM) lenses.[178].

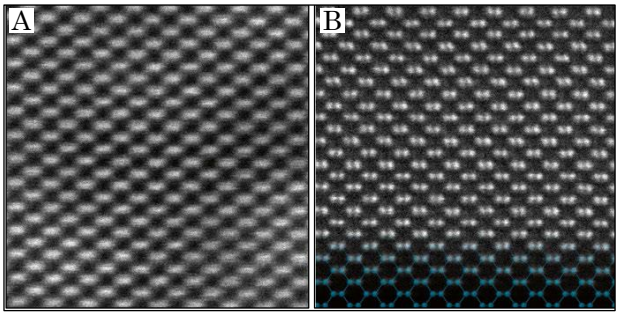

Figure 2.7 Image of an uncorrected (A) and corrected (B) Si crystal. Model of the structure presented in blue color. Dumbbells are separated at 1.3 Å in silicon [110].[174]

Modern TEMs allow *in-situ* imaging, making possible studying e.g. metallic nanoparticles in solutions, disclosing reaction mechanisms and even 3D imaging with atomic

resolution.[179] TEM image enhanced by a C_s corrector is shown in Fig. 2.7. Having such an advanced aberration correction system, the intensity of the electron beam can be dramatically lowered, allowing non-destructive and detailed imaging of sensitive samples. Chromatic aberration effects are reduced by passing the electrons through a monochromator which lowers the energy spread of the electrons before they hit the sample. Accelerating voltage of 80 keV has been used to study 2D structure of graphene without damaging the sample, since the damage threshold for C is 86 keV.[180]
Defects and dislocations in the 2D structure were imaged to have a deeper understanding of material properties under a load or applied strain, Fig. 2.8. This technology allowed for sub-ångstrom resolution and the ability to pinpoint single carbon atom position within the graphene lattice. Defects and dislocations in the 2D structure were imaged to have a deeper understanding of material properties under a load or applied strain, Fig. 2.8. This technology allowed for sub-ångstrom resolution and the ability to pinpoint single carbon atom position within the graphene lattice. Edge dislocations and carbon-carbon bond elongation/compression were imaged for the first time with true atomic resolution. In atomic characterization of the sample besides TEM, STEM mode imaging is getting recognition for having many advantages.

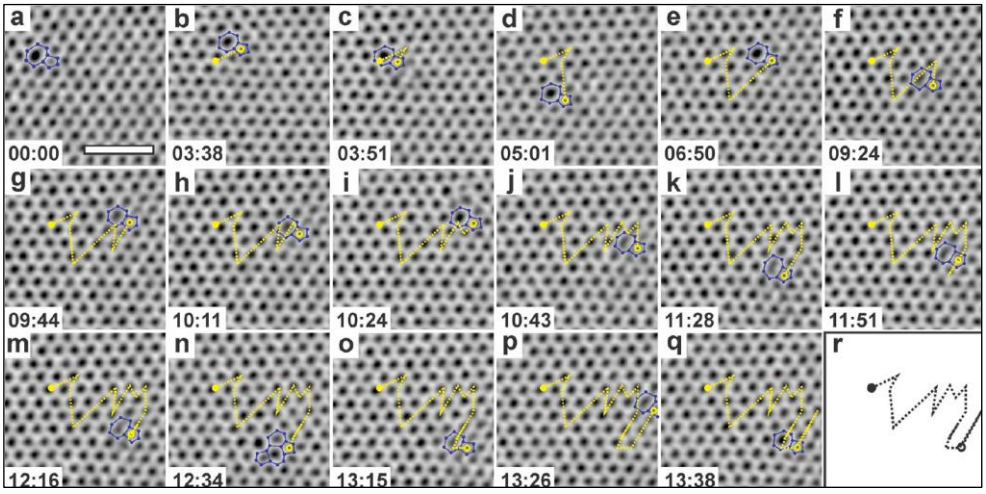

Figure 2.8 Trajectory of a dislocation in graphene at 700 °C. 63 frames over 14.5 min. [180] The scale bar in panel (a) is 1 nm.

This refers to the use of a particular detector geometry in STEM.[181] A large annular detector is placed in the optical far field beyond the specimen. The total intensity detected over the detector is recorded and displayed as a function of the position of the illuminating probe. The detector only receives a signal when the sample is present (the vacuum

appears dark in the image) and the heavier the atom, the higher the intensity of the scattering, leading to atomic number (Z) contrast in the image.[174] This mode provides great resolution improvement, allowing elemental studies at sub-50 Å resolution.[182]

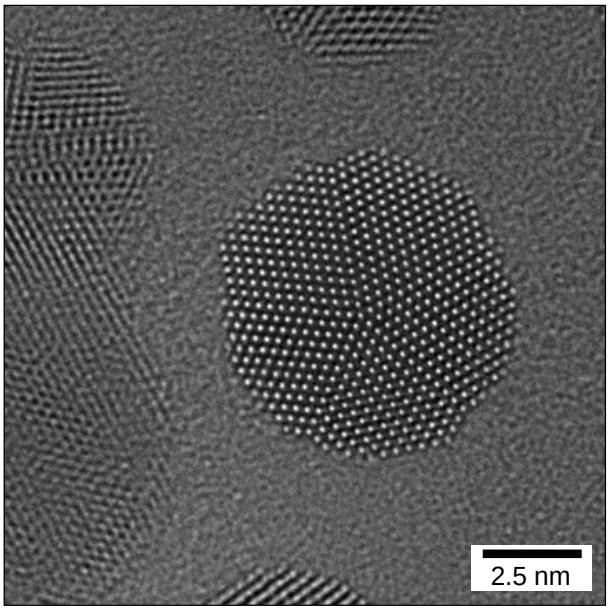

Figure 2.9 HR-TEM images of Au NPs recorded by aberration corrected Titan 80-300ST.

Au NPs have been imaged in HR-TEM Titan 80-300ST. Particles were deposited at a standard TEM carbon grid, positioned in single-tilt holder. The high resolution allowed for facile recognition of individual atomic rows. Crystal faceting could be determined from clear images due to the implemented aberration correction system. Fig. 2.9 shows the HR-TEM images of Au NPs with typical five-fold symmetry for nano-sized noble materials such as Au, Ag and Pt. This structure is known as decahedron and consists of five tetrahedron parts with fcc structure. Such arrangement of atoms is under strain because of mismatch between angles of crystallographic planes. In fcc structure the angle between adjacent (111) facets is 70.53 °, but for decahedron this angle should be 72 °. The 1.47 ° angle deficiency causes intrinsic strain and lattice distortion.[183]

2.3.4 Atomic-force microscopy

Atomic-force microscopy (AFM) is a high-resolution type of scanning probe microscopy (SPM). The information is gathered by "feeling" or "touching" the surface with a mechanical probe. Piezoelectric elements that facilitate tiny but accurate and precise

movements on (electronic) command enable very precise scanning. AFM has three major abilities: force measurement, imaging, and manipulation.

In force measurement, AFMs can be used to measure the forces between the probe and the sample as a function of their mutual separation distance, i.e. force spectroscopy. For imaging, the force of the probe to the sample can be used to form an image of the three-dimensional shape (topography) of a sample surface at high resolution. Scanning over the sample with the tip and recording the height of the tip profile corresponds to a constant probe-sample interaction. The surface topography is commonly displayed based on the height (z) of each point of the surface (x, y), meaning that each point contains information about position in three dimensions (x, y, z).

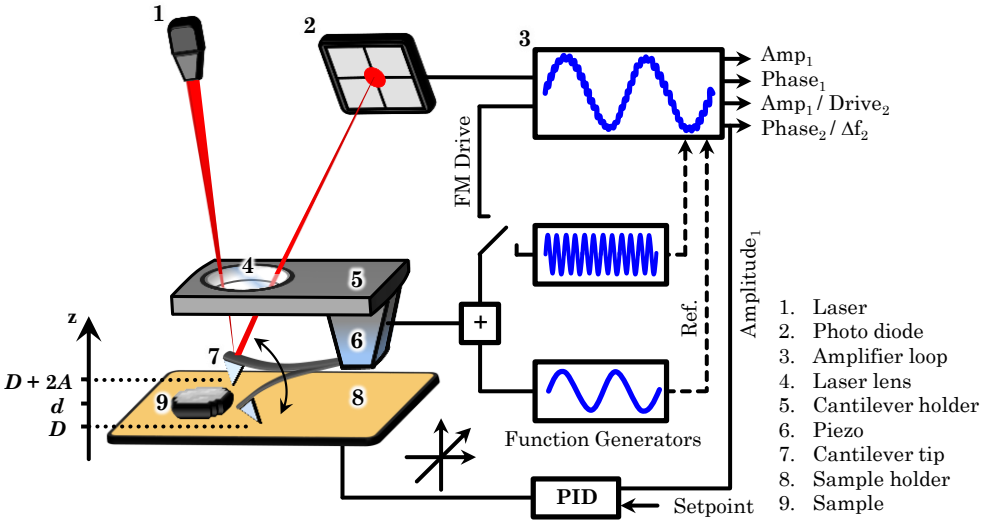

Figure 2.10 Schematic representation of AFM.

In manipulation, the forces between tip and sample can also be used to change the properties of the sample in a controlled way, e.g. atomic manipulation, scanning probe lithography and local stimulation of single living cells under physiological conditions.

Simultaneously with the acquisition of topographical images, other properties of the sample can be measured locally and displayed as an image, often with similar high resolution, e.g. mechanical properties like stiffness, adhesion strength, and electrical as conductivity or surface potential. Fig. 2.10 is a scheme showing a typical AFM setup. The small spring-like cantilever (1) is carried by the support (2). A piezoelectric element (3) oscillates the cantilever (1). The sharp tip (4) is fixed to the free end of the cantilever (1). The detector (5) records the deflection and motion of the cantilever (1). The sample (6) is

mounted on the sample stage (8). An xyz drive (7) permits displacing the sample (6) and the sample stage (8) in x, y, and z directions with respect to the tip apex (4).

2.4 Electrochemical techniques

2.4.1 Cyclic voltammetry

Cyclic voltammetry (CV) is a potentiodynamic electrochemical measurement in which the working electrode (WE) potential is ramped forward and backwards, linearly versus time. The resulting plot exhibits the current at the working electrode response versus the applied voltage.

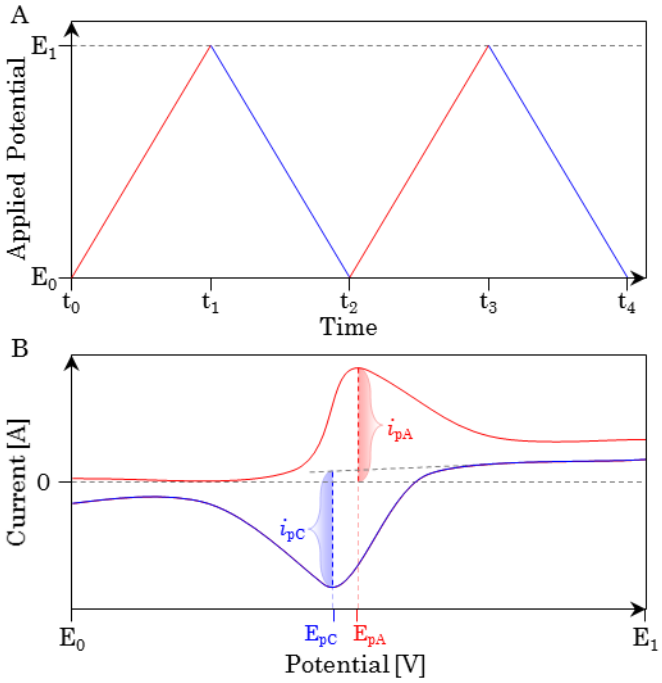

Figure 2.11 (A) Typically applied waveform potential signal in cyclic voltammetry. (B) Typical reversible cyclic voltammogram where i_{pA} and i_{pC} show the peak anodic and cathodic currents respectively with corresponding E_{pA} and E_{pC} peak potentials.

CV is often used to study the kinetics and reversibility/irreversibility of electrochemical reactions, as well as the electrochemical properties of an analyte in solution. Different electrochemical setups can be used for conducting CV measurements, such as two-, three- or four-electrode electrochemical cells. The electrodes are immersed in an electrolyte solution (often in mM range), with an ionic conductor, and often degassed by an inert gas

(Ar, N_2) to avoid contribution from dissolved electroactive gases, such as O_2. The electrolyte ensures good conductivity and minimizes iR drop so the recorded potentials correspond to actual potentials. For aqueous solutions, many electrolytes are available - typically alkali metal salts of perchlorate and nitrate. In non-aqueous solvents, the electrolyte range is more limited. Three-electrode electrochemical cells are mostly applied, with a working electrode (WE), a reference electrode (RE) with a stable potential value, and a counter electrode (CE) to which current is being drained. The potential is applied between the WE and the RE, while the current is measured between the WE and the CE. These data are plotted as current (I) versus applied potential (E). The positive current is ascribed to oxidation processes and is called anodic current, while negative current corresponds to reduction processes in the system is denoted as cathodic current. CV can, therefore, give information about redox potentials and electrochemical reaction rates, diffusion limitations, surface adsorbents, etc. The electrodes are positioned in an unstirred solution during CV. This stationary environment gives rise to characteristic diffusion-controlled peaks. Provided electron transfer at the working electrode is fast and the current limited by diffusion of analyte species to the WE electrode surface, the peak current will be proportional to the square root of the scan rate. This is expressed in Randles-Sevcik equation:[184]

$$i_p = 0.4463\mathrm{nFAC}\left(\frac{\mathrm{nFA}\nu\mathrm{D}}{\mathrm{RT}}\right)^{1/2} \tag{2.4}$$

where n is the number of exchanged electrons, F a Faraday's constant (96 485 C/mol), A the geometrical area of the electrode (cm^2), C is concentration of analyte (mol/cm^3), ν the scan rate (V/s), D is diffusion coefficient for species in cm^2/s, R the gas constant (J/Kmol), and T the temperature (K). Materials usually used for the WE include glassy carbon electrodes (GCEs), edge- and basal-plane pyrolytic graphite electrodes (EPG and BPG), platinum and gold. These electrodes are fitted in a insulator (commonly Teflon) with an electrode disk exposed at one end. A regular WE has a radius in the mm range. A controlled and well-defined shape surface area is essential for interpreting CV results.
The CE can be any conducting material inert towards the system-driving reaction. Reactions that may occur at the CE are often oxidizing or reducing the solvent or bulk electrolyte in order to maintain the observed current constant. The reactions are irrelevant as long as CE conducts current well.

2.4.2 Chronoamperometry

Chronoamperometry (CA) is an electrochemical technique in which the potential of the WE is ramped and the faradaic current monitored as a function of time. The information about the identity of the electrolyzed species is rather limited, but as with all pulse techniques, CA generates high charging currents which decay exponentially with time –

this can give us the information about the kinetic factor of the reaction. The Faradaic current is due to electron transfer event and it decays as described in the Cottrell equation:[185]

$$i = \frac{nFA\, c_j^0 \sqrt{D_j}}{\sqrt{\pi t}} \tag{2.5}$$

where c_j^0 is initial concentration of the reducible analyte j (mol/cm^3), D_j the diffusion coefficient for species j (cm^2/s), and t the time (s).
Since the current is integrated over long time intervals, CA provides a better signal-to-noise ratio in comparison to other amperometric techniques.

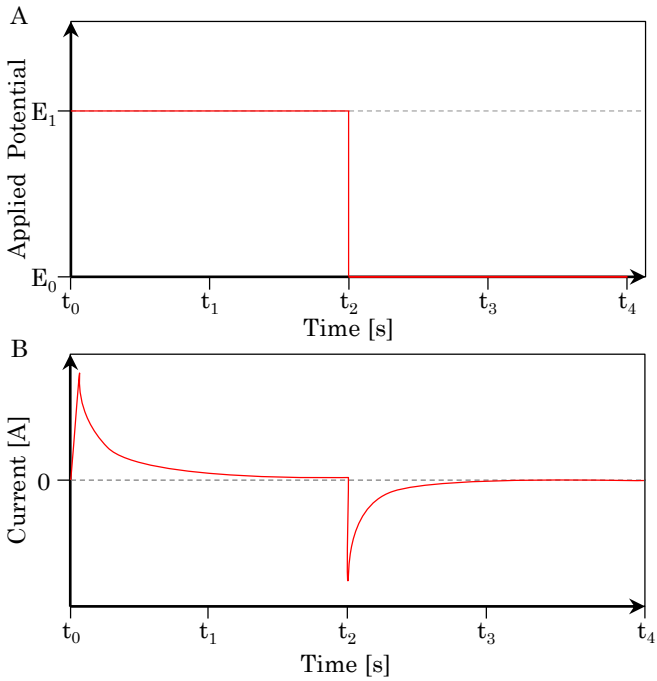

Figure 2.12 (A) Typically applied waveform potential signal in chronoamperometry. (B) Typical chronoamperometric response where current responds to the applied potential signal.

Chronoamperometry can be used to investigate the stability of electrocatalysts. By applying a potential at which reaction occurs at the catalyst deposited on WE, current is evolved and starts decaying after a period of time. By investigating the current decay over time, the stability of electrocatalysts within the electrochemical environment can be determined.

2.4.3 Rotating disk electrode experiments

A rotating disk electrode (RDE) is a hydrodynamic WE used in a three-electrode system. The electrode rotates along its vertical axes with a controlled angular velocity, usually given in rotations per minute (rpm). These WEs are often used in electrochemical studies when investigating reaction mechanisms related to redox chemistry, such as dioxygen reduction reaction (ORR), Fig. 2.13.

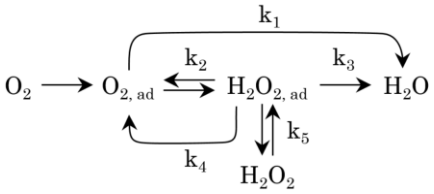

Figure 2.13 Proposed mechanism elucidating the complex mechanism of O_2 reduction on metallic surfaces.[42]

A more complex RDE system can be used in a rotating ring-disk electrode (RRDE). The RDE includes a conductive disk embedded in an inert casing and is attached to an electric motor with fine control of the rotation rate. The disk is made of a generally used electrode materials. During an experiment, the rotation induces a controlled convection flux of analyte to the electrode. Solution flows up perpendicularly to the RDE resulting in a laminar flow of solution towards and across the electrode, Fig. 2.14. The rate of the electrolyte flow can be controlled by the RDE's angular velocity and precisely modeled mathematically. In this setup, the electrolyte flow can achieve conditions in which the steady-state current is controlled by the solution convective flow rather than diffusion, in contrast to the steady-state CV where current is limited by the diffusion of species in solution. By variation of rotational velocity and running linear sweep voltammetry (LSV: CV in either positive or negative potential sweeping direction), different electrochemical phenomena can be examined, such as multi-electron transfer, the kinetics of a slow interfacial electron transfer, adsorption/desorption processes and reaction mechanisms. The peak current in a CV for a RDE is a plateau-like region, governed by the Levich equation:

$$I_L = (0.620) \cdot nFAD^{2/3} \omega^{1/2} v^{-1/6} C \quad (2.6)$$

where I_L is the Levich current (A), n the number of electrons transferred in the half reaction, ω the angular rotation rate of the electrode (rad/s), v is the kinematic viscosity (cm^2/s), and C the analyte concentration (mol/cm^3). The limiting current is usually higher than the peak current of a stationary electrode. The reason for this is in the mass transport of reactants which is actively supplied to the WE by the rotational motion of the RDE, eliminating diffusion.

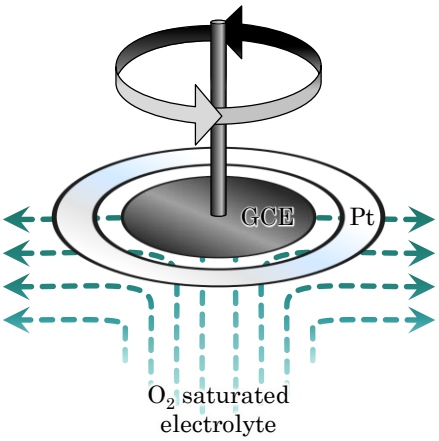

Figure 2.14 The laminar flow profile showing supply of fresh reactants to the electrode surfaces. The flow is developed for a circular object rotated in solution and can be modeled mathematically.

Rotation of RDE successfully removes any reaction products away from the surface by the electrolyte flow. In cases the products are the species of interest for the investigation, the RRDE can be used. It has a ring-shaped electrode closely surrounding the disc electrode. If certain product is expected from a reaction (H_2O_2 in ORR) occurring at the disc, it can be quantified at the ring electrode. A CV experiment is first required to determine the onset potential for the product undergoing a reaction. By applying that constant potential at the ring electrode, the evolved product is quantitatively transported to the ring by electrolyte flow, where it reacts on the ring electrode surface producing a current. This current can, for example, elucidate the extent of intermediate H_2O_2 in a 4 e^- reaction that is ORR. Based on the ratio of the ring current to disk current, the average electron transfer number (n) can be determined.

2.4.4 Polarization plots in fuel cells

FC performance can be assessed by (1) polarization plots, which are essentially current vs. voltage (i vs. E) curves showing the voltage output of a FC for a given current load, and (2) power plots (i vs. P) which describe the generation of power density at given current density values, Fig. 2.15. The polarization curve of a single PEMFC can be described by the expression:

$$E_{cell} = E_{OCV} - \eta_{act} - \eta_{ohm} - \eta_{conc} \quad (2.7)$$

where E_{cell} is the voltage of a FC, E_{OCV} is the open circuit voltage (OCV), η_{act} the activation overpotential in the two electrodes, η_{ohm} the ohmic overpotential (ionic and electronic) and η_{conc} the concentration overpotential difference in the two electrodes.

The ideal FC performance is, therefore, governed by reaction thermodynamics. The real FC performance is always less than ideal one due to different types of losses:

1. Activation loss (due to electrochemical reaction),
2. Ohmic loss (due to ionic and electronic conduction),
3. Concentration loss (due to mass transport limitations).

Since the power is a product of current and potential, the power density depends directly on both produced current density and OCV of the cell:[186]

$$P = \frac{EQ}{t} = E \cdot I \tag{2.8}$$

where E is electric potential or voltage (V), Q the electric charge (C), I the electric current (A). FC power density increases with increasing current density, reaches a maximum, and then starts decreasing during further increase of current density.

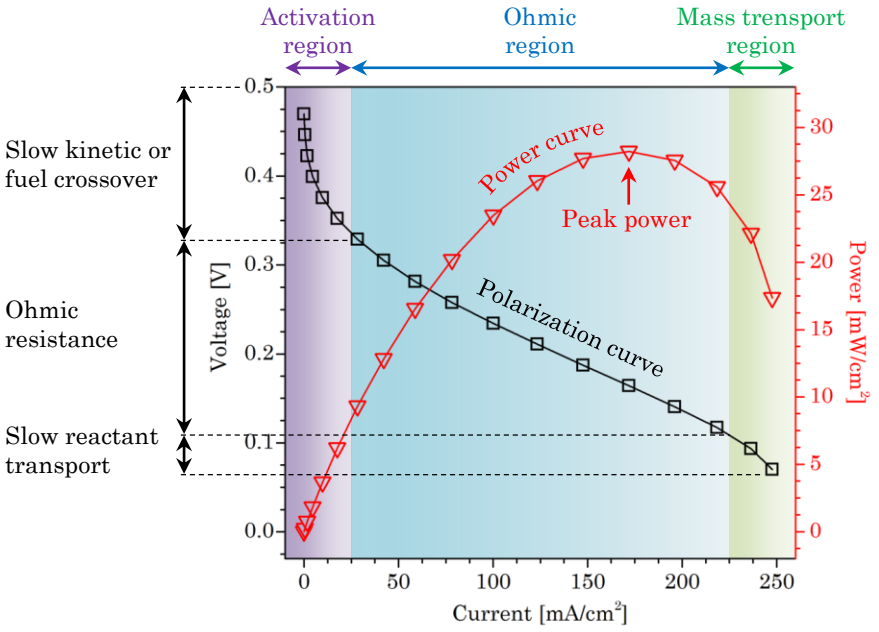

Figure 2.15 Polarization (i vs. E, black) and power (i vs. P, red) plots scheme with highlighted activation (purple), ohmic (blue) and mass transport (green) regions.

The main reason for this is in the ohmic resistance of a FC, which results in voltage loss with continuous production of current.[187] Being a product of the two (equation 2.8), power decreases at high current density values. At current densities above the power density maximum, therefore, both voltage efficiency and power density decrease. At current densities below the power density maximum, voltage efficiency improves but power density decreases. General practice in FC operation is at the running conditions of higher efficiency, preferably below the power density maximum.[186]

PEMFC operation at peak power density conditions induces stress to the FC due to high current densities forced to be produced at lower power and voltage efficiency. Furthermore, catalytic poisons accumulate rapidly at the catalyst surface as a result of the accelerated propagation of reactions. However, this unwanted effect can be exploited for FC stability measurements by chronoamperometry. If FC is conditioned at the potential value that corresponds to peak power density, over a longer period of time, the current density decay provides information about FC catalyst stability.

Chapter 3

Preparation, characterization and electrocatalysis of graphene-Pt catalyst

3.1 Introduction: materials design and application

Pt-based catalysts have been extensively used for polymer electrolyte fuel cells (PEMFCs) due to their high activity towards fuel oxidation and oxygen reduction reactions at temperatures lower than 100 °C. Due to environmental and economic reasons, directed by Pt scarcity, high demand and thus high price, have stimulated optimization of Pt-based catalysts. Among key factors governing the catalysis rate of Pt NPs, the most important ones are NP size and surface crystallinity. The active catalyst surface is related to the mass of the catalyst by the term "specific surface". It describes the relation between catalyst mass and its active surface directly exposed to the electrochemical environment, available for reactions. The increase of specific surface is a continued goal. Advances in nanotechnology have yielded a plethora of reliable and reproducible syntheses methods for < 5 nm Pt NPs. The decrease in catalyst NP size induces increase of the specific surface, with improvement often in orders of magnitude. On the other hand, constituted from up to 100 Pt atoms, simple Pt NPs cannot efficiently form extended and stable crystalline facets, resulting in plummeting catalytic activity. The "structural sensitivity" therefore sets a limit of maximum mass-to-surface specific activity to Pt NPs sized at ~ 2.2 nm, Fig. 3.1.[188][189][190]

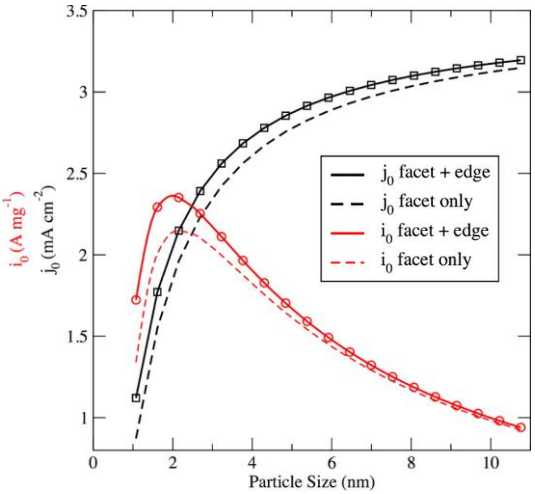

Figure 3.1 Activity trend versus Pt NP size. Exchange current is normalized against the NP mass and surface area for i_0 and j_0, respectively. Reprinted with permission from ref. [190]. Copyright © (2015) American Chemical Society.

In this chapter, designs of PEMFC catalysts are discussed, focusing on their benefits as well as drawbacks. Aiming at diminishing the general issues of electrocatalysts, graphene-supported Pt NP catalysts have been synthesized. SAMENS synthesis[149] yielded homogeneous size distribution of 1.2 nm Pt NPs which were covalently immobilized on cysteine-functionalized graphene support (G-Cys-Pt). The as-synthesized catalyst was electrochemically tested towards ORR and electrochemical oxidation reactions of fuel molecules. The electrocatalytic performance was compared to the commercially available catalyst currently used in the industry, Pt NPs (< 5 nm) on graphitized carbon support (C-Pt). The catalytic performance of both kinds of Pt NP materials on carbon-based support are qualitatively very similar. Therefore, the focus here is on examining the alterations of electrocatalytic activities by enhancing the morphology and chemistry of the as-synthesized graphene-based Pt NP catalysts. Insight in G-Cys-Pt electrocatalysts served as a reference point for further improved SAMENS synthesis of graphene-supported Au-Pt core-shell NPs electrocatalysts, described in Chapter 4.

3.2 Nanoparticle immobilization on graphene support

The cost and degradation of electrocatalysts are two major obstacles to the commercialization of PEMFCs. Along with the activity and poisoning inhibition, catalyst stability is one of the main focuses of research in the field of electrocatalysis. Investigating

and controlling degradation mechanisms of nanocatalysts during electrochemical aging in FC systems has been the driving force towards the improvement of catalyst stability. The stability of a catalyst practically relates to NP surface migration, aggregation, and detachment from the catalyst support material. Generally, coalescence effects such as aggregation and Ostwald ripening, are affected by NP migration at the support material surface due to insufficient immobilization forces.[191] Recent research shed light on the mechanism of catalyst sintering by dividing the process into three phases.[192] The first phase exhibits a rapid decay of surface area dominated by Ostwald ripening. The disappearance of the smallest NPs results in promoted surface area loss, Fig. 3.2. This was observed via in-situ TEM and Monte Carlo simulations.[192] In a later phase, particle coalescence resulted in further particle growth. Furthermore, prominent aggregation was noticed at elevated temperatures and when NPs were in close proximity. Sintering slowed down with increased (1) particle size and (2) interparticle separation.

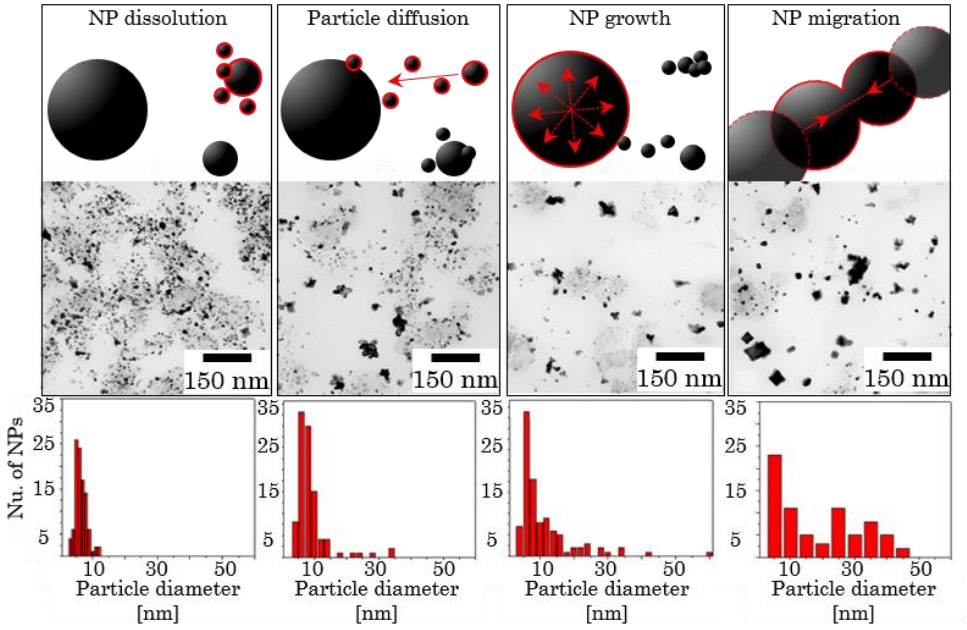

Figure 3.2 Sequentially obtained TEM images of cycled MEA cathode catalyst with corresponding Pt NPs size histograms measured from the cross-sectional cycled MEA. All four histograms were obtained from 100 particle assembly. Adapted with permission from ref. [193] © Springer Science+Business Media, LLC 2007.

A prepared approach to control the sintering effect was based on immobilization of metal NPs within a porous support, resulting in enhanced electrocatalytic performance compared to the same metal NPs deposited on conventional supports.[194] The mechanism

behind the improved stability is hindered NP surface migration. The reduced overall rate of sintering was a result of physical NP separation and increased metal-to-support contact within the porous structure. Covalent NP immobilization via amidation reactions proved to be an effective method in further prevention of migration and sintering of Au NP at GO nanosheets.[195] Typically weak interactions between NPs and GO surface were replaced by strong thiol-based covalent bonds, leading to improved properties of the prepared hybrid material. Another proposed approach is the addition of a second component such as another metallic or oxide phase applied as an "overcoat".[196] Alumina shells on Pd lead to improved catalytic performance, attributed to blocked edge and corner sites from where atoms would normally be emitted during the ripening process. All the improvements mentioned are related to changes in the composition of NPs or support surface structure, morphology and chemistry, resulting in altered rates of atom emission and transport on the support.

A suitable support material with strong interactions with the target NPs is needed to fully exploit the catalyst function. The major targets for supports are low price, stability, high conductivity and large surface area. Chemical inertness in applied conditions and conductivity of the catalysts are essential. Carbon black or graphitized carbon black are commercially used as support materials for Pt NPs in PEMFC application.[197] However, these carbon materials can be oxidized at potentials above 0.8 V vs. standard hydrogen electrode (SHE). Resulting conductivity degradation leads to loss of FC performance.[198] Such issues can be effectively avoided by the use of graphene as a supporting material, due to the large surface area (2600 $m^2 g^{-1}$), chemical inertness under PEMFC operating conditions and high electrical conductivity.[199] Graphene has been used as a support for metal NPs such as Pt[200], Pt-Fe[201], Pt-Co[201], Pt-Au alloy[202], and Fe/Co-N[203].

In this Ph.D. work, graphene was functionalized by L-cysteine (Cys) molecules, the synthesized material denoted as G-Cys. A simple amino acid Cys was utilized as covalent NP anchors due to its ability to easily attach to graphene and NPs via surface reactions. Both constituents, graphene and Cys, allowed for a synthesis of a low price and stable support material that offers highly uniform distribution of molecular anchors for the Pt NPs. The G-Cys-Pt nanocatalyst was prepared by a green, two-step synthesis route consisting of (1) GO functionalization with Cys followed by (2) formation of Pt NPs. The Cys linker was introduced to the GO via surface reactions, based on the 1-Ethyl-3-(3-dimethylaminopropyl)carbodiimide (EDC) and N-Hydroxysuccinimide (NHS) coupling method.[204] The synthesis was performed in aqueous environment, followed by hydrothermal GO reduction, resulting in G-Cys. The amine group of Cys was covalently anchored on graphene and the thiol group utilized to attract Pt atoms for immobilization of Pt NPs.

3.3 Syntheses and sample preparations

3.3.1 Chemicals

Table 3.1 Chemicals used for syntheses of GO, G-Cys and G-Cys-Pt

Chemical name, formula	**Pur. (%)**	**CAS**	**Mw (g/mol)**	**Co. name City, Country**
2-(N-morpholino)ethanesulfonic acid, MES hydrate, $C_6H_{13}NO_4S \cdot xH_2O$	≥ 99.5	4432-31-9	195.24	S-A St. Louis, USA
Chloroplatinic acid hydrate, $H_2PtCl_6 \cdot xH_2O$	≥ 99.9	26023-84-7	409.81	
D-(+)-glucose, $C_6H_{12}O_6$	≥ 99.5	50-99-7	180.16	
Ethanol, CH_3CH_2OH	≥ 99.9	64-17-5	46.07	Uvasol Darmstadt, DE
Formic acid, HCOOH	98-100	64-18-6	46.03	S-A, Steinheim, DE
Graphite powder	99.99	7782-42-5	12.01	S-A, Buchs SG., CH
Graphene oxide, GO, Linear Formula: $C_xO_yH_z$	A	Homemade		Kgs. Lyngby, DK
Hydrogen peroxide, H_2O_2	30(*aq.*)	7722-84-1	34.01	S-A, Steinheim, DE
Hydrochloric acid, HCl	37	7647-01-0	36.46	
N-(3-Dimethylaminopropyl)-N'-ethylcarbodiimide hydrochloride, (EDC), $C_8H_{17}N_3 \cdot HCl$	≥ 98.0	25952-53-8	191.7	S-A Tokyo, JP
N-Hydroxysuccinimide, (NHS), $C_4H_5NO_3$	97	6066-82-6	115.09	S-A Steinheim, DE
Nitric acid, HNO_3	≥ 65	7697-37-2	63.01	
Phosphorus pentoxide, P_2O_5	98%	1314-56-3	141.94	S-A, Bengaluru, IN
Platinum on graphitized carbon	20 [B]	product nu: 38549-1G	Pt: 195.08	S-A St. Louis, USA
Potassium hydroxide, pellets, KOH	99.99 [C]	1310-58-3	56.11	
Potassium permanganate, $KMnO_4$	97	7722-64-7	158.03	
Potassium persulfate, $K_2S_2O_8$	> 99.0	7727-21-1	270.32	Fluka St. Louis, USA
(R)-2-amino-3-mercaptopropionic acid, L-cysteine, $C_3H_7NO_2S$	≥ 99.5	52-90-4	121.16	
Sulfuric acid, H_2SO_4, TraceSELECT®	≥ 95[C]	7664-93-9	98.08	Fluka, Lyon, FR

[A] Dialysis purification, [B] wt.% of Pt NPs, [C] (10 - 15% H_2O), Sigma-Aldrich (S-A), United States of America (USA), Germany (DE), Switzerland (CH), Denmark (DK), Japan (JP), India (IN), France (FR).

3.3.2 Graphene oxide synthesis

Graphene oxide (GO) was prepared by a modified Hummer's method following two steps.[205] Firstly, pre-oxidized graphite was prepared. 5.0 g of graphite powder, 2.5 g of P_2O_5 and 2.5 g of $K_2S_2O_8$ was slowly added to 21.0 mL concentrated H_2SO_4 which was kept in a water bath at 80 °C under strong stirring for 3 h. The dark-green mixture was cooled to the room temperature and diluted with Millipore water. The mixture was then filtered and washed several times with Millipore water until pH of the waste solution had reached neutral. Pre-oxidized graphite powder was collected and dried at 50 °C overnight, Fig. 3.3.

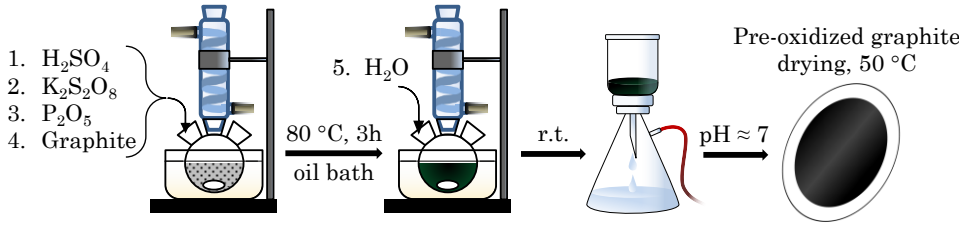

Figure 3.3 Synthesis scheme of pre-oxidized graphite powder.

Secondly, 1.0 g of pre-oxidized graphite powder was slowly added to 23.0 mL of concentrated H_2SO_4, within a round-bottomed flask placed in an ice-water bath (0 °C). $KMnO_4$ (3.0 g) was then added to the mixture under slow stirring, keeping the temperature below 20 °C. After removing the ice-water bath, 46 mL Millipore water was added and the mixture was reacted at 35 °C for 2 h with stirring. After a few minutes, Millipore water (140 ml) and 2.5 ml 30% H_2O_2 solution were further added to the mixture, leading to the solution color rapidly changing to dark-yellow, Fig. 3.4.

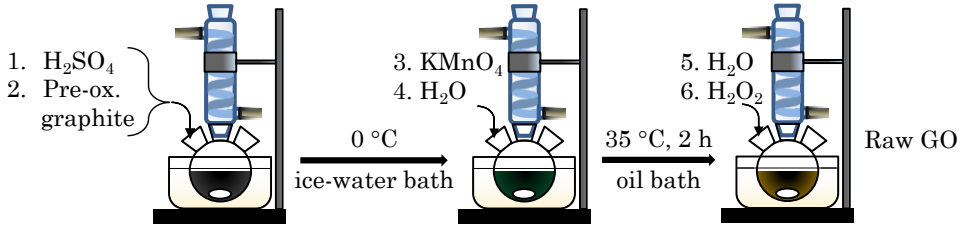

Figure 3.4 Synthesis scheme of raw GO solution.

The mixture was then washed with 1:10 HCl solution (v/v, 250 ml) and filtered to remove residual metal ions. The raw GO suspended in Millipore water was centrifuged at a high rotation speed (12 krpm). The supernatant containing highly dispersed and stable GO nanosheets was collected. To remove residual salts and acids, the supernatant was

further dialyzed using a dialysis tube (with a cut-off molecular mass of 12 to 14 kDa) for at least one week by changing water bath regularly (2 to 3 times per day), Fig. 3.5.

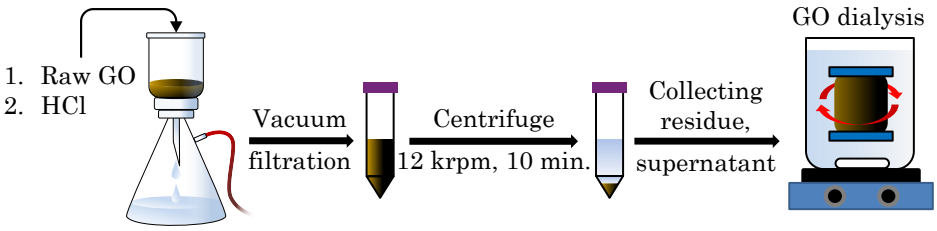

Figure 3.5 Scheme of raw GO solution purification.

AFM images of GO deposited onto mica sheets (Fig. 3.13A) indicate successful exfoliation of single layer GO sheets, with thickness averaging at 0.9 nm.

3.3.3 Graphene-Cys synthesis

Graphene functionalized by L-cysteine (G-Cys) support material synthesis started by dissolving 38.0 mg of EDC in 0.50 mL Millipore water and adding the solution to 98.0 mL 0.20 mg/mL GO solution which was then stirred at room temperature for 10 and sonicated for 45 minutes. 23.0 mg of NHS was dissolved in 0.50 mL Millipore water and added to the solution, followed by repeated stirring and sonicating at the same conditions. 24.0 mg of Cys was dissolved in 1.0 mL Millipore water, added to the solution and heated at 80 °C for 8 hours in a round bottomed flask, with a condenser setup. During the reaction, the solution changed color from brown to black. The solution was then sonicated for 1 hour and purified by three centrifugation cycles to remove excess chemicals and impurities. Each centrifugation cycle was performed at 12 krpm for 10 min, discarding the supernatant and re-dispersing the residue. Purified G-Cys was finally re-dispersed in 50.0 mL Millipore water resulting in c (G-Cys) = 0.40 mg/mL, Fig. 3.6.

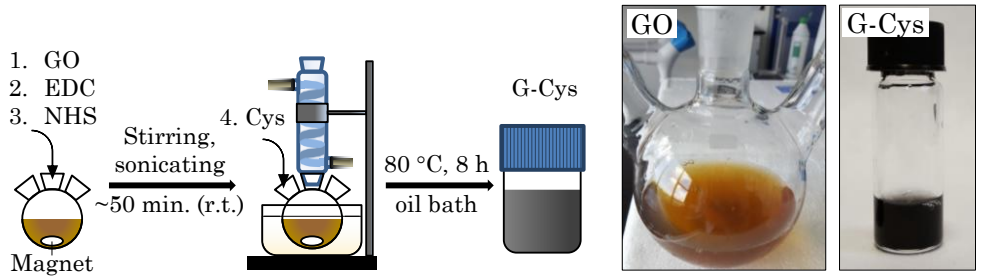

Figure 3.6 Synthesis scheme of G-Cys.

3.3.4 G-Cys-Pt synthesis

The synthesis was performed at 95 °C in a round-bottomed flask equipped with a magnet. 8.75 mL of 0.40 mg/mL G-Cys solution was added to the vial followed by 2.5 mL 0.10 M glucose and 2.5 mL 0.10 M (pH = 7.0) MES buffer. The solution was diluted by 85.25 mL Millipore water. After 10 minutes of pre-heating, 1.0 mL 20.0 mM H_2PtCl_6 was added to the reaction flask. During the synthesis, the solution color changed from dark-yellow to black, Fig. 3.7.

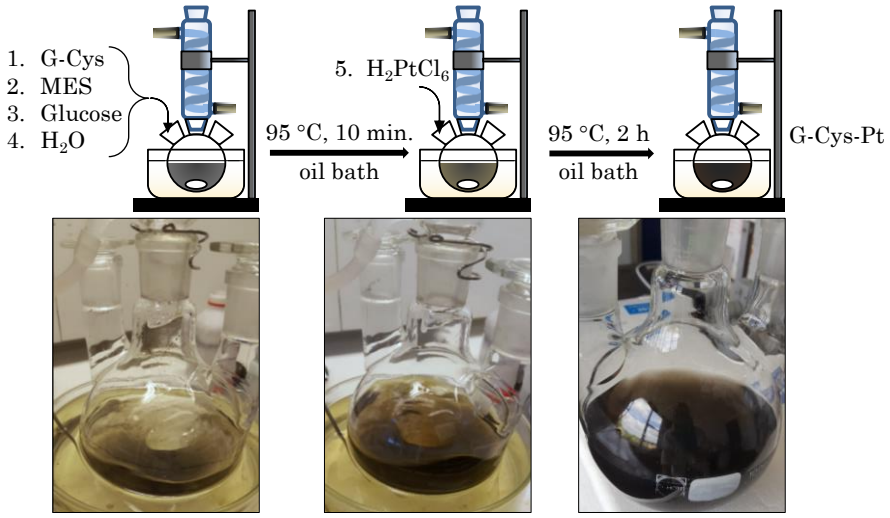

Figure 3.7 Synthesis scheme of G-Cys-Pt with corresponding photographs.

The excess Pt NPs was removed from G-Cys-Pt by vacuum filtration. The vacuum filtration setup was equipped with filter paper from Pall Corporation (0.2 μm pore size, ϕ = 47 mm, HPLC certified). The filter was rinsed with ethanol in order to activate it, followed by Millipore water washing. The catalyst was washed with a copious amount of Millipore water, until clear filtrate started coming out through the filtration funnel. The wet catalyst on the filter paper was immersed in a centrifuge tube containing Millipore water. G-Cys-Pt was then re-dispersed in water by 10 minutes sonication. The filter paper was then removed from the centrifuge tube. Diluted G-Cys-Pt dispersion was concentrated by centrifugation. Three cycles at 12 krpm for 10 minutes were performed where the supernatant was discarded and the residue collected and re-dispersed in a fixed volume of Millipore water. The supernatants of the second and third centrifugation cycles were completely transparent indicating that free Pt NPs were absent in the solution. The final volume of G-Cys-Pt was 10.0 mL with c (G-Cys) = 0.35 mg/mL, Fig. 3.8.

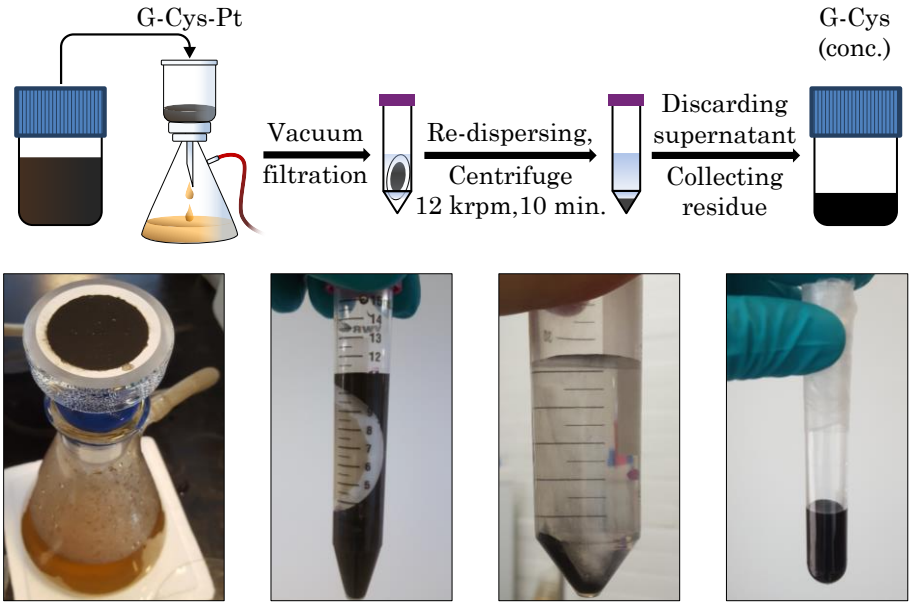

Figure 3.8 Filtration and concentration of G-Cys-Pt electrocatalyst.

3.3.5 Electrode preparation for electrochemical experiments

Electrode polishing and cleaning

The glassy carbon electrodes (GCE, ϕ = 4 mm, A = 0.1256 cm^2) and the rotating ring (Pt) disk (GCE) electrode RRDE (ϕ = 5.61 mm, A_{disc} = 0.2472 cm^2, A_{ring} = 0.1859 cm^2, ring collection efficiency = 37 %) were wet-polished by sand paper (grit roughness 2000, followed by 4000) for 10 min by hand. For alumina slurry (particle sizes of 1.0, 0.3 and 0.05 μm in diameter), a polishing machine was used, using the largest particle size first (rough polishing) and finishing with the finest particle size (mirror-like electrode surface finish). The rotation speed of the polishing machine was 300 rpm, for 5 min at each polishing cycle. Afterwards, all the electrodes were sonicated for 30 min in total with intermittent water exchange (1. time after 5 min, 2. time after 10 min and 3. time after 15 min). Clean electrodes were dried in the fume hood at room temperature for 5 min. prior to drop-casting.

All electrochemical measurements were performed at room temperature (20 ± 2° C) using an Autolab System (Eco Chemie, Netherlands) controlled by the GPES/NOVA 1.11 software and a Faradaic cage. Unless stated otherwise, all the measurements were performed in 0.1 M H_2SO_4 under acidic condition (pH ≈ 1.0) using a three-electrode system consisting of the glassy carbon electrode (GCE) as working electrode (WE), a reversible

hydrogen electrode (RHE) as reference electrode (RE), and a platinum coiled wire with a large surface area as counter electrode (CE), Fig. 3.9. The CE was cleaned in a hydrogen flame followed by washing at least three times with Millipore water. A fresh RHE was prepared prior to each experiment using the same supporting electrolyte as for the measurements. After the measurements, the RHE potential was checked against a saturated calomel electrode (SCE). All results are reported against the SCE, unless stated otherwise All glassware including electrochemical cells was boiled in 15 % HNO_3 for 20 minutes, copiously washed with Millipore water, and sonicated for 30 minutes in two intervals, prior to each experiment.

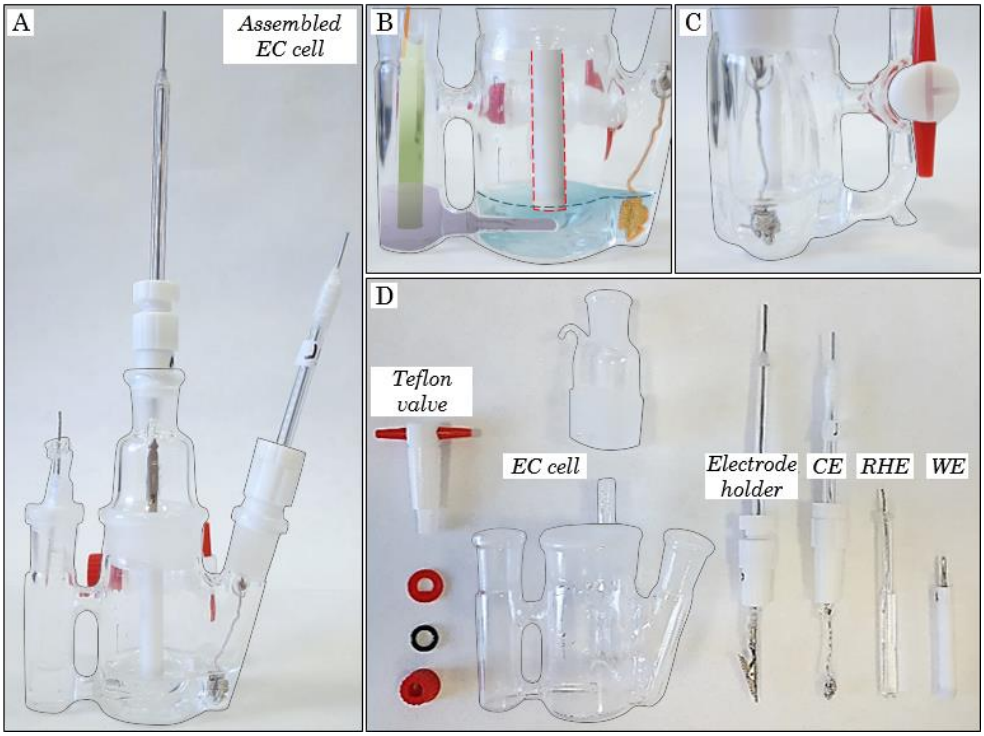

Figure 3.9 (A) Three-electrode compartment electrochemical (EC) cell containing (B) WE (red dashed line), Pt wire (orange) CE and RHE (green) in RE compartment separated from WE by Luggin capillary (purple). (C) Gas supply to the cell can be set for bubbling through or above the electrolyte. (D) Dissembled components of EC cell.

Drop-casting catalysts

Electrochemical performance of G-Cys-Pt catalyst was compared to commercial catalyst from Sigma-Aldrich, 20 wt.% of Pt (NP size ~ 5 nm) on graphitized carbon (C-Pt). In case of ORR experiments (setup in Fig. 3.11A), the Pt loading on the RRDE for G-Cys-Pt was

4.7 µg (19.0 $\mu g_{Pt}/cm^2$), and for C-Pt 5.0 µg (20.2 $\mu g_{Pt}/cm^2$), Fig. 3.11B-E. For the electrochemical oxidation of fuel molecules the Pt loading of G-Cys-Pt was 6.3 µg (50.2 $\mu g_{Pt}/cm^2$), and C-Pt 3 µg of Pt on GCEs (23.9 $\mu g_{Pt}/cm^2$). The catalyst layer was protected by 5 µL of 0.05 % Nafion® (dissolved in ethanol).

In order to compare the two catalyst per Pt loading, TGA measurements were performed for G-Cys as a reference material for the G-Cys-Pt catalyst, Fig. 3.10. The G-Cys-Pt shows catalyzed oxidation of support by small Pt NPs, compared to G-Cys. This is especially observable from DTA plots showing 230 °C temperature difference between the two samples for the largest energy release points. After 660 °C the curves are approach a plateau at 1.72 wt.% for G-Cys and 32.58 wt.% for G-Cys-Pt. The actual metal loading in G-Cys-Pt was determined to be ~ 31 wt.% by subtracting the residual relative mass of the reference material, G-Cys.

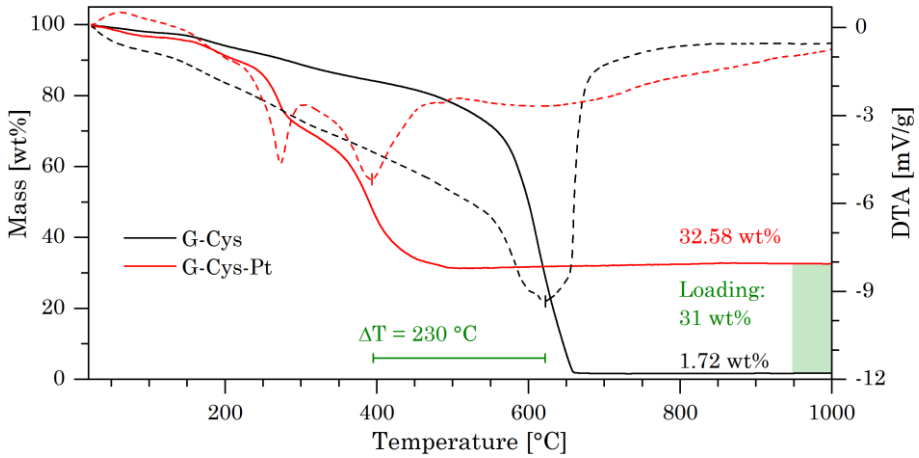

Figure 3.10 TGA measurements for G-Cys (black) and G-Cys-Pt (red) in solid lines. The Pt NP loading in G-Cys-Pt is 31 wt.% (green shaded area). DTA measurements are represented by dashed lines.

The Pt loading calculations for G-Cys-Pt and C-Pt catalysts are as follows:

G-Cys-Pt

$Pt_{(wt.\%)}$ = 31 % (TGA)
c(G-Cys) = 350 µg/mL
$V_{drop\text{-}casted}$(G-Cys-Pt) = 30 µL

The total mass of G-Cys-Pt deposited on electrodes is equal to sum of the support and Pt NPs masses, equation 3.1.

$$m(\text{G-Cys-Pt}) = m(\text{G-Cys}) + m(\text{Pt NPs}) \tag{3.1}$$

Since all the Pt NPs are immobilized on G-Cys, the volume of G-Cys-Pt equals to the volume of pure support, G-Cys. The mass of G-Cys can therefore be expressed as a product of c(G-Cys) and drop-casted volume V(G-Cys-Pt), equation 3.2.

$$m(\text{G-Cys-Pt}) = c(\text{G-Cys}) \cdot V(\text{G-Cys}) + m(\text{Pt NPs}) \tag{3.2}$$

The mass of the Pt NPs is the product of Pt metal loading percentage, obtained from TGA, and total G-Cys-Pt mass deposited on GCE, equation 3.3.

$$m(\text{G-Cys-Pt}) = c(\text{G-Cys}) \cdot V(\text{G-Cys}) + m(\text{G-Cys-Pt}) \cdot \text{Pt}_{(\text{wt.\%})} \tag{3.3}$$

By rearranging equation 3.3, the mass of the deposited G-Cys-Pt can be obtained, equation 3.4.

$$\begin{aligned} m(\text{G-Cys-Pt}) - m(\text{G-Cys-Pt}) \cdot \text{Pt}_{\text{loading}} &= c(\text{G-Cys}) \cdot V(\text{G-Cys}) \\ m(\text{G-Cys-Pt}) \cdot (1 - \text{Pt}_{\text{loading}}) &= c(\text{G-Cys}) \cdot V(\text{G-Cys}) \\ m(\text{G-Cys-Pt}) &= \frac{c(\text{G-Cys}) \cdot V(\text{G-Cys})}{(1 - \text{Pt}_{(\text{wt.\%})})} \\ &= \frac{350\ \mu\text{g/mL} \cdot 0.03\ \text{mL}}{(1 - 0.31)} \\ &= \frac{10.5\ \mu\text{g}}{0.69} \\ &= 15.2\ \mu\text{g} \end{aligned} \tag{3.4}$$

The mass of the Pt NPs is equal to the total catalyst mass deposited on the electrode multiplied by the percentage of the total metal loading, equation 3.5.

$$\begin{aligned} m(\text{Pt NPs}) &= m(\text{G-Cys-Pt}) \cdot \text{Pt}_{(\text{wt.\%})} \\ &= 15.2\ \mu\text{g} \cdot 0.31 = 4.7\ \text{g} \end{aligned} \tag{3.5}$$

The Pt NP mass deposited on GCEs and RRDE was 4.7 µg. According to the respective areas of electrodes, the mass/area loading was 19.0 $\mu g_{Pt}/cm^2$ at GCE and 50.2 $\mu g_{Pt}/cm^2$ at RRDE.

C-Pt

The catalytic ink was prepared by dispersing 1.3 mg of C-Pt catalyst powder in 0.5 mL of Millipore water, 0.45 mL of ethanol and 50 µL of 5 wt.% Nafion® solution (dissolved in ethanol). The ink was sonicated for 30 minutes prior to each drop-casting procedure.

$\text{Pt}_{\text{loading}}$ = 20 wt. %
c(C-Pt) = 1.3 mg/mL

3 µg of Pt on GCE equals the total catalyst mass multiplied by the pure Pt loading:

$$m(\text{Pt on GCE}) = c(\text{C-Pt}) \cdot V(\text{C-Pt}) \cdot \text{Pt loading} \tag{3.6}$$

The drop-casting volume can be expressed from eq. 3.7.

$$V(\text{C-Pt}) = \frac{m(\text{Pt on GCE})}{c(\text{C-Pt}) \cdot \text{Pt loading}} \tag{3.7}$$

$$= \frac{3\ \mu g}{1300\ \mu g/mL \cdot 0.2} = 11.5\ \mu L$$

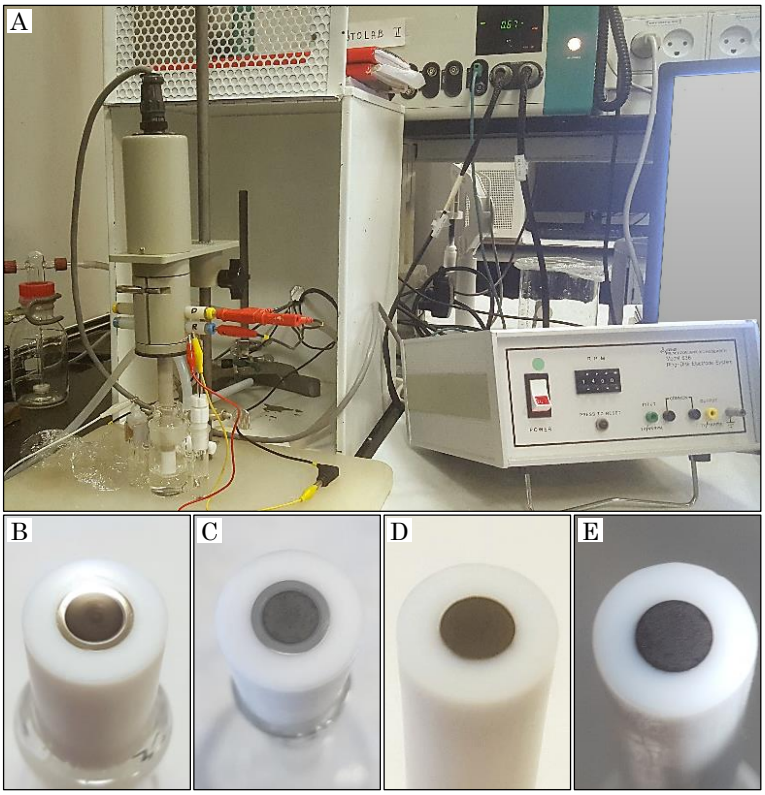

Figure 3.11 (A) Rotating electrode electrochemical setup. RRDEs with deposited (B) 20.2 $\mu g_{Pt}/cm^2$ C-Pt and (C) 19.0 $\mu g_{Pt}/cm^2$ G-Cys-Pt. GCEs with deposited (D) 23.9 $\mu g_{Pt}/cm^2$ C-Pt and (E) 50.2 $\mu g_{Pt}/cm^2$ G-Cys-Pt.

11.5 µL of C-Pt is a volume equivalent to 3 µg of Pt NP mass deposited on GCEs and RRDE. According to the respective areas of electrodes, the mass/area loading was 20.2 $\mu g_{Pt}/cm^2$ for the RRDE and 23.9 $\mu g_{Pt}/cm^2$ for the GCE.

3.4 Structure and compositional characterization of G-Cys-Pt

The syntheses of G-Cys-Pt catalysts are briefly described in Fig. 3.12. The G-Cys-Pt nanocatalyst was prepared by a green, two-step synthesis route consisting of (1) GO functionalization with Cys followed by formation and deposition of (2) Pt NPs.

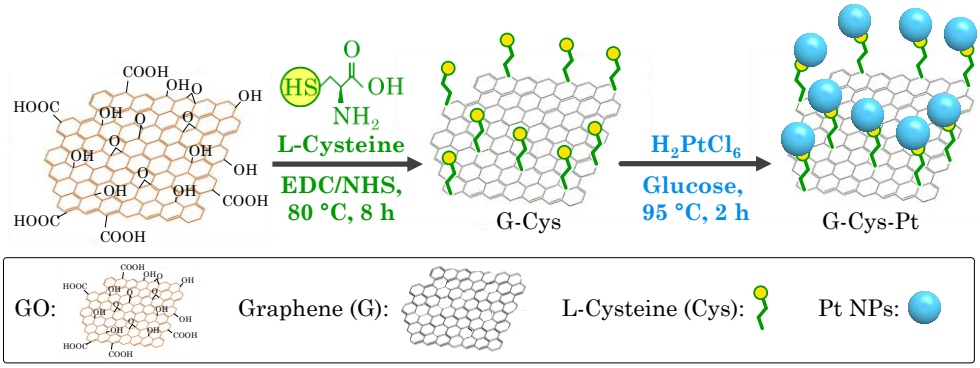

Figure 3.12 Two-step synthesis route of G-Cys-Pt: 1) GO functionalization with Cys via EDC/NHS coupling and thermal reduction to graphene, G-Cys, (2) Pt NP growth on the Cys anchors by reduction of $PtCl_6^{2-}$, G-Cys-Pt.

As noted (section 3.3.2), GO was prepared by a modified Hummer's method,[205] where single-layered sheets of thickness 0.9 nm (Fig. 3.13B) and lateral dimensions ranging from several hundred nanometers to 5 μm were obtained. Upon the successful GO reduction, graphene exhibits decreased amounts of O-H, C=O and C-O functional groups, as seen from FTIR spectra in Fig. 3.13C. Retention of the C-H and C=C bonds indicates that the original graphene electronic conjugations are restored. The UV-Vis spectra of different GO solution concentrations are presented in Fig. 3.13D. The two GO-characteristic absorption peaks are observed (1) at 232 nm originating from $\pi \rightarrow \pi^*$ transitions of aromatic C–C and C=C bonds, and (2) at 301 nm peak from $n \rightarrow \pi^*$ transitions of C=O bonds.[153]

The Cys linker was introduced to the GO in the presence of EDC and NHS coupling reactions in aqueous environment followed by hydrothermal reduction, resulting in G-Cys, in which the amine group of Cys was covalently anchored on the graphene surface, as checked by X-ray photoelectron spectroscopy (XPS), Fig. 3.14.

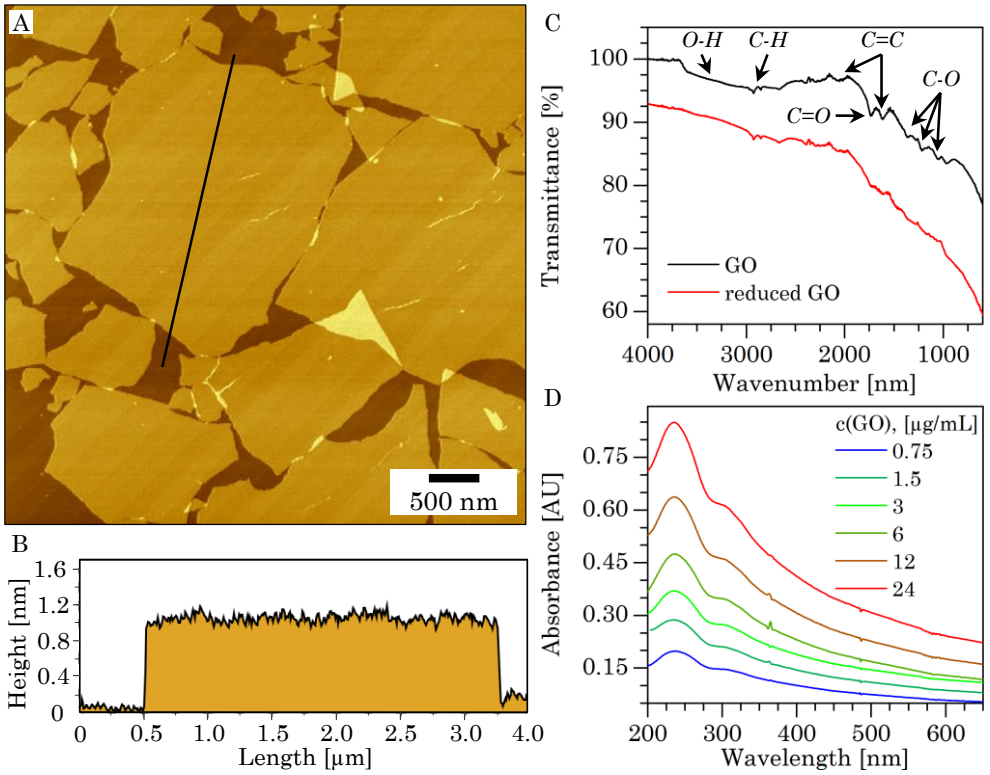

Figure 3.13 (A) Atomic force microscopy (AFM) image of graphene oxide (GO) with a (B) cross section topography profile of a line in (A). (C) FTIR spectra of GO (black) and graphene (red). (D) UV-Vis spectra of GO solutions with different concentrations.

The Cys thiol group attracts platinum atoms for immobilization of Pt NP cores on the graphene (G-Cys-Pt). During the synthesis, the color of the colloidal suspension changed from black of G-Cys to dark-brown of G-Cys-Pt. The synthesized G-Cys-Pt nanocatalyst was purified and concentrated by repeated centrifugation in Millipore water.

XPS was performed on G-Cys obtaining sulfur (S), nitrogen (N) and carbon (C) spectra, disclosing the chemical states of these elements, Fig. 3.14. 100 µL of 0.40 mg/mL G-Cys was drop-casted onto a clean Si wafer (0.5 x 0.5 cm) and dried at 60 °C. XPS was carried out using an ESCALABMKII X-ray photoelectron spectrometer (Thermo Scientific™, USA). The S spectrum exhibits only the presence of free thiol groups (163.8 and 165.0 eV) and oxidized S in the form of SO_4^{2-} (167.8 and 169.1 eV). The nature of chemical bonds of thiol to Pt is similar to thiol–Au bonds,[206] which were studied by XPS in the Chapter 4, Fig. 4.10. Furthermore, Cys self-assembled monolayers on Au(111) single-crystal electrodes were investigated by electrochemical techniques and STM in the Chapter 6.

The N spectrum shows no 398.2 eV peaks for metal-nitride bonds indicating the absence of amine group binding to the Pt NPs.

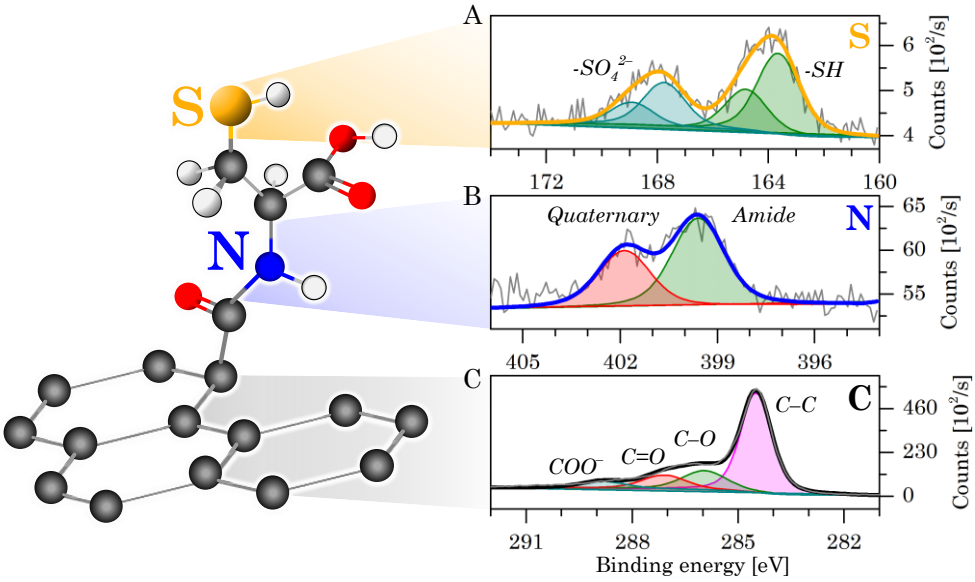

Figure 3.14 G-Cys elemental X-ray photoelectron spectroscopy (XPS) analysis of: (A) sulfur, (B) nitrogen and (C) carbon spectra.

Peaks at 399.6 eV and 401.9 correspond to amide/pyrrolic and quaternary N, respectively, indicating graphene functionalization by Cys molecules. The C spectrum shows peaks at 284.5, 286.0, 287.1 and 288.8 eV, assigned to C–C, C–O, C=O and COO^-, respectively. The small peaks at 286.0 eV and 287.1 eV have been found in N-doped graphene for N–C(sp^2) and N–C(sp^3) bonds as well.[207]

The G-Cys-Pt catalyst was imaged by TEM, Fig. 3.15. The morphological characterization of the catalyst showed uniform Pt NP dispersion and size distribution of 1.2 ± 0.8 nm, Fig. 3.15C inset. The "wet" synthesis of Cys functionalized graphene nanosheets allowed for homogeneous distribution of molecular anchors, creating a uniform Pt NP dispersion during the second synthesis step. The disadvantage of aqueous graphene dispersions is the graphene tendency towards sheet re-stacking, due to its hydrophobicity.[208] The more graphene is reduced to its pristine structure, the more hydrophobic it becomes, thus the easier the re-stacking process occurs.

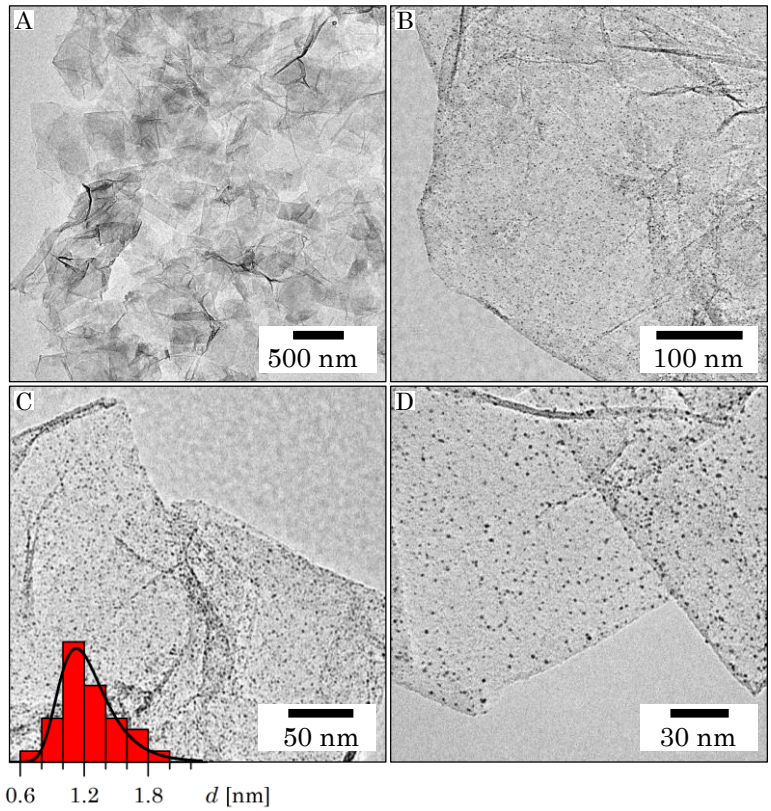

Figure 3.15 TEM images of G-Cys-Pt at different magnifications, inset in (C) is Pt NPs size distribution histogram.

This can be overcome by (1) functionalization of graphene, (2) immobilization of nanostructures or (3) introduction of physisorbed "spacers". Since G-Cys-Pt was stored in a concentrated form, the probability of G-Cys re-stacking was increased. However, TEM images prove mainly single-layered G-Cys nanosheets. The nanosheet stability was achieved by Cys functionalization as well as immobilization of densely-packed Pt NPs, both of which affected the inherent residual charge of reduced GO. By introduction of positively- and negatively-charged sites, originating from metallic NPs and molecular surface decorations (Cys), the typically neutrally charged graphene nanosheets were successfully dispersed in a polar solvent (water). The hydrolyzed G-Cys-Pt nanosheets allowed a concentrated aqueous dispersion to be stable for three months without noticeable sedimentation.

G-Cys-Pt will be utilized as a reference catalyst to graphene-supported core-shell Au-Pt catalysts, synthesized via SAMENS procedure and described in Chapter 4. Both pure Pt

NPs and bimetallic Au-Pt core-shell electrocatalysts are immobilized on the same type of support materials, G-Cys. Besides the compositional difference, the only morphological distinction between the two types of NPs synthesized by the SAMENS recipe is the NP size. The obvious morphological difference of 1.2 nm Pt NPs in G-Cys-Pt, compared to 9.5 nm for Au-Pt core-shell NPs, resulted in facile identification of the respective NPs.

3.5 Electrochemical properties and electrocatalysis on G-Cys-Pt

3.5.1 Voltammetry of G-Cys-Pt and C-Pt

G-Cys-Pt was electrochemically characterized to determine whether the modified catalyst morphology would show improvement compared to commercial C-Pt catalysts. Theoretically, the size of as-synthesized Pt NPs (1.2 nm compared to 5 nm in C-Pt) should show high mass-to-surface specific activity, but the risk of aggregation also increases.[46] Furthermore, linking Pt NPs to graphene via Cys molecular anchors presents a more robust and electrically efficient system than simple NP adsorption, as is the case for C-Pt. To investigate this assumption, electrocatalytic experiments were performed, testing G-Cys-Pt and C-Pt catalysts towards the dioxygen reduction reaction (ORR) and electrochemical oxidation of 0.1 M formic acid (FA), methanol (MeOH) and ethanol (EtOH). The main constituents of these two catalysts are qualitatively the same - support is a carbon material and the electrocatalyst is pure Pt. The main purpose of the comparison is therefore to examine the electrocatalytic activity of G-Cys-Pt, the influenc of NPs size decrease, and their chemical immobilization. If catalytic performances are compared to the same Pt mass loading, larger Pt surface area would be obtained for G-Cys-Pt due to four times smaller linear scale of the NPs than in C-Pt. Since the catalytic activity is heavily governed by the active surface area, both electrocatalysts were compared according to their respective electrochemically active surface areas of Pt ($ECSA_{Pt}$), effectively excluding the function of catalyst mass loading, Fig. 3.16.

$ECSA_{Pt}$ were obtained from cyclic voltammograms for both materials at 50 mV/s in Ar-saturated 0.10 M H_2SO_4. The $ECSA_{Pt}$ can be quantitatively determined by integrating the hydrogen underpotential deposition region (H-UPD) of Pt surfaces under the cathodic peaks from – 0.3 to 0.0 V. Using equation 3.8, $ECSA_{Pt}$ is obtained in cm^{-2}.[209][210]

$$ECSA_{Pt} = \frac{A_{H\text{-}UPD}\ [AV]}{\nu\ [V\ s^{-1}] \cdot 210\ [\mu C\ cm^{-2}]} \tag{3.8}$$

where $A_{H\text{-}UPH}$ is integrated hydrogen underpotential deposition region obtained from cyclic voltammograms ($A \cdot V$), ν is the scan rate (V/s) and 210 $\mu C\ cm^{-2}$ the experimentally well-established specific charge of hydrogen deposition at solid, planar polycrystalline platinum electrodes.[209][210] G-Cys-Pt exhibited a typical cyclic voltammogram observed

for carbon-supported Pt NP in Ar-saturated 0.10 M H_2SO_4, Fig. 3.16A. The hydrogen region shows prominent peaks in the anodic and cathodic potential ranges from – 0.3 to 0.0 V. The Pt oxide (Pt_{ox}) formation starts at 0.55 V, exhibiting a steady current increase as the Pt_{ox} layer grows thicker and contributes to the interfacial capacitance. The Pt_{ox} layer is being removed in the cathodic scan, reaching the maximum currents at 0.33 V where pristine metallic Pt surface is obtained. As expected, G-Cys-Pt catalyst showed no significant difference in Ar-saturated 0.10 M H_2SO_4 when compared to C-Pt per $ECSA_{Pt}$.

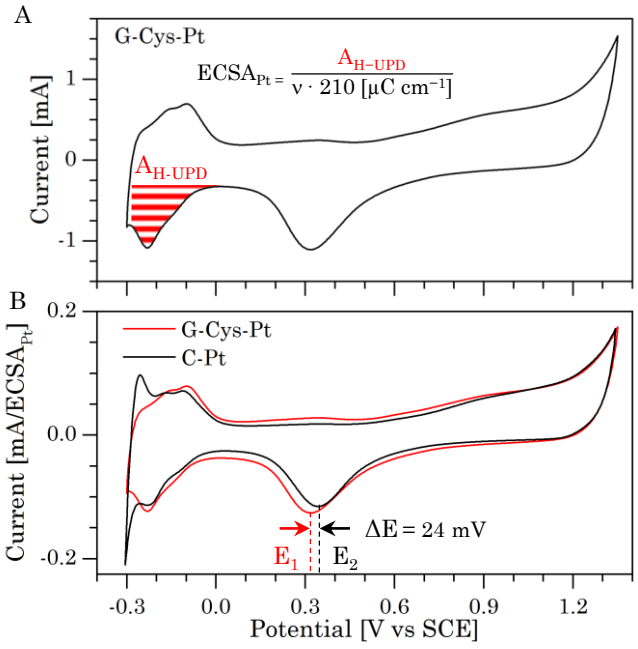

Figure 3.16 Voltammogram of G-Cys-Pt at 50 mV/s in Ar-saturated 0.1 M H_2SO_4 showing the integrated charge of hydrogen underpotential deposition region on the Pt NPs surface.

The only observable difference is a 24 mV negative shift of Pt_{ox} reduction peak on the G-Cys-Pt catalyst, Fig. 3.16B. This is attributed to graphene diffusion limitations rather than Pt modification by Cys molecules, which is evident from the peak potential (E_p) separations in the voltammograms at different scan rates, Fig. 3.17A. Large graphene nanosheets extend molecular pathways, resulting in augmented diffusion effect compared to planar or microporous electrodes. The diffusion-limited signature behavior is especially noticeable at the fastest scan rate used (100 mV/s), where the anodic peak currents tend to have positive while cathodic currents have negative potential offset values. From the close overlaps of the hydrogen regions in the voltammograms in Fig. 3.16B, it is obvious

that the $A_{H\text{-}UPH}$ integration and $ECSA_{Pt}$ estimation were successfully performed. Comparing the same Pt active surface areas of both catalysts thus provides the information of qualitatively the same catalyst profiles in the electrochemical environment without fuels.

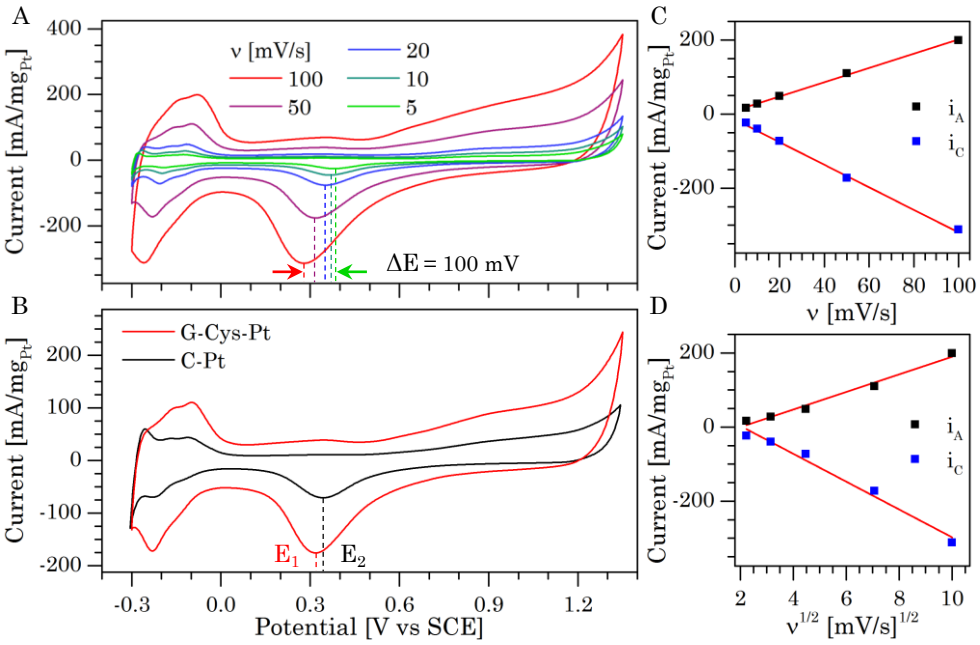

Figure 3.17 Cyclic voltammograms of (A) G-Cys-Pt at different scan rates and (B) G-Cys-Pt (red) and C-Pt (black) at 50 mV/s. All the measurements were performed in Ar-saturated 0.1 M H_2SO_4. Fitted anodic (black) and cathodic (blue) peak currents versus (C) scan rate for diffusion-less and (D) square root of scan rate for diffusion-limited system. Catalyst loading was 50.2 $\mu g_{Pt}/cm^2$ for G-Cys-Pt and 23.9 $\mu g_{Pt}/cm^2$ for C-Pt.

Since the TGA measurements performed (Fig. 3.10) showed 31 wt.% Pt metal loading in G-Cys-Pt, the catalysts were further electrochemically characterized with the respect of Pt mass loading, Fig. 3.17. Again, G-Cys-Pt exhibited peak potential shift due to mentioned diffusion limitations. The peak currents were plotted versus scan rates and square root of scan rates to further confirm the diffusion-limited or diffusion-less dominated behavior, respectively (Fig. 3.17C-D). Although the plots show close to linear relation in both cases, the diffusion-less dominated system fits better with the experimental data.

The diagnostic criteria for a reversible reaction (not influenced by diffusion processes) in CV are:

1. E_p = const.	peak potential is unchanged by the change of scan rate,
2. $I_p \propto \nu$	peak current is proportional to the scan rate,
3. $\lvert I_p^a / I_p^c \rvert = 1$	ratio of peak currents absolute values equals 1,
4. $\Delta E_p = \lvert E_{pC} - E_{pA} \rvert = \frac{56.5\ mV}{n}$	peak separation potential follows a simple relation for an n-electron process. For a reversible reaction of adsorbed species $\Delta E_p = 0$.

Since the Ep is not constant, the peak current ratio is 1.5 and ΔE_p 127 mV, the system can be classified as quasi-reversible. To understand the origin of the diffusion limitations present in graphene structures, we have to consider the assembly of graphene nanosheets at the electrode surface.

3.5.2 Structure of graphene deposited on electrodes

Arbitrarily orientated graphene sheets, during catalyst deposition and drying, act as a barrier extending the molecular pathway through the boundary.[211] During graphene paper assembly nanosheets also align arbitrarily, therefore graphene paper was used as a model to investigate graphene surface morphology when deposited on electrodes. Graphene papers have been studied since the discovery of graphene and are usually applied as gas membranes.[212] Syntheses of graphene papers were performed in a vacuum filtration setup equipped with a filter paper from Pall Corporation. 20 mL 0.19 mg/mL GO solution is vacuum filtered over a period of two days. Dried GO paper was then detached from the filter paper and put in an autoclave reactor containing 5.0 µL of 99.9 % hydrazine at 95 °C for 1 hour. The as-synthesized graphene paper was imaged in SEM with topographical and cross-sectional images shown in Fig. 3.18A and B,C respectively.

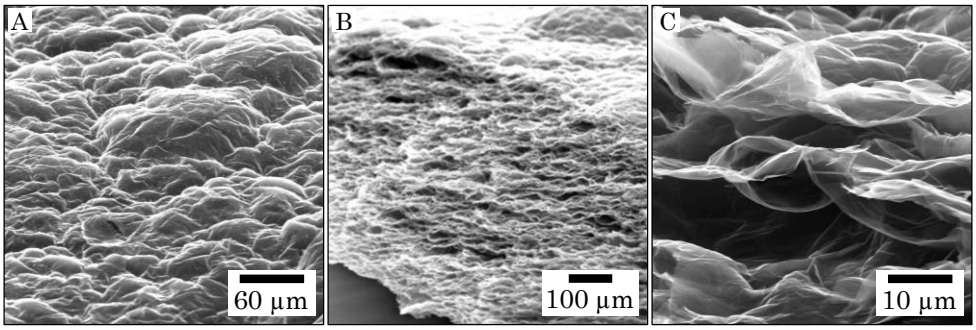

Figure 3.18 Graphene paper synthesized by the hydrazine reduction method. (A) Topographical view, (B) and (C) cross-sectional views.

During GO reduction by hydrazine, nitrogen gas and water are released.[213] The gas evolution helps delaminating the graphene oxide structure, but topography images show no pores able to release the accumulated N_2 (g). The "bubble-like" surface indicates the confinement of N_2, which in fact is released through the lateral pores at the paper edges, as seen from the delaminated structure in the cross-sectional view, Fig. 3.18 B-C. A similar drying mechanism is achieved during graphene deposition at the electrodes. Gravitational forces deposit graphene nanosheets at the electrode while the solvent (ethanol and water, usually in ratio 1:2) is evaporated at 60 °C. Lower concentration and volumes were used for electrode depositions so the "membrane effect" is not as prominent as in graphene paper. Nevertheless, nanosheet re-stacking cannot be excluded since it interferes with molecular mass transport, resulting in diffusion effects.[208] Such issues can be avoided by e.g. catalyst deposition in small volumes from diluted dispersions or spin-coating procedures. To eliminate diffusion effects during electrocatalytic characterization of G-Cys-Pt, the ORR was conducted in the rotating electrode setup, which successfully distinguishes kinetic from mass transport features of electrocatalysts.

3.5.3 The electrochemical dioxygen reduction reaction (ORR) at RDE and RRDE

The rotating disk electrode (RDE) ORR experiments for G-Cys-Pt and C-Pt were run under the same conditions and rotation speeds, Fig. 3.19. The limiting currents (from 0.0 to ~ 0.7 V) originate from dioxygen diffusion to the catalytic sites on the electrode surface, and are limited only by the electrode rotation speeds. The kinetic part of the plot (from ~ 0.8 to ~ 1.0 V) shows the positive half-wave potential (E_{HW}) shift for the G-Cys-Pt catalyst compared to C-Pt, representing the overpotential reduction towards the ORR at the G-Cys-Pt electrocatalyst. The slight distortion of the S-shaped G-Cys-Pt plot indicates the presence of slight O_2 mass transport inhibition, even with a forced O_2 supply by electrode rotation. This diffusion effect is negligible for C-Pt due to porous and larger particles of graphitized carbon (< 20 μm).

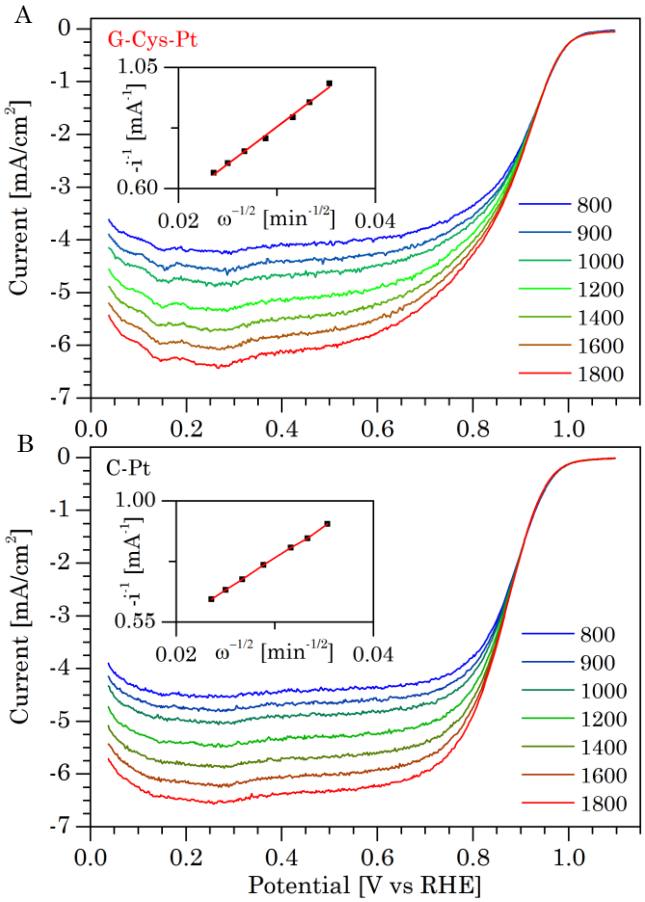

Figure 3.19 Dioxygen reduction reaction (ORR) for (A) G-Cys-Pt and (B) C-Pt. Linear sweep voltammograms in dioxygen saturated 0.10 M $HClO_4$ are recorded at 20 mV/s. Insets are Koutecky-Levich plots. The catalyst loading was 19.0 $\mu g_{Pt}/cm^2$ for G-Cys-Pt and 20.2 $\mu g_{Pt}/cm^2$ for C-Pt.

The insets in Fig. 3.19 are Koutecky-Levich plots, which describe the linear relation between limiting currents and the square root of the angular speeds of the electrode. The kinetic parameters of ORR can be analyzed on the basis of the Koutecky-Levich equation:[214]

$$\frac{1}{i}=\frac{1}{i_k}+\left(\frac{1}{0.62nFC_0(D_0)^{2/3}\nu^{-1/6}}\right)\omega^{-1/2} \qquad (3.9)$$

where i (mA/cm^2) is the measured current density, i_k (mA/cm^2) kinetic current density, ω the angular velocity of the rotating electrode ($\omega = (2\pi \cdot f)/60$ in rad/s, f is the linear rotating speed in rpm), n the overall number of electrons transferred during ORR, F (C/mol) the Faraday constant, C_0 the bulk concentration of oxygen in saturated 0.10 M H_2ClO_4 ($1.2 \cdot 10^{-6}$ mol/mL), D_0 the diffusion coefficient of O_2 ($1.9 \cdot 10^{-5}$ cm^2/s), and ν is the kinematic viscosity of the electrolyte (0.01 cm^2/s in 0.10 M $HClO_4$ solution). If limiting currents and square root of angular speeds are plotted versus each other, a linear plot is obtained with a slope equal to:

$$\text{Slope} = \frac{1}{0.62nFAC_0(D_0)^{2/3}\nu^{-1/6}\omega^{-1/2}} \tag{3.10}$$

From equation 3.10 the average electron number n in ORR can be estimated. From the plot slopes, obtained from Koutecky-Levich diagrams in Fig. 3.19A-B, the average number of electrons for G-Cys-Pt was found to be 4.0 and for C-Pt 3.7. However, the method is not completely reliable due to approximations in the equation[215], so in this Ph.D. work, n was obtained from experimentally measured currents during rotating ring disk electrode (RRDE) ORR experiments, Fig. 3.20.

The RRDE cathodic linear sweep voltammograms of G-Cys-Pt (red) and C-Pt (black) were performed at 1600 rpm. Solid and dashed lines represent currents from dioxygen reduction (disk electrode) and the corresponding H_2O_2 oxidation (ring electrode), respectively. The C-Pt catalyst exhibits an onset potential at 950 mV, and a E_{HW} of 870 mV vs. RHE. The onset potential and E_{HW} are shifted to 990 mV and 890 mV vs. RHE, respectively, for the G-Cys-Pt catalyst. The 20 mV overpotential reduction towards ORR on the G-Cys-Pt results in a catalytic activity of 121 A/g_{Pt} (measured at 0.900 V) outperforming C-Pt (89 $A/g_{Pt,}$ measured at 0.900 V) by 36 %.

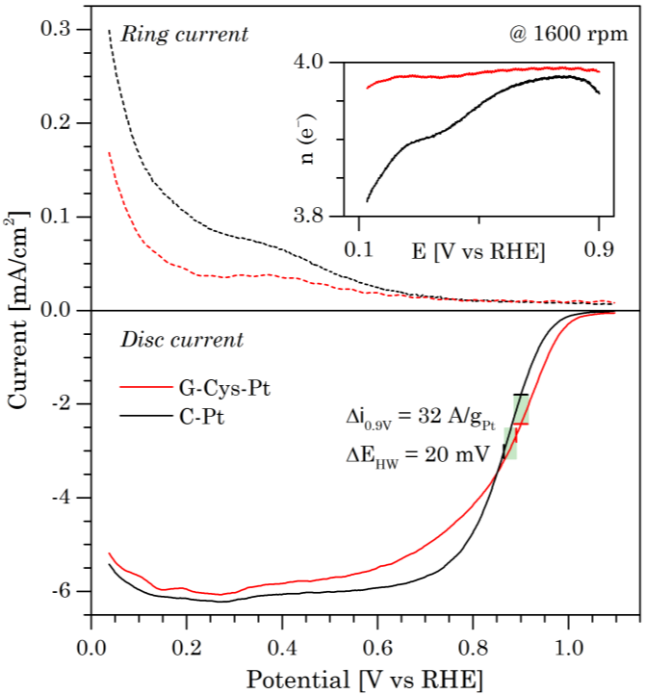

Figure 3.20 Voltammetry of RRDE on the ring electrode (upper) and disk electrode (bottom) for G-Cys-Pt (red) and C-Pt (black). Disk currents represent catalyst performance towards ORR (solid lines) and ring currents simultaneous oxidation of H_2O_2 formed during ORR (dashed lines). Linear sweep voltammetry at 20 mV/s and 1600 rpm in oxygen saturated 0.10 M $HClO_4$. The Pt ring potential was kept at 1.100 V vs. RHE. The catalyst loading was 19.0 $\mu g_{Pt}/cm^2$ for G-Cys-Pt and 20.2 $\mu g_{Pt}/cm^2$ for C-Pt.

As discussed in Chapter 1, dioxygen reduction proceeds either via a direct 4-electron pathway or via an unfavorable 2-electron formation of peroxide. The electron transfer number n was estimated from the ratio of the experimentally obtained currents at the disk and the ring electrodes since recent studies have pointed out the unreliability of the Koutecky-Levich analysis, due to relative errors of kinetic current density, standard rate constant and calculation errors originating in neglecting certain kinetic.[215] On the disk, both 2-electron (O_2 reduction to H_2O via intermediate H_2O_2) and 4-electron (O_2 reduction to H_2O) ORR occurs. H_2O_2 is oxidized to H_2O on the ring electrode. The 2-electron reduction current (I_{2e^-}) is expressed as:[216]

$$I_{2e^-} = \frac{I_R}{N} \tag{3.2}$$

where I_{2e^-} is the 2-electron ORR current on the disk electrode, N is the collection efficiency of the ring (37 %) and I_R the ring current.[216] The ORR current on the disk electrode (I_D) can be expressed as:[216]

$$I_D = I_{2e^-} + I_{4e^-} \tag{3.3}$$

where I_{4e^-} is the 4-electron ORR current. The average electron number n involved in ORR can be obtained by the following equation:[216]

$$\frac{I_D}{n} = \frac{I_{4e^-}}{4} + \frac{I_{2e^-}}{2} \tag{3.4}$$

By rearranging equation 3.4 and using expressions for I_{2e^-} from equation 3.2 and I_D from equation 3.3, the following relation is obtained:[216]

$$n = \frac{4I_D}{I_D + \left(\frac{I_R}{N}\right)} \tag{3.5}$$

The inset in Fig. 3.20 shows that both G-Cys-Pt and C-Pt reduce dioxygen to water almost exclusively through the direct 4-electron pathway, $O_2 + 4H^+ + 4e^- \rightarrow 2H_2O$. The average n for G-Cys-Pt at 0.2 V vs. RHE is 3.98 and for C-Pt 3.87. The improved interaction between small Pt NPs and G-Cys kinetically enhances the electrocatalytic performance for ORR, evidenced by more positive half-wave and onset potentials, as well as higher electron transfer number than for C-Pt.

3.5.4 Oxidation of fuel cell target molecules

The catalytic performance of G-Cys-Pt was further studied by electrochemical oxidation of 0.10 M FA, MeOH and EtOH in 0.10 M H_2SO_4 supporting electrolyte, Fig. 3.21 and Fig. 3.22. The FA oxidation reaction (FAOR) voltammetry displays four peaks, three in the anodic and the highest peak in the cathodic scan, Fig. 3.21A. Peak (1) at ca. 0.3 V, shoulder on the anodic scan, originates from oxidation of adsorbed formate to CO_2 (the direct pathway) which is then suppressed by the subsequent adsorption of CO.[217] The 0.6 – 0.7 V sharp anodic peak represents the oxidation of CO_{ads} to CO_2 (the indirect path), while the 1.2 V broad anodic peak is caused by the reaction of intermediates (e.g. adsorbed formate [218]) and FA at the oxidized Pt surface.[217] A strong and sharp peak at ~ 0.3 V during the cathodic scan originates from the direct oxidation of HCOOH to CO_2 at the metallic Pt surface after the reduction of Pt_{ox}.[219]

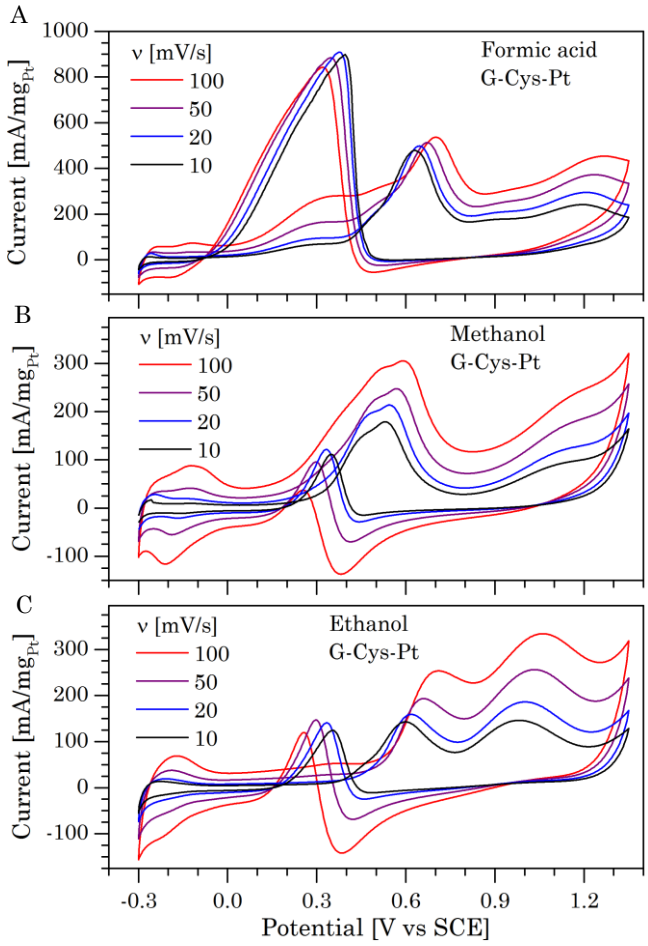

Figure 3.21 Electrochemical oxidation on G-Cys-Pt at different scan rates in (A) 0.10 M FA, (B) 0.10 M MeOH and (C) 0.10 M EtOH. All the measurements were performed in Ar-saturated 0.10 M H_2SO_4 supporting electrolyte. The catalyst loading was 50.2 $\mu g_{Pt}/cm^2$.

Fig. 3.22A shows 55 % higher currents at G-Cys-Pt (512 mA/mg_{Pt}) at 0.6 V, than that for C-Pt. Fig. 3.21B shows MeOH oxidation reactions (MOR) at G-Cys-Pt, producing four peaks which originate from direct/indirect MeOH oxidation with less peak separation at 0.5 V.[217] G-Cys-Pt shows 248 mA/mg_{Pt} for the anodic peak at 0.6 V, 17 % higher currents than the corresponding C-Pt peak, Fig. 3.22B. EtOH oxidation reaction (EOR) voltammograms of G-Cys-Pt are presented in Fig. 3.21C. The anodic peak at 0.7 V

represents CO_{ads} oxidation where G-Cys-Pt shows 193 mA/mg_{Pt}, 78 % higher currents than those obtained at C-Pt, Fig. 3.22C.

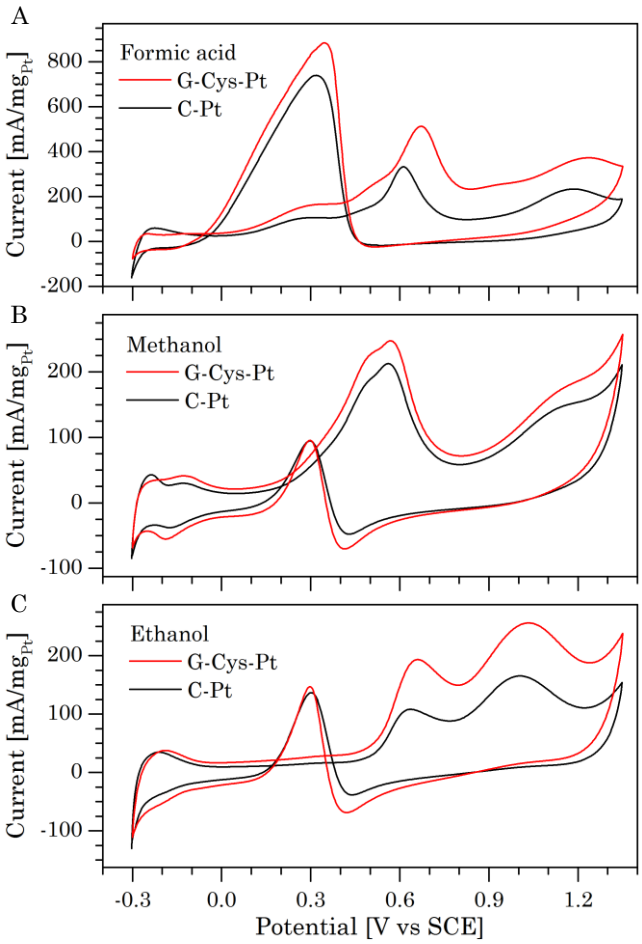

Figure 3.22 Electrochemical oxidation on G-Cys-Pt (red) and C-Pt at 50 mV/s in (A) 0.10 M FA, (B) 0.10 M MeOH and (C) 0.10 M EtOH. All the measurements were performed in Ar-saturated 0.10 M H_2SO_4 supporting electrolyte. The catalyst loading was 50.2 $\mu g_{Pt}/cm^2$ for G-Cys-Pt and 23.9 $\mu g_{Pt}/cm^2$ for C-Pt.

From electrochemical oxidation experiments, it is evident that G-Cys-Pt gives enhanced catalytic behavior compared to qualitatively very similar C-Pt catalysts. Since the catalysis was reported to the same Pt mass loading, the observed increase in electrocatalytic activity at G-Cys-Pt does originate from the synthesis optimization, i.e. reduced Pt NPs size increased $ECSA_{Pt}$ while efficient immobilization secured high conductivity through the catalyst. Covalent Cys linkers provide stronger molecular

interactions between G-Cys and Pt NPs than adsorbed Pt NP in C-Pt. As a result, faster electron pathways are created within the G-Cys-Pt electrocatalyst. This was primarily observed in RRDE ORR experiments where G-Cys-Pt goes favorably via 4-electron pathway with significant reduction in H_2O_2 production.
The optimization of morphology and composition in G-Cys-Pt will be applied in syntheses of graphene-supported core-shell electrocatalysts, which will focus on further electronic enhancement (1) of metallic NPs surface, (2) by replacing the Pt NP bulk material that is unavailable for electrochemical reactions and (3) by increasing crystalline faceting. These new catalysts will be described in Chapters 4 and 5.

3.6 Conclusions

The synthesized graphene was successfully functionalized by Cys molecules. Pt NPs were chemically immobilized on graphene sheets by Cys molecules to improve the electron transfer rates through the catalyst. G-Cys-Pt catalysts exhibited uniform NP dispersion and size distribution of 1.2 ± 0.8 nm. Electrochemical characterization confirmed the presence of Pt NPs on graphene, with increased electrocatalytic properties than for the commercial C-Pt. The G-Cys-Pt activity was tested towards ORR and electrochemical oxidation reactions of FA, MeOH and EtOH to examine the effect of covalent NP immobilization and size reduction. As the cathode catalyst, G-Cys-Pt exhibited current increase at 0.9 V vs. RHE by 32 A/g_{Pt} with average electron transfer number of 3.98, as well as 20 mV overpotential reduction for ORR compared to C-Pt. Modified Pt activity of G-Cys-Pt resulted in 55, 17 and 78 % higher FAO, MOR and EOR current densities at ~ 0.6 V, compared to C-Pt.
Although qualitatively the same catalysts, Pt NPs supported on a carbon material, G-Cys-Pt showed superior electrocatalysis to C-Pt. These slight but significant improvements for G-Cys-Pt indicated enhancement of its electronic features. Higher $ECSA_{Pt}$, more efficient immobilization via chemical bonding, and highly-conductive graphene support contributed to faster rates of electrochemical reactions. The morphological and compositional modifications of G-Cys-Pt offer a basis of further catalyst design optimization.

Chapter 4

Graphene-Au@Pt catalysts

4.1 Introduction: goals and application

Catalyst plays a crucial role in the performance of a FC system. As the most efficient catalyst for FCs, platinum (Pt) has been widely used for both anodes and cathodes in PEMFCs. However, the high price of Pt, poisoning by CO-like intermediates and challenges regarding stability drive us to develop catalyst systems ultra-low in Pt or even Pt-free. Since bulk Pt (sheet or foil form) is neither economical or provides high catalysis due to decreased electrochemical surface area (ECSA) per mass of the material, Pt-based nanocatalyst are developed. Increasing the electrochemically active surface area (ECSA) of Pt-based catalysts by nanostructure formation offers an approach to optimize their catalytic activity. Reducing the nanoparticle (NP) size decreases the relative amount of Pt needed and boosts the specific ECSA, resulting in better catalytic performance. However, a size limitation occurs around 2.2 nm, below which the activity declines due to the loss of low-index crystal faceting and aggregation during the catalysis.[188] Nanostructured material properties significantly depend on chemical composition, size, crystallinity and morphology. Preservation of high catalytic activity by joining both merits of small particle size and favorable low-index faceting is achieved through "nanostructuring" approach, targeted at resolving catalytic limitations originating in NP morphology. Bimetallic core-shell NPs reduce the amount of inactive bulk atoms, at the same time preserving the crystalline surface faceting of the target Pt shell. Synergetic effects between core and shell can even reduce catalytic poisoning.[220] Replacement of inactive Pt bulk by gold (Au) produces stable NPs with more efficient Pt utilization.[221] Au nanostructures have been widely studied and their application as CO oxidation catalysts are well established.[222] Moreover, having an atomic diameter size close to Pt and being a stabilizing agent for reactions in PEMFC application,[221][223] Au is an ideal candidate for core material in core-Pt_{shell} NP architectures. Au@Pt NPs can be prepared by three main syntheses routes: (1) underpotential deposition (UPD) of copper (Cu) on Au followed by galvanic displacement of Cu with Pt precursors [224], (2) precursor co-reduction followed by thermal treatment [225], and (3) by reduction via seed-mediated growth [226].

Large-scale production is not economically viable through UPD methods, despite the possibility of creating atomically thin shells. High thermal treatment syntheses, require harsh operating conditions and often non-aqueous solvents.[225] Seed-mediated syntheses often result in poor yield and morphology control of the product.[227]
This chapter describes developments of Au-Pt core-shell NPs (Au@Pt NPs) seed-mediated syntheses, using a glucose recipe.[150] The Au@Pt NPs show catalytic function towards electrochemical oxidation of sustainable fuels such as formic acid (FA), methanol (MeOH) and ethanol (EtOH), as well as selective hydrogenation of benzene derivatives.[150] The presence of Au can easily oxidize catalytic poisons generated from small organic molecules.[228] Further development of electrocatalysts is, therefore, based on Au@Pt NPs for FC systems. The new Au@Pt NPs may hold a perspective for large-scale production of catalysts that requires uniform products prepared under mild conditions with low cost.

A suitable support material with strong interactions with the target NPs is, however, needed to fully exploit the catalyst function. Stability and conductivity of the catalysts are essential, e.g. fast electron transfer from the active site at the catalyst surface through the support material to the external circuit. Carbon black or graphitized carbon black are commercially used as support materials for Pt NPs in PEMFC application.[197] However, these carbon materials can be oxidized at potentials above 0.8 V vs. standard hydrogen electrode (SHE). Resulting conductivity degradation leads to loss of FC performance.[198] Such issues can be effectively avoided by the use of graphene as a supporting material, due to the large surface area (2600 m^2g^{-1}), chemical inertness under PEMFC operating conditions and high electrical conductivity of this material.[199] Graphene has been used as a support for metal NPs such as Pt[200], Pt-Fe[201], Pt-Co[201], Pt-Au alloy[202], and Fe/Co-N[203]. In this chapter, a three-step method for the preparation of electrocatalysts equipped with 9.5 ± 2 nm Au@Pt NPs covalently anchored on graphene (G-Cys-Au@Pt) is demonstrated. The Au@Pt NPs with atomically thin Pt shells are synthesized using 2-(N-morpholino)ethanesulfonic acid (MES) and glucose as environmentally harmless reducing and shape-directing agents. High loading of uniformly distributed Au@Pt NPs on graphene was achieved through covalent bonding via L-Cysteine (Cys) molecules. Graphene precursor, graphene oxide (GO), was functionalized by Cys via 1-Ethyl-3-(3-dimethylaminopropyl)carbodiimide (EDC) and N-Hydroxysuccinimide (NHS) surface-based coupling reactions, while Au@Pt NPs were immobilized on Cys anchors by covalent thiol-Au bonds. Cys linked G-Cys-Au@Pt electrocatalyst exhibited high activity for FA, MeOH and EtOH electrochemical oxidation, as well as for dioxygen reduction reaction (ORR). The G-Cys-Au@Pt catalyst was further applied in direct formic acid fuel cell (DFAFC), direct methanol fuel cell (DMFC) and direct ethanol fuel cell (DEFC) for functional tests. Pt-based commercial catalyst was utilized as a reference in power density and stability analysis. The superior performance was found for G-Cys-Au@Pt catalysts.

Systematic structure and compositional mapping suggested that the enhanced performance originated in (1) the tailored electron transfer pathway through the Cys linker of G-Cys-Au@Pt, (2) improved Pt utilization and activity from the synergy between atomic Pt shells and Au cores, (3) covalent and stable anchoring of catalyst NPs, and (4) the highly conductive and robust graphene support.

4.2 Synthesis and sample preparation

4.2.1 Chemicals

Table 3.1 Chemicals used for syntheses of GO, G-Cys and G-Cys-Au@Pt

Chemical name, formula	Pur. (%)	CAS	Mw (g/mol)	Co. City, Country
2-(N-morpholino)ethanesulfonic acid, MES hydrate, $C_6H_{13}NO_4S \cdot xH_2O$	≥ 99.5	4432-31-9	195.24	S-A St. Louis, USA
Chloroplatinic acid hydrate, $H_2PtCl_6 \cdot xH_2O$	≥ 99.9	26023-84-7	409.81	
D-(+)-glucose, $C_6H_{12}O_6$	≥ 99.5	50-99-7	180.16	
Ethanol, C_2H_6O	≥ 99.9	64-17-5	46.07	Uvasol Darmstadt, DE
Formic acid, HCOOH	98-100	64-18-6	46.03	S-A, Steinheim, DE
Gold (III) chloride trihydrate, $HAuCl_4 \cdot 3H_2O$	≥ 99.9	16961-25-4	393.83	S-A St. Louis, USA
Graphite powder	99.99	7782-42-5	12.01	S-A, Buchs SG., CH
Graphene oxide, $C_xO_yH_z$, GO,	A	Homemade		Kgs. Lyngby, DK
Hydrogen peroxide, H_2O_2	30(*aq.*)	7722-84-1	34.01	S-A, Steinheim, DE
Hydrochloric acid, HCl	37	7647-01-0	36.46	
Methanol, CH_3OH, MeOH	≥ 99.9	67-56-1	32.04	
N-(3-Dimethylaminopropyl)-N'-ethylcarbodiimide hydrochloride, EDC, $C_8H_{17}N_3 \cdot HCl$	≥ 98.0	25952-53-8	191.7	S-A Tokyo, JP
N-Hydroxysuccinimide, NHS, $C_4H_5NO_3$	97	6066-82-6	115.09	S-A Steinheim, DE
Nitric acid, HNO_3	≥ 65	7697-37-2	63.01	
Phosphorus pentoxide, P_2O_5	98%	1314-56-3	141.94	S-A, Bengaluru, IN
Platinum on graphitized carbon	20 [B]	product nu: 38549-1G	Pt: 195.08	S-A St. Louis, USA
Potassium hydroxide, pellets, KOH	99.99 [C]	1310-58-3	56.11	
Potassium permanganate, $KMnO_4$	97	7722-64-7	158.03	
Potassium persulfate, $K_2S_2O_8$	> 99.0	7727-21-1	270.32	Fluka St. Louis, USA
(R)-2-amino-3-mercaptopropionic acid, L-cysteine, $C_3H_7NO_2S$	≥ 99.5	52-90-4	121.16	
Sulfuric acid, H_2SO_4, TraceSELECT®	≥ 95[C]	7664-93-9	98.08	Fluka, Lyon, FR

[A] Dialysis purification, [B] Pt wt.%, [C] (10 - 15% H_2O), Sigma-Aldrich (S-A), United States of America (USA), Germany (DE), Switzerland (CH), Denmark (DK), Japan (JP), India (IN), France (FR).

4.2.2 G-Cys-Au@Pt synthesis

Synthesis of G-Cys-Au@Pt synthesis route consisting of (1) GO functionalization with Cys followed by formation of (2) Au NPs as cores and (3) Au core-Pt shell NP preparation. The G-Cys was synthesized first, as described in section 3.3.3, Chapter 3.

For G-Cys-Au@Pt synthesis, a solution containing 2.50 mL 0.10 M MES (pH = 7.03), 2.50 mL 0.10 M glucose, 8.75 mL 0.40 mg/mL G-Cys and 8.75 mL Millipore water was heated at 95 °C for 10 minutes in a water bath, Fig. 4.1A. Addition of 2.50 mL of 20.3 mM $HAuCl_4$ for 1 hour at 95 °C resulted in Au NP formation. G-Cys-Au solution had a dark red color, Fig. 4.1B. After the Au NP seed formation, 74.0 mL of water was added to the flask followed by 1.0 mL of 20.0 mM H_2PtCl_6 and continued heating at 70 °C for 2 hours to obtain an atomically thin Pt layer on Au NP seeds. The final G-Cys-Au@Pt solution was dark brown, Fig. 4.1D.

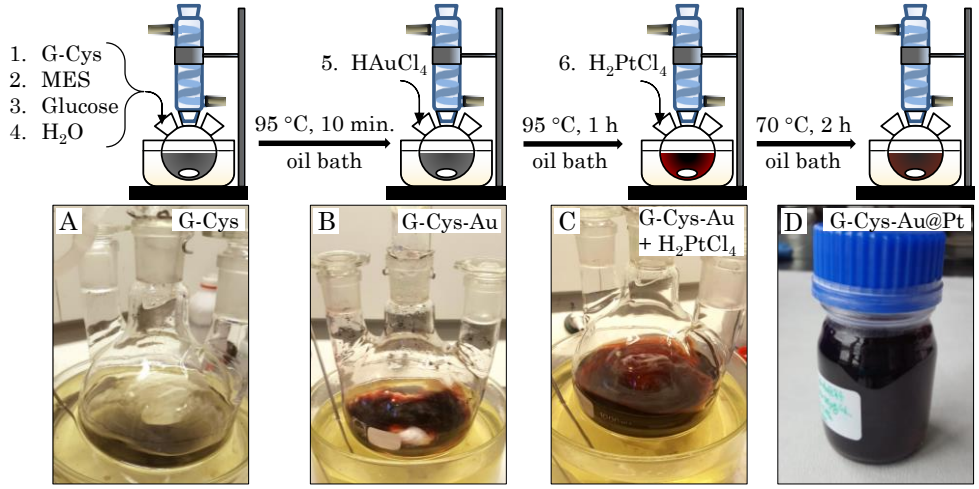

Figure 4.1 The scheme of G-Cys-Au@Pt synthesis.

Afterwards, the solution was sonicated for 1 hour and purified by 4 centrifugation cycles to remove excess NPs and impurities, Fig 4.2. Centrifugation cycles were performed at 12 krpm for 10 min, discarding the supernatant and re-dispersing the residue. Final cycle was performed at 8 krpm for 5 min, to make sure all the impurities have been disposed of as supernatant. Purified G-Cys-Au@Pt residue was finally re-dispersed in 50 mL Millipore water resulting in c_{final}(G-Cys) = 0.35 mg/mL.

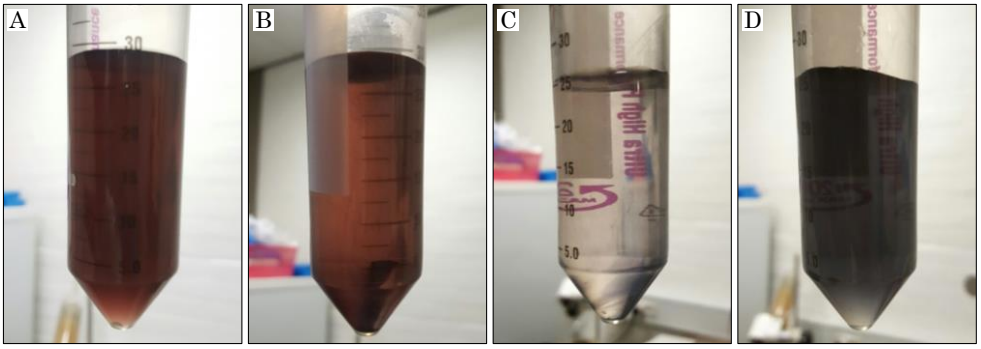

Raw solution | After 1st cycle | After 4th cycle | Re-dispersed after 4th cycle

Figure 4.2 (A) As-synthesized G-Cys-Au@Pt before centrifugation purification. G-Cys-Au@Pt (B) after 1st cycle of centrifugation, and (C) after 4th centrifugation cycle, supernatant is completely transparent. (D) G-Cys-Au@Pt re-dispersed and purified after 4th cycle of centrifugation.

4.2.3 Electrode preparation for electrochemical experiments

Electrode polishing and cleaning

All glassware was cleaned by boiling in 15% HNO_3 solution followed by washing in Millipore water. The glassy carbon electrode (GCE, ϕ = 4.0 mm, A = 0.1256 cm^2) and rotating ring (Pt) disk (GCE) electrode (RRDE, ϕ_{disk} = 5.61 mm, A_{disk} = 0.2472 cm^2, ϕ_{ring} (inner) = 6.25 mm, ϕ_{ring} (outer) = 7.92 mm, A_{ring} = 0.1859 cm^2, ring collection efficiency = 37 %) was first wet-polished by sand paper (grit roughness 2000, followed by 4000) for 10 min by hand. They were further polished by Al_2O_3 slurry (particle diameter sizes of 1.0, 0.3 and 0.05 µm), using the largest particle size first (rough polishing) and finishing with the finest particle size (mirror-like electrode surface finish). The electrodes were sonicated in Millipore water for 30 min in total with intermittent water exchange (1st time after 5, 2nd time after 10, and 3rd time after 15 minutes). Freshly cleaned electrodes were dried in the fume hood at room temperature for 5 min. prior to drop-casting. The RRDE was purchased from Pine Research Instrumentation, Inc. (USA).

Drop-casting catalysts

Electrochemical performance of G-Cys-Au@Pt catalyst has been compared to commercial catalyst from Sigma-Aldrich, 20 wt. % of Pt (NP size ~ 5 nm) on graphitized carbon (C-Pt). Au core in G-Cys-Au@Pt is not catalytically active towards oxidation of used biofuels or ORR, however, the Pt shell catalyzes these reactions. Pt was, therefore, maintained in the same amount for all the electrodes as a catalytic material. In case of ORR experiments, the Pt loading on RRDE was 5 µg (20.2 µgPt/cm^2), while the loading for the

rest of the electrochemical experiments was 3 µg of Pt on GCEs (23.9 $\mu g_{Pt}/cm^2$). Catalyst layer was protected by 5 µL of 0.05 % Nafion® (dissolved in ethanol). Prior to the calculation procedure, TGA experiments determined the metal loading in the catalyst, Fig. 4.4. EDX measurements were performed for G-Cys-Au@Pt to obtain the metal composition of the bimetallic structure, Fig. 4.8. From these two data sets, it is possible to calculate Pt loading for G-Cys-Au@Pt catalyst. The calculation for drop-casting procedure for both G-Cys-Au@Pt and C-Pt, containing 3 µg of Pt on GCE, is as follows:

G-Cys-Au@Pt

$Au@Pt_{(wt.\%)}$ = 42 % (TGA, Fig. 4.4)
Au : Pt metal ratio = 2.95 : 1 (EDX, Fig. 4.8)
c_{final}(G-Cys-Au@Pt) = 0.35 mg/mL

Relative Pt loading ($Pt_{relative}$) is first calculated using equation 4.1:

$$Pt_{relative} = \frac{Pt}{Au+Pt} \cdot 100 \tag{4.1}$$

$$\frac{1}{3.95} \cdot 100 = 25.32\ \%$$

The actual Pt loading in G-Cys-Au@Pt can be calculated as a mass percentage using equation 4.2:

$$Pt_{(wt.\%)} = Au@Pt_{(wt.\%)} \cdot Pt_{relative} \tag{4.2}$$

$$42.0\% \cdot 0.2532 = 10.63\%$$

3 µg of Pt on GCE equals to the total catalyst mass multiplied by the pure Pt loading, $Pt_{(wt.\%)}$:

$$m(\text{Pt on GCE}) = m(\text{G-Cys-Au@Pt}) \cdot Pt_{(wt.\%)} \tag{4.3}$$

$$3\ \mu g = m(\text{G-Cys-Au@Pt}) \cdot 0.1063$$

$$m(\text{G-Cys-Au@Pt}) = 28.2\ \mu g$$

3 µg of pure Pt on GCE corresponds to 28.2 µg of G-Cys-Au@Pt. Such small volume cannot be weighed on a scale, therefore, volumetric amount containing 28.2 µg of G-Cys-Au@Pt is calculated. According to equation 4.4, mass of G-Cys-Au@Pt is equal to the sum of the support material (G-Cys) and Au@Pt NP masses:

$$m(\text{G-Cys-Au@Pt}) = m(\text{G-Cys}) + m(\text{Au@Pt}) \tag{4.4}$$

The mass of Au@Pt NPs is a product of the total catalyst mass and the total metal loading percentage. Equation 4.5 substitutes the mass of Au@Pt NPs by such an expression:

$$m(\text{G-Cys-Au@Pt}) = m(\text{G-Cys}) + m(\text{G-Cys-Au@Pt}) \cdot Au@Pt_{(wt.\%)} \tag{4.5}$$

$$m(\text{G-Cys}) = m(\text{G-Cys-Au@Pt}) \cdot (1 - Au@Pt_{(wt.\%)})$$

$$28.2\ \mu g \cdot (1 - 0.42)$$

$$28.2\ \mu g \cdot 0.58$$
$$16.4\ \mu g$$

Calculated mass of G-Cys corresponds to 3 µg of Pt via the m(G-Cys-Au@Pt) calculated by equation 4.3. Mass of G-Cys equivalent to the desired Pt loading is used for final drop-casting volume calculation. The Au@Pt NPs are immobilized on G-Cys, meaning that the volume of G-Cys is equal to the catalyst volume V(G-Cys-Au@Pt):

$$m(\text{G-Cys}) = c(\text{G-Cys}) + V(\text{G-Cys}) \tag{4.6}$$
$$V(\text{G-Cys-Au@Pt}) = \frac{m(\text{G-Cys})}{c(\text{G-Cys})}$$
$$\frac{16.4\ \mu g}{350\ \mu g/mL} = 47.0\ \mu L$$

C-Pt

The catalytic ink was prepared by dispersing 1.3 mg of C-Pt catalyst powder in 0.50 mL of Millipore water, 0.45 mL of ethanol and 50 µL of 5.0 wt.% Nafion® solution (dissolved in ethanol). The ink is sonicated for 30 min prior to each drop-casting.

$Pt_{(wt.\%)} = 20\ \%$
$c(\text{C-Pt}) = 1.3\ mg/mL$

3 µg of Pt on GCE equals to the total catalyst mass multiplied by the pure Pt loading:

$$m(\text{Pt on GCE}) = c(\text{C-Pt}) \cdot V(\text{C-Pt}) \cdot Pt_{(wt.\%)} \tag{4.7}$$

The drop-casting volume can, therefore, be calculated from equation 4.9:

$$V(\text{C-Pt}) = \frac{m(\text{Pt on GCE})}{c(\text{C-Pt}) \cdot Pt_{(wt.\%)}} \tag{4.8}$$
$$\frac{3\ \mu g}{1300\ \mu g/mL \cdot 0.2} = 11.5\ \mu L$$

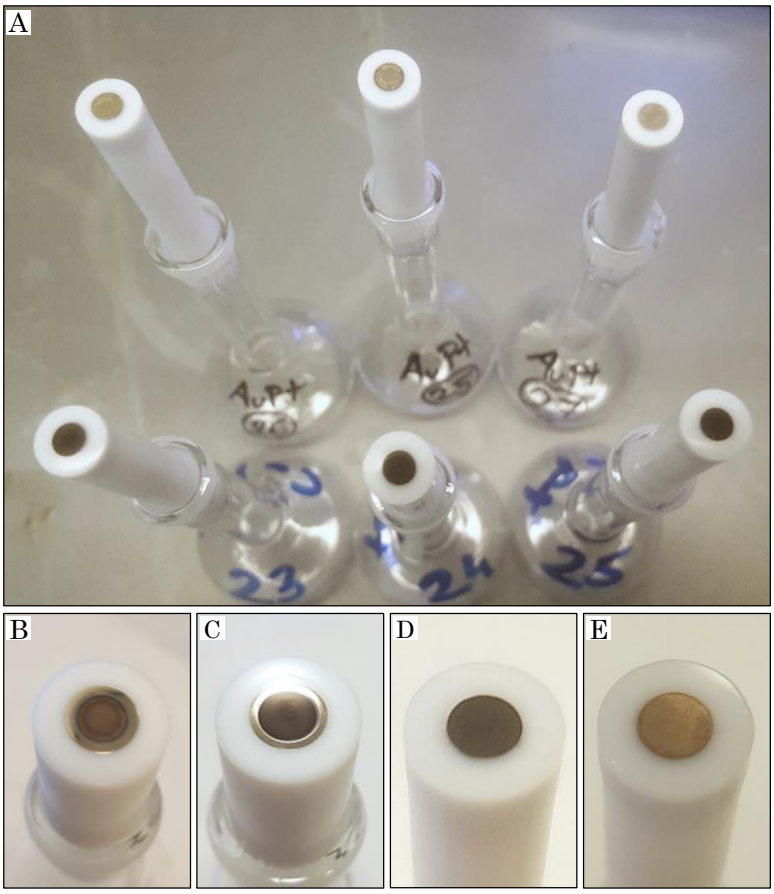

Figure 4.3 (A) 3 GCEs with G-Cys-Au@Pt (3 µg of Pt on GCE) in the upper row and 3 GCEs with C-Pt (3.0 µg of Pt on GCE) lower row. Magnified: (B) G-Cys-Au@Pt and (C) C-Pt on RRDE (5.0 µg of Pt), (D) C-Pt and (E) G-Cys-Au@Pt on GCE and (3.0 µg of Pt).

According to the respective areas of electrodes, the mass/area loading was 20.2 $\mu g_{Pt}/cm^2$ for the RRDE and 23.9 $\mu g_{Pt}/cm^2$ for the GCE, for both G-Cys-Au@Pt and C-Pt electrocatalysts.

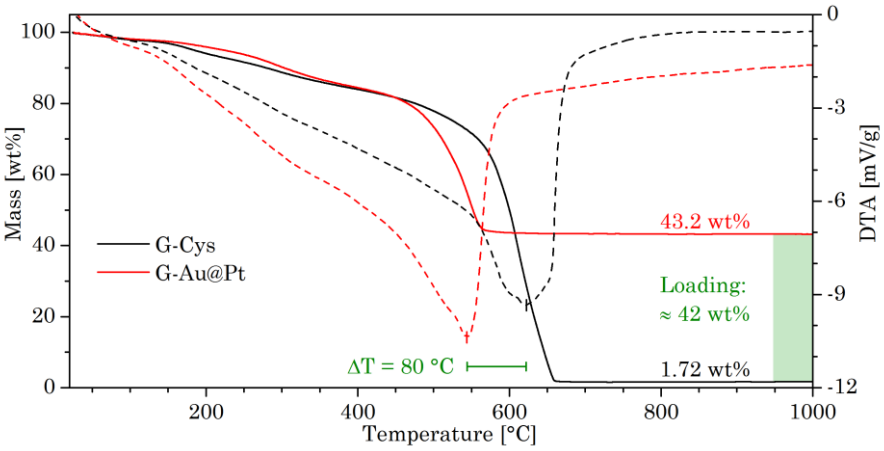

Figure 4.4 TGA measurements for G-Cys (black) and G-Cys-Au@Pt (red) in solid lines. The Pt NP loading in G-Cys-Pt is ≈ 42 wt.% (green shaded area). DTA measurements are presented in dashed lines.

The TGA measurements were performed for G-Cys as a reference material and G-Cys-Au@Pt catalyst. The G-Cys and G-Cys-Au@Pt show the same trend in both TGA and DTA data sets. After 660 °C the curves are plateauing at 1.72 wt.% for G-Cys and 43.2 wt.% for G-Cys-Au@Pt. The actual metal loading in G-Cys-Au@Pt was determined to be ≈ 42 wt.% by subtracting the residual relative mass of the reference material, G-Cys. It is noticeable that the burning of the graphene was catalyzed by the metallic NPs. The highest energy release representing the burning of the graphene support occurred at 475 °C for G-Cys-Au@Pt, which is 80 °C lower than for G-Cys, as seen in DTA plots.

4.3 Structure, compositions and optical properties

GO has been prepared by a modified Hummer's method, as described in the experimental part. AFM images of GO deposited onto mica sheets (Fig. 3.13) indicate successful exfoliation of single layered GO sheets, with thicknesses averaging at 0.8 nm and lateral size distribution ranging from several hundred nanometers to 5 µm. The G-Cys-Au@Pt nanocatalyst was successfully prepared by a green, three-step synthesis route consisting of (1) GO functionalization with Cys followed by formation of (2) Au NP cores and (3) Au core-Pt shell NP preparation, illustrated in Fig.4.5. The Cys linker was introduced to the GO in the presence of EDC and NHS coupling reactions in aqueous environment followed by hydrothermal reduction, resulting in G-Cys, in which the amine group of Cys was covalently anchored on graphene. The prepared material was purified and utilized as a Au NP support in the following step. The thiol group was utilized to attract gold atoms

for immobilization of Au NP cores on the graphene (G-Cys-Au). Pt precursor was subsequently slowly added and reduced by glucose, forming atomically thin Pt shells around the anchored Au NP cores (G-Cys-Au@Pt). Accompanied color change from G-Cys black to strong, dark-red indicated successful G-Au formation. Consecutively, Pt precursor was slowly reduced by glucose, forming atomically thin Pt shells on Au NP cores. The significant modification of Au NP surface was suggested from a color change to dark-brown for G-Cys-Au@Pt. The synthesized G-Cys-Au@Pt nanocatalyst was purified and concentrated by repeated centrifugation in Millipore water.

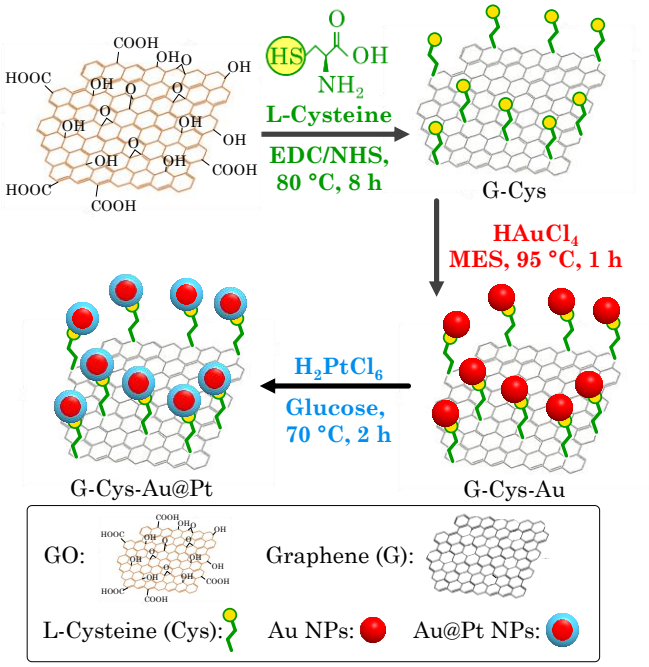

Figure 4.5 Three-step synthesis route of G-Cys-Au@Pt: 1) GO functionalization with Cys via EDC/NHS coupling and thermal reduction to graphene, G-Cys, 2) Au NPs synthesis and anchoring through Au-S bonding, G-Au, 3) Pt shell growth on the Au NPs by reduction of $[PtCl_6]^{2-}$, G-Cys-Au@Pt.

4.3.1 Microscopic characterization of G-Cys-Au@Pt

As a reference, Pt NPs were synthesized through the same route and immobilized on G-Cys. These are noted as G-Cys-Pt (Chapter 3). G-Cys-Pt showed a morphological difference from G-Cys-Au@Pt with a narrow and homogeneous Pt NPs size distribution of 1.2 ± 0.8 nm. The G-Cys-Au@Pt catalyst showed no presence of 1.2 ± 0.8 nm NPs

indicating the absence of separately synthesized Pt NPs. The controllable loading of Au@Pt NPs on graphene was achieved by tuning the density of Cys on GO. The regulating parameter crucial for quantitative coupling of Cys to graphene was altering the concentrations of EDC (from 0.5 to 5.0 mM) and NHS (from 1.0 to 5.0 mM) used in the G-Cys synthesis route. It allowed for high or low surface coverage of graphene adsorption sites available for Cys to attach, depending on higher or lower EDC and NHS concentrations used, respectively, Fig. 4.6.

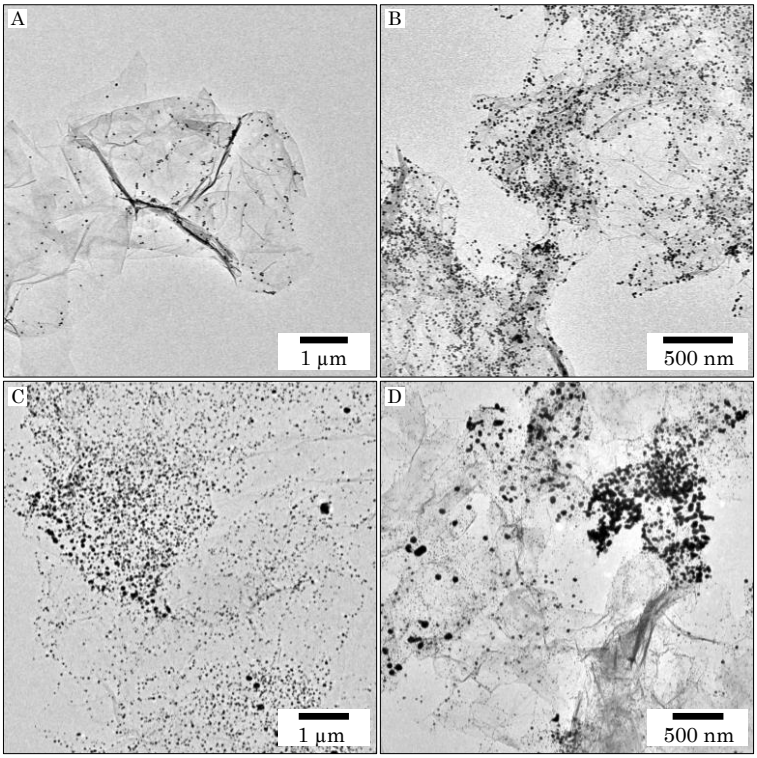

Figure 4.6 TEM images of G-Cys-Au@Pt with various Au@Pt NP loadings tuned by varying EDC and NHS concentrations, (A) EDC 0.5, NHS 1.0 mM, (B) both 2.0 mM, (C) EDC 4.0, NHS 2.0 mM and (D) both 5.0 mM.

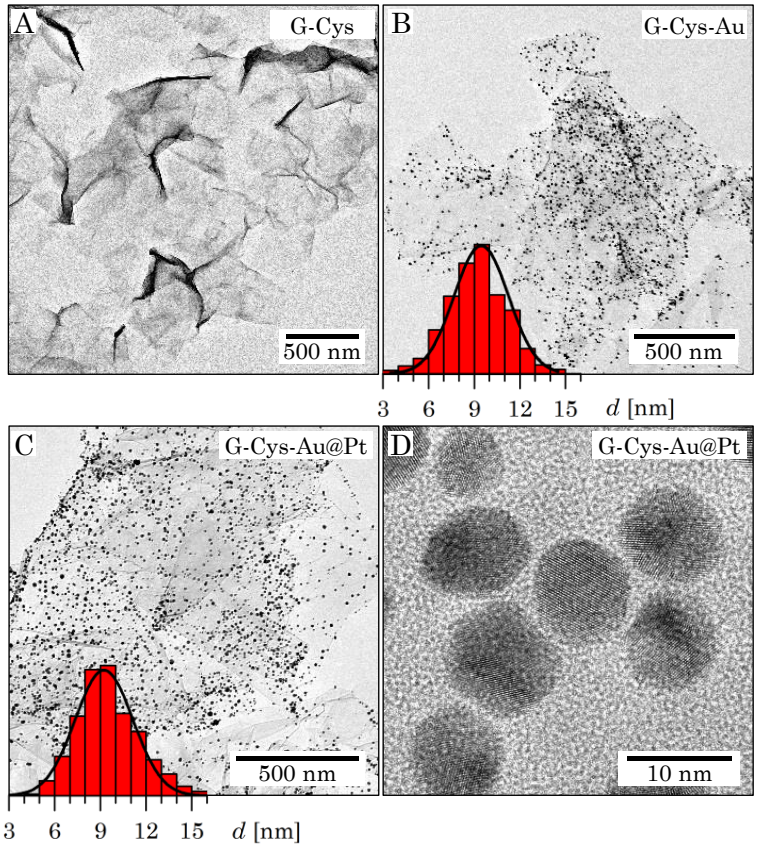

Figure 4.7 TEM images of (A) G-Cys, (B) G-Cys-Au and (C) G-Cys-Au@Pt. The size distributions of Au NPs and Au@Pt NPs are shown as inset in (B) and (C), respectively. (D) HR-TEM image of G-Cys-Au@Pt.

The morphology, size and elemental composition of the synthesized materials were mapped by transmission electron microscopy (TEM), high-resolution TEM (HR-TEM), Fig. 4.7 and by energy-dispersive X-ray spectroscopy (EDX), Fig. 4.8. G-Cys is composed of large, Cys-modified graphene sheets in ranges of hundreds of nanometers up to 5 µm, confirmed by TEM, Fig. 4.7A and XPS, Fig. 4.10. Au NP synthesis conducted in the presence of G-Cys resulted in uniform NPs of 9.5 ± 1.8 nm, immobilized on the graphene (G-Cys-Au), Fig. 4.7B. Subsequent chemical deposition of Pt shells on the Au-cores generated G-Cys-Au@Pt, Fig. 4.7C-D. EDX measurements confirm that the G-Cys-Au@Pt particles contain 75 ± 1% Au and 25 ± 1% Pt. From the formal statistical analysis, the size of the Au@Pt NPs from TEM was found to be 9.5 ± 2 nm (Fig. 4.7C), was in fact almost identical to the size of the Au NP in G-Cys-Au. The atomically thin Pt shells (3-4 Å) on

Au NPs were hardly detectable directly from TEM (Fig. 4.7D) and instead evaluated on the basis of the metal ratio and NP size obtained from TEM and EDX (Fig. 4.8), as established previously.[150] In SAMENS, a successful formation of 1-atom thin Pt shells was achieved with starch as a strong NP size directing and stabilizing agent. A slight Pt shell thickness increase in G-Cys-Au@Pt is justifiably attributed to the absence of starch in the synthesis route. The lack of starch, however, results in more efficient Au@Pt NP immobilization through stronger Au NP interactions with thiol anchoring centers. NP aggregation is prevented by the rapid adsorption on graphene support, eliminating any need for additional stabilizing agents.

A

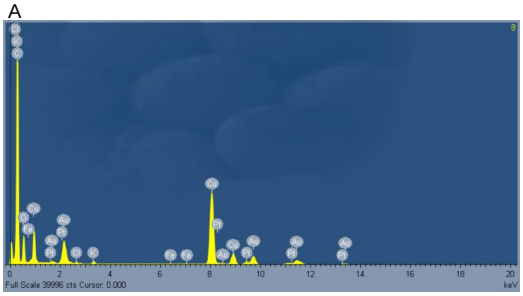

B

Element	Peak Area	Area Sigma	k factor	Abs Corrn.	Weight%	Weight% Sigma	Atomic%
O K	8256	197	1.903	1.000	16.21	0.36	52.92
Cl K	408	81	0.975	1.000	0.41	0.08	0.61
K K	1762	97	0.957	1.000	1.74	0.10	2.32
Fe K	1362	81	1.154	1.000	1.62	0.10	1.52
Co K	1372	86	1.219	1.000	1.73	0.11	1.53
Cu K	26423	264	1.337	1.000	36.45	0.43	29.97
Pt L	4018	199	2.543	1.000	10.54	0.48	2.82
Au L	11742	266	2.585	1.000	31.31	0.54	8.31
Totals					100.00		

C

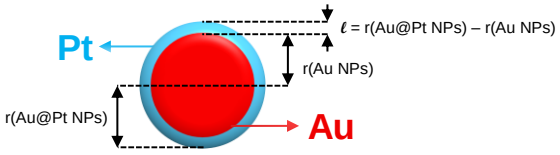

Figure 4.8 The energy-dispersive X-ray spectroscopy (EDX) measurements of G-Cys-Au@Pt: (A) diagram and (B) elemental analysis table. Au (atomic %) and Pt (atomic %) represent atomic percentages of Au and Pt obtained directly from EDX measurements. The analysis was performed by INCA software. (C) A model showing r(Au@Pt NP) the Au@Pt nanoparticle radius, r(Au NP) the Au nanoparticle radius and ℓ the thickness of the Pt shell.

4.3.2 Detailed calculation for the Pt shell thickness in Au@Pt

The thickness of Pt shells around Au NP cores in G-Cys-Au@Pt is achieved on the basis of EDX data and TEM Au@Pt NP size measurements.

r (Au@Pt NPs) ≅ 4.80
d (Pt atom) = 2.78 Å
Au (atomic %) = 8.31
Pt (atomic %) = 2.82

From the EDX measurements (Fig. 4.8B) the metal ratio Au : Pt can be obtained:

$$\text{Au (atomic \%)} : \text{Pt (atomic \%)} = 2.95 : 1 \tag{4.9}$$

Multiplying the molar masses (Mw) of Au and Pt by their respective atomic ratios, mass percentages are obtained:

$$\text{Au (mass \%)} = \text{Au (atomic \%)} \cdot \text{Mw (Au)} \tag{4.10}$$
$$2.95 \cdot 196.97 = 581.06$$

$$\text{Pt (mass \%)} = \text{Pt (atomic \%)} \cdot \text{Mw (Pt)} \tag{4.11}$$
$$1 \cdot 195.08 = 195.08$$

The volume percentages of the metals are obtained by dividing the mass percentages by the respective crystal densities of Au and Pt:

$$\text{Au (vol. \%)} = \text{Au (mass \%)} : \rho\,(\text{Au}) = 581.06 : 19.32 = 30.08 \tag{4.12}$$

$$\text{Pt (vol. \%)} = \text{Pt (mass \%)} : \rho\,(\text{Pt}) = 195.08 : 21.45 = 9.09 \tag{4.13}$$

Relative volume percentages of Au and Pt in the Au@Pt NPs can be calculated from volume percentages of metals obtained in equations 4.12 and 4.13:

$$\text{Au (relative vol. \%)} = \frac{\text{Au (vol. \%)}}{\text{Au(vol. \%)} + \text{Pt(vol. \%)}} \tag{4.14}$$
$$\frac{30.08}{39.17} = 0.7679 = 76.79\ \%$$

$$\text{Pt (relative vol.\%)} = 100\ \% - 76.79\ \% = 23.21\ \% \tag{4.15}$$

Since the Au@Pt NPs are approximately spherical, as observed in TEM images, the volume of Au@Pt NPs was calculated from equation 4.16. The radius of Au@Pt NPs was obtained from an ensemble of 1400 measurements of NP size using TEM and high resolution TEM imaging ($d_{Au@Pt}$ = 9.6 nm).

$$V\,(\text{Au@Pt NP}) = \frac{4}{3}\pi r^3 \tag{4.16}$$

$$\frac{4}{3}\pi \cdot (4.8 \cdot 10^{-9}\,\mathrm{m})^3 = 4.63 \cdot 10^{-25}\,\mathrm{m}^3$$

The volume of the Au core is given in equation 4.17 from the Au@Pt NP volume and Au relative volume percentage obtained from equation 4.14:

$$\begin{aligned} &\mathrm{V\ (Au\ core)} = \mathrm{V\ (Au@Pt\ NP)} \cdot \mathrm{Au\ (relative\ vol.\%)} \\ &4.63 \cdot 10^{-25} \cdot 0.7679 = 3.56 \cdot 10^{-25}\,\mathrm{m}^3 \end{aligned} \tag{4.17}$$

The radius of the Au core is calculated from equation 4.18:

$$\begin{aligned} &\mathrm{r\ (Au\ core)} = \sqrt[3]{\frac{3 \cdot \mathrm{V\ (Au\ core)}}{4 \cdot \pi}} \\ &\sqrt[3]{\frac{3 \cdot 3.56 \cdot 10^{-25}\,\mathrm{m}^3}{4 \cdot \pi}} = 4.40 \cdot 10^{-9}\,\mathrm{m} \end{aligned} \tag{4.18}$$

Pt shell thickness ($\boldsymbol{\ell}$) equals the difference of the Au core and Au@Pt NP radii:

$$\begin{aligned} &\boldsymbol{\ell} = \mathrm{r\ (Au@Pt\ NPs)} - \mathrm{r\ (Au\ core)} \\ &4.80 \cdot 10^{-9}\,\mathrm{m} - 4.40 \cdot 10^{-9}\,\mathrm{m} = 4.00\ \text{Å} \end{aligned} \tag{4.19}$$

Finally, $\boldsymbol{\ell}$ in number of Pt atomic layers ($\boldsymbol{\ell}_{\mathrm{atomic}}$) is further calculated by dividing $\boldsymbol{\ell}$ with the diameter of a single Pt atom (2.78 Å):

$$\begin{aligned} &\boldsymbol{\ell}_{\mathrm{atomic}} = \boldsymbol{\ell} : \mathrm{d\ (Pt\ atom)} \\ &4.00\ \text{Å} : 2.78\ \text{Å} = 1.4 \end{aligned} \tag{4.20}$$

The Pt shell is 1.4 Pt atoms thin, as obtained from equation 4.20.

4.3.3 Spectroscopic characterization of G-Cys-Au@Pt

An overview of the UV-Vis spectroscopic characterization of component interactions in the G-Cys-Au@Pt catalysts is shown in Fig. 4.9. The evidence of Pt shells around Au NPs is supported by the UV-vis spectra. Damping and broadening of the Au NP localized surface plasmon resonance (LSPR) peak at 520 nm strongly indicates Pt shell formation, Fig. 4.9A. Such observations agree with reports for a variety of core-Pt_{shell} NPs.[229] The UV-vis spectra of the synthesized G-Cys-Au@Pt catalyst and its constituents are presented in Fig. 4.9B.

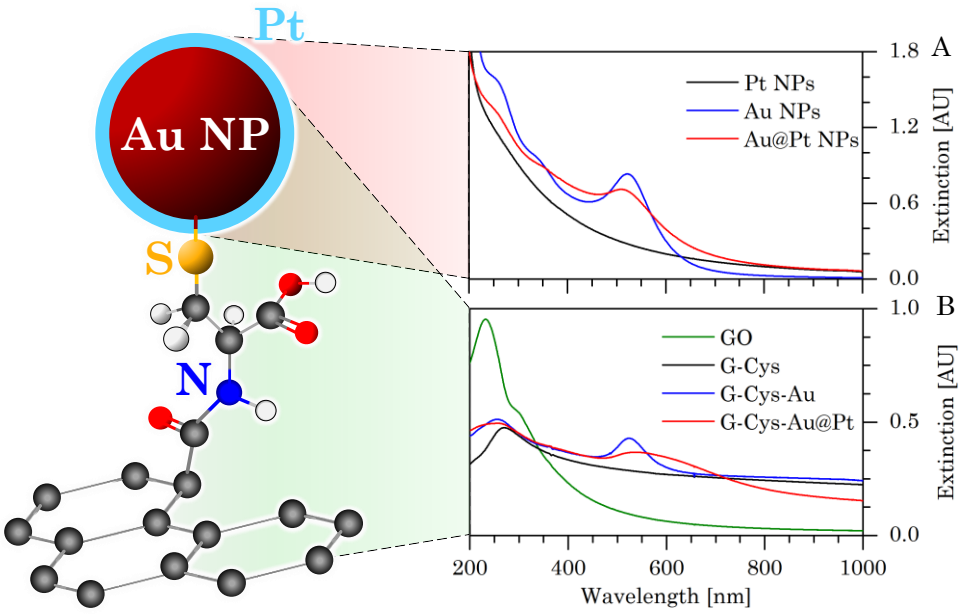

Figure 4.9 UV-vis analysis of (A) unsupported Pt (black), Au (blue) and Au@Pt (red) NPs; (B) purified GO (green), G-Cys (black), G-Cys-Au (blue) and G-Cys-Au@Pt (red).

Two GO-characteristic absorption peaks at 232 and 301 nm, from $\pi \rightarrow \pi^*$ transitions in aromatic C=C bonds, and $n \rightarrow \pi^*$ transitions in C=O bonds, respectively[153] are observed. Upon GO reduction, graphene exhibits a single characteristic peak at 269 nm due to the restoration of the original electronic conjugation. The presence of Pt shell around the Au NP core surface results in red-shift and damping of the LSPR peak. G-Cys-Au@Pt, i.e. Au@Pt NPs immobilized on graphene cause further red-shift and broadening of the LSPR peak, Fig. 4.9B, due to altering the localized electromagnetic field.[230][231] When G-Cys-Au@Pt is excited, created dipoles within the graphene sheets become antiparallel to the dipoles in NPs.[232] Such conformation inhibits the internal NP electric field, causing the

red-shift and broadening of LSPR peak, as observed in Fig. 4.9B.[233] The electric field distortion is greatly amplified by chemical bonds between the Au@Pt NPs and graphene acting as a direct electron sink. Fast electron transfer is essential for high catalytic rates. Ideally, a short chain length of the linker molecule between the catalytically active sites and the electrode enhances the electron transfer rate.[234] As a short organic molecule with only three carbon atoms, Cys is specifically chosen as a linker due to the ability of selectively bonding to graphene and Au NPs via amine and thiol groups, respectively.
The interconnected structure of G-Cys-Au@Pt and the presence of Cys covalent bonding was studied by XPS, Fig. 4.10A-C.

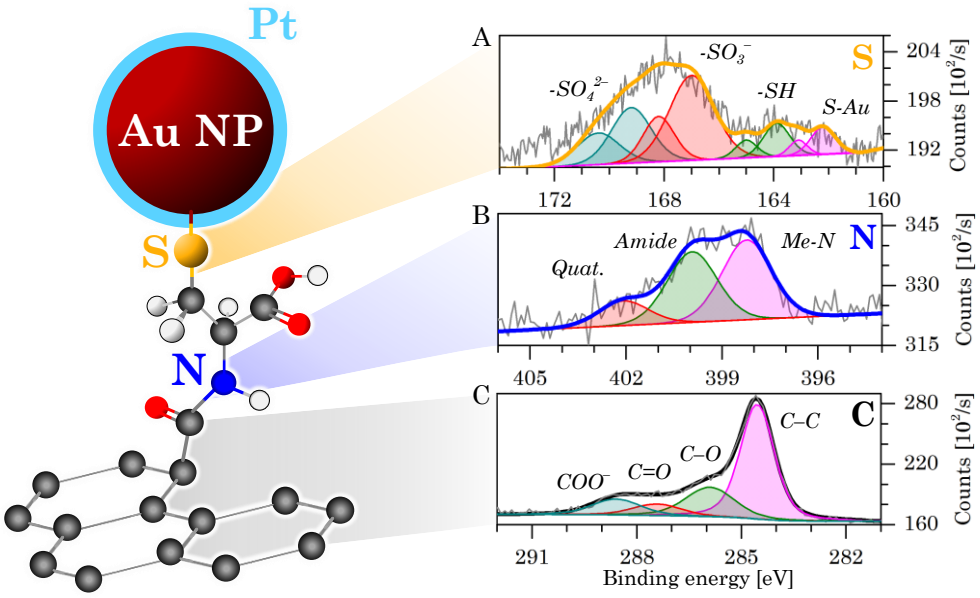

Figure 4.10 G-Cys-Au@Pt elemental XPS analysis of: (A) sulfur, (B) nitrogen and (C) carbon spectra.

XPS spectra of S 2p, deconvoluted into spin-orbit doublets at 162.2 and 163.1 eV are assigned to S–Au interactions.[235] This shows that covalent thiol-Au bonds have successfully integrated Au@Pt NPs into the graphene framework. Peaks at 163.8 and 165.0 eV are from free thiol (-SH)[235][236] and peaks at 166.9 and 168.2 eV for SO_3^- [237] from MES capping around the Au NP surface. The SO_3^- species dominate the sulfur spectrum due to a larger NP surface coverage than the local thiol-NP bonding sites of Cys. This is confirmed by the absence of S–Au (162.2 eV) and SO_3^- (166.9 eV) peaks in the XPS S 2p spectrum of G-Cys (Fig. 3.14A). Peaks at 169.2 and 170.4 eV represent a small amount of the oxidized sulfur in the form of SO_4^{2-} species.[238] The nature of Cys thiol bonds on Au single-crystal electrodes

was studied by electrochemistry and STM in the Chapter 6. Similarly, the C 1s spectrum (Fig. 4.10C) is deconvoluted into peaks at 284.6, 286.0, 287.4 and 288.6 eV, assigned to C–C, C–O, C=O and COO^-, respectively.[239] Small peaks at 285.9 eV and 287.1 eV have been found in N-doped graphene for N–C(sp^2) and N–C(sp^3) bonds, respectively.[207] Such features are also observed in the G-Cys C 1s spectrum (Fig. 3.12C). The presence of N–graphene bonding is evidenced in the N 1s XPS spectrum of G-Cys-Au@Pt (Fig. 4.10B) with three peaks centered at 398.2 eV, 400.0 eV and 402.1 eV corresponding to metal-nitride,[240] amide/pyrrolic, and quaternary N, respectively.[207] The metal-nitride peak originates from MES at the Au NP surface, dominating the N spectrum due to significantly larger domains of MES capping than Cys anchors. This is in contrast to the N spectrum of G-Cys (Fig. 3.14B). Amide/pyrrolic N signals come from chemical bonds between graphene and Cys.[241] There is a weak quaternary N peak caused by N imbedded in the graphene structure (Fig. 4.10B), also present in the N spectrum of G-Cys (Fig. 3.14B). Both C and N XPS spectra clearly confirm that graphene has become functionalized with Cys dominated by amide/pyrrolic chemical bonds, and covalent attachment of Au@Pt NPs to graphene through the Cys linker. An electron pathway between the graphene and Au@Pt NPs via the Cys linker in G-Cys-Au@Pt has thus been created.

4.4 Electrochemical properties and electrocatalysis

4.4.1 Oxidative desorption of adsorbed carbon monoxide and hydrogen

It was discovered recently that Pt–Au NPs offer efficient catalysis towards oxidation of small organic molecules with less adsorbed CO (CO_{ads}) than on pure Pt surfaces,[228] suggesting a potential application of Au@Pt NPs in FCs. The electronic properties of the new G-Cys-Au@Pt were investigated by electrochemical techniques. Three new main features are observed compared to platinum nanoparticles (≤ 5 nm) on graphitized carbon catalyst (C-Pt): (1) The Pt-specific hydrogen region has been augmented from 264 mV for C-Pt to 317 mV for G-Cys-Au@Pt, (2) the Pt_{ox} reduction peak experienced a 37 mV positive shift for G-Cys-Au@Pt while (3) the Au oxide (Au_{ox}) reduction peak was shifted 35 mV negatively compared to a single-crystal Au(111) surface, Fig. 4.11. Such electronic modifications of Pt shell benefit the interactions with the target fuel molecules by strengthening the adsorption energy.[242]

Cyclic voltammetry was used to study CO oxidative desorption on G-Cys-Au@Pt and C-Pt catalysts, Fig. 4.12. Both catalysts were conditioned at -0.2 V during CO adsorption from CO-saturated 0.1 M H_2SO_4. Solid lines in the plots represent the first cycles in which CO is desorbed from the catalyst surfaces during the anodic scans, and dashed lines the second cycles with full catalyst profile restoration.

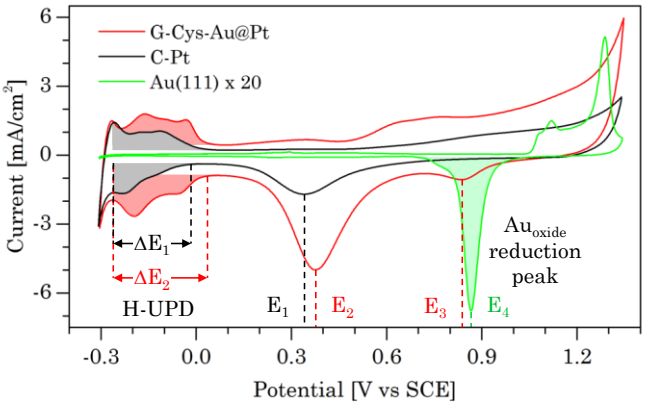

Figure 4.11 Cyclic voltamogramms of G-Cys-Au@Pt (red), C-Pt (black) and Au(111) (green) recorded at 50 mV/s in Ar saturated 0.1 M H_2SO_4. The underpotential hydrogen deposition (H-UPD) region of C-Pt (gray-filled area, ΔE_1 = 264 mV) is extended for G-Cys-Au@Pt (red-filled area, ΔE_2 = 317 mV). The Pt_{ox} reduction peak potentials are shifted from E_1 = 340 mV for C-Pt to E_2 = 377 mV for G-Cys-Au@Pt. The Au_{ox} reduction peak (green-filled area) potentials shift from E_4 = 867 mV for Au(111) to E_3 = 832 mV for G-Cys-Au@Pt. Au(111) plot is multiplied 20 times for a better visualization. All currents are normalized per geometrical areas of electrodes. The Pt loading of G-Cys-Au@Pt and C-Pt was 23.9 $\mu g_{Pt}/cm^2$ on GCE.

CO oxidation on C-Pt starts at 0.420 V and exhibits a sharp peak with the maximum at 0.521 V, while the onset on G-Cys-Au@Pt NP is shifted positively to 0.440 V and the maximum to 0.527 V. This positive potential shift for G-Cys-Au@Pt is usually recognized as hindered CO oxidation due to stronger adsorption on Au-modified Pt surface.[243] Heterometallic bonding induces tensile strain on the Pt shells because of different lattice constants from Au. Effectively, the Pt d-band energy is increased resulting in stronger bonding to CO.[244] However, Au acts as an excellent catalyst for CO oxidation[245] and when introduced to Pt, the number of active sites available for CO adsorption decreases. The resulting effect is a decrease in Pt poisoning for G-Cys-Au@Pt. Integrating the peaks provides the charges associated with CO (A_{CO}) and hydrogen ($A_{H\text{-}UPD}$) desorption, where $A_{H\text{-}UPD}$ represents the total electrochemically active Pt surface area ($ECSA_{Pt}$). The ratio between the two gives the index of CO poisoning per Pt surface area ($CO/ECSA_{Pt}$). Fig. 4.12A and B show CO/ECSAPt indexes of 1.14 ± 0.02 (G-Cys-Au@Pt) and 1.25 ± 0.02 (C-Pt), i.e. 8 – 11% more CO is adsorbed on C-Pt than on G-Cys-Au@Pt. Insets in Fig. 4.12 show the CO desorption peaks at a slow scan rate, i.e. 10 mV/s. G-Cys-Au@Pt undergoes a significant peak shift towards negative values, stabilizing at 0.487 V, while C-Pt has an oxidation peak at 0.555 V. The more efficient CO_{ads} removal on G-Cys-Au@Pt at low scan rates is contrary to the postponed CO_{ads} oxidation at fast scan rates. Cyclic voltammetry

was performed at different scan rates to observe the CO peak shift for G-Cys-Au@Pt and C-Pt, Fig. 4.13.

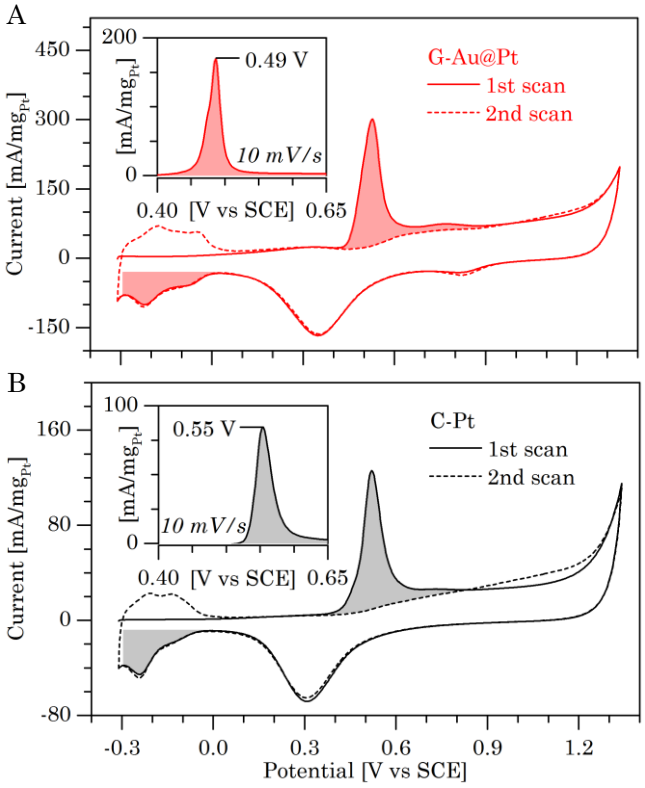

Figure 4.12 CO desorption from CO-saturated Pt surfaces (solid line), and clean, CO-free surfaces (dashed line), for (A) G-Cys-Au@Pt and (B) C-Pt catalysts. The charges associated with CO and H_2 desorption at ca. 0.5 and -0.2 V, respectively, are indicated with filled areas. Cyclic voltammograms were recorded at 50 mV/s in 0.1 M H_2SO_4 while insets represent CO oxidation at 10 mV/s.

The CO peak shift can be explained by (1) diffusion issues through graphene layers and (2) low mobility of CO due to the low potential at which the adsorption and oxidation processes take place. If zero mobility of CO molecules is assumed, only CO adsorbed at the Pt step sites would be oxidized.[246] In case the diffusion rate is slow, CO molecules close to the Pt step sites can also get oxidized (along with the already step-adsorbed CO molecules) during the time in which the CO desorption (CO_{des}) peak appears.[246] Depending on the time window of the experiment (scan rate) the peak potential and charge can therefore, be changed.

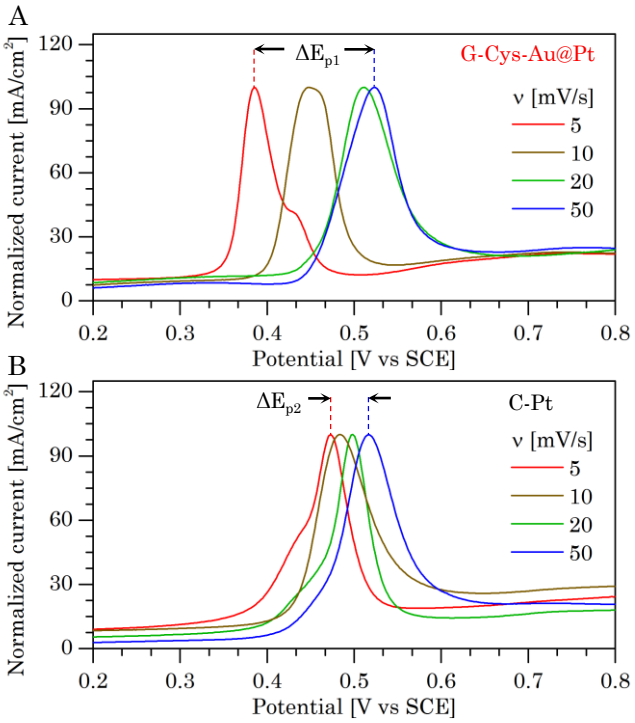

Figure 4.13 Normalized cyclic voltammograms of CO desorption peak shift from CO-saturated Pt surfaces for (A) G-Cys-Au@Pt and (B) C-Pt catalysts at different scan rates. Cyclic voltammograms were recorded at 5, 10, 20 and 50 mV/s in 0.1 M H_2SO_4.

At higher scan rates (50 mV/s) there is not enough time for CO molecules to adsorb/desorb to/from the Pt shell. This results in 6 mV larger overpotential on G-Cys-Au@Pt than on C-Pt. Additionally, layered graphene structure extends the pathway for CO to diffuse in or out of G-Cys-Au@Pt which further promotes the phenomenon. On the other hand, at steady-state conditions, the diffusion effect is not as pronounced and the CO oxidation on G-Cys-Au@Pt occurs at 68 mV lower overpotential. The CO_{des} peak shifts to more negative values with decreasing scan rate speed, and is more pronounced on G-Cys-Au@Pt (ΔE_{p1} = 138 mV) than on C-Pt (ΔE_{p2} = 44 mV). This is a confirmation of higher CO oxidation catalysis at slow scan rates on G-Cys-Au@Pt than on C-Pt. The enhancement of the catalytic properties will be further demonstrated in studying dioxygen reduction and oxidation of fuel molecules, Sections 4.4.2 and 4.4.3, representing the reactions at FC cathode and anode, respectively.

4.4.2 The electrochemical dioxygen reduction reaction (ORR)

The electrocatalytic activity for oxygen reduction reaction (ORR) was examined by voltammetry in oxygen-saturated 0.1 M $HClO_4$ solution. Increasing currents with increasing electrode rotation rates signify the electrocatalytic activity of both materials for dioxygen reduction, Fig. 4.14. The RDE and RRDE ORR experiments for G-Cys-Au@Pt and C-Pt were run under the same conditions and rotation speeds. The limiting currents (from 0.0 to ~0.7 V) originate from dioxygen diffusion to the catalytic sites on the electrode surface, and are limited by the rotation speed.

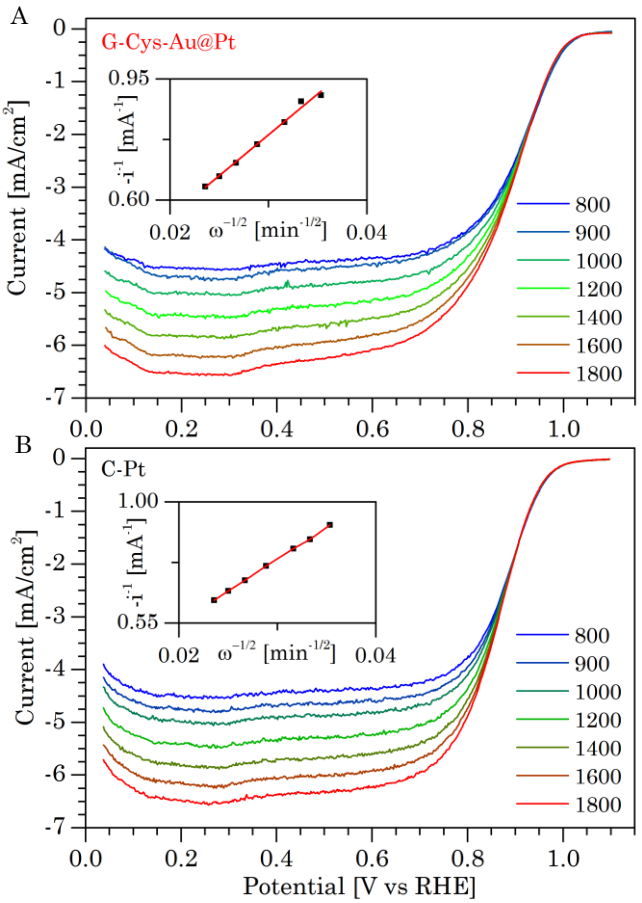

Figure 4.14 Dioxygen reduction reaction (ORR) for (A) G-Cys-Au@Pt and (B) C-Pt. Linear sweep voltammograms recorded at 20 mV/s in dioxygen saturated 0.1 M $HClO_4$. Pt loading on RRDE for both catalysts corresponded to 20.2 µgPt/cm^2. Insets are Koutecky-Levich plots.

The kinetic part of the plot (from ~0.8 to ~1.0 V) shows the 25 mV positive shift for the G-Cys-Au@Pt catalyst compared to C-Pt, representing the overpotential reduction towards the ORR at the G-Cys-Au@Pt catalyst. Fig. 4.15A and B show the catalytic responses of G-Cys-Au@Pt and C-Pt, respectively, in Ar- (dashed lines) and oxygen-saturated (solid lines) electrolyte.

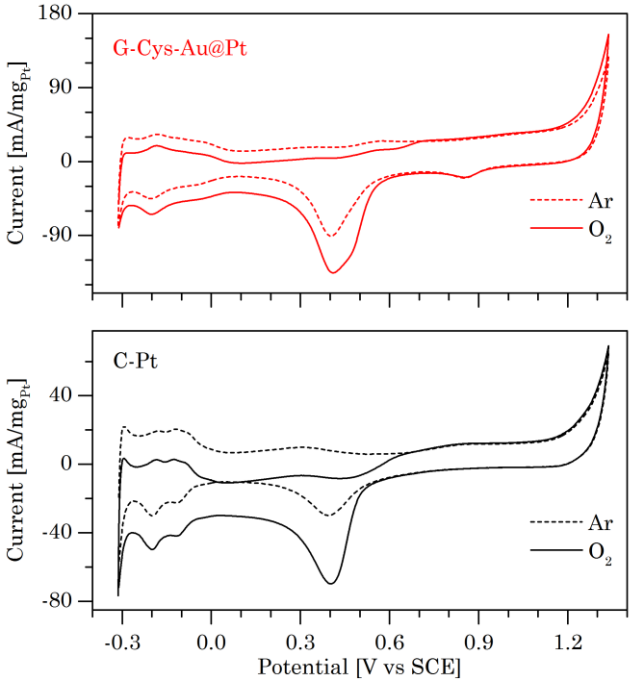

Figure 4.15 Cyclic voltammetry of (A) G-Cys-Au@Pt and (B) C-Pt in oxygen saturated 0.1 M $HClO_4$ (solid lines) and Ar (dashed lines) at 50 mV/s. Pt loading of G-Cys-Au@Pt and C-Pt catalysts was 20.2 $\mu g_{Pt}/cm^2$.

Both catalysts give electrocatalysis toward ORR, as observed from the cathodic peak at ~ 0.410 V, with the onsets at 0.540 V for G-Cys-Au@Pt and 0.498 V for C-Pt, indicating slightly lower overpotential towards ORR at G-Cys-Au@Pt. However, a larger current density change between Ar and O_2 saturated solution is found on C-Pt, implying better catalytic performance than on G-Cys-Au@Pt. This is caused by diffusion limitations of graphene-based catalysts. The packing of graphene sheets during G-Cys-Au@Pt deposition and drying on the electrode extends the pathway of dioxygen molecules through the graphene layer compared to carbon black particles.[211] Even small molecules can be trapped within the graphene sheets effectively hindering a reaction in which the reactant diffuses to the catalyst surface. Diffusion of dioxygen through the graphene

layers therefore plays a role in the catalyst efficiency. This was supported by rotating disk and ring-disk electrode techniques, in which diffusion and kinetics at the electrode surface are separated. Fig. 4.16 shows rotating ring-disk electrode (RRDE) cathodic linear sweep voltammograms of C-Pt (black) and G-Cys-Au@Pt (red) at 1600 rpm. Solid and dashed lines represent currents from dioxygen reduction (at the disk electrode) and the corresponding H_2O_2 oxidation (at the ring electrode), respectively. The C-Pt catalyst exhibits an onset potential at 950 mV, and a half-wave potential (E_{HW}) of 870 mV vs. RHE, consistent with previous reports[247]. The onset potential and E_{HW} are shifted to 1.00 V and 895 mV vs. RHE, respectively, for the G-Cys-Au@Pt catalyst. The 25 mV overpotential reduction towards ORR on the G-Cys-Au@Pt results in a catalytic activity of 132 A/g_{Pt} (measured at 0.900 V) outperforming C-Pt (89 A/$g_{Pt,}$ measured at 0.900 V) by 43 A/g_{Pt} (50 %).

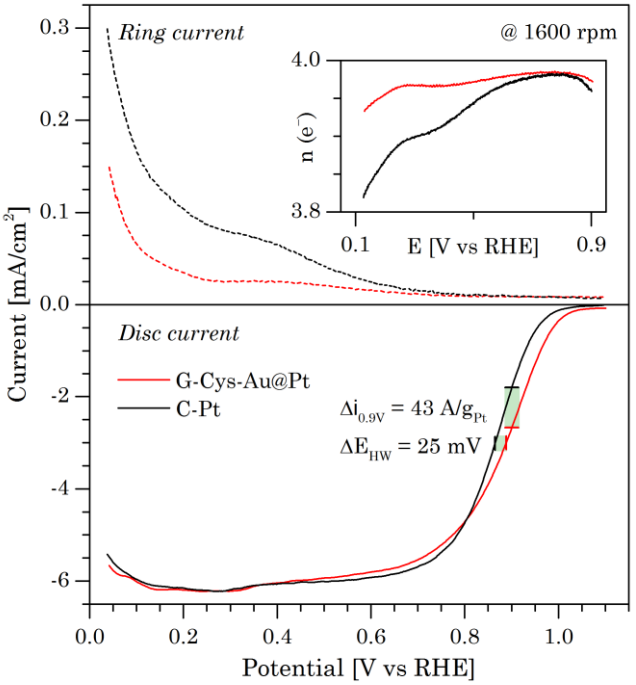

Figure 4.16 Voltammetry of RRDE on the ring electrode (upper) and disk electrode (bottom) for G-Cys-Au@Pt (red) and C-Pt (black). Disk currents represent catalyst performance towards ORR (solid lines) and ring currents simultaneous oxidation of H_2O_2 formed during ORR (dashed lines). Linear sweep voltammetry at 20 mV/s and 1600 rpm in dioxygen saturated 0.1 M $HClO_4$. The Pt ring potential was kept at 1.1 V vs. RHE. Pt loading of G-Cys-Au@Pt and C-Pt catalysts was 20.2 µg$_{Pt}$/cm^2.

Dioxygen reduction proceeds either via a direct 4-electron pathway or via an unfavorable 2-electron formation of peroxide.[248] The electron-transfer mechanism of ORR was not quantified by the Koutecky-Levich analysis since recent studies have pointed out the unreliability of this method due to the relative errors of kinetic current density, standard rate constant and the calculation errors originating in disregarding the kinetic terms of the equation.[215] However, from equation 3.10 and Koutecky-Levich plot slopes in Fig. 4.14A-B, the average electron number *n* in ORR was estimated to be 3.8 for G-Cys-Au@Pt and 3.7 for C-Pt, at 0.2 V vs. RHE. More precisely, the electron transfer number was estimated from the ratio of the experimentally obtained currents at the disk and the ring electrodes, following the equation 3.5, Chapter 3.[249] The inset in Fig. 4.16 highlights that both catalysts reduce dioxygen to water almost exclusively through the direct 4-electron pathway, $O_2 + 4H^+ + 4e^- \rightarrow 2H_2O$, but it is noted that G-Cys-Au@Pt demonstrates a higher reaction efficiency in the entire potential range. Measured n values at 0.2 V vs. RHE were 3.9 for G-Cys-Au@Pt and 3.8 for C-Pt. G-Cys-Au@Pt electrocatalyst outperformed G-Cys-Pt, as well. E_{HW} was improved by 5 mV, while recorded current density at 0.900 V was higher by 9 A/mg_{Pt}. The synergetic interaction between Au core and Pt shell thus enhances kinetically the catalytic performance for ORR, evidenced by more positive half-wave and onset potentials, as well as higher electron transfer numbers than for C-Pt. Such enhanced catalysis for the system core reaction holds promise for appropriate application of G-Cys-Au@Pt as a cathode catalyst in FCs.

4.4.3 Oxidation of fuel cell target molecules

The catalytic performance of G-Cys-Au@Pt was further explored by conducting electrochemical oxidation of 0.1 M target fuel molecules in 0.1 M H_2SO_4 supporting electrolyte, i.e. formic acid (FAOR), methanol (MOR) and ethanol (EOR) oxidation reactions, Fig. 4.17. FAOR voltammetry displays four typical peaks, three in the anodic and one in the cathodic scan, Fig. 4.17A. Peak (1) at ca. 0.3 V, shoulder on the anodic scan, originates from oxidation of adsorbed formate to CO_2 (the direct pathway) which is then suppressed by the subsequent adsorption of CO.[217] The 0.6 – 0.7 V anodic and sharp peak represents the oxidation of CO_{ads} to CO_2 (the indirect path), while the 1.2 V anodic and broad peak appears is caused by the reaction of intermediates and FA at the oxidized Pt surface.[217] The very strong and sharp cathodic scan peak at ~ 0.3 V originates from the direct oxidation of HCOOH to CO_2 at the freshly reformed Pt surface following reduction of Pt_{oxide}.[219] The 4.4 times higher currents (464 mA/mg_{Pt}) were obtained for the G-Cys-Au@Pt at 0.3 V, than for C-Pt. Compared with recently reported, state-of-the art catalysts, the G-Cys-Au@Pt exhibits significant performance even with 5 times lower fuel molecule concentration.[250][251][252][228] Fig. 4.18A shows the chronoamperometric response on both G-Cys-Au@Pt and C-Pt catalysts for FAOR. The oxidizing potential (E_{ox}) was kept at 0.1

V and currents monitored for 6000 s. As for FAOR the final current values and the decay slope indicates higher catalyst stability for G-Cys-Au@Pt with 2.3 times higher currents than C-Pt at the end of the measurements. Similarly, MOR in Fig. 4.17B produces four peaks. In the study by Okamoto et al. [217], peaks origins are established to be closely connected to processes occurring for FAOR (direct/indirect MeOH oxidation), with less of peaks separation at 0.5 V.[217]

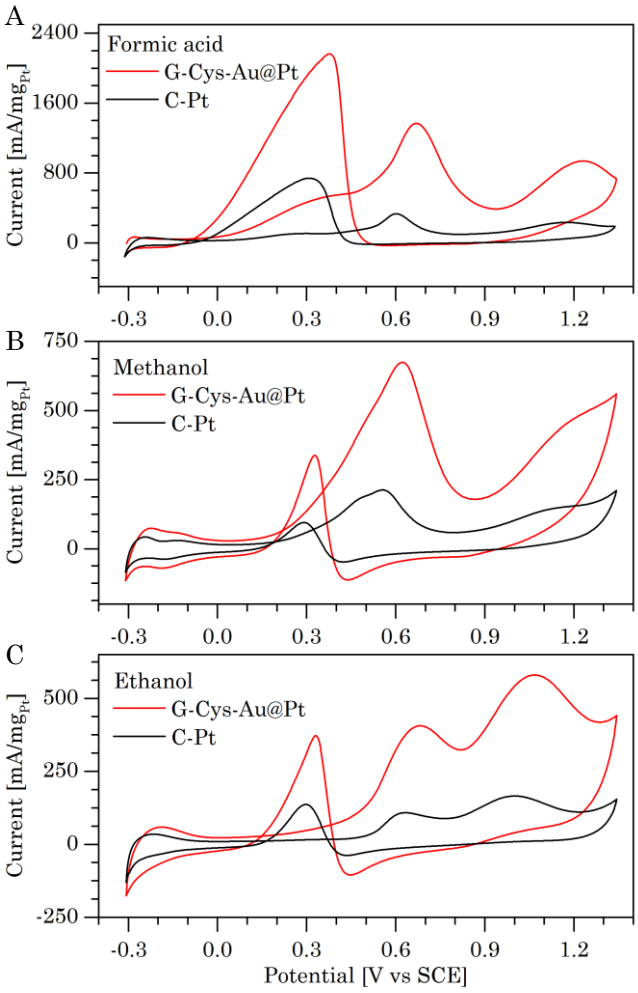

Figure 4.17 Cyclic voltammograms of G-Cys-Au@Pt (red) and C-Pt (black) during electrochemical oxidation of (A) 0.1 M FA, (B) 0.1 M MeOH and (C) 0.1 M EtOH at 50 mV/s. The supporting electrolyte in all the measurements was 0.1 M H_2SO_4. Pt loading of G-Cys-Au@Pt and C-Pt catalysts was 23.9 $\mu g_{Pt}/cm^2$.

G-Cys-Au@Pt shows 674 mA/mg$_{Pt}$ for the anodic peak at ca. 0.6 V representing the indirect MeOH oxidation via CO adsorbate and 3.2 times higher than the corresponding C-Pt peak. Even for 5 to 10 times lower MeOH concentrations, the electrocatalytic performance of G-Cys-Au@Pt exceeds, or is similar to recently reported electrocatalysts.[253][254]

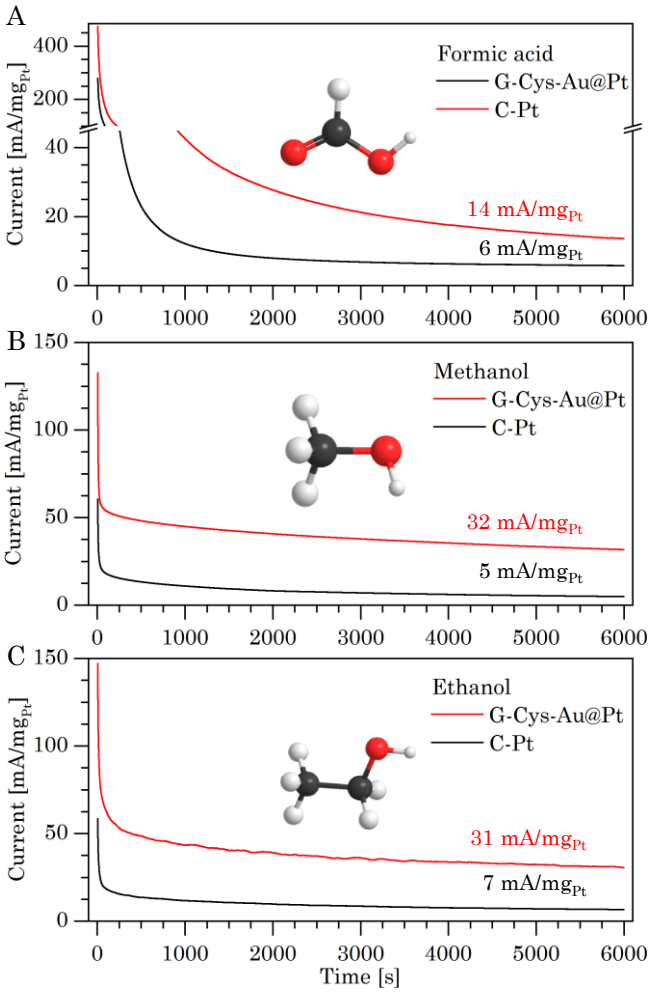

Figure 4.18 Chronoamperometric (CA) response of G-Cys-Au@Pt and C-Pt in (B) 0.10 M FA at 0.100 V, (D) 0.10 M MeOH at 0.300 V, and (F) 0.10 M EtOH at 0.300 V. The supporting electrolyte in all the measurements was 0.10 M H_2SO_4. Pt loading of G-Cys-Au@Pt and C-Pt catalysts was 23.9 μg$_{Pt}$/cm^2.

Fig. 4.18B shows the stability of catalytic currents at 0.3 V over 6000 s, with the current density for G-Cys-Au@Pt 6.4 times that of C-Pt at the end of the measurements. EOR profiles of G-Cys-Au@Pt and C-Pt catalysts are presented in Fig. 4.17C. Due to the need for breaking C–C bonds for full oxidation of EtOH, EOR often gives low current densities. The anodic peak at 0.7 V represents the reaction pathway via CO_{ads} oxidation where G-Cys-Au@Pt exhibits 406 mA/mg_{Pt}, and 3.8 times larger currents than those obtained with C-Pt and greatly improved stability with currents 4.4 times higher after 6000 s of continuous reaction, Fig.4.18C.

Cyclic voltammograms of G-Cys-Au@Pt in the three target fuels are shown in Fig. 4.19. The peak separation of ~80 mV for G-Cys-Au@Pt and ~50 mV for C-Pt (for scan rates from 20 to 100 mV/s) suggests diffusion control, as expected for a process depending on fuel/product diffusion to/from the catalytic surface. Notably, the current peaks are sensitive to the scan rate. The exact reactions of the three studied systems are presently unresolved, but some mechanisms can be proposed, e.g. a two-step process.[255][256][257][258] Firstly, a chemical reaction occurs at the Au@Pt NP surface as the step independent on the scan rate change. This is followed by the electrochemical electron transfer process within the G-Cys-Au@Pt which does depend on the scan rate.[259] Cyclic voltammograms of FA, MeOH and EtOH electrochemical oxidation on C-Pt are shown in Fig. 4.20. Lower current densities than for G-Cys-Au@Pt are recorded, however qualitative behavior remains the same.

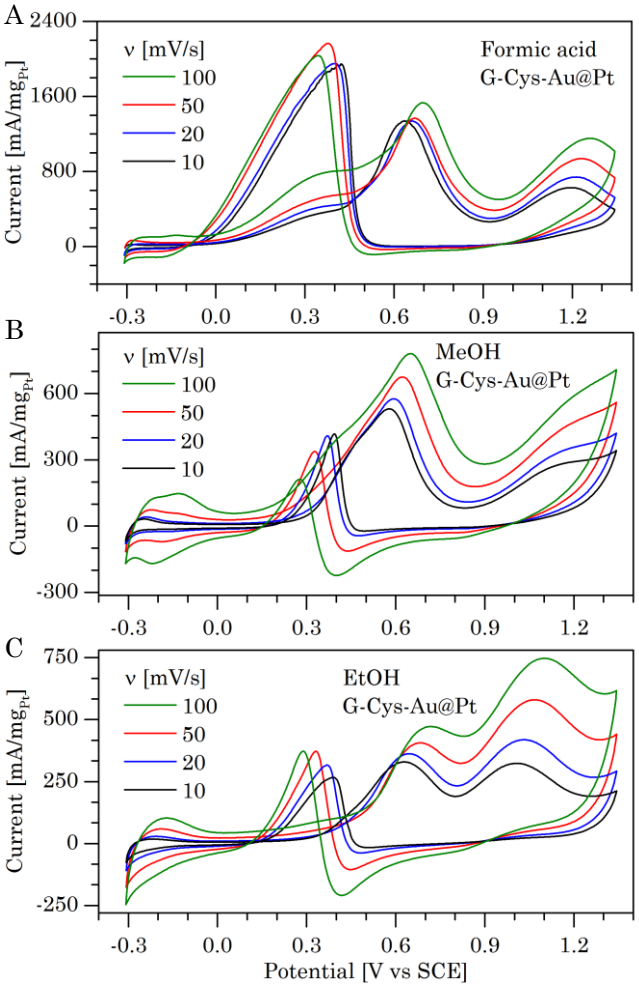

Figure 4.19. Electrochemical oxidation on G-Cys-Au@Pt at different scan rates in (A) 0.10 M FA, (B) 0.10 M MeOH and (C) 0.10 M EtOH. All the measurements were performed in Ar-saturated 0.10 M H_2SO_4 supporting electrolyte. Pt loading of G-Cys-Au@Pt and C-Pt catalysts was 23.9 $\mu g_{Pt}/cm^2$.

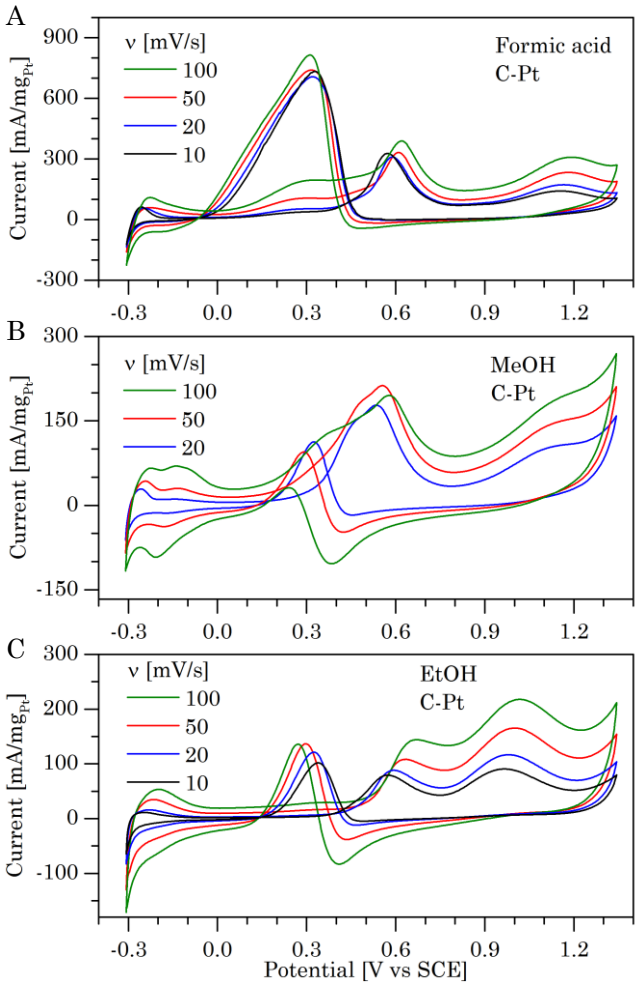

Figure 4.20 Electrochemical oxidation on C-Pt at different scan rates in (A) 0.10 M FA, (B) 0.10 M MeOH and (C) 0.10 M EtOH. All the measurements were performed in Ar-saturated 0.10 M H_2SO_4 supporting electrolyte. Pt loading of G-Cys-Au@Pt and C-Pt catalysts was 23.9 $\mu g_{Pt}/cm^2$.

The G-Cys-Au@Pt shows significant enhancement when compared to G-Cys-Pt, as well. The synergy of Au cores increased adsorption energies of fuel molecules, resulting in enhanced electrocatalysis. G-Cys-Au@Pt shows 2.9, 1.9 and 2.1 times higher current densities than G-Cys-Pt, at 0.3 V for FA, 0.6 V for MeOH, and at 0.7 V for EtOH oxidation reactions, respectively.

A plethora of catalysts has been studied for EOR in both acidic and alkaline environments. Akhairi et al. reported the significance of fuel concentration on the FC performance, showing 4 times higher current densities for EOR in 1.0 M compared to 0.1 M ethanol with a Pt/C catalyst.[260] Experiments presented in this chapter show that G-Cys-Au@Pt gives enhanced catalytic behavior compared to recently reported Pt catalysts, tested in acidic conditions and with 10 times higher EtOH concentration.[261][262][263] This improvement originates from (1) the large amount of available Pt atoms at the surface shell structures of G-Cys-Au@Pt, (2) the engineered electron pathway and (3) beneficial synergy between Au_{core} and Pt_{shell}. Stronger molecular interactions with Au-modified Pt shells provide extremely active sites for biofuel oxidation. As-presented catalytic robustness of G-Cys-Au@Pt towards FAOR, MOR and EOR ensures further application within direct formic acid fuel cell (DFAFC), direct methanol fuel cell (DMFC) and direct ethanol fuel cell (DEFC) systems as the anode catalyst.

4.5 Conclusions

Homogeneously dispersed Au@PtNPs with atomically-thin Pt shells were covalently immobilized to graphene support by a green and facile route. The engineered approach to nanocatalyst structuring through covalent bonding of NPs to graphene and altering electronic properties of Pt, resulted in significant electrocatalytic enhancement. The G-Cys-Au@Pt catalyst exhibited 2.9, 3.2 and 3.5 higher FAO, MOR and EOR currents for C-Pt. As the cathode catalyst, G-Cys-Au@Pt exhibits current increase at 0.9 V vs. RHE by 43 A/g_{Pt} as well as 25 mV overpotential reduction for ORR. Finally, the catalyst stability towards biofuel oxidation was tested by chronoamperometry. The retained current densities at the end of the experiments were 2.3, 6.4 and 4.4 greater for G-Cys-Au@Pt towards FAOR, MOR and EOR than C-Pt, due to ~ 10% increase in CO_{ads} poisoning tolerance and 60 mV lower poison removal potential. G-Cys-Au@Pt showed superior performance to G-Cys-Pt electrocatalyst in both, fuel oxidation and ORR. While slight improvement was recorded for ORR, synergetic effect of Au significantly improved FAOR, MOR and EOR. As-presented catalytic robustness of G-Cys-Au@Pt towards biofuel oxidation and ORR ensures a fitting application within DFAFC, DMFC and DEFC systems.

Chapter 5

Electrochemical energy conversion in fuel cells

5.1 Historical development of PEMFCs

The idea of the gaseous FC dates back to Sir William Grove, a Welsh judge, inventor, and physicist, recognized as "the father of the fuel cell." His scheme of a first FC (1838) is shown in Figure 5.1.[264] Grove found that electrolysis (splitting water into hydrogen and oxygen by using electricity) also works in reverse with the right catalyst, producing electricity. He developed a stack of 50 fuel cells (1842) naming it "gaseous voltaic battery". However, for almost a century after Grove's discovery, FCs did not make any practical progress, remaining only a scientific curiosity. Francis T. Bacon started working on practical FCs in 1937. By the end of the 1950s he had developed a 40-cell stack capable of 5 kW, powering a welding machine, circular saw, and a forklift.[265]

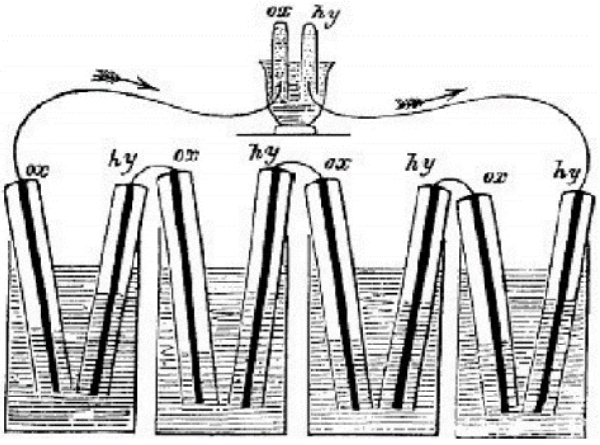

Figure 5.1 Sir William Grove's scheme of the first FC.[264]

During the early 1960s, a PEMFC was invented at General Electric (GE), USA. Thomas Grubb and Leonard Niedrach used sulfonated polystyrene membranes as solid electrolytes that were soon replaced by Nafion® membranes (1966). The Nafion®

membrane had superior performance and durability, which is the reason it is still the most broadly used membrane. PEMFC technology served as part of NASA's Gemini Program, with a goal to test equipment and procedures for the Apollo program. GE's earliest PEMFC model (PB2 cell) repeatedly encountered technical difficulties, such as internal cell contamination and leakage of O_2 through the membrane. Gemini I to IV therefore flew with batteries. Afterwards, a new model was designed, P3. The first mission using PEMFCs was Gemini V. They were later replaced by alkaline fuel cells (AFCs) in the Apollo program. Due to high cost, PEMFCs were limited to space missions and other applications that entailed little to no financial concern. In 1983, Ballard Power Systems (founded in Canada, 1979) began working on the development of PEMFCs with research focused at realistic and wide applications. They developed the first FC stack operating on pressurized air in 1986, and by the 1990 the milestone in FC technology was achieved – development of a 5 kW FC stack.

Since then, PEMFC research and development have increased, with universities and institutes all over the world becoming involved. Key innovations, such as low platinum catalyst loading and novel membranes made the application of PEMFCs realistic. A definite milestone in applied PEMFC technology was British Columbia's Hydrogen Highway (2010) which is both a demonstration program and a market development program. It features an evolving network of FC technologies, including vehicle-fueling infrastructure. Soon after the Canadian government announced funding the world's first "hydrogen highway", development in PEMFC public-private investments started on a global scale.

5.2 Fuel cell significance and application

The FC technology is a recently developed approach aiming at preserving the environmental sustainability while solving the global energy challenges. As electrochemical power devices, FC convert chemical energy from fuel molecules into electric energy via electrochemical reactions.[3] Basic elements of a FC system are cathode, anode and electrolyte. FCs are usually classified according to the electrolyte employed. Most common technologies are polymer electrolyte membrane fuel cells (PEMFCs), alkaline fuel cells (AFCs), phosphoric acid fuel cells (PAFCs), molten carbonate fuel cells (MCFCs) and solid oxide fuel cells (SOFCs). The interest in relatively new PEMFCs is rapidly overtaking use of other FCs. Unlike other types, PEMFCs utilize a quasi-solid electrolyte, which is based on a polymer backbone with side-chains possessing acid-based groups (Nafion® usually applied).[265] The advantages of this family of electrolytes make the PEMFCs attractive mainly for smaller-scale applications such as transportation, home-based power distribution and portable power applications. Characteristic features of PEMFCs include relatively low operation temperature (< 90 °C), high power density,

compact dimensions, and robustness in handling liquid fuel. Commonly used fuels are hydrogen, methanol, ethanol, formic acid, etc.[4]

Table 5.1 Electrocatalysts for application in PEMFC and key properties.

Electrocatalyst	NP size (nm)	Load. (wt.%)	ECSA (m^2/g)	*i* / *P*	FC	Ref
Pt-G	3-5	-	16.9	161[C]	PEMFC	[266]
Pt-FGS	2	20	108	-		[67]
Pt/f-G-f-MWNT	2.9-3.4	50	108±15	540[C]		[267]
Pt-GNP	3.5	20	-	-		[268]
Pt/Ni-G	-			1.63[B]		[269]
Pt-G	4-5	0.2[D]	65	790[C]		[75]
Pt_3Co			57	895[C]		
Pt_3Cr			55	985[C]		
PtPt-sG/fMWNT	3.1	30	82	675[C]		[270]
Pt-GH	3.3		101.3	673[C]		[271]
Pt-G	3.1	20	77.3	-		[272]
Pt-NG	3-5	-	25.15			[273]
PSFA/Pt-GNS	1-4	20	74.2			[274]
Pt/Co-G	1-2	50	78.25			[275]
Pt-G/CB	5	21	57			[276]
Pt_3Fe-NG/MWNT	3.0	30	71.2	347[C]		[277]
Pt_3Co-NG/MWNT	3.3		98.5	935[C]		
Pt-G	2-3	70	113	128[C]	DMFC	[278]
Pt/Au-G	9-10 µm	-	82.2	-		[72]
Pt-G	5	10	-	182.6[A]		[279]
Pt-G	5-6	45	44.6	199.6 [A]		[68]
Pt-PDDA/GO	4.6	18-78	141.6	2.53[B]		[70]
Pt-EDTA/rGO	2.2-4.6	-	-	6.3[B]		[280]
Pd/Pt-G	30		49.8	394[A]		[281]
Pt/Ru-G	2-2.5		68	20.8[B]		[282]
Pt-G	3.2±0.1	40	-	91[C]	DFAFC	[283]
Pt/Au-G	6			185[C]		

Maximum current density (*i*) expressed in: [A] mA/mgPt, [B] mA/cm². Maximum power density (*P*) expressed in [C] mW/cm². Loading reported in [D] mg_{Pt}/ cm².

Due to the high activity at mild operating conditions, Pt-based materials are normally used catalysts in low-temperature PEMFCs. The main drawback is the high price of Pt catalysts. Generally, the catalyst development has to rely on optimization of the structural sensitivity of platinum surfaces and fundamental understanding of the platinum–electrolyte interfacial reactions. Recently reported high-activity Pt-based catalysts are presented in the Table 5.1.

Table 5.2 Bimetallic and trimetallic Pt catalysts for FC application.

Composite catalyst	**Electrode application**	**Function**	**Ref**
Pt-Cu	Cathode	ORR	[284]
Pt-Co			[285]
Pt-Cr			[286]
Pt-Mn			[287]
Pt-Co-Cr			[288]
Pt-Co-Ni			
Pt-Au-Pd			[289]
Pt-Pd-Fe			[290]
Pt-Ru-W	Anode	MOR	[291]
Pt-Ru-Rh			[292]
Pt-Ir		EOR	[293]
Pt-Ru-Mo			[294]
Pt-Au	Anode and Cathode	ORR, FAOR	[221]
Pt-Pd-Ru			[295]
Pt-Ni		ORR, MOR	[288][296]
Pt-Rh			[297]
Pt-Pd		ORR, MOR, EOR	[71][298]
Pt-Ru		ORR, MOR, EOR, FAOR	[74][299][300]

Oxygen reduction reaction (ORR), methanol oxidation reaction (MOR), ethanol oxidation reaction (EOR), formic acid oxidation reaction (FAOR).

Most promising electrocatalysts involve optimizing the catalyst surface area and modifying the intrinsic activity of Pt. Introduction of bimetallic nanostructures thus have become a major step forward. Such NP compositions enhance the catalysis and resistance

to catalytic poisoning.[71][72][73] These alloyed electrocatalysts generally show enhanced ORR and fuel oxidation reactions (FAOR, MOR and EOR), high electrocatalysis and low overpotentials due to the combined properties of individual NPs via synergetic effects. Reports on bi- and trimetallic Pt-based catalysts are summarized in Table 5.2. The focus of this chapter is on Au@Pt NP electrocatalysts in direct PEMFCs as robust energy devices capable of utilizing different liquid organic fuels with Nafion® PEM as the solid electrolyte membrane. Representative setups of FCs studied are DMFC, DEFC and DFAFC.[6][7][8] Furthermore, assembly of FC test station and software are built and described. Our research has been targeting optimization of shape, size and facet distribution of the Au@Pt NPs, leading to improved activity and selectivity. As the basis of high catalytic activity, electron transfer must occur uninterruptedly from the active site at the Pt surface to the current collectors of a FC. The Au@Pt NPs have therefore been immobilized on the Cys-functionalized graphene support (G-Cys), ensuring high NP stability and low electrical resistance resulting in high electron transfer rates. General FC test station assembly, G-Cys-Au@Pt catalyst membrane electrode assembly (MEA) preparation, and its FC performance are discussed in the following sections.

5.3 Fuel cell test station description and assembly

The FC test station (Fig. 5.2) has been assembled from components that can be divided into controllers and measuring elements. The controllers allow a high-precision overview and input of the desired parameters. FC parameters that require rigorous control are fuel feed flow, oxygen feed flow and temperature. Each of the FC parameter controllers have their own designated measuring elements, such as rotation dial for the fuel flow, gas flow dial for the oxygen flow and the temperature probe for the heating elements. However, in the sense of a FC operation, a crucial component is a potentiostat. By applying potential and recording current, potential and power generated during the operation of a FC system, the potentiostat is simultaneously a controller and a measuring element. The in-house programmed LabVIEW 2015 software manages oxygen feed and temperature input, while NOVA 1.10.3 software is used for potentiostat control.

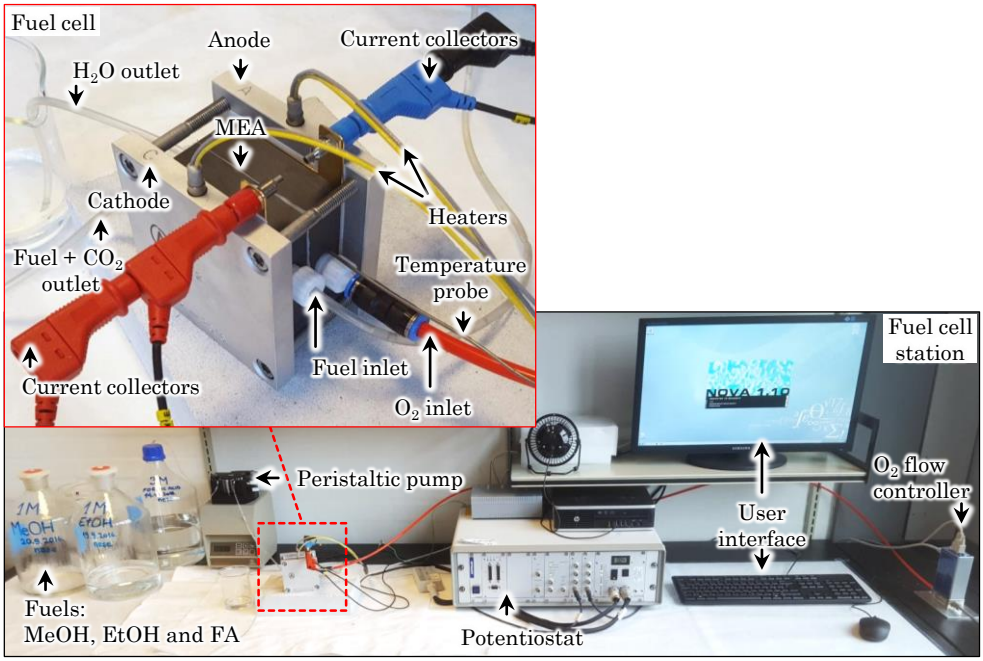

Figure 5.2 The in-house built FC test station.

The hardware components comprising the FC test station and maintaining the constant input/output control as well as recording the signals are:

Measurement Computing (USA) USB-TC, is data acquisition (DAQ) device that provides highly accurate temperature measurements. It is a communicating device between a computer, temperature probes and thermocouples, i.e. a digital-to-analog (DAC) and analog-to-digital (ADC) converter. The probe is directly plugged in to USB-TC and measures real-time temperature. Digital output of USB-TC is connected to a voltage amplifying relay (outputting 230 V), since the USB-TC cannot create voltage high enough to heat up thermocouples. USB-TC signals the relay to start or stop heating. It is upgradeable to 8 thermocouple pairs and temperature probes. USB-TC is therefore used for precise FC heating and measurements of real-time temperature.

Gilson, Inc. (USA) MINIPULS 3,

HPLC certified peristaltic pump that achieves precise control of liquid flow rates in the range from 0.3 µL/min to 30 mL/min at 0.5 MPa maximum pressure. It can handle 4 separate fuel feeds and provides precise fuel flow (2.0 mL/min) to the anode compartment of a FC. During the catalyst activation process, it provides a steady water supply to both anode and cathode compartments. The pump is controlled manually by the interface on the pump itself.

MKS (USA) MFC GE50A,
mass flow controller (MFC) is a multi-gas, multi-range, elastomer-sealed mass flow controller, suited for a wide variety of applications with flow control capability from 5 mL/min to 50 L/min of N_2 flow equivalent. It incorporates the latest in digital flow control electronics with patented thermal sensor and mechanical design. It is powered by the electrical relay and controlled by LabVIEW 2015 software, limiting the output O_2 flow at 200 mL/min. MFC provides O_2 feed to the cathode with 100.0 mL/min working flow.

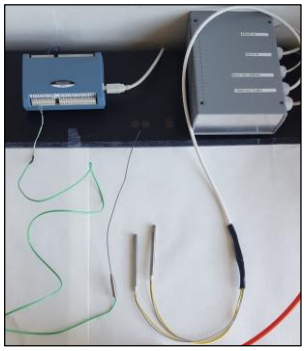

ABB (DK) Thermocouple heating elements type K,
built from 2 thermocouples (type K - max. temperature 1260 °C) and powered by an electrical relay transforming the electrical signal output from the USB-TC into a 230 V input to heat up thermocouples. The heating system is controlled by LabVIEW 2015 software, limiting the output temperature. The operating conditions used in low temperature PEMFCs are 40, 60 and 80 °C. Thermocouples are hardware elements responsible for heat input and are directly plugged in a FC aluminium casing.

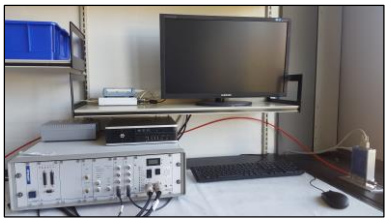

HP desktop computer (USA),
run by Windows 7 operating system, is a user interface unit, controlling the FC station. Directly connected elements are USB-TC, MKS MFC and potentiostat, with a possibility of integrating MINIPULS 3 peristaltic pump. The computer performs and controls LabVIEW 2015 and NOVA 1.10.3 FC station procedures.

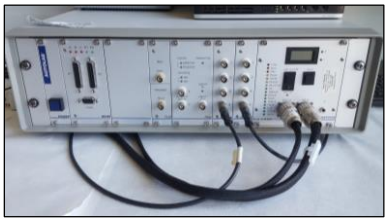

Metrohm-Autolab (NL) PGSTAT30,
bi-potentiostat used for current, potential and power measurements, controlled by NOVA 1.10.3 software with a programmed procedure for FC experiments. It is capable of controlling two FCs simultaneously. Open circuit voltage (OCV) value of the assembled cell is first measured. Then a sequence of linearly dependent potential steps (vs. OCV) is applied. Since the system is taken away from the equilibrium state, reactions are triggered. Fuel is being oxidized at the anode and O_2 is reduced at the cathode. As reactions propagate, current is being generated and recorded. At each potential step the current is recorded for 10 to 30 s, depending on the user input. The 30 last, stable data points are averaged and used in plotting the final power and polarization diagrams. All of the processes are plotted as E vs. t and i vs. t. From the obtained values, the procedure is calculating power and plotting the data as P vs. t. Finally, all the raw data are plotted as polarization curve (E vs. i) and power curves (P vs. i).

The schematics of the FC test station hardware components are shown in the Fig. 5.3.

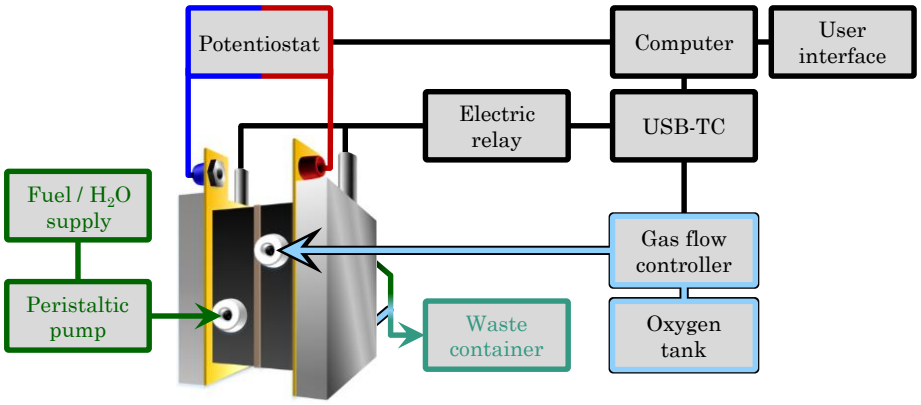

Figure 5.3 Schematic representation of the assembled fuel cell test station.

5.3.1 Software programming – Heating system and oxygen flow control

The LabVIEW 2015 software control of the FC test station is managing the heating system and the oxygen feed flow, Fig. 5.4. The software is divided into a user interface (UI) panel and a "block diagram" panel.

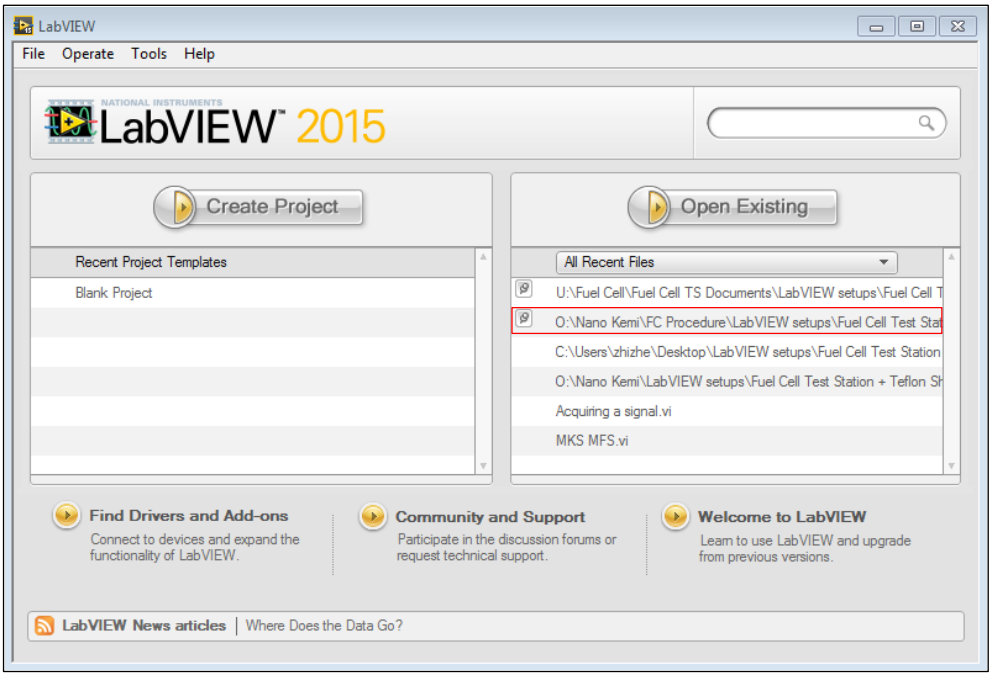

Figure 5.4 LabVIEW 2015 main menu with FC test station procedure (red).

The UI allows the user to set and manage the heating and gas flow parameters in live mode during the FC operation. The "block diagram" is a software-programming panel where the user can modify the procedures, effectively changing the software features. Upon the startup of the FC station software, the UI opens and is in the stand-by mode. The user is required to input the desired parameters that will initiate the procedure only after the user presses a "play procedure" button (►). Users are strongly encouraged to slowly elevate the temperature to avoid any damage to the test station or the catalyst due to the rapid thermocouple heating up. After the procedure is initiated, the interface loses the gridded background, replacing it by a solid grey-colored tone accompanied by the heating and mass flow interface animations. The software controls the temperature with the accuracy of ± 0.1 ºC and O_2 flow at 99.8 ± 0.2 % efficiency upon reaching stable values, Fig. 5.5.

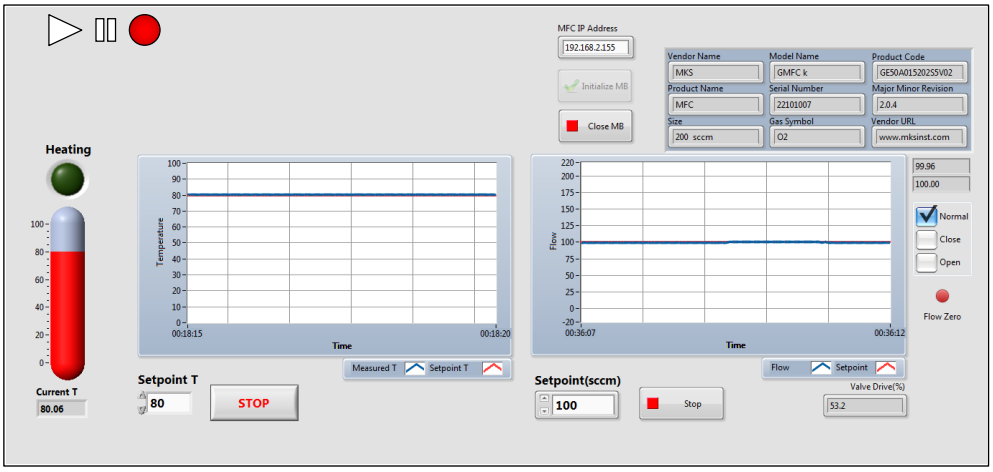

Figure 5.5 LabVIEW 2015 UI panel of a running procedure. The heating system (left) and O_2 flow control (right).

5.3.1.1 Heating system program

The heating UI is comprised of a "ON/OFF heating" light indicator, temperature bar indicator, current temperature numerical indicator, setpoint temperature numerical controller, waveform graphical chart displaying measured temperature by the temperature probe (blue line), the setpoint temperature (red line), and a stop procedure button, Fig. 5.6.

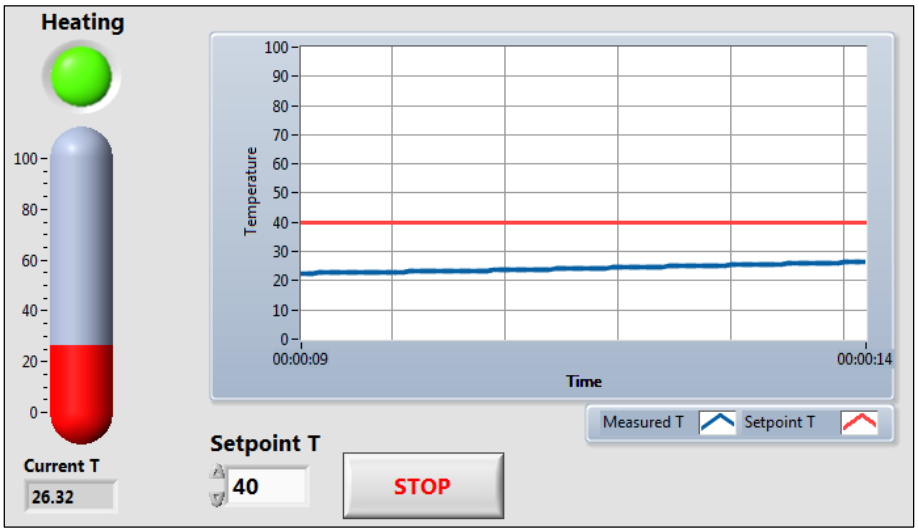

Figure 5.6 LabVIEW 2015 UI panel interface of a heating control running procedure.

The block diagram panel of the heating control program is presented in Fig. 5.7. The program contains digital input, digital output, analog input, indicators and digital control commands directing the virtual instruments (VIs). The digital input commands are ULx Read, VI, ULx Write VI, ULx Clear VI, and setpoint temperature numerical controller command. The digital output command ULx Create Channel (DO-Digital Output) VI sends the digital signal to the electric relay to start/stop heating the thermocouples according to the temperature deviation between the actually measured temperature by the probe and the required setpoint temperature. The signal is regulated by the proportional-integral-derivative (PID) controller. PID command has to be experimentally tuned (numerical input in Fig. 5.7) due to the heat transfer hysteresis, originating from a specific physical separation between the heaters and the temperature probe (current collector + Teflon gasket + graphite block). The analog input command ULx Create Channel (AI-Temperature) VI reads the actual temperature of the FC, measured by the thermocouple temperature probe plugged in the FC. The indicators in the program are a temperature bar, the digital light indicator and the waveform chart. The main digital control command in the program is the PID controller, a control feedback loop that continuously calculates the error value as the reference between a desired setpoint and a measured process variable and then applies a correction based on:

1. proportional (P, accounts for present values of the error, e.g. large positive error means large and positive output),
2. integral (I, accounts for past values of the error), and

3. derivative (D, accounts for possible future trends of the error, based on its current rate of change) terms.

Other digital control commands are the bundle function that combines digital information into a joint signal generating a waveform diagram, comparator function (greater or equal) allowing for a binary (ON or OFF) system control, the "Wait" and the "While Loop" functions. All the commands are visually represented and described in the Table 5.3.

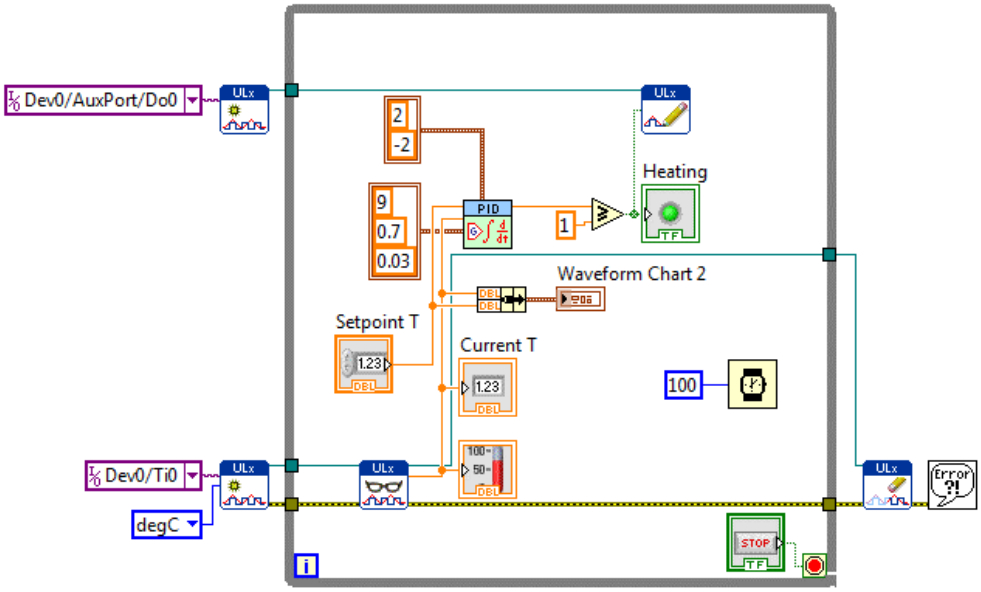

Figure 5.7 Heating system programing scheme displayed as a LabVIEW 2015 "block diagram" panel.

Table 5.3 Description of LabVIEW commands used for the heating system programming.

VI visual representation	VI/command name	VI/command description
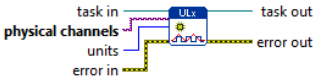	ULx Create Channel (AI-Temp.) VI	Creates channel(s) to measure temp.
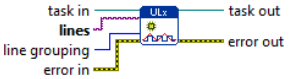	ULx Create Channel (DO-Dig. Output) VI	Creates channel(s) generating digital output from analog input.
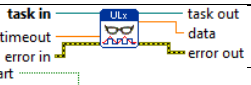	ULx Read (A. DBL 1Chan1Samp) VI	Reads one sample from an analog input.
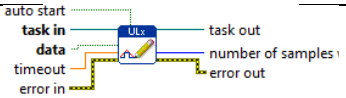	ULx Write (Dig. Bool 1Line1Point) VI	Writes a Boolean sample to a task with a digital output.
	ULx Clear Task VI	Stops and clears tasks.
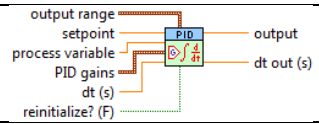	PID controller	Implements PID control for high-high-speed applications requiring an efficient algorithm.
	Temp. bar indicator	Indicating real-time temp. as a bar diagram.
	Current temp. indicator	Numerical indicator of a real-time temp.
	Numerical temp. setpoint	Digital input element for setting the desired temp.
	"ON/OFF heating" light indicator	Real-time light indicator of the heating status.
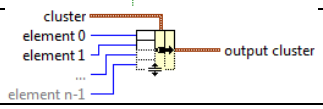	Bundle function	Assembles a cluster signal from individual elements.
	Waveform Chart	Diagram unit plotting the output cluster signal.
	Greater or Equal function	TRUE or FALSE signal outputting element.
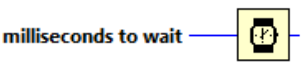	Wait function (ms)	Delays procedure report to relieve computer memory.
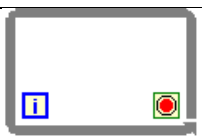	While Loop function	Repeats the code within its subdiagram until a specified condition occurs.

5.3.1.2 Oxygen flow control program

The oxygen control UI contains an Internet Protocol (IP) address indicator of the MKS GE50A mass flow controller (MFC), the mass controller bandwidth (MB) initialization button, the MB close button, and MFC information panel. Furthermore, the UI contains the oxygen flow setpoint input window allowing user to change the desired gas feed flow, numerical indicator of the actual and setpoint gas flow, the "stop procedure" button, and a waveform graphical chart displaying the gas flow measured by the mass controller (blue line) and the setpoint gas flow (red line), Fig. 5.8.

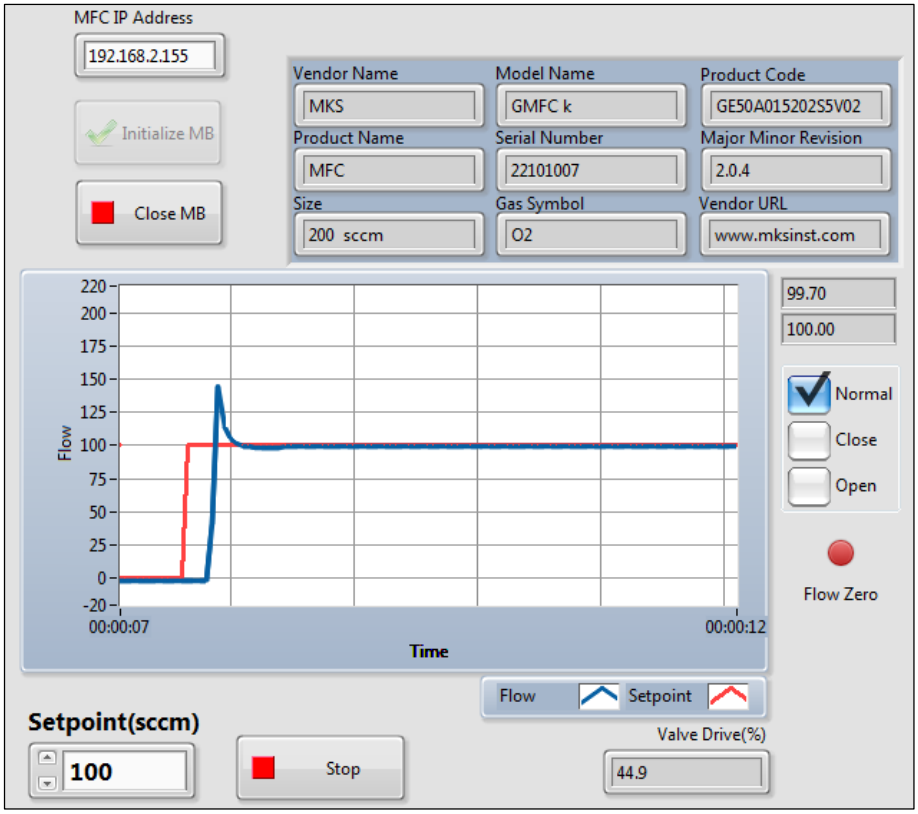

Figure 5.8 LabVIEW 2015 UI panel of a O_2 flow control running procedure. The upper limit is set to 200 mL/min (Size).

The program for the oxygen flow control contains digital input and digital output VIs, digital control commands and indicators. Digital controls present in all programming windows are the "Case" and the "Event" structures as well as the "While Loop" function. The "Time Delay" command is present in the final Event Structure, (6) "Flow Zero": Value Change. All the commands are visually represented and described in Table 5.4.

In the Event Structure, (0) Timeout, digital input is MB MFC Setpoint VI while MB MFC Flow VI, MB MFC Valve Position VI are numerical indicators informing about the flow and valve position of the device. The Bundle function combines the Setpoint and the Flow digital outputs into a graphical Waveform Chart, Fig. 5.9.

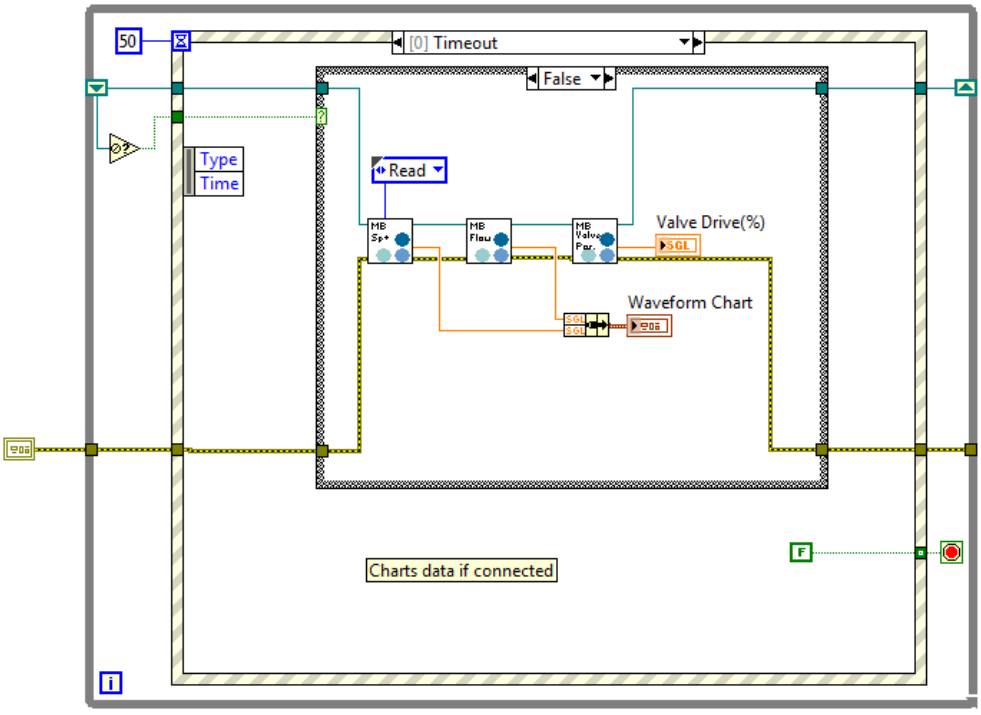

Figure 5.9 Gas flow system programing scheme displayed as a LabVIEW 2015 "block diagram" panel, (0) Timeout Event Structure.

In the Event Structure, (1) “Setpoint”: Value Change, the digital input MB MFC Setpoint VI allows the user to set the required oxygen flow value within the specified range (from 10 to 200 ml/min), Fig. 5.10.

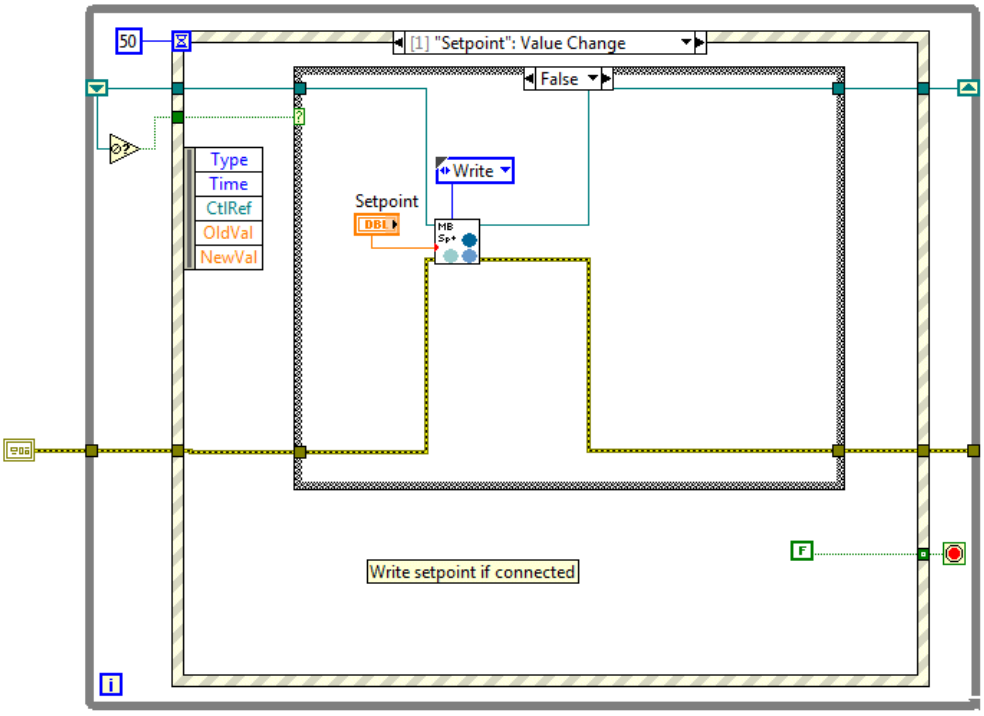

Figure 5.10 Gas flow system programing scheme displayed as a LabVIEW 2015 “block diagram” panel, (1) “Setpoint”: Value Change Event Structure.

The Event Structure, (2) “Valve Override”: Value Change, contains the digital input and output MB MFC Valve Override VI allows the user to override the controller if such connection is required and established. The VI operates as: (1) a digital input for the for the user to override the controls and (2) the digital output sending the signal to the valve in case of the override procedure, Fig. 5.11.

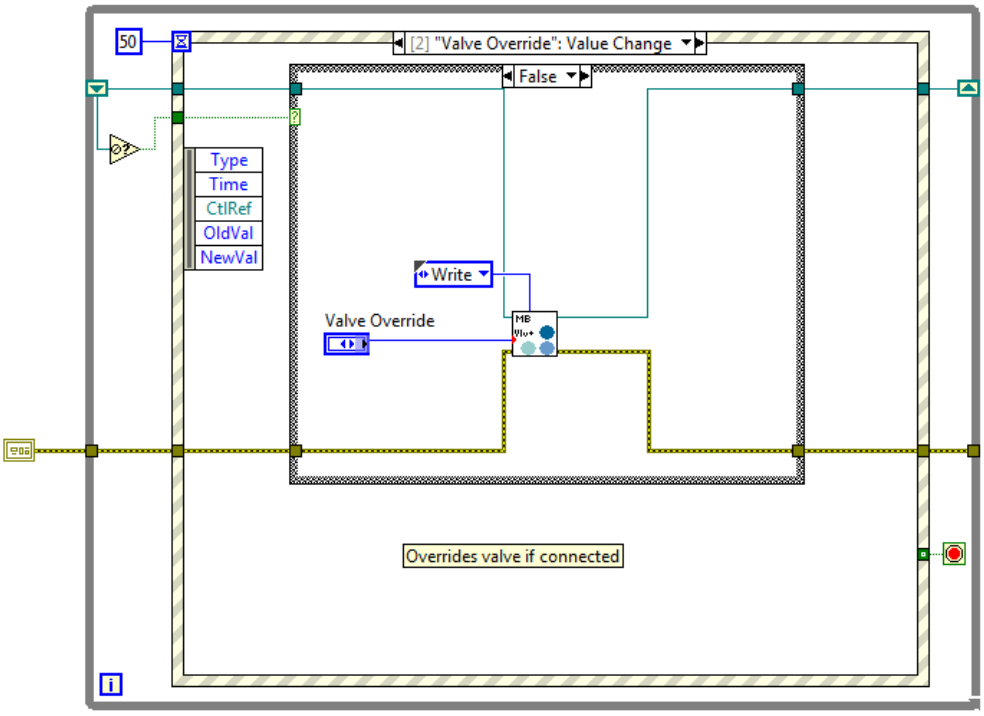

Figure 5.11 Gas flow system programing scheme displayed as a LabVIEW 2015 “block diagram” panel, (2) “Valve Override: Value Change” Event Structure.

In the Event Structure, (3) “Initialize”: Value Change, the digital input MB ENet GoOnline VI establishes internet connection between the computer and the MKS controller via its designated IP address. After the communication between the devices has been established, the MB Get Device Info VI tracks down a 9-point identification of the mass flow controller and displays it in the appropriate window at the UI panel. The MB ENet GoOline VI also checks the valve position and the setpoint value, in case the user has changed parameters from startup values (always zero) before the communication has been established, Fig. 5.12.

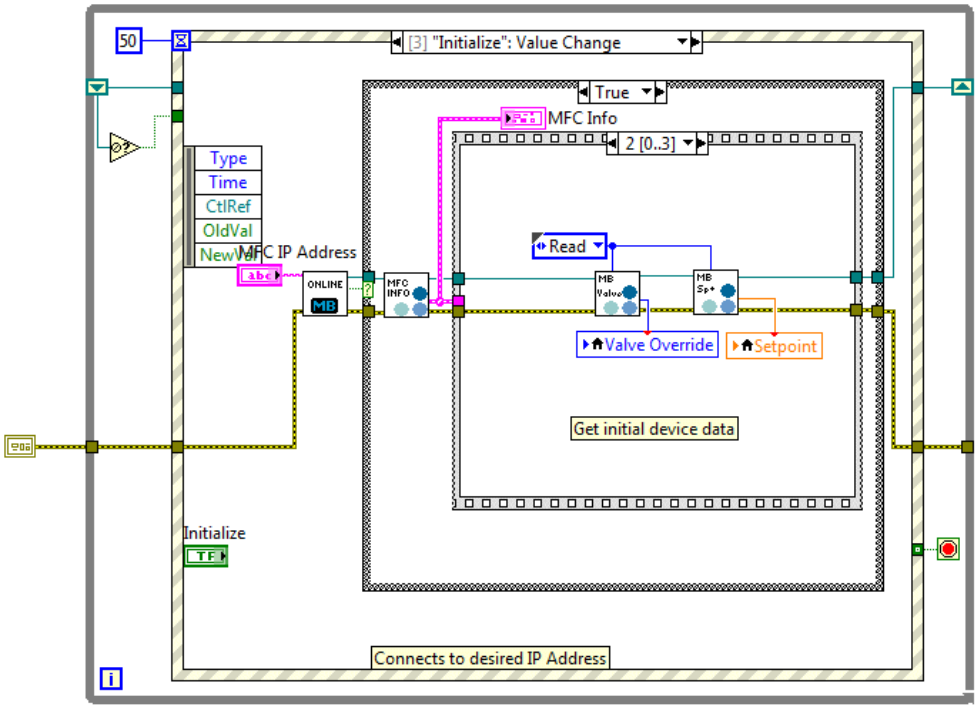

Figure 5.12 Gas flow system programing scheme displayed as a LabVIEW 2015 “block diagram” panel, (3) “Initialize: Value Change” Event Structure.

The Event Structure, (4) “Close MB”: Value Change, contains one digital input that ends the internet connection of the mass controller, effectively discontinuing the communication between the computer with the UI and the mass controller itself, MB ENet GoOffline VI, Fig. 5.13.

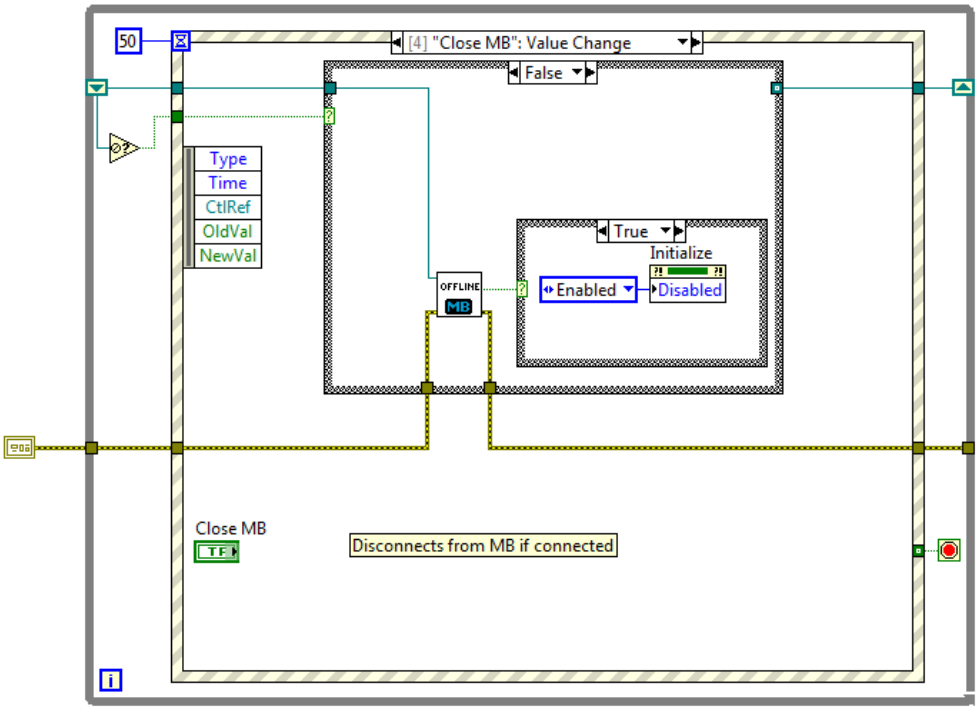

Figure 5.13 Gas flow system programing scheme displayed as a LabVIEW 2015 “block diagram” panel, “Close MB: Value Change” Event Structure.

The Event Structure, (5) “Stop”: Value Change, contains one digital input that disconnects the mass controller from the internet and stops the ongoing procedure, Fig. 5.14.

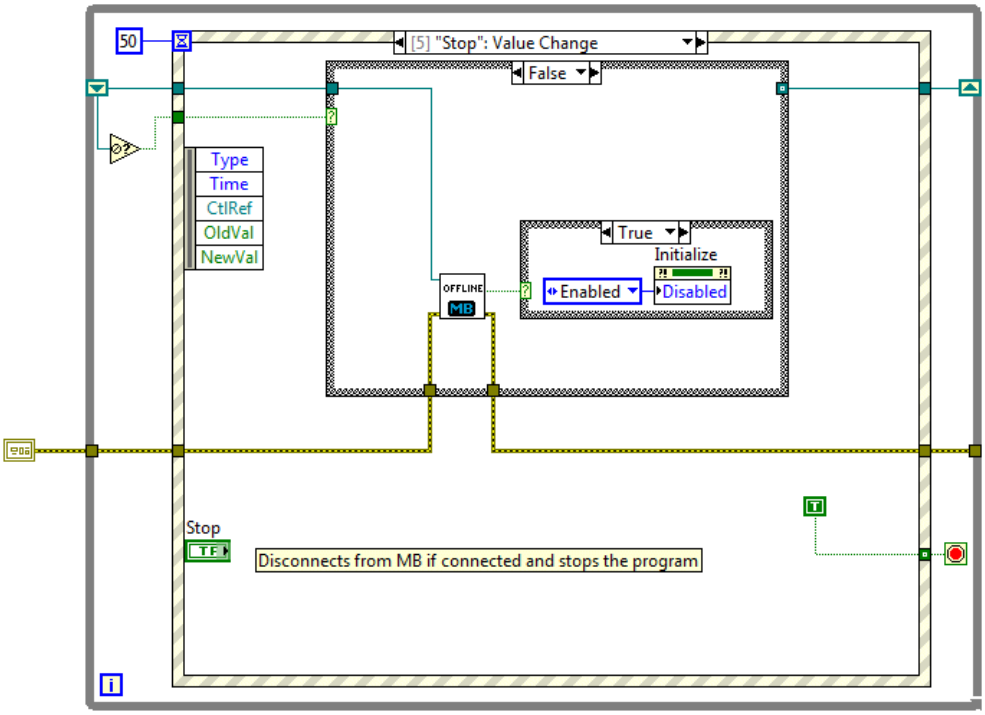

Figure 5.14 Gas flow system programing scheme displayed as a LabVIEW 2015 “block diagram” panel, (5) “Stop”: Value Change Event Structure.

The Event Structure, (6) “Flow Zero”: Value Change, contains one digital output command that sends a stopping signal to the MFC’s valve control system, MB MFC Zero Flow VI. The command is directed by a 15 s time delay in case the user wants to keep the procedure running, Fig. 5.15.

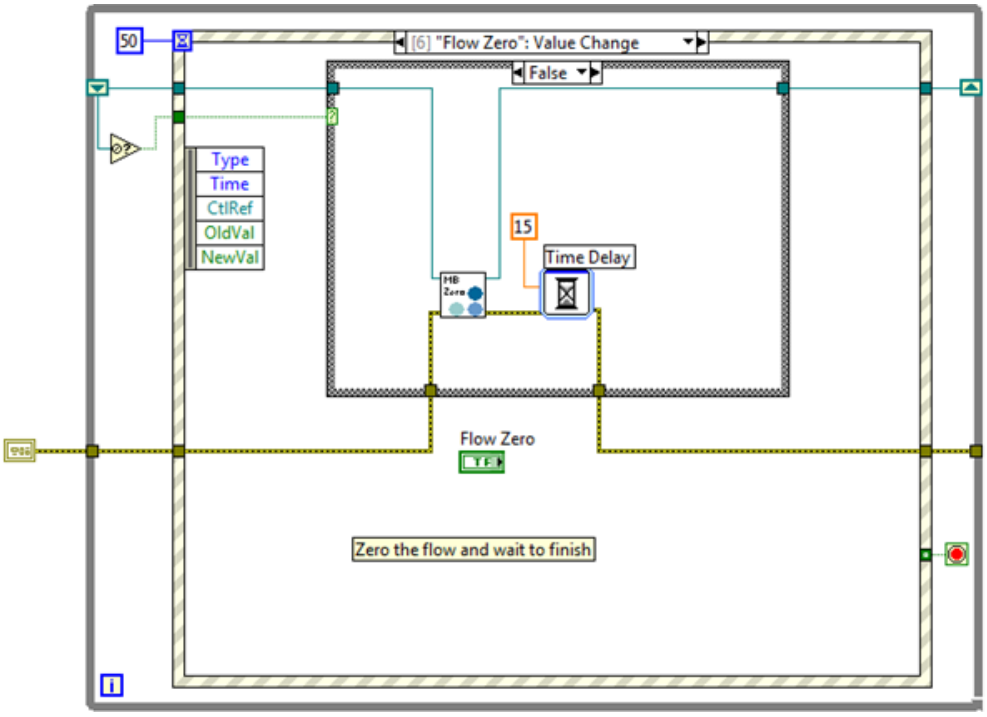

Figure 5.15 Gas flow system programing scheme displayed as a LabVIEW 2015 “block diagram” panel, (6) “Flow Zero”: Value Change Event Structure.

Table 5.4 Description of LabVIEW commands used for the gas flow system programming.

VI visual representation	VI/command name	VI/command description
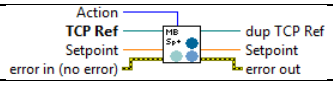	MB MFC Setpoint VI	Reads and writes the setpoint value of MFC.
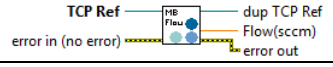	MB MFC Flow VI	Reads gas flow of MFC.
	MB MFC Valve Position VI	Reads valve position of MFC and reports as percentage.
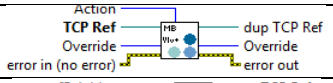	MB MFC Valve Override VI	Reads and writes the valve override of MFC.
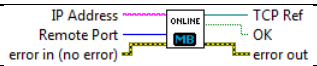	MB ENet GoOnline VI	Establishes MB internet connection.
	MB Get Device Info VI	Reads MFC's 9-point identification and displays as cluster.
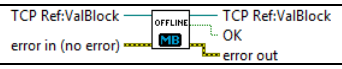	MB ENet GoOffline VI	Closes MB internet communication.
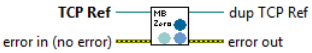	MB MFC Zero Flow VI	Send a stopping signal to MFC's valve control.
	Time Delay	Inserts a time delay into initializing procedure.
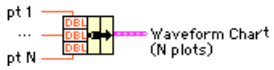	Bundle function, Waveform Chart	Assembles a cluster signal from individual elements and plots waveform chart
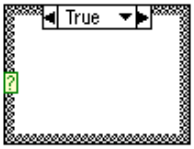	Case Structure	Contains one/more subdiagrams where exactly one executes when the structure executes.
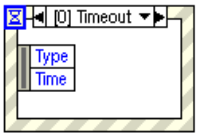	Event Structure	Waits until an event occurs, then executes a case. Contains one/more subdiagrams allowing an event timeout.
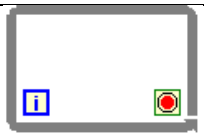	While Loop function	Repeats the code within its subdiagram until a specified condition occurs.

5.3.2 Software programming – Potentiostat control procedure

The FC voltage, current and power monitoring was carried out using an Autolab PGSTAT12 potentiostat that runs NOVA 1.10.3 software. The specific processes in the FC systems require the appropriate voltage and current control. The NOVA 1.10.3 software was utilized due to the facile procedural programing that controls and records ongoing processes during the FC operation, Fig. 5.16.

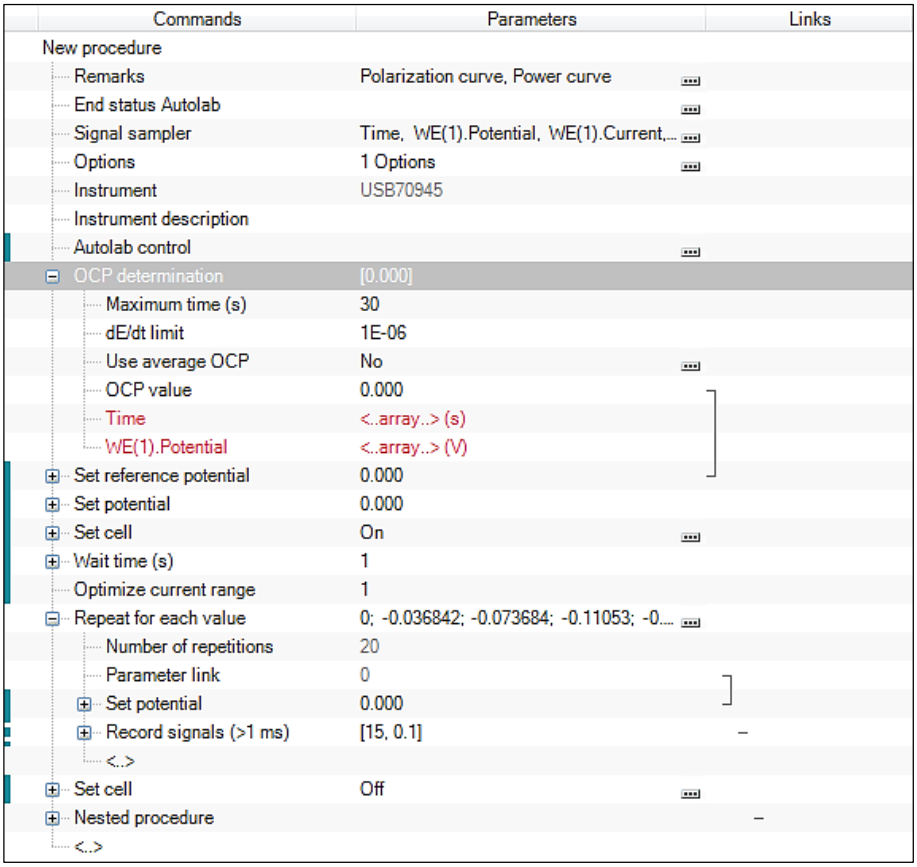

Figure 5.16 The NOVA 1.10.3 software procedure programmed for controlling and measuring the FC current, voltage and power.

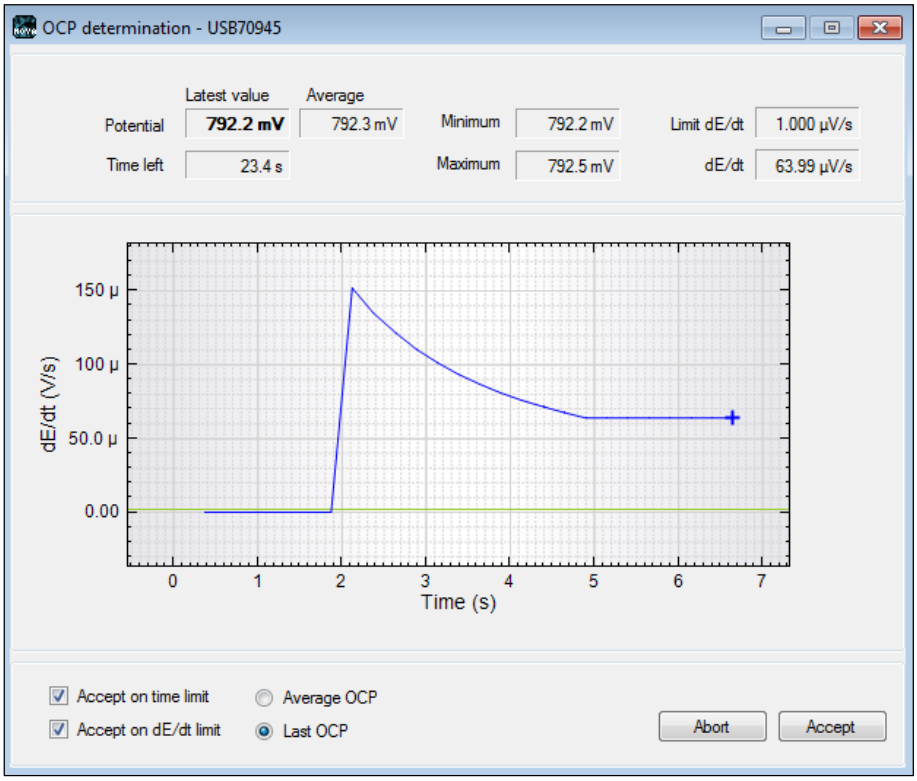

Figure 5.17 The NOVA 1.10.3 software UI window during OCV measurement.

The software starts the FC testing procedure by measuring the OCV between the two electrodes over a period of 30 s, Fig. 5.17. After recording the final OCV value, the software has a 1 s resting time after which it applies negative potential steps to the FC, previously determined by the user. The user sets the limits of the potential control and the number of measured points, Fig. 5.18. The upper limit should always be 0 V (in reference to OCV). The lower limit should be a value following relation:

$$OCV + x \approx 0.1 \text{ [V]} \tag{5.1}$$

where the measured OCV [V] and x [V] is the unknown potential range in which the FC will be tested. In condition of 0 V potential difference between the electrodes (bias voltage), the FC is forced to produce the highest currents at low voltage efficiency. This induces stress to catalytic layer and Nafion® membrane that has to conduct H^+ at high rates to satisfy ongoing reactions. Since the degradation of entire MEA is amplified at these conditions, the FC should not be taken to a state of 0 V bias.

A

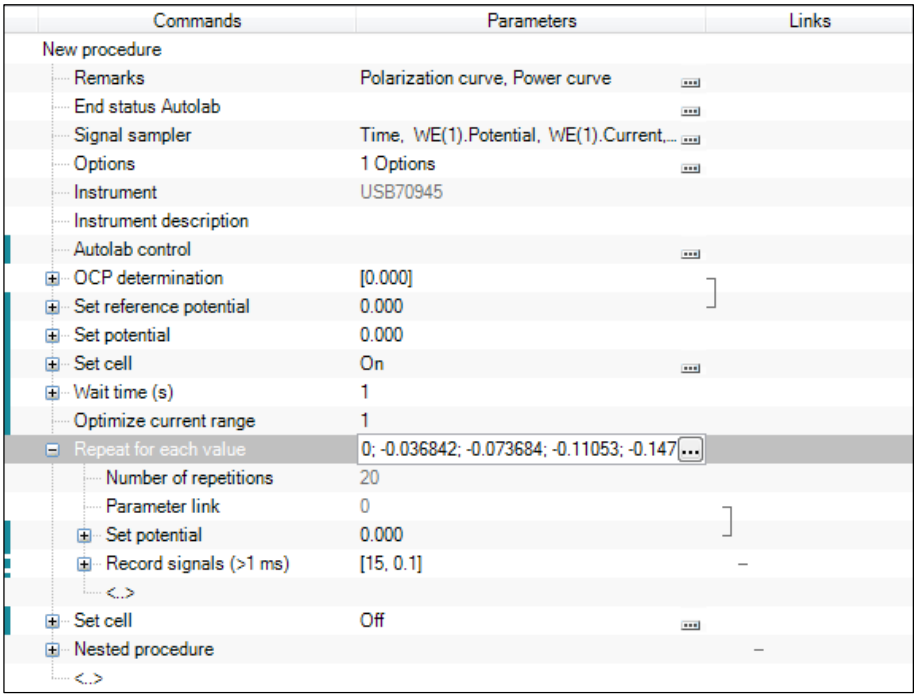

B

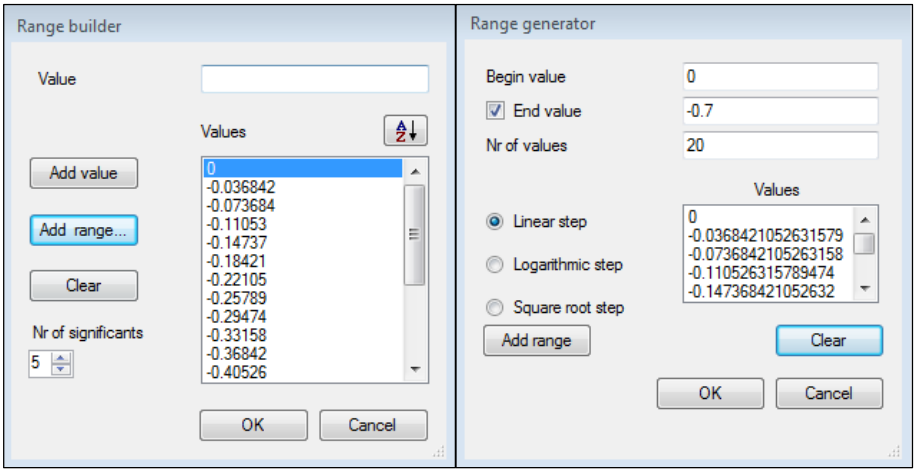

Figure 5.18 (A) The NOVA 1.10.3 main procedure potential control with (B) pop-up menu allowing user to modify potential steps within the applied range.

Example

If the measured OCV is 0.8 V, the start value should be 0, meaning 0 V applied compared to OCV. In this case, no matter the value of the OCV, the first potential step will always measure 0 current. The end value should be -0.7 V. This means that in the final measurement point, the procedure will apply negative 0.7 V compared to OCV. The actual bias between the anode (negative electrode) and cathode (positive electrode) in the final measuring point will be 0.1 V.

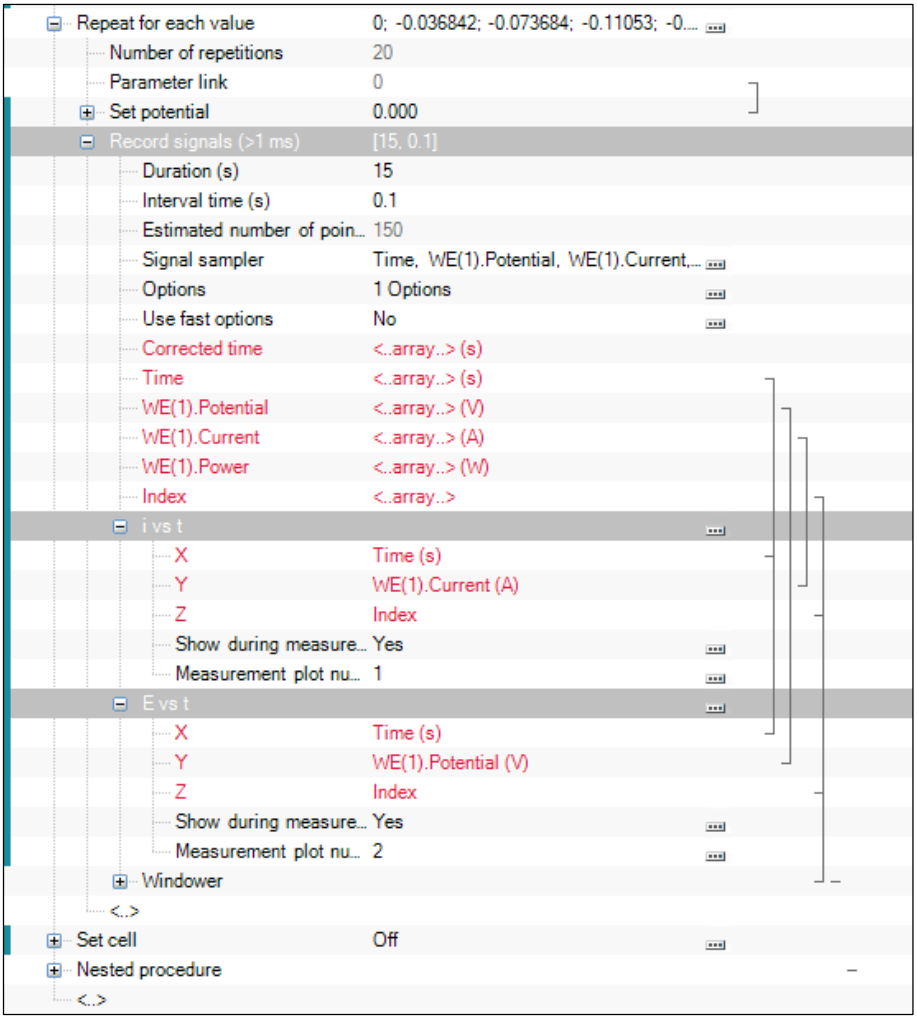

Figure 5.19 The NOVA 1.10.3 software procedure recording signals at each of the applied potential steps for 15 seconds with 100 ms interval time. Software procedure

plotting i vs. t and E vs. t diagrams in real time as the measurements are being performed.

At each measurement step, the potential and current are measured for 15 s over intervals of 0.1 s, resulting in 150 recorded points for each step, Fig. 5.20. The recorded signals are further plotted as chronoamperometric (i vs. t) and chronopotentiometric (E vs. t) raw data plots.

Afterwards, the calculating function "Windower" multiplies data points of potential and current measurements generating a plot of power performance over time (P vs. t) for every step, as the measurements are performed. The last 30 stable data points from i vs. t, E vs. t and P vs. t measurements are averaged and used for the final polarization and power curve diagrams. Due to the nature of the applied potential signal to the FC, the recorded potential is positive while the current and power have negative values.

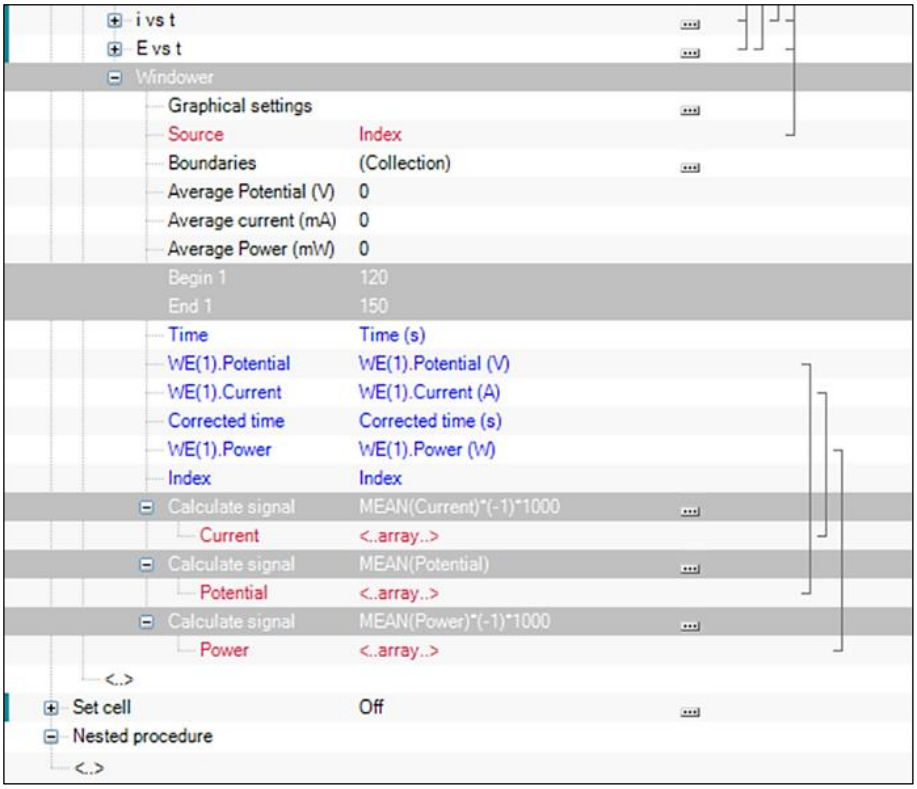

Figure 5.20 The NOVA 1.10.3 software "Windower" calculating function.

"Windower" then multiplies the raw data by "–1" to correct for the negative sign and "1000" to plot the final diagrams with units in mA/cm^2 (current density) and mW/cm^2

(power density) since the current recorded by Autolab PGSTAT12 outputs raw data initially in A, Fig. 5.20. The "Nested" function clusters *i* vs. *t, E* vs. *t*, *P* vs. *t,* polarization curve (*E* vs. *i*) and power curve (*P* vs. *i*) within the same UI window as the measurements are being performed, Fig. 5.21. Polarization and power curves are generated from last 30 stabile data points of each potential step.

Figure 5.21 The NOVA 1.10.3 software "Nested" function.

The UI of an operating FC testing procedure is presented in Fig. 5.22. The final polarization and power curves are results of 20 negatively applied, linearly dependent potential steps to the initial OCV. At each step, the bias potential between the electrodes is decreased, which results in progressive current generation. The measured raw potential and current data are multiplied to obtain power data points. The last 30 data points from each step are then averaged and presented as a single set of data points for *E* vs. *i* and *P* vs. *i* diagrams.

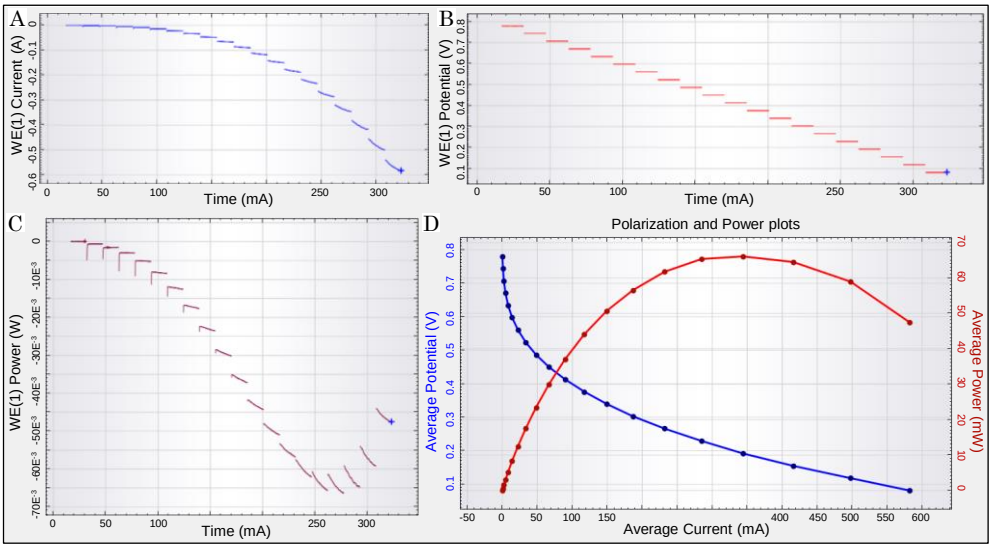

Figure 5.22 The NOVA 1.10.3 software UI during the operation of FC testing procedure. (A) i vs. t, (B) E vs. t, (C) P vs. t and (D) polarization curve E vs. i (blue) and power curve P vs. i (red).

5.4 Sample preparation and testing procedures

This section describes the sample preparation for FC experiments. The carbon-based samples were prepared as mixtures of powder or concentrated catalysts, Nafion®®, water and ethanol. The mixture itself is denoted as "(catalytic) ink". Homogeneous ink is then drop-casted on the carbon paper support, maintaining the Pt mass loading comparable for all the tested materials. Immobilized catalyst at the carbon paper support is denoted as the "FC anode/cathode electrode". The obtained electrode is further utilized for membrane electrode assembly (MEA) and inserted into a FC casing. Both anode and cathode are activated prior to FC testing procedures.

5.4.1 Catalytic ink preparation

The purpose of making the catalytic ink is to obtain: (1) the homogeneous dispersion of the catalyst to have a uniform active layer within the carbon paper structure and (2) the accurate ratio of the catalyst to Nafion®. The ink is generally composed of four constituents (Fig. 5.23):

1. Dry or concentrated catalysts,
2. Nafion®,
3. Ethanol,

4. Millipore water.

The catalytic material is the main active component in the ink. It is beneficial to prepare catalyst-concentrated ink dispersions for the ease-of-use while preparing the electrode by a drop-casting procedure. However, too concentrated dispersions result in rapid sedimentation of the catalyst eliminating the homogeneity. Targeting a precise concentration of the ink is not crucial, since it is dried on the carbon paper and the catalyst mass loading determined by an analytical scale procedure, described in the section 5.3.2.

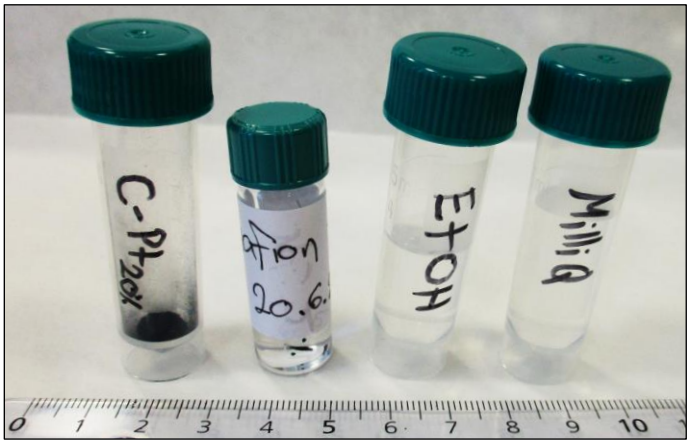

Figure 5.23 Catalytic ink constituents. From left to right: commercial catalyst 20 wt.% Pt on graphitized carbon (C-$Pt_{20\%}$), 5 wt.% Nafion® solution in ethanol and Millipore water.

It is preferable to have dry catalysts in powder form with NP loadings ranging from 20 to 60 wt.%. Low metallic loading yields high carbon content in the material resulting in increased thickness of the catalytic layer on the electrodes. Thick catalytic layers are unfavorable due to the amplified ohmic losses in current as well as fuel and gas diffusion issues. In case the material undergoes morphological changes upon drying, as graphene-based materials do,[208] the catalyst can be used in a concentrated dispersion form. For such catalysts, it is important to know the metal concentration in the catalyst dispersion. This can be achieved by combination of gravimetric experimental methods (TGA) and concentration calculations. G-Cys-Au@Pt catalyst is in a concentrated aqueous dispersion form after the purification procedure by centrifugation. The mass of G-Cys-Au@Pt can be determined by weighing the specific volume of the dispersion. The masses of water and the empty vial are then subtracted from the measured mass of G-Cys-Au@Pt dispersion:

$$m(\text{catalyst})_{\text{dry}} = m(\text{catalyst})_{\text{dispersion in vial}} - V \cdot \rho(\text{water}) - m(\text{vial}) \qquad (5.2)$$

The mass of dry G-Cys-Au@Pt catalyst can also be calculated using equation 4.6 for m(G-Cys) since the c(G-Cys) is known after the centrifugation procedure and a specific V(G-

Cys) is taken into a vial. From m(G-Cys) the m(G-Cys-Au@Pt) can be obtained using equation 4.5. Based on the catalyst mass used for ink preparation, the appropriate amount of Nafion® added to the ink can be calculated. The role of the Nafion® is twofold: (1) Nafion® acts as a proton conductor through the MEA (Fig. 5.25C) and (2) as a catalyst/electrode binder to the Nafion® membrane. The presence of Nafion® is necessary for fast reaction rates since the cathodic ORR depends on the efficient H^+ delivery in order for the reaction to propagate. However, excess Nafion® reduces the overall conductivity, damaging the performance of a FC. Due to such issues, experimental trial-and-error efforts have established an optimal amount of Nafion® within the catalytic ink. The Nafion® mass is depends directly on the total catalyst mass. Generally, the ideal amount of Nafion® is 15 wt.% to 85 wt.% of the added catalyst mass. The Nafion® solution concentration used here is 5 wt.% of Nafion® dissolved in ethanol, so the calculation for Nafion® mass to be added in the ink is expressed in equation (5.3):

$$\frac{\text{m (catalyst)}}{85\%} = \frac{\text{m(5\% Nafion®)}}{15\%} \tag{5.3}$$

$$\text{m(Nafion®)} = 3.53 \cdot \text{m(catalyst)} \tag{5.4}$$

Ethanol is added to the ink to make the catalyst dispersions more uniform due to better solubility of carbon-based materials in alcohols. Ethanol also reduces the drying time of the catalyst deposited on the carbon paper. The addition of Millipore water, in the ratio of 1 : 1 = ethanol : water, controls the drying time by preventing too fast ethanol evaporation, resulting in more uniform catalyst layers on the electrodes.
After all the ink constituents have been added, the vial is sealed and sonicated for a minimum of 30 minutes. Once the homogeneous dispersion is obtained, the ink is ready to be drop-casted. Optical images of a concentrated catalyst ink are shown in Fig. 5.24.

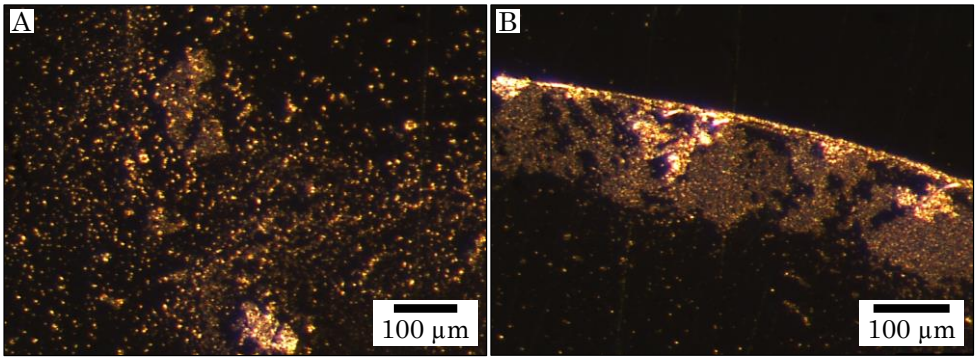

Figure 5.24 Optical microscope images of G-Cys-Au@Pt ink dried on a glass slide.

5.4.2 Ink drop-casting

Before the deposition of the ink on carbon paper (Fig. 5.24A-B), it is important to set the desired catalyst loading of the electrodes. The catalyst loading for G-Cys-Au@Pt is calculated according to the Pt content, as the Pt shell being the active material in G-Cys-Au@Pt, while the Au core is considered as "support" in this aspect. To perform these calculations, TGA and EDX measurements have to be performed to obtain the information about NP loading and metal-to-metal ratio, respectively, Fig. 4.7 and Fig. 4.12.

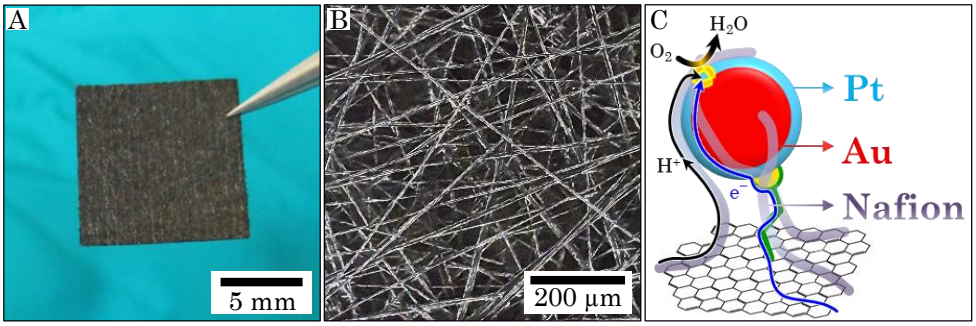

Figure 5.25 (A) Photograph of Toray carbon paper, 1.0 x 1.0 cm. (B) Optical microscopy image of Toray carbon paper used as a support for G-Cys-Au@Pt in FC experiments. (C) Scheme of ORR on Nafion® coated G-Cys-Au@Pt with H^+ and e^- pathway routes to the reaction site on Pt shell.

Pt loading calculation:

Total metal loading in G-Cys-Au@Pt (from TGA, Fig. 4.4):
$Au@Pt_{\text{loading}} = 42\ \%$

Metal ratio (from EDX, Fig. 4.8):
Au : Pt = 2.95 : 1

$$Pt_{\text{relative}} = \frac{Pt}{Au+Pt} \cdot 100 \tag{5.5}$$

$$\frac{1}{3.95} \cdot 100 = 25.32\%$$

$$Pt_{\text{actual}} = Au@Pt_{\text{loading}} \cdot Pt_{\text{relative}} \tag{5.6}$$

$$42.0\% \cdot 0.2532 = 10.63\%$$

To obtain the target Pt loading of the electrode, 0.5 mg_{Pt}/cm^2 on carbon paper, calculation of deposited mass of the catalyst must be performed:

$$m(\text{catalyst}) = \frac{\text{Target } Pt_{\text{loading}}}{Pt_{\text{actual}}} \tag{5.7}$$

$$\frac{0.5\ \text{mg}}{0.1063} = 4.7\ \text{mg of G-Cys-Au@Pt}$$

The loading of 0.5 mg_{Pt}/cm^2 corresponds to 4.7 mg of G-Cys-Au@Pt. The ink is being drop-casted, dried at ~ 60 °C and weighed to assure that the loading is precise, Fig. 5.26.

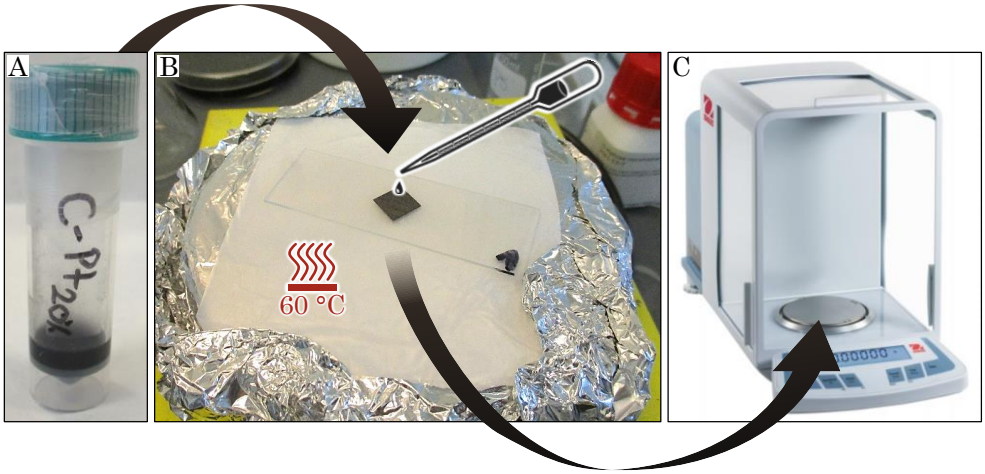

Figure 5.26 The drop-casting procedure of the catalyst ink on carbon paper. (A) C-Pt catalyst ink (B) drop-casted on carbon paper and dried at ~ 60 °C. (C) The Pt loading is monitored by weighing the carbon paper with dried catalyst using an analytical scale.

5.4.3 The MEA fabrication

The prepared electrodes were further made into sandwich-like structures containing the anode, Nafion® membrane and cathode, denoted as MEAs, Fig. 5.27. The fabrication of MEAs must be performed with precaution due to chloride impurities that can occur on the ppm level arising from the MEA preparation process or contamination of humidified feed streams. This represents a significant issue since even a 4 ppm chloride impurity can result in a voltage loss of 50 mV and equally affect the open circuit cell voltage.[41] In addition, the extensive H_2O_2 production can damage the perfluorinated membranes and ionomers in the catalyst layer.[57] MEAs therefore require highly clean conditions.

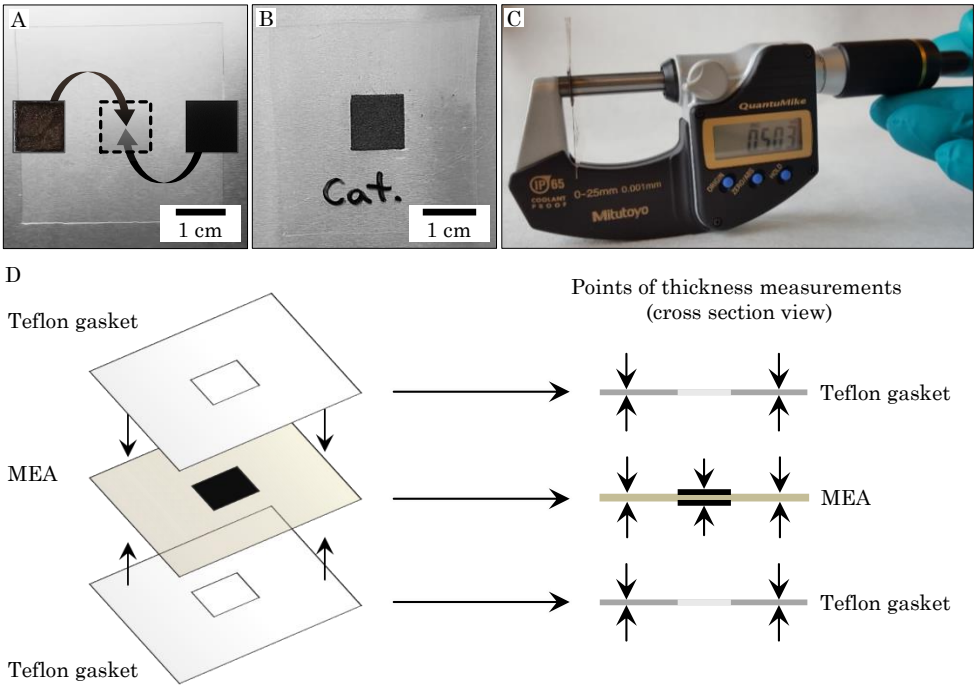

Figure 5.27 (A) The MEA components (anode, Nafion® membrane and cathode) are made into (B) hot-pressed MEA. (C) Micrometer measurements of the MEA showing a thickness of 503 µm. (D) Scheme of MEA protection by Teflon gaskets prior to insertion in FC and indication of points of thickness measurements by a micrometer.

After the electrode preparation, MEA is assembled within the hot-press. The hot-pressing parameters used are the optimal conditions established from a long-term practical experience of the group of Prof. Dr. Yi Ding at the Institute for New Energy Materials and Low-Carbon Technologies at Tianjin University of Technology (TJUT). Close collaboration with Prof. Dr. Yi Ding allowed for FC technology transfer to the NanoChemistry group at Department of Chemistry, Technical University of Denmark (DTU). The applied MEA fabrication parameters in this Ph.D. work were:

- Temperature: 135.0 °C,
- Pressure: 120 kg/cm^2,
- Duration: 3.0 min.

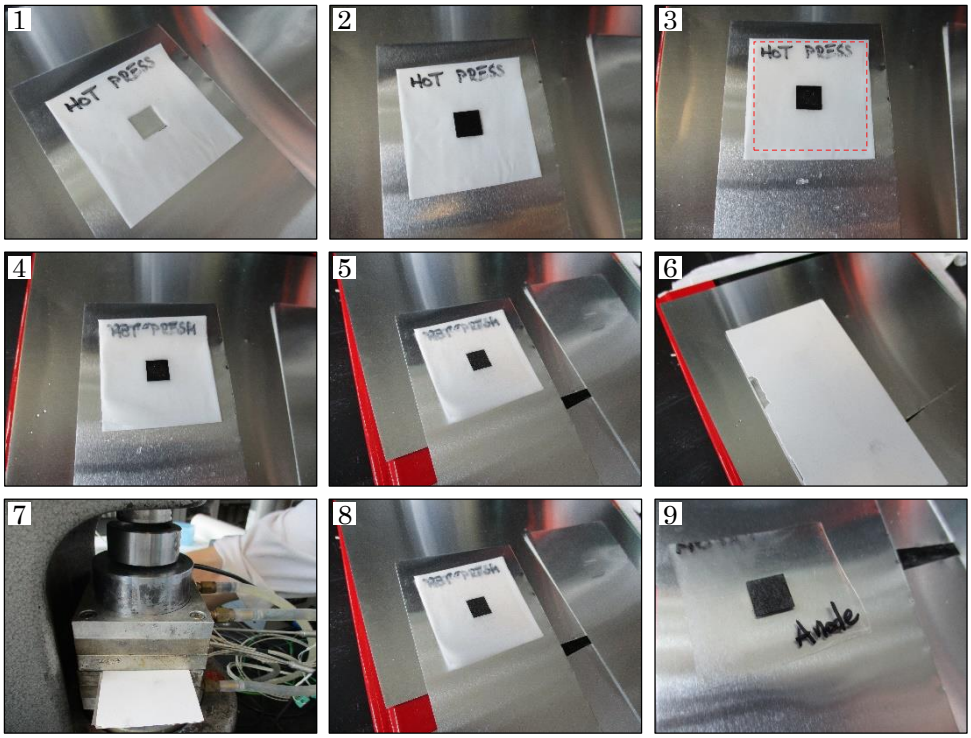

Figure 5.28 The hot-pressing procedure for MEA fabrication.

The Fig. 5.28 represents the procedure for MEA fabrication. The aluminium sheets and Teflon gaskets (1) are cleaned with ethanol to prevent electrode sticking to the sheet after the MEA preparation. The Teflon gasket (300 μm) is placed onto the aluminium sheet and (2) the anode is inserted in an empty window (1.0 x 1.0 cm). (3) The wet Nafion® sheet (4.0 x 4.0 cm, highlighted in red) is then placed on top of the anode. (4) The second Teflon gasket (the same thickness and dimensions as the first in the step 1) is placed on top of Nafion® sheet, followed by (5) the insertion of cathode into the 1.0 x 1.0 cm window. (6) The second aluminium sheet covers and protects MEA from direct hot-press contact. (7) The electrode "sandwich" assembly is then placed into the hot-pressing machine and after 3 minutes, (8) the MEA is taken out and (9) the Teflon gaskets are removed. Upon the disassembly, types of electrodes have to be noted down at their respective sides of the Nafion® sheet (anode or cathode side) to avoid any confusion or incorrect placement while conducting FC experiments.

Once placed in the FC, the MEA is protected by a set of Teflon gaskets at both electrodes, corresponding to the thickness of assembled MEA. These Teflon gaskets protect the porous structure of the electrodes from collapsing during the FC assembly. The FC is

tightly sealed by a set of screws, applying high pressure in order for MEA to be in an air-tight environment. For this reason, the thicknesses of a Nafion® sheet, Teflon gaskets and MEA have to be measured with a micrometer, Fig. 5.27C-D. Components are measured > 3 times at different places and average value is taken. Measured components are:

1. MEA (anode, cathode and Nafion® sheet, ~ 500 μm),
2. Nafion® sheet (~ 115 μm),
3. Teflon gasket (~ 60 μm).

A single Teflon gasket used in these experiments was ~ 60 μm thick. A number of Teflon gasket layers at each electrode was calculated using the following equation:

$$\text{No. of Teflon gaskets} = \frac{\text{d(MEA)} - \text{d(Nafion® sheet)}}{\text{d(Teflon gasket)} \cdot 2} \tag{5.8}$$

5.4.4 FC assembly

The MEA is sealed within FC components, as shown in Fig. 5.29. As noted, MEA is protected by Teflon gaskets. Surrounding the gaskets are graphite blocks that act as current conductors and suppliers of fuel and O_2 flow to anode and cathode, respectively. Au-plated Cu (Cu/Au) sheets are placed on the back of the graphite blocks. They act as current collectors, and are therefore made from highly conductive materials. The current collectors are further insulated by 300 μm thick Teflon sheets in order not to short circuit the FC when aluminium plates are connected by screws. The aluminium casing envelops the entire assembly and contains the thermocouple heating components. The plates are joined together by four screws, which apply enough pressure to the MEA for air-tight sealing. Table 5.5 lists the FC components, their dimensions and materials.

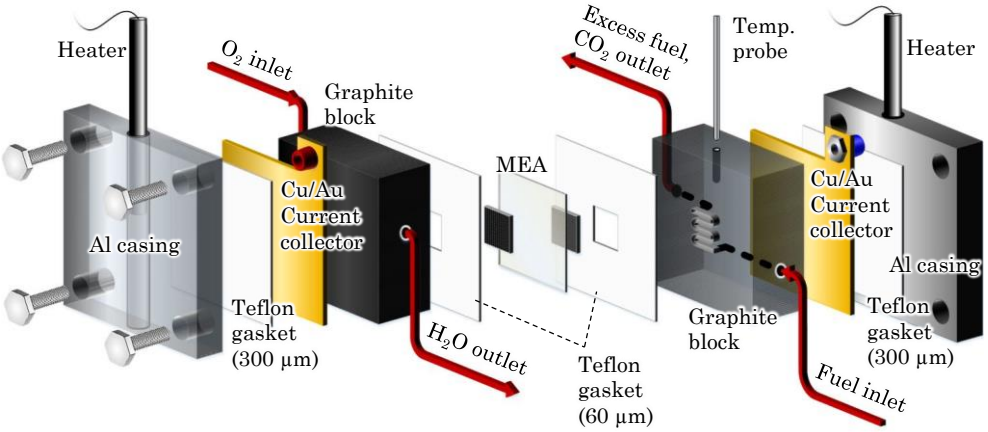

Figure 5.29 The schematic, exploded view of PEMFC components.

The actual FC assembly is shown in Fig. 5.30. (1) The insulating Teflon gasket is placed at the aluminium anode casing. (2) The Cu/Au anode current collector is placed on the Teflon gasket. (3) The anode graphite block supplying fuel through internally drilled channels is placed on top of the current collector. The serpentine channel dimensions are 1.0 x 1.0 cm and correspond to the electrode placed on top of it. (4) Corresponding to the measured MEA thickness, appropriately thick Teflon gasket goes on top of the anode graphite block. (5) The MEA is carefully placed on Teflon gasket, so that the anode fits into the 1.0 x 1.0 cm opening. (6) The MEA is protected by another Teflon gasket with the same thickness as the first one, to have the force evenly distributed over the MEA. (7) The second, cathode graphite block is placed on the second Teflon gasket. This graphite block conducts current from the cathode and has the same serpentine channel pattern as the first graphite block. The cathode graphite block provides oxygen to the electrode. (8) The cathode Cu/Au current collector is then placed on the cathode graphite block. (9) The second insulating Teflon gasket is placed on top of the cathode current collector. (10) The second aluminium casing covers the entire assembly and (11) is tightly secured with four screws. (12) The current collector plug-ins are mounted as well as fuel inlet to the anode (transparent tube) and oxygen inlet (red tube) to the cathode. (13) The fuel and oxygen outlets are mounted onto the FC. (14) The two thermocouple heaters and a temperature probe are inserted into appropriate openings in the aluminium plates in the anode graphite block, respectively. (15) The potentiostat leads (working electrode in red and counter electrode in black/blue) are connected to the current plug-ins at the FC current collectors. (16) The FC is then assembled and ready to be tested.

Table 5.5 FC components, materials and dimensions.

FC component	Material	Dimensions (cm) height/width/thickness
Casing	Aluminium	8/8/0.8
Outer gasket	Teflon	6/6/300[A]
Current collector	Au-plated Cu sheet	6/6/0.3
Fuel/O_2 supply block	Graphite	6/6/1.5
Inner gasket	Teflon	6/6/60[A]
Anode/Cathode	Graphite paper	1/1/~150[A]
Polymer electrolyte	Nafion® membrane	4/4/~115[A]

Thickness dimension expressed in [A] [μm].

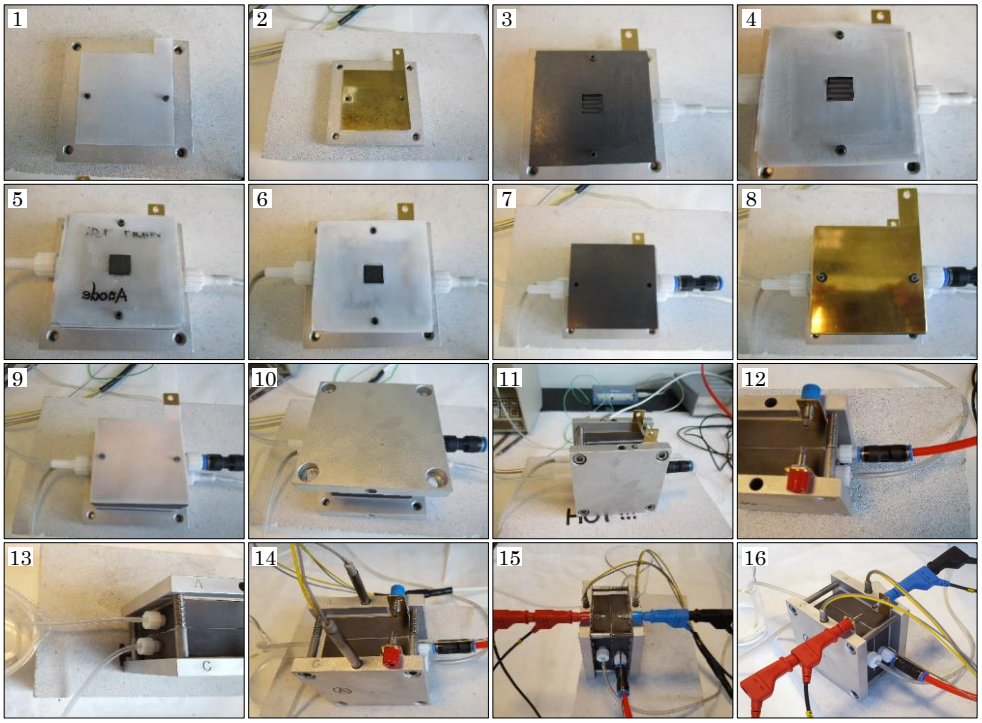

Figure 5.30 The process of FC assembly.

To obtain optimal FC performance, both electrodes are activated by water humidification for a minimum of 4 hours. Nafion® in the MEA has to be wetted to be proton conductive. Once all the steps have been performed correctly, the FC can be gradually heated from 40, 60 to 80 °C. Fuel supply is maintained at 2.0 mL/min and dioxygen at 100 mL/min.

5.5 Fuel cell experiments

Performance of the developed catalyst was tested in a PEMFC system. The anode electrodes were prepared by the catalyst ink drop-casting on microporous carbon paper Toray (Japan), reaching the loading from 0.50 to 0.68 mgPt/cm^2. The cathode used was a commercial 1.0 mg$_{Pt}$/cm^2 (BC-H225-10F from Quintech, Germany). The MEA was prepared for the synthesized catalysts. The two electrodes and Nafion®™-115 membrane (Quintech) were hot-pressed at 135.0 °C and pressure of 120.0 kg/cm^2. The MEAs had 1.0 cm^2 active area. A in house-built PEMFC test station was equipped with heating thermocouples type K, flow of fuel molecules and O_2 controlled by Gilson MINIPULS 3 and MKS GE50A gas flow meter. The FC test station was built up according to standards of practice.[283][301] The PEMFC was operated at 40, 60 and 80 °C. The fuel flow was kept

constant at 2.0 mL/min and dry O_2 flow rate was 100 mL/min without humidification process. The FC experiments were performed in DFAFC, DMFC and DEFC systems. The used fuels were fed to the anode at a flow rate of 2.0 mL/min with concentrations of 3.0 and 1.0 M for FA and MeOH/EtOH, respectively, without additional supporting electrolytes boosting the catalytic activity. The G-Cys-Au@Pt catalyst performance within DFAFC, DMFC and DEFC is shown in Fig. 5.31A,C,E respectively, and correspondingly compared to C-Pt standard performances in Fig. 5.31B,D,F. The highest recorded open circuit voltages (OCVs) and power densities for G-Cys-Au@Pt are: 0.833 V and 127.0 mW/cm^2 for DFAFC, 0.511 V and 41.1 mW/cm^2 for DMFC, 0.485 V and 9.3 mW/cm^2 for DEFC. The G-Cys-Au@Pt exhibits 153, 52 and 35 mV higher OCV values with corresponding 95.4, 53.4 and 106.7 % power density increases in the DFAFC, DMFC and DEFC setups, respectively, compared to the C-Pt catalyst.

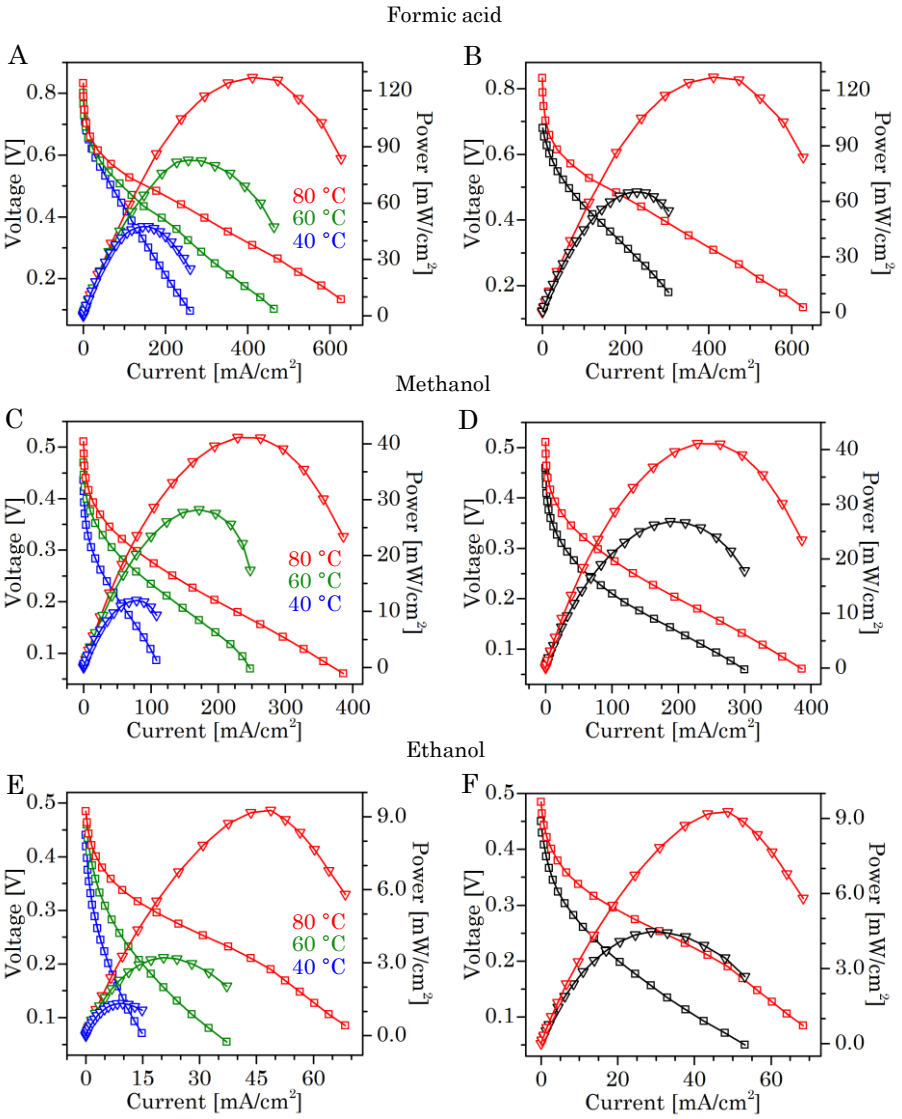

Figure 5.31 FC performance for G-Cys-Au@Pt catalyst in (A) 3.0 M FA, (C) 1.0 M MeOH and (E) 1.0 M EtOH at 40 (blue), 60 (green) and 80 (red) ºC. Comparison of FC performance at 80 ºC for G-Cys-Au@Pt (red) and C-Pt (black) in (B) 3.0 M FA, (D) 1.0 M MeOH and (F) 1.0 M EtOH. G-Cys-Au@Pt was used as the anode catalyst in all the experiments with loadings of 0.64 mg_{Pt}/cm^2 (FA), 0.52 mg_{Pt}/cm^2 (MeOH) and 0.50 mg_{Pt}/cm^2 (EtOH). C-Pt anode loadings were 0.52 mg_{Pt}/cm^2 (FA), 0.52 mg_{Pt}/cm^2 (MeOH) and 0.50 mg_{Pt}/cm^2 (EtOH). Commercial 1.0 mg_{Pt}/cm^2 catalyst was used in all assembled MEAs. Fuel flow was 2.0 mL/min, non-humidified O_2 flow 100.0 mL/min. In all the figures (□) represents *i* vs. *E* and (▽) *i* vs. *P* plots.

The enhanced electrocatalytic performance of G-Cys-Au@Pt in the anode setup (Fig. 5.31) was sought within the setup where G-Cys-Au@Pt is catalyst at both anode and cathode, Fig. 5.32. However, this FC system did not parallel the anode setup results. As previously argued, the outcome is closely related to diffusion properties of the graphene support, effectively diminishing the reactant concentration at the catalyst surface. Recently reported studies by Kim et al. [302] and Ma et al. [303] shine light on the phenomena. By selective wetting of the ordinarily hydrophobic graphene surface, water molecules are brought to space out, interact with, and diffuse into the graphene framework at unusually high rates. This curious feature is omitted when the structure is dry. Having an un-wetted gas flow in a heated FC cathode catalyst setup, graphene's compact structure inhibited sufficient dioxygen flux to Pt, consequently diverging from the noteworthy results when G-Cys-Au@Pt is used as anode catalyst (Fig. 5.31). Nevertheless, cathode application of G-Cys-Au@Pt catalyst is surely a basis for imminent research.

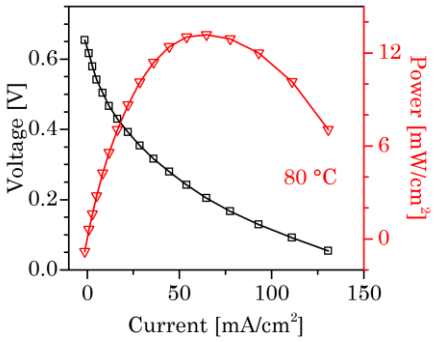

Figure 5.32 DFAFC performance of G-Cys-Au@Pt as catalyst on both electrodes: anode 0.62 mg_{Pt}/cm^2, cathode 1.11 mg_{Pt}/cm^2. Fuel flow was 2.0 mL/min, non-humidified O_2 flow 100.0 mL/min. (□) represents *i* vs. *E* and (▽) *i* vs. *P* plots.

C-Pt catalyst in the MEA was extensively tested in DFAFC, DMFC and DEFC systems. The performance of C-Pt is presented in Fig. 5.33. Comparing the performance of G-Cys-Au@Pt (Fig. 5.31) and C-Pt (Fig. 5.33) in DFAFC, DMFC and DEFC, at 40, 60 and 80 °C, consistent doubling of power density can be observed for G-Cys-Au@Pt. More favorable electronic configuration of Au-modified Pt surface oxidizes fuel molecules at higher rates than pure Pt NPs in C-Pt. Covalent Au@Pt NP immobilization on highly conductive graphene nanosheets benefits efficient electron transfers, resulting in increased overall electrocatalytic performance compared to for C-Pt with adsorption immobilized Pt NPs.

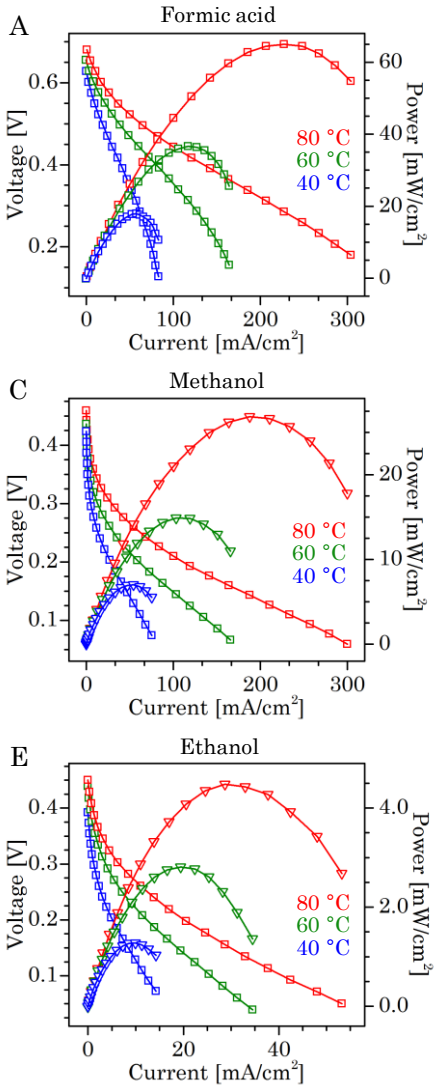

Figure 5.33 FC measurement of C-Pt catalyst in (A) DFAFC, (B) DMFC and (C) DEFC systems at different temperatures. C-Pt anode loadings were 0.52 mgPt/cm^2 (A, B) and 0.50 mgPt/cm^2 (C). Commercial 1.0 mgPt/cm^2 catalyst was used in all assembled MEAs. Fuel flow was 2.0 mL/min, non-humidified O_2 flow 100.0 mL/min. In all the figures (□) represents i vs. E and (▽) i vs. P plots.

The stability measurements of the G-Cys-Au@Pt and C-Pt catalysts were performed by chronoamperometry in DFAFC, DMFC and DEFC systems. E_{ox} was maintained at the peak power of both catalysts for 6000 s. The current density vs. time plots (i vs. t) are shown in Fig. 5.34, The G-Cys-Au@Pt catalyst exhibits higher currents than C-Pt for all

of the FC setups over the entire duration of the measurements, demonstrating its superior performance. G-Cys-Au@Pt retains 16, 7 and 9% greater currents than C-Pt, in DFAFC, DMFC and DEFC setups, respectively and generally shows a significantly lower rate of deactivation. This is most pronounced in DFAFC where current retention for G-Cys-Au@Pt was 92 % and for C-Pt 85 %. The current density degradation observed for both catalysts stems from the gradual accumulation of CO_{ads}. The current stabilization observed for G-Cys-Au@Pt is attributed to the improved poisoning tolerance and more facile CO_{ads} removal, as demonstrated in CO adsorption measurements, Fig. 4.16 and Fig. 4.17 in Chapter 4.

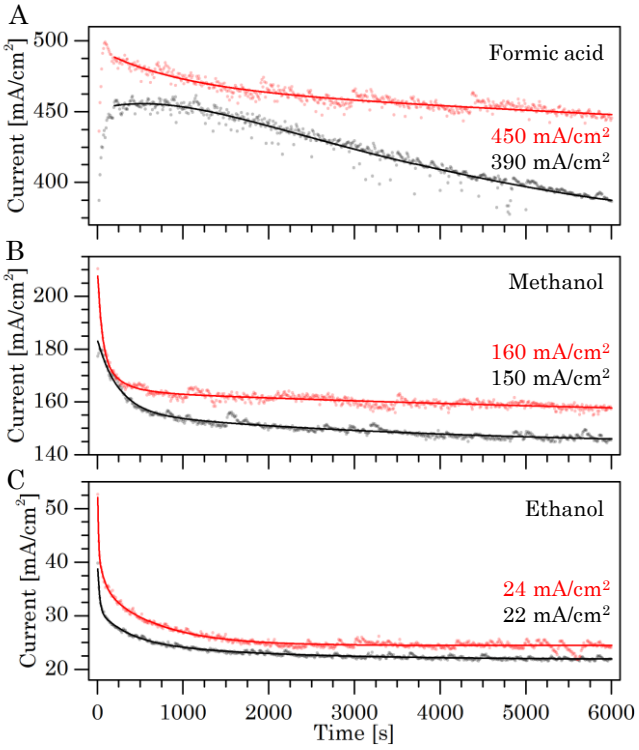

Figure 5.34 Chronoamperometry plots exhibiting catalyst stability in FCs at 80 ºC for G-Cys-Au@Pt (red) and C-Pt (black) in (A) 3.0 M FA, (B) 1.0 M MeOH and (C) 1.0 M EtOH. Constant potential was maintained for 6000 s at the peak power performance of each catalyst.

G-Cys-Au@Pt and C-Pt was systematically tested for three target fuels obtaining the benchmark values.

Table 5.6 (A) DFAFC, (B) DMFC and (C) DEFC average performances of G-Cys-Au@Pt and C-Pt MEAs with different Pt loadings at 40, 60 and 80 °C, 100 mL/min O_2 flow and 2.0 mL/min 3.0 M FA, 1.0 M MeOH and EtOH fuel flows. The average values are taken from 71 different measurements of G-Cys-Au@Pt and 52 measurements of C-Pt FC performance.

A

DFAFC Average:	**T** (°C)	**G-Cys-Au@Pt** 0.50 mg_{Pt}/cm^2	**G-Cys-Au@Pt** 0.52 mg_{Pt}/cm^2	**G-Cys-Au@Pt** 0.64 mg_{Pt}/cm^2	**C-Pt** 0.52 mg_{Pt}/cm^2	**C-Pt** 0.61 mg_{Pt}/cm^2	**C-Pt** 0.68 mg_{Pt}/cm^2
P (mW/cm^2)	40	30 ± 3	30 ± 1	40 ± 2	20 ± 1	20 ± 1	10 ± 4
	60	50 ± 6	80 ± 13	80 ± 2	40 ± 1	40 ± 1	60 ± 1
	80	100 ± 2	100 ± 6	120 ± 3	60 ± 2	60 ± 3	60 ± 1
i (mA/cm^2)	40	120 ± 1	120 ± 2	150 ± 7	60 ± 2	70 ± 1	50 ± 6
	60	250 ± 15	370 ± 62	260 ± 11	120 ± 1	150 ± 11	250 ± 9
	80	380 ± 42	460 ± 30	420 ± 17	210 ± 13	250 ± 14	250 ± 40
OCV (mV)	40	730 ± 15	740 ± 3	790 ± 11	630 ± 6	680 ± 4	680 ± 47
	60	740 ± 18	780 ± 22	810 ± 10	650 ± 3	690 ± 24	740 ± 9
	80	810 ± 13	800 ± 3	830 ± 10	700 ± 16	730 ± 8	720 ± 15

B

DMFC Average:	**T** (°C)	**G-Cys-Au@Pt** 0.50 mg_{Pt}/cm^2	**G-Cys-Au@Pt** 0.52 mg_{Pt}/cm^2	**C-Pt** 0.52 mg_{Pt}/cm^2
P (mW/cm^2)	40	10 ± 1	10 ± 1	10 ± 1
	60	20 ± 2	30 ± 1	20 ± 1
	80	30 ± 1	40 ± 3	20 ± 4
i (mA/cm^2)	40	70 ± 5	80 ± 4	50 ± 3
	60	120 ± 8	170 ± 6	110 ± 2
	80	160 ± 5	230 ± 17	190 ± 3
OCV (mV)	40	430 ± 6	430 ± 7	420 ± 2
	60	480 ± 2	470 ± 2	440 ± 1
	80	510 ± 1	540 ± 33	450 ± 11

C

DEFC Average:	**T** (°C)	**G-Cys-Au@Pt** 0.50 mg_{Pt}/cm^2	**C-Pt** 0.52 mg_{Pt}/cm^2
P (mW/cm^2)	40	1 ± 0	1 ± 0
	60	3 ± 1	3 ± 1
	80	8 ± 2	4 ± 1
i (mA/cm^2)	40	10 ± 1	9 ± 1
	60	21 ± 1	19 ± 1
	80	42 ± 6	28 ± 1
OCV (mV)	40	439 ± 2	402 ± 8
	60	470 ± 21	434 ± 6
	80	504 ± 20	446 ± 4

The experiments obtaining the average open circuit voltages (OCVs), current densities (i) and power densities (P) within the DFAFC, DMFC and DEFC for the G-Cys-Au@Pt and C-Pt with different Pt loadings are summarized in Table 5.6A-C.

5.6 Conclusions

The G-Cys-Au@Pt catalyst was tested in DFAFC, DMFC and DEFC systems exhibiting maximum power outputs of 127.0, 41.14 and 9.26 mW/cm^2 at 80 ºC, an increase of 95.4, 53.4 and 106.7 % compared to C-Pt, respectively. Au-modified Pt electronic configuration resulted in stronger bonding of fuel molecules to Au@Pt NPs, giving rise to higher electrocatalytic rates than pure Pt NPs in C-Pt. Covalent Au@Pt NP immobilization on graphene enhanced electron transfer rates, compared to C-Pt with adsorption immobilized Pt NPs on graphitized carbon. These improvements resulted in increased overall G-Cys-Au@Pt FC performance at all tested temperatures and in all three FC systems. The catalyst stability was tested by chronoamperometry. The retained current densities at the end of the experiments were 16, 7 and 9 % higher for G-Cys-Au@Pt than for C-Pt in DFAFC, DMFC and DEFC. The enhanced catalytic stability was especially pronounced in DFAFC system where G-Cys-Au@Pt retained 92 % of its initial current density. The 10 % increase in CO_{ads} poisoning tolerance and 60 mV lower removal potential originated from Au NP cores, a well-established CO oxidation catalysts.[222] Unique G-Cys-Au@Pt design therefore strongly attracts and binds fuel molecules, but retains selectivity towards desorption of catalytic poisons. Chemical anchoring of Au@Pt NPs on graphene creates efficient electron transfer pathways, further enhancing the electrocatalysis.

As-presented catalytic robustness and durability of G-Cys-Au@Pt towards biofuel oxidation and ORR offers application within DFAFC, DMFC and DEFC systems. “Green” and scalable synthesis of G-Cys-Au@Pt provides a basis for new generation PEMFC electrocatalysts tailored with ultra-low Pt loadings and highly efficient electronic structures.

Chapter 6

Scanning tunneling microscopy: Molecular assembly of cysteine on Au(111) in ionic liquids

6.1 Scanning tunneling microscopy

All matter including even vacuum is electrochemically conducting at atomic or molecular scale, by the quantum mechanical tunneling effect.[304] Scanning tunneling microscopy (STM) is a technique that provides atomic resolution of a conductive sample by the quantum mechanical tunneling effect. Bias voltage is applied between an atomically sharp tip and a conducting sample surface. A tunneling current flows when the tip is brought only few angstroms (Å = 10^{-10} m) from the sample. As the tip scans across the surface, information about its position, piezoelectricity and the tunneling current is acquired and displayed in a form of an image. The most significant feature of STM is atomic resolution.

Simply speaking, the atomic resolution is achieved based on the exponential dependence of the tunneling current on the separation of the tip and the sample. The electronic wave functions extending from the tip and sample surfaces thus decay exponentially within the gap between these two surfaces. If the gap is thin enough, the decaying wave functions overlap with each other, and electron tunneling takes place.[305] In STM experiments, a bias voltage is applied between the tip and sample to shift their corresponding Fermi levels. The current is measured with an amplifier and is in the range of pA to nA.[306]

There are two distinct modes under which STM can generate images: constant-current and constant-height mode. In the former mode a feedback mechanism uses a constant current, while a constant bias is applied between the tip and the sample. As the tip is scanning the sample, the constant separation between the two is maintained. Piezoelectric elements control the motion in all three directions (x, y and z).[305] The topographic image is created from the voltage signal required to change the position of the tip in the z direction so the tunneling current can be maintained constant, i.e. the height of the tip z(x, y) as a function of position is recorded. In this mode, the image represents a constant charge density contour of the sample surface. The constant-current

mode is used for sample surfaces which are not completely atomically flat (stepped surfaces). The disadvantage of using this mode is a limited response time of the feedback loop which results in relatively low limits for the scan speed.[307] In the constant-height mode, a constant applied bias and height are being maintained. As the tip scans across the sample surface, the variation in current results in topographic structure variations. In this mode, the image is being created directly from the current and is related to averaging charge density.[305] Since the feedback loop is significantly slowed or even turned off, the tip is able to scan sample surface considerably faster. The disadvantage of this mode is limitation to only atomically flat surfaces since the tip is not being retracted when approaching a protrusion in the sample. Another drawback is that topographic height information from variations of the tunneling current is difficult to extract since the distance dependence of the tunneling current is often not precisely known.[307] Atomic resolution is possible only under optimized sample and tip preparations. As a general note of observation, STM images do not directly represent sample topography, but rather tunneling currents, and the current-distance relation must be identified to have a true topographic image of the surface.

6.1.1 The concept of tunneling

As a simple illustration of the fundamental concept we consider the one-dimensional motion of an electron. Classical mechanics describes an electron with the total energy E by the Hamiltonian function:

$$E = \frac{p_z^2}{2m} + U(z) \tag{6.1}$$

where m is the electron mass, p_z the electron momentum along the single dimension z, and U(z) the potential energy of the electron.[308] In regions where the total energy of the electron E > U(z), the electron has a non-zero momentum, and the electron can be found nowhere outside the z-range where E > U(z). Quantum mechanics describes the electron as a wavefunction ψ(z) by Schrödinger's equation:

$$E\psi(z) = -\frac{\hbar^2}{2m}\frac{d^2}{dz^2}\psi(z) + U(z)\psi(z) \tag{6.2}$$

where $2\pi\hbar$ is reduced Planck's constant.

One of the most notable results of even simple quantum mechanics is that there is now also a finite probability of finding the electron outside the E > U(z) range. The probability (P) for an electron of energy E < U(z) to pass a barrier U(z) of width a can be described by the Gamov equation [309] reduced to an expression:

$$P = \exp\left[-\frac{2}{\hbar}a\sqrt{2m(U(z)-E)}dz\right] \tag{6.3}$$

The tunneling current (I_t) is proportional to the tunneling probability for a rectangular and constant barrier of height U [305]:

$$I_t \propto \exp\left[-\frac{2}{\hbar}a\sqrt{2m(U-E)}\right] \tag{6.4}$$

The exponential dependence on the gap width and barrier height indicates that all current in STM is transferred by the most protruding atoms of the tip where small changes in sample-tip distance results in significant changes in tunneling current. The minimum energy required to remove one electron from the bulk of the material to the vacuum level is defined as the work function, ϕ.[308] If it is assumed that the work function of the tip and the sample are equal and a bias voltage (V) is applied, the electron can tunnel from sample to the tip and vice versa, Fig. 6.2.

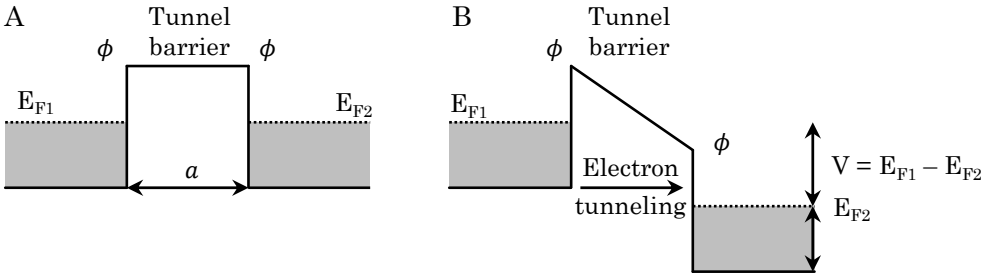

Figure 6.1 The energy levels of two metal electrodes separated by an insulating vacuum barrier with (A) no bias applied and (B) applied bias. E_{F1} and E_{F2} represent Fermi levels of the two materials. The applied bias is $V = E_{F1} - E_{F2}$ and a is the distance between them.

The energy diagram in Fig. 6.1 is a general representation of two macroscopic flat and parallel metal electrodes. The STM configuration, i.e. tip-plane geometry is different but the figure still applies qualitatively. By applying the bias voltage, net tunneling takes place where the electrons can tunnel from filled levels below the Fermi level E_{F1} of the electrode to the left to vacant levels above the Fermi level, E_{F2} of the electrode to the right.

6.2 In-situ scanning tunneling microscopy

From the fundamental, biotechnological and electrochemical aspect, two-dimensional organization of functional proteins on solid surfaces is of a great interest. Several issues are here in focus: high-resolution mapping of the electronic structure and transport of organic thin films on solid surfaces. Advances of self-assembled monolayer (SAM) chemistry and surface-ultrasensitive techniques such as STM, currently offer effective tools to address this challenging task. Electrochemical, in-situ STM (ECSTM) is a technique that can image real-life processes taking place in conductive samples, such as

SAM structural changes and adsorption/desorption processes. Measurements conducted in ECSTM are described in this chapter with a focus on a deeper insight into morphology of cysteine (Cys) SAM on the single-crystal Au(111) surfaces.

ECSTM was employed in an ionic liquid environment for the purpose of avoiding oxygen and water influence on the Cys assembly and interaction with Au(111). An ionic liquid (IL) may be described as a compound composed entirely of ions in its liquid state at temperatures around 298 K and below. Due to the ionic composition, ILs possess wide electrochemical windows (often in excess of 5 V). For such reasons, ILs are seen as attractive potential solvents and electrolytes used for electrochemical investigation.

The electrochemical interactions of air/water-free stabile IL, 1-ethyl-3-methylimidazolium bis(trifluoromethylsulfonyl)imide (EMITFSI) with Cys SAMs at the surface of Au(111) was studied by cyclic voltammetry (CV) and STM. Cys molecules were assembled on Au(111) surfaces to form highly ordered monolayers with a periodic lattice structure. Adsorption of cysteine molecules was confirmed by reductive desorption experiments using voltammetric methods. Aqueous solution of 0.1 M NaOH was used as a reference system to Cys desorption in pure EMITFSI. In both systems a single desorption peak was present indicating successful reductive removal of Cys molecules. In-situ STM allowed the examination of stable, highly ordered Cys SAMs, as well as their change and dissipation with the change of applied potential.

6.3 Experimental procedures

The STM measurements were conducted using a Nanoscope E (Digital Instrument, USA) instrument with Nanoscope 5.30 software, in glove box, in under constant-current mode. The STM electrochemical cell was a four-electrode system with the: (1) Cys SAMs on Au(111) as a working electrode (WE), (2) Pt coiled wire as counter electrode (CE), (3) a shorter Pt wire as a reference electrode (Pt/PtO RE) and (4) electrode made of tungsten (W) or platinum-iridium (Pt/Ir) etched wire functioning as an STM tip, Fig. 6.2.

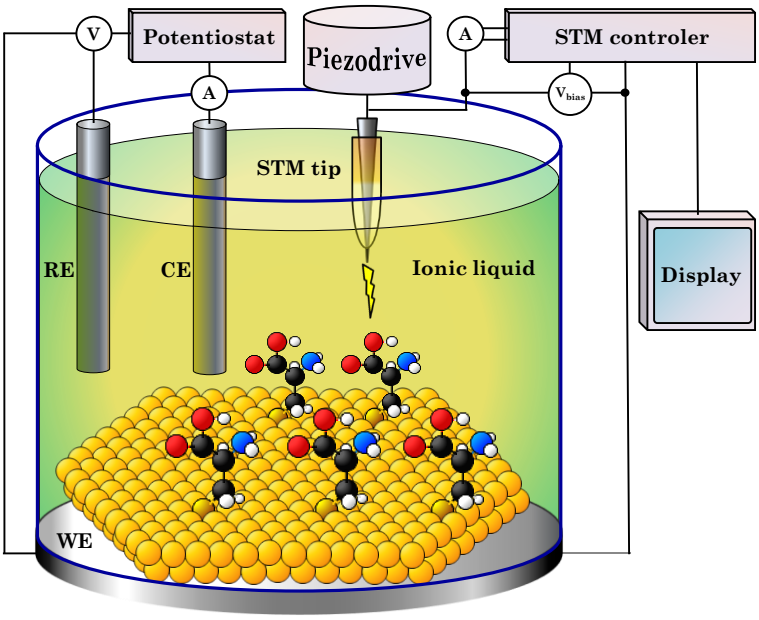

Figure 6.2 Scheme of in-situ STM setup with Cys SAMs on Au(111) as working electrode.

Pt/PtO RE was used due to the small dimensions of the ECSTM cell. After the STM and electrochemical experiments in EMITFSI the electrochemical potentials were checked versus SCE and all potentials have been reported versus this RE.

6.3.1 STM tip preparation

The STM tips were prepared from W or Pt/Ir alloy (80/20 %) wires (ϕ = 0.25 mm). W tips were prepared by electrochemical etching of W wire (ϕ = 0.25 mm) in 1.0 M KOH or NaOH aqueous solutions. Approximately 30.0 mL of the solution was poured into a beaker with a coiled, H_2 flame annealed Pt wire, as a CE. The W wire was mounted above the electrolyte, perpendicular to the solution surface, and inserted into the electrolyte by approximately 2.0 mm. The W wire was then connected to the AC source and 10 to 15 V applied to start etching the wire. The surface tension of the electrolyte created a meniscus around the wire during etching, Fig. 6.3A. The wire grew thinner as it was oxidized and dissolved into the electrolyte. As the etching progresses, the meniscus enveloping the wire produces a sharp tip. Once the W wire is thin enough, the electrolyte meniscus detaches from the tip, effectively breaking the electric circuit, and stopping the current flow leading to atomically sharp tip to be made, Fig. 6.3B.

The sharpness of the tips was examined under an optical microscope. If the sharpness was not satisfactory, the tips were re-done by repeating the etching procedure. Sharp tips

were copiously cleaned and sonicated in Millipore water with resistivity of 18.2 MΩ·cm at 25 °C.

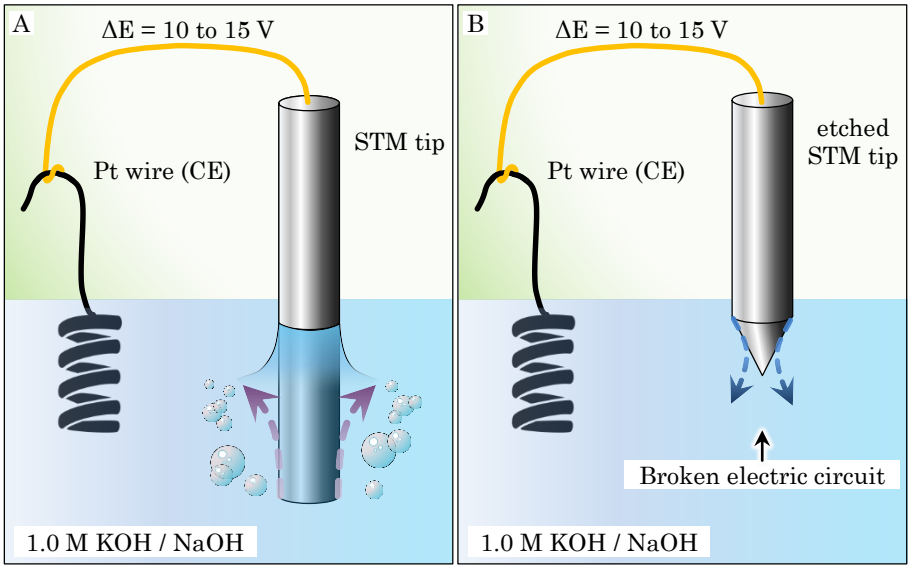

Figure 6.3 Electrochemical etching of a W STM tip. (A) The bias voltage is applied to start the oxidation of the W surface. (B) The electrical circuit is broken by the electrolyte meniscus being detached from the W wire.

Similarly to W tip preparation, Pt/Ir tips can be electrochemically etched. An alternative procedure is cutting Pt/Ir wire with a sharp cutting tool. The process requires an experienced user. Although the procedure needs less time and preparation, the reproducibility and quality of the tips present challenges. Pt/Ir tips were prepared by cleaning the Pt/Ir (80/20 %) wire in the H_2 flame followed by washing in Millipore water. The procedure was repeated several times. The Pt/Ir wire was then cut at an angle of 45°, applying an abrupt detaching movement, with a sharp pair of scissors that had been cleaned in ethanol prior to the cut. As-prepared Pt/Ir tips were cleaned by copious amounts of Millipore water. To avoid tip surface oxidation, all tips were freshly prepared before the STM experiments.

6.3.2 STM tip coating procedure

Atomic resolution in STM greatly depends on the tip quality. In order to eliminate Faradaic currents for in-situ STM measurements, the tips were coated by polyethylene (PE). The PE was melted by heating the PE rod at ~ 100 °C on a fork-like resistance heater. When the PE was melted, the tip was slowly inserted upwards from the bottom of

the melting PE, so that ~ 5.0 mm of the tip would stick above the melted PE. By doing so, only the atomically sharp tip of the wire could get exposed from the PE coating. After 10 to 15 seconds, the PE hardened around the metal tip and was slowly taken out from the melting PE. The very outmost part of the tip was exposed, while the main body of the tip was protected by ~ 1 mm wide, hardened PE layer. Due to its small size, the exposed tip cannot be examined under an optical microscope but rather tested in the STM setup. Insulating the W or Pt/Ir tips allowed for the current flow only through the atomically sharp top of the tip, avoiding Faradaic currents and eliminating imaging noise during in-situ STM experiments.

6.3.3 Functionalization of the Au(111) electrode surface by cysteine SAMs

Prior to each in-situ STM experiment, 2.0 mL of EMITFSI was vacuum dried in a glovebox overnight. Sigma Aldrich L-cysteine (≥ 98 %) was grinded up into a fine powder, by a mortar and pestle and used to prepare 0.1 mM solution in EMITFSI. After the addition of the powder to the IL, the dispersion was magnetically stirred and heated at 80 °C for 5 to 8 hours followed by 2 hours of sonication. The solution was continuously vacuum-pumped in order to avoid contact with air or water. Au(111) beads were electro-polished in 0.1 M H_2SO_4 and 0.1 M HCl followed by H_2 flame annealing for a minimum of 5 minutes. As-prepared Au(111) electrodes were transferred to a glovebox with Ar atmosphere where it was immersed into 2.0 mL of 0.1 mM Cys (dissolved in EMITFSI) solution and heated at 80 °C for 3 to 8 hours. After the Cys had adsorbed on the Au(111) surface, the sample was washed with ethanol, assembled in an STM electrochemical cell, and transferred to the STM setup, Fig. 6.4.

The in-situ STM setup had to be assembled in a quick and efficient way in order not to prolong the exposure of the sensitive sample to air and moisture. The ethanol-washed Cys functionalized Au(111) electrode was placed onto a steel current collector which also acted as a WE slider. The assembled EC cell could be moved in the x, y directions by ~ 5 mm. A rubber o-ring was placed on top of Au(111) bead electrode so that IL cannot leak out due to the air-tight seal. The Teflon ECSTM cell round opening was aligned with the o-ring and placed on top of it. Four screws secured the EC cell to the steel current collector. After the insertion of the tip into the STM scanner and connection of the electrodes, the sample was covered by 200 μL of the pure and overnight-dried EMITFSI IL. The setup described was covered with an acrylic box equipped with N_2 gas inlet to protect the sample from air and moisture.

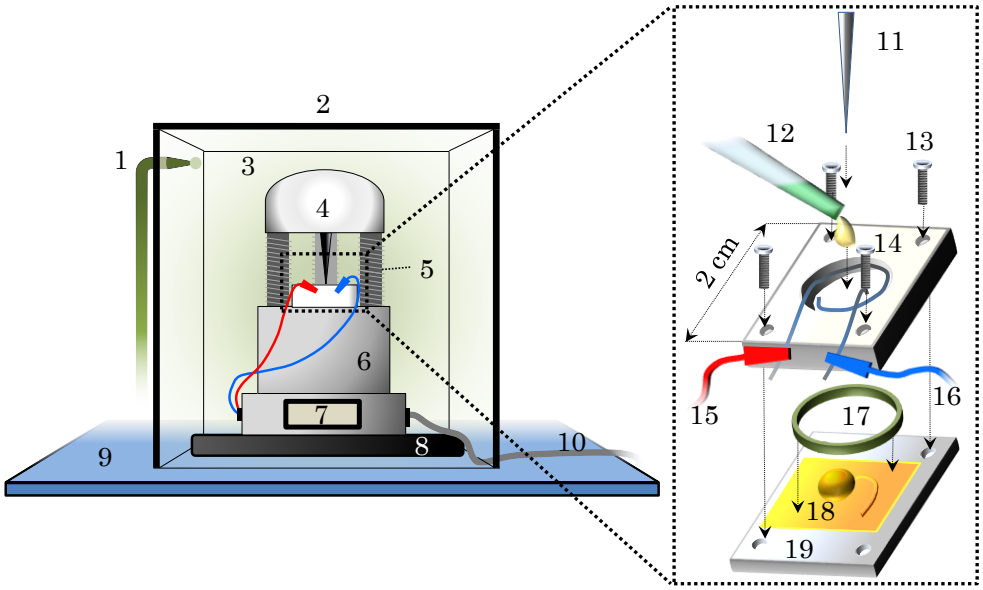

Figure 6.4 In-situ STM experimental setup: (1) inlet of N_2, (2) acrylic box for atmosphere protection, (3) N_2 saturated atmosphere, (4) scanner with mounted STM tip, (5) three micrometer screws for scanner positioning, (6) potentiostat for potential and current control, (7) voltage bias display, (8) vibration damping pad, (9) vibration damping table, (10) current leads to computer, (11) W or Pt/Ir STM tip, (12) IL application (after the EC cell assembly), (13) four EC cell assembly screws, (14) Teflon EC cell, (15) Pt wire CE, (16) Pt wire RE, (17) rubber o-ring, (18) Cys functionalized Au(111) WE electrode and (19) steel current collector.

6.4 Cys SAMs on Au(111): Electrochemistry and STM

The purpose of conducted in-situ STM experiments was to get a deeper insight into Cys SAMs on single-crystal Au(111) surfaces. ILs were used as an electrolyte due to their good properties such as low volatility, high potential window and high conductivity. Challenges met prior to conduction of STM experiments were low solubility of Cys in the ILs. Dissolution of the amino acid in four ILs was tried, Fig. 6.5: 1-Butyl-1-Methylpyrrolidinium-bis (trifluoromethylsulfonyl)imide (BMPTFSI), 1-methyl-3-octylimidazolium hexafluorophosphate ($OMIPF_6$), EMITFSI and 1-n-butyl-3-methylimidazolium ($BMIPF_6$). Cys indicated good solubility after heating at 80 °C and sonication in EMITFSI and $BMIPF_6$. In BMPTFSI and $OMIPF_6$ fine Cys powder was continuously present during all of the dissolution procedures, such as long heating, stirring and sonicating. Due to very high hygroscopicity and lower thermostability of

$BMIPF_6$ (rapid color change from light orange to dark brown in several minutes), EMITFSI was used as a solvent for Cys in the following experiments.[310]

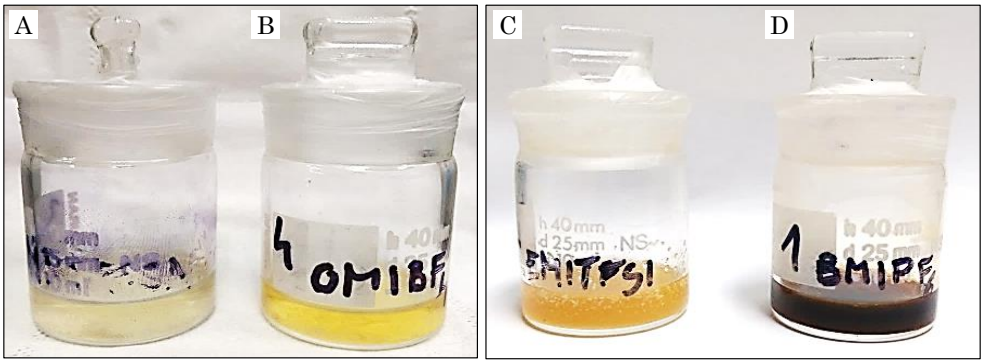

Figure 6.5 Cys dissolution in four different ILs before heating: (A) BMPTFSI, (B) $OMIPF_6$, (C) EMITFSI and (D) $BMIPF_6$.

Formation of Cys SAMs on Au(111) was investigated by electrochemical reductive desorption in both 0.1 M NaOH and pure EMITFSI. CV and capacitance analysis can qualitatively distinguish adsorption of Cys on Au(111) surface. The coverage of Cys SAMs was estimated from a prominent and sharp peak in cyclic voltammograms observed during reductive desorption of Cys in 0.1 M NaOH.[311] Investigation of SAMs was conducted in basic medium (pH = 13) in order to avoid hydrogen evolution during reductive desorption at negative potentials. A well-defined cathodic peak implies a one-electron process. Its potential depends on electrolyte pH, crystallinity of Au surface, the bond strength and molecular structure of the SAM. Fig. 6.6A shows a sharp cathodic peak of cysteine at -0.720 V vs. SCE in 0.1 M NaOH at 20 mV/s and charge density of $2.4 \cdot 10^{-5}$ C cm^{-2}. This peak is usually found at -0.7 V vs. SCE in 0.1 M NaOH so the slight peak shift could indicate minor electronic modifications of interactions between Cys and Au(111). Fig. 6.5A shows that the peak dissipates during the second scan indicating successful reductive SAM removal from the Au(111) surface.

In pure EMITFSI electrolyte, peaks are not as well defined as in 0.1 M NaOH. The first and second CV scans in Fig. 6.6B exhibit the same profile with the exception of the peak at – 1.510 V where current density from the first scan is reduced by 17 % in the second scan, indicating reductive removal of Cys. The inset of the Fig. 6.6B shows the same scan rate voltammograms as in Fig. 6.6A. The current density change is obvious from the cathodic peak at – 1.380 V. The reductive desorption of Cys in pure EMITFSI was later pursued by in-situ STM measurements.

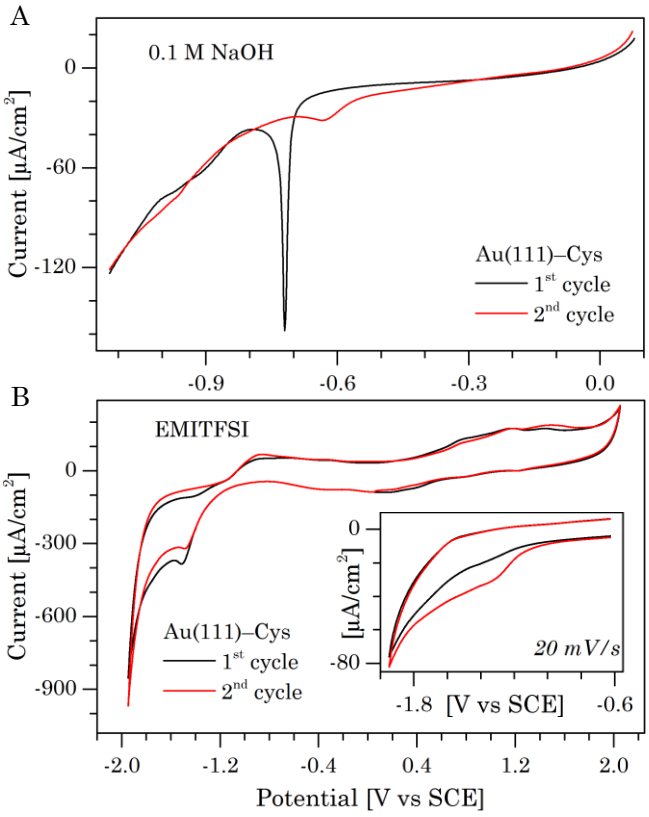

Figure 6.6 Reductive desorption voltammograms of Cys SAMs adsorbed on Au(111) performed by (A) LSV in 0.1 M NaOH at 20 mV/s, (B) CV in pure EMITFSI IL at 50 mV/s, inset scan rate is 20 mV/s.

In-situ STM at the clean Au(111) electrode in pure EMITFSI was performed as a reference experiment, Fig. 6.7A. Large terrace domains of (111) faceting was observed, without any presence of adsorbed molecules. Contrary to these images, Cys SAMs were observed from samples treated in 0.1 mM Cys solutions, Fig. 6.7B. Cys dissolution and adsorption to Au(111) electrodes were performed under Ar-protected EMITFSI and imaged in the same, pure IL. The SAMs were recognized by the characteristic pits of the monolayer, not observed in clean Au(111) samples under any conditions.

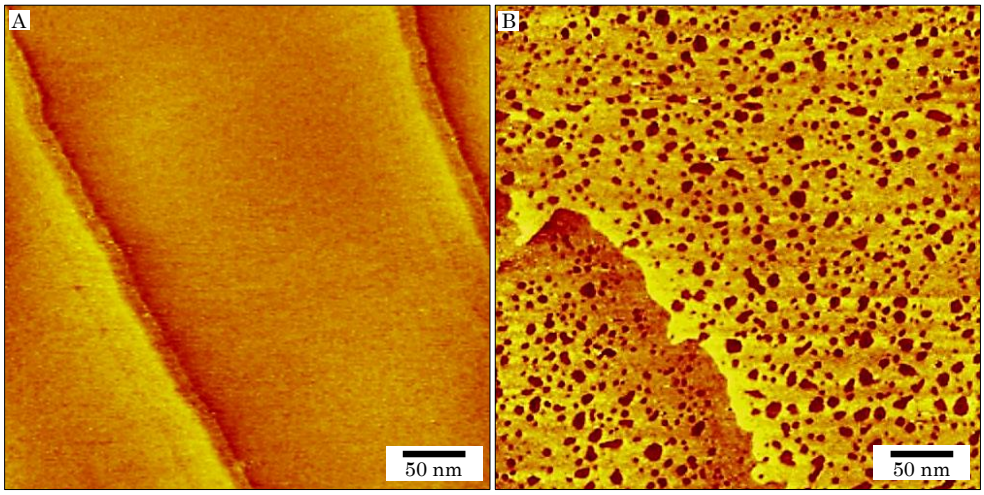

Figure 6.7 In-situ STM images in pure EMITFSI under Ar flow of (A) clean Au(111) and (B) Cys SAMs on Au(111).

In-situ STM reductive desorption of Cys SAMs from Au(111) surface in 0.1 M NaOH and pure EMITFSI was tried to confirm the removal potential established from the electrochemical experiments, at – 0.720 and – 1.510 V, respectively. However, Cys SAM desorption could not be clearly imaged in EMITFSI in-situ STM experiments due to the strong adsorption of large IL cations at potentials more negative than – 1.1 V, Fig. 6.8. IL cations saturated the sample surface, making it impossible to distinguish Cys molecules on Au(111) from IL contributions even at high magnifications, Fig. 6.8C.

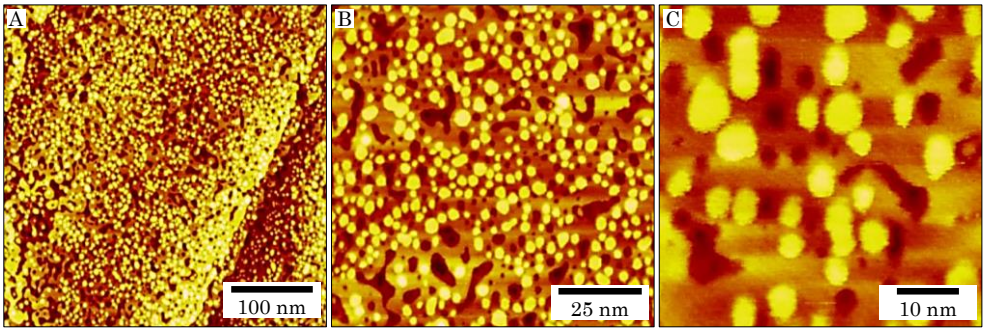

Figure 6.8 In-situ STM images of IL cation adsorption on Cys SAMs chemisorbed on the Au(111) surface in Ar-protected EMITFSI at – 1.3 V.

High-resolution in-situ STM was performed under Ar-protected pure EMITFSI IL as electrolyte at the potential range from – 0.8 V to – 1.0 V. The stable Cys SAMs were

imaged at atomic resolution showing ordered structures of Cys molecules adsorbed on Au(111) electrode. The molecular assembly followed Au faceting, as seen from Fig. 6.9.

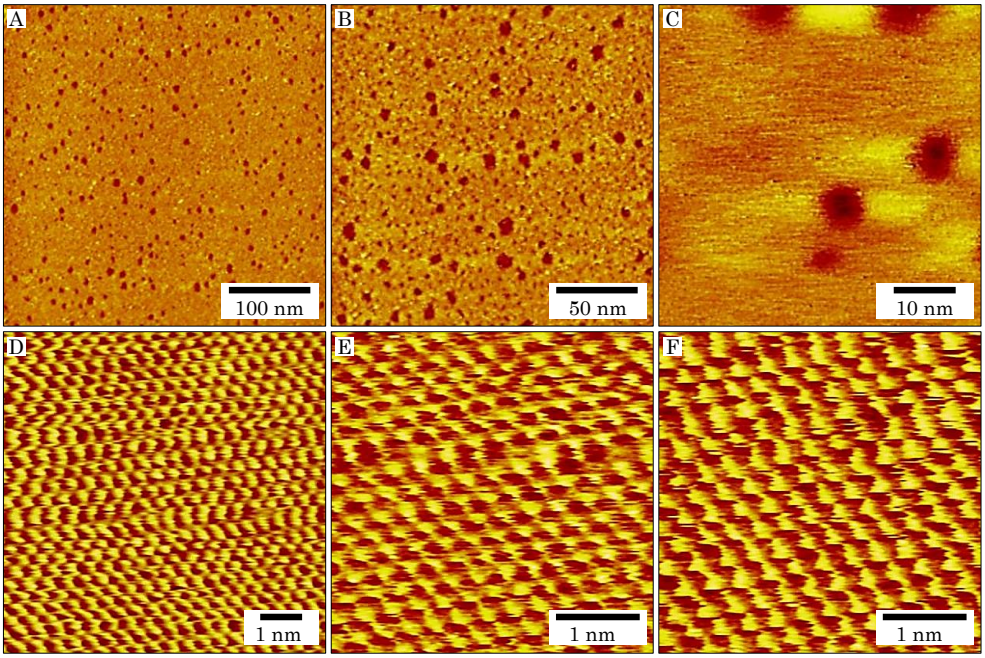

Figure 6.9 Cysteine SAMs on Au(111) surface in Ar-protected pure EMITFSI at different magnifications.

As a reference experiment, the clean Au(111) surface was imaged under the same conditions and magnifications. The interatomic distances were measured for both clean Au(111) and Cys functionalized Au(111) samples, Fig. 6.10. The average atomic distance for clean Au(111) was measured to be 3.05 Å, which was close to the theoretical Au(111) interatomic distance of 2.84 Å. The minor discrepancy was attributed to calibration errors.

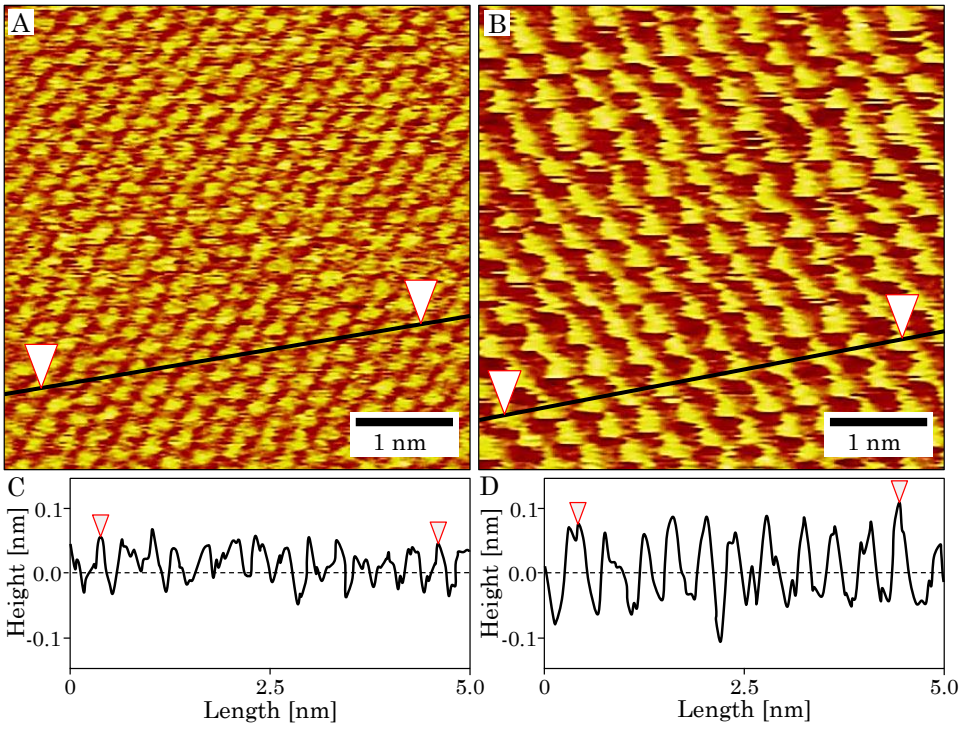

Figure 6.10 STM images of (A) clean Au(111) under Ar flow and (B) in-situ Cys SAMs on Au(111) in pure EMITFSI under Ar flow. Extracted topography profiles for (C) clean Au(111) and (D) Au(111)-Cys.

On the other hand, Cys functionalized Au(111) showed significant interatomic distances. The average distance between the neighboring atoms was 3.11 Å. Moreover, the topography profiles showed almost doubling in height for Cys SAM sample with 1.82 Å compared to clean Au(111) sample with height of 1.07 Å. This was a direct indication that Cys molecules did adsorb on the Au(111) surface from EMITFSI, forming chemisorbed and ordered structures (SAMs) that follow the crystallinity of Au(111) surface.

6.5 Conclusions

Cys SAMs were successfully dissolved in pure EMITFSI IL and characterized by cyclic voltammetry and in-situ STM. The reductive desorption potential in 0.1 M NaOH and pure EMITFSI was found at – 0.720 and – 1.510 V, respectively, with a charge density of $2.4 \cdot 10^{-5}$ C cm^{-2}. In-situ STM showed that the structure of Cys SAMs followed the crystal faceting of the Au(111) electrode. The presence of adsorbed Cys molecules was further proved by measuring the interatomic distances and topography profiles of Cys adsorbed Au(111) samples and clean Au(111) samples at same conditions. The average atomic distance increased by 0.1 Å and topography by 70 % for Cys functionalized Au(111) compared to clean Au(111) electrodes indicating chemisorption of Cys molecules on the Au(111) surface from IL EMITFSI. Cys is, therefore, chemically immobilized on Au(111) electrodes which can be observed from: (1) strong and sharp reductive desorption peak, and (2) interatomic distances and topography measurements indicate adsorption of Cys molecules into ordered structure that follows the crystallinity of the electrode. Presence of strong chemical bonds, therefore, indicated that Cys would have covalent bonds to Au NP cores in Au@Pt NPs, as well.

Chapter 7

Conclusions

The PEMFC technology is governed by used electrocatalysts, their activity and stability. In this Ph.D. project, catalyst optimization was pursued to efficiently utilize Pt, and enhance electronic features, along with stability, by employing graphene. Active surface area of Pt was significantly increased by synthesizing small Pt NPs, enhancing the electrocatalysis. Bimetallic Au@Pt NPs were synthesized with atomically thin Pt shells, further increasing the Pt utilization. Graphene was used as a support for these nanostructures, due to high electrical conductivity, mechanical strength, large surface area and chemical inertness in PEMFC operating conditions. One of the key features of as-synthesized electrocatalysts was the NP immobilization method. Although highly active towards electrochemical oxidation of FA, EtOH and MeOH, Au@Pt NPs only showed significant improvement when covalently immobilized on graphene by Cys molecules. This indicated the importance of an electron transfer process for the electrocatalysis, i.e. when pathways for electron transfers were not created, reactions were not fully propagating. Secondly, the Au cores in Au@Pt NPs were beneficial for multiple reasons. With close atomic sizes and similar properties, Au and Pt did not create high structural tension, thus NPs were stable. Au increased Pt d-band energy, resulting in stronger bonding to fuel molecules, giving rise to higher current densities, and power densities in PEMFCs. Furthermore, being a well-established catalyst for CO oxidation, Au cores protected Pt atomic layers from catalytic poisoning. Both ORR and electrochemical oxidation experiments indicated a promising PEMFC performance of G-Cys-Au@Pt electrocatalyst, which it proved to be in anode setup. Graphene diffusion limitations arose several times, during catalyst characterization or application. Robust structure of graphene, when deposited and dried on electrodes, acted as a barrier for both fuel and oxygen molecules. This effect was, however, less noticeable with fuels. Anode G-Cys-Au@Pt application exhibited superior performance to the commercial catalyst used in industry, which was mainly attributed to unique behavior of water while interacting with hydroscopic graphene. Cathode application, on the other hand, underperformed due to dry graphene structure acting as an oxygen barrier, decreasing the gas flux in PEMFC. The increased stability of G-Cys-Au@Pt in anode setups of DFAFC, DMFC, and DEFC

over C-Pt ensured long-term and high-power performance of the catalyst. At the time of energy crisis and depleting fossil fuels, electrochemical power sources pose a reasonable alternative. Energy- and Pt-efficient electrocatalysts are promising solution to PEMFC technology.

Bibliography

[1] S. Stankovich, D. A. Dikin, G. H. B. Dommett, K. M. Kohlhaas, E. J. Zimney, E. A. Stach, R. D. Piner, S. T. Nguyen, R. S. Ruoff, *Nature* **2006**, *442*, 282.

[2] M. Winter, R. J. Brodd, *Chem. Rev.* **2004**, *104*, 4245.

[3] H. Liu, C. Song, L. Zhang, J. Zhang, H. Wang, D. P. Wilkinson, *J. Power Sources* **2006**, *155*, 95.

[4] a S. Aricò, S. Srinivasan, V. Antonucci, *Fuel Cells* **2001**, *1*, 133.

[5] A. Aricò, V. Baglio, V. Antonucci, *Electrocatal. Direct Methanol Fuel Cells From Fundam. to Appl.* **2009**, 1.

[6] E. Antolini, *J. Power Sources* **2007**, *170*, 1.

[7] N. Shang, P. Wang, **2010**, 15837.

[8] X. Yu, P. G. Pickup, *J. Power Sources* **2008**, *182*, 124.

[9] V. Mehta, J. S. Cooper, *J. Power Sources* **2003**, *114*, 32.

[10] Q. Li, R. He, J.-A. Gao, J. O. Jensen, N. J. Bjerrum, *J. Electrochem. Soc.* **2003**, *150*, A1599.

[11] K. S. Novoselov, A. K. Geim, S. V Morozov, D. Jiang, Y. Zhang, S. V Dubonos, I. V Grigorieva, A. A. Firsov, *Science (80-.).* **2004**, *306*, 666.

[12] L. Jiang, Z. Fan, *Nanoscale* **2014**, *6*, 1922.

[13] C. Liang, Z. Li, S. Dai, **2008**, 3696.

[14] C. Zhu, S. Dong, *Nanoscale* **2013**, *5*, 1753.

[15] S. Eigler, M. Enzelberger-heim, S. Grimm, P. Hofmann, W. Kroener, A. Geworski, C. Dotzer, M. Röckert, J. Xiao, C. Papp, O. Lytken, H. Steinrück, P. Müller, A. Hirsch, **2013**, 3583.

[16] Z. Li, Y. Yao, Z. Lin, K.-S. Moon, W. Lin, C. Wong, *J. Mater. Chem.* **2010**, *20*, 4781.

[17] L. Tang, X. Li, R. Ji, K. S. Teng, G. Tai, J. Ye, C. Wei, S. P. Lau, *J. Mater. Chem.* **2012**, *22*, 5676.

[18] G. Ning, Z. Fan, G. Wang, J. Gao, W. Qian, F. Wei, *Chem. Commun.* **2011**, *47*, 5976.

[19] W. Gao, L. B. Alemany, L. Ci, P. M. Ajayan, *Nat Chem* **2009**, *1*, 403.

[20] V. H. Pham, S. H. Hur, E. J. Kim, B. S. Kim, J. S. Chung, *Chem. Commun.* **2013**, *49*, 6665.

[21] S. Pei, J. Zhao, J. Du, W. Ren, H.-M. Cheng, *Carbon N. Y.* **2010**, *48*, 4466.

[22] S. Stankovich, D. A. Dikin, R. D. Piner, K. A. Kohlhaas, A. Kleinhammes, Y. Jia, Y. Wu, S. T. Nguyen, R. S. Ruoff, *Carbon N. Y.* **2007**, *45*, 1558.

[23] D. R. Dreyer, S. Murali, Y. Zhu, R. S. Ruoff, C. W. Bielawski, *J. Mater. Chem.* **2011**, *21*, 3443.

[24] Z. Lei, L. Lu, X. S. Zhao, *Energy Environ. Sci.* **2012**, *5*, 6391.

[25] M. J. Fernández-Merino, L. Guardia, J. I. Paredes, S. Villar-Rodil, P. Solís-Fernández, A. Martínez-Alonso, J. M. D. Tascón, *J. Phys. Chem. C* **2010**, *114*, 6426.

[26] W. Chen, L. Yan, P. R. Bangal, *J. Phys. Chem. C* **2010**, *114*, 19885.

[27] R. S. Dey, S. Hajra, R. K. Sahu, C. R. Raj, M. K. Panigrahi, *Chem. Commun.* **2012**, *48*, 1787.

[28] D. C. and L. L. and L. Guo, *Nanotechnology* **2011**, *22*, 325601.

[29] Y. Wang, Z. Shi, J. Yin, *ACS Appl. Mater. Interfaces* **2011**, *3*, 1127.

[30] S. Thakur, N. Karak, *Carbon N. Y.* **2012**, *50*, 5331.

[31] H.-P. Cong, J.-F. Chen, S.-H. Yu, *Chem. Soc. Rev.* **2014**, *43*, 7295.

[32] Y. Zhao, C. Hu, Y. Hu, H. Cheng, G. Shi, L. Qu, *Angew. Chemie Int. Ed.* **2012**, *51*, 11371.

[33] X. Zhu, X. Song, X. Ma, G. Ning, *ACS Appl. Mater. Interfaces* **2014**, *6*, 7189.

[34] M. A. Worsley, P. J. Pauzauskie, T. Y. Olson, J. Biener, J. H. Satcher, T. F. Baumann, *J. Am. Chem. Soc.* **2010**, *132*, 14067.

[35] Z. Chen, W. Ren, L. Gao, B. Liu, S. Pei, H.-M. Cheng, *Nat Mater* **2011**, *10*, 424.

[36] W. M. Haynes, in *CRC Handb. Chem. Phys.*, Taylor And Francis, **2014**, pp. 14–18.

[37] P. J. Craig, *Appl. Organomet. Chem.* **1998**, *12*, 880.

[38] H. Bönnemann, R. M. Richards, *Eur. J. Inorg. Chem.* **2001**, *2001*, 2455.

[39] H. Bönnemann, G. Khelashvili, *Appl. Organomet. Chem.* **2010**, *24*, 257.

[40] J. Chen, B. Lim, E. P. Lee, Y. Xia, *Nano Today* **2009**, *4*, 81.

[41] N. M. Marković, T. J. Schmidt, V. Stamenković, P. N. Ross, *Fuel Cells* **2001**, *1*, 105.

[42] H. S. Wroblowa, Yen-Chi-Pan, G. Razumney, *J. Electroanal. Chem. Interfacial Electrochem.* **1976**, *69*, 195.

[43] D.-H. Lim, J. Wilcox, *J. Phys. Chem. C* **2012**, *116*, 3653.

[44] K. Miyabayashi, S. Nakamura, M. Miyake, *Cryst. Growth Des.* **2011**, *11*, 4292.

[45] T. Herricks, J. Chen, Y. Xia, *Nano Lett.* **2004**, *4*, 2367.

[46] N. M. Markovica, S. T. Sarraf, H. A. Gasteiger, P. N. Ross, *J. Chem. Soc. Faraday Trans.* **1996**, *92*, 3719.

[47] F. G. Will, *J. Electrochem. Soc.* **1965**, *112*, 451.

[48] H. A. Gasteiger, P. N. Ross, *J. Phys. Chem.* **1996**, *100*, 6715.

[49] K. T. Kim, S. Jin, S. Chang, D. Park, **2013**, *34*, 3835.

[50] J. Zeng, *J. Mater. Chem.* **2012**, *22*, 3170.

[51] L. Wang, Y. Yamauchi, *J. Am. Chem. Soc.* **2009**, *131*, 9152.

[52] C. Engelbrekt, K. H. Sørensen, T. Lübcke, J. Zhang, Q. Li, C. Pan, N. J. Bjerrum, J. Ulstrup, *ChemPhysChem* **2010**, *11*, 2844.

[53] D. Tongsakul, K. Wongravee, C. Thammacharoen, S. Ekgasit, *Carbohydr. Res.* **2012**, *357*, 90.

[54] S. Wu, J. Liu, Z. Tian, Y. Cai, Y. Ye, Q. Yuan, C. Liang, *ACS Appl. Mater. Interfaces* **2015**, *7*, 22935.

[55] C. Liu, G. Li, D. R. Kauffman, G. Pang, R. Jin, *J. Colloid Interface Sci.* **2014**, *423*,

123.

[56] C. Wang, H. Daimon, Y. Lee, J. Kim, S. Sun, *J. Am. Chem. Soc.* **2007**, *129*, 6974.

[57] J. Qiao, M. Saito, K. Hayamizu, T. Okada, *J. Electrochem. Soc.* **2006**, *153*, A967.

[58] M. Shirai, K. Igeta, M. Arai, *Chem. Commun.* **2000**, 623.

[59] I. K. Moon, J. Lee, R. S. Ruoff, H. Lee, *Nat Commun* **2010**, *1*, 73.

[60] X. Zhu, Y. Zhu, S. Murali, M. D. Stoller, R. S. Ruoff, *ACS Nano* **2011**, *5*, 3333.

[61] B. Mayers, X. Jiang, D. Sunderland, B. Cattle, Y. Xia, *J. Am. Chem. Soc.* **2003**, *125*, 13364.

[62] N. C. Bigall, T. Härtling, M. Klose, P. Simon, L. M. Eng, A. Eychmüller, *Nano Lett.* **2008**, *8*, 4588.

[63] Y. Yamauchi, A. Takai, T. Nagaura, S. Inoue, K. Kuroda, *J. Am. Chem. Soc.* **2008**, *130*, 5426.

[64] Y. Song, R. M. Garcia, R. M. Dorin, H. Wang, Y. Qiu, J. A. Shelnutt, *Angew. Chemie Int. Ed.* **2006**, *45*, 8126.

[65] E. Yoo, T. Okata, T. Akita, M. Kohyama, J. Nakamura, I. Honma, *Nano Lett.* **2009**, *9*, 2255.

[66] X. Fu, F. Bei, X. Wang, S. O'Brien, J. R. Lombardi, *Nanoscale* **2010**, *2*, 1461.

[67] R. Kou, Y. Shao, D. Wang, M. H. Engelhard, J. H. Kwak, J. Wang, V. V Viswanathan, C. Wang, Y. Lin, Y. Wang, I. A. Aksay, J. Liu, *Electrochem. commun.* **2009**, *11*, 954.

[68] Y. Li, L. Tang, J. Li, *Electrochem. commun.* **2009**, *11*, 846.

[69] S. M. Choi, M. H. Seo, H. J. Kim, W. B. Kim, *Carbon N. Y.* **2011**, *49*, 904.

[70] J.-D. Qiu, G.-C. Wang, R.-P. Liang, X.-H. Xia, H.-W. Yu, *J. Phys. Chem. C* **2011**, *115*, 15639.

[71] S. Guo, S. Dong, E. Wang, *ACS Nano* **2010**, *4*, 547.

[72] Y. Hu, H. Zhang, P. Wu, H. Zhang, B. Zhou, C. Cai, *Phys. Chem. Chem. Phys.* **2011**, *13*, 4083.

[73] J. L. Cuya Huaman, S. Fukao, K. Shinoda, B. Jeyadevan, *CrystEngComm* **2011**, *13*, 3364.

[74] L. Dong, R. R. S. Gari, Z. Li, M. M. Craig, S. Hou, *Carbon N. Y.* **2010**, *48*, 781.

[75] C. V. Rao, A. L. M. Reddy, Y. Ishikawa, P. M. Ajayan, *Carbon N. Y.* **2011**, *49*, 931.

[76] J.-J. Lv, J.-N. Zheng, Y.-Y. Wang, A.-J. Wang, L.-L. Chen, J.-J. Feng, *J. Power Sources* **2014**, *265*, 231.

[77] J. Liu, D. Takeshi, K. Sasaki, S. M. Lyth, *J. Electrochem. Soc.* **2014**, *161*, F838.

[78] H. Huang, S. Yang, R. Vajtai, X. Wang, P. M. Ajayan, *Adv. Mater.* **2014**, *26*, 5160.

[79] A. Paneri, Y. Heo, G. Ehlert, A. Cottrill, H. Sodano, P. Pintauro, S. Moghaddam, *J. Memb. Sci.* **2014**, *467*, 217.

[80] L. Li, M. Chen, G. Huang, N. Yang, L. Zhang, H. Wang, Y. Liu, W. Wang, J. Gao, *J. Power Sources* **2014**, *263*, 13.

[81] P. Gellings, H. Koopmans, A. Burggraaf, *Appl. Catal.* **1988**, *39*, 1.

[82] R. S. Nicholson, *Anal. Chem.* **1965**, *37*, 1351.

[83] T. J. Schmidt, H. A. Gasteiger, G. D. Stäb, P. M. Urban, D. M. Kolb, R. J. Behm, *J. Electrochem. Soc.* **1998**, *145*, 2354.

[84] A. Lavacchi, H. Miller, F. Vizza, *Nanotechnology in Electrocatalysis for Energy*, **2013**.

[85] A. S. Bandarenka, E. Ventosa, A. Maljusch, J. Masa, W. Schuhmann, *Analyst* **2014**, *139*, 1274.

[86] A. J. Bard, F. R. F. Fan, J. Kwak, O. Lev, *Anal. Chem.* **1989**, *61*, 132.

[87] Y. Takahashi, A. I. Shevchuk, P. Novak, Y. Murakami, H. Shiku, Y. E. Korchev, T. Matsue, *J. Am. Chem. Soc.* **2010**, *132*, 10118.

[88] X. Li, Y. Cui, Y. Feng, Z. Xie, J.-D. Gu, *Water Res.* **2005**, *39*, 1972.

[89] T. McCreedy, P. R. Fielden, *Analyst* **1995**, *120*, 2343.

[90] J. R. Heuser, J. E. Girard, *Anal. Chem.* **1985**, *57*, 2847.

[91] S. W. Xie, S. Chen, Z. Q. Liu, C. W. Xu, *Int. J. Electrochem. Sci.* **2011**, *6*, 882.

[92] H. Baltruschat, *J. Am. Soc. Mass Spectrom.* **2004**, *15*, 1693.

[93] K. Jambunathan, S. Jayaraman, A. C. Hillier, *Langmuir* **2004**, *20*, 1856.

[94] P. Kebarle, Y. Ho, *Electrospray Ioniz. Mass Spectrom.* **1997**, 3.

[95] W. Zhao, Z. Jusys, R. J. Behm, *Anal. Chem.* **2010**, *82*, 2472.

[96] L. W. Liao, S. X. Liu, Q. Tao, B. Geng, P. Zhang, C. M. Wang, Y. X. Chen, S. Ye, *J. Electroanal. Chem.* **2011**, *650*, 233.

[97] H. Shiroishi, Y. Ayato, K. Kunimatsu, T. Okada, *J. Electroanal. Chem.* **2005**, *581*, 132.

[98] M. Brandhorst, S. Cristol, M. Capron, C. Dujardin, H. Vezin, G. Le bourdon, E. Payen, *Catal. Today* **2006**, *113*, 34.

[99] M. Belén Molina Concha, M. Chatenet, F. H. B. Lima, E. A. Ticianelli, *Electrochim. Acta* **2013**, *89*, 607.

[100] Y. X. Chen, S. Ye, M. Heinen, Z. Jusys, M. Osawa, R. J. Behm, *J. Phys. Chem. B* **2006**, *110*, 9534.

[101] H. Yang, Y. Yang, S. Zou, *J. Phys. Chem. B* **2006**, *110*, 17296.

[102] Y. X. Chen, M. Heinen, Z. Jusys, R. J. Behm, *Angew. Chemie Int. Ed.* **2006**, *45*, 981.

[103] B. C. H. Steele, A. Heinzel, *Nature* **2001**, *414*, 345.

[104] J. Perez, E. R. Gonzalez, E. A. Ticianelli, *Electrochim. Acta* **1998**, *44*, 1329.

[105] X. Cheng, Z. Shi, N. Glass, L. Zhang, J. Zhang, D. Song, Z.-S. Liu, H. Wang, J. Shen, *J. Power Sources* **2007**, *165*, 739.

[106] H. Uchida, H. Ozuka, M. Watanabe, *Electrochim. Acta* **2002**, *47*, 3629.

[107] G. Inzelt, B. Berkes, Á. Kriston, *Electrochim. Acta* **2010**, *55*, 4742.

[108] A. A. Topalov, I. Katsounaros, M. Auinger, S. Cherevko, J. C. Meier, S. O. Klemm, K. J. J. Mayrhofer, *Angew. Chemie Int. Ed.* **2012**, *51*, 12613.

[109] K. J. J. Mayrhofer, S. J. Ashton, J. C. Meier, G. K. H. Wiberg, M. Hanzlik, M. Arenz,

J. Power Sources **2008**, *185*, 734.

[110] N. Hodnik, M. Zorko, M. Bele, S. Hočevar, M. Gaberšček, *J. Phys. Chem. C* **2012**, *116*, 21326.

[111] R. L. Borup, J. R. Davey, F. H. Garzon, D. L. Wood, M. A. Inbody, *J. Power Sources* **2006**, *163*, 76.

[112] J. Wu, X. Z. Yuan, H. Wang, M. Blanco, J. J. Martin, J. Zhang, *Int. J. Hydrogen Energy* **2008**, *33*, 1735.

[113] H. Hanawa, K. Kunimatsu, M. Watanabe, H. Uchida, *J. Phys. Chem. C* **2012**, *116*, 21401.

[114] W. -F. Lin, J. -T. Wang, R. F. Savinell, *J. Electrochem. Soc.* **1997**, *144*, 1917.

[115] O. N. Fuel, C. Anodes, **1996**, 1112.

[116] J. P. I. de Souza, S. L. Queiroz, K. Bergamaski, E. R. Gonzalez, F. C. Nart, *J. Phys. Chem. B* **2002**, *106*, 9825.

[117] W. J. Zhou, S. Q. Song, W. Z. Li, G. Q. Sun, Q. Xin, S. Kontou, K. Poulianitis, P. Tsiakaras, *Solid State Ionics* **2004**, *175*, 797.

[118] P. J. Ferreira, G. J. la O', Y. Shao-Horn, D. Morgan, R. Makharia, S. Kocha, H. A. Gasteiger, *J. Electrochem. Soc.* **2005**, *152*, A2256.

[119] E. Antolini, L. Giorgi, A. Pozio, E. Passalacqua, *J. Power Sources* **1999**, *77*, 136.

[120] J.-T. Wang, S. Wasmus, I. F. Savinell, *J. Electrochem. Soc.* **1996**, *143*, 1233.

[121] R. Nolte, K. Ledjeff, M. Bauer, R. M??lhaupt, *J. Memb. Sci.* **1993**, *83*, 211.

[122] P. Xing, G. P. Robertson, M. D. Guiver, S. D. Mikhailenko, K. Wang, S. Kaliaguine, *J. Memb. Sci.* **2004**, *229*, 95.

[123] Z.-S. Wu, S. Yang, Y. Sun, K. Parvez, X. Feng, K. Müllen, *J. Am. Chem. Soc.* **2012**, *134*, 9082.

[124] Y. Liang, Y. Li, H. Wang, J. Zhou, J. Wang, T. Regier, H. Dai, *Nat Mater* **2011**, *10*, 780.

[125] H. Wang, Y. Liang, Y. Li, H. Dai, *Angew. Chemie Int. Ed.* **2011**, *50*, 10969.

[126] B. E. Logan, B. Hamelers, R. Rozendal, U. Schröder, J. Keller, S. Freguia, P. Aelterman, W. Verstraete, K. Rabaey, *Environ. Sci. Technol.* **2006**, *40*, 5181.

[127] S. K. Chaudhuri, D. R. Lovley, *Nat Biotech* **2003**, *21*, 1229.

[128] S. Calabrese Barton, J. Gallaway, P. Atanassov, *Chem. Rev.* **2004**, *104*, 4867.

[129] R. A. Bullen, T. C. Arnot, J. B. Lakeman, F. C. Walsh, *Biosens. Bioelectron.* **2006**, *21*, 2015.

[130] Z. Du, H. Li, T. Gu, *Biotechnol. Adv.* **2007**, *25*, 464.

[131] C. Liu, S. Alwarappan, Z. Chen, X. Kong, C.-Z. Li, *Biosens. Bioelectron.* **2010**, *25*, 1829.

[132] Y. Zhang, G. Mo, X. Li, W. Zhang, J. Zhang, J. Ye, X. Huang, C. Yu, *J. Power Sources* **2011**, *196*, 5402.

[133] K. Bahartan, J. Gun, S. Sladkevich, P. V Prikhodchenko, O. Lev, L. Alfonta, *Chem. Commun.* **2012**, *48*, 11957.

[134] J. Filip, J. Tkac, *Electrochim. Acta* **2014**, *136*, 340.

[135] T. Miyake, S. Yoshino, T. Yamada, K. Hata, M. Nishizawa, *J. Am. Chem. Soc.* **2011**, *133*, 5129.

[136] D. K. Heyse, *Practice* **2003**, *1*, 36.

[137] R. Sabbah, A. Xu-wu, J. S. Chickos, M. L. P. Leitão, M. V. Roux, L. a. Torres, *Thermochim. Acta* **1999**, *331*, 93.

[138] S. Marklund, W. Yong-liang, **1992**, *82*, 137.

[139] L. Skoog, D.A.; J.J, *Principles of Instrumental Analysis*, Saunders College Publishing, **1971**.

[140] D. F. Swinehart, *J. Chem. Educ.* **1962**, *39*, 333.

[141] R. S. Khandpur, *Handbook of Analytical Instruments*, McGraw-Hill, New York, USA, **2007**.

[142] L. Salasnich, *Quantum Physics of Light and Matter*, Springer International Publishing, **2014**.

[143] S. Zeng, D. Baillargeat, H.-P. Ho, K.-T. Yong, *Chem. Soc. Rev.* **2014**, *43*, 3426.

[144] P. K. Jain, K. S. Lee, I. H. El-Sayed, M. A. El-Sayed, *J. Phys. Chem. B* **2006**, *110*, 7238.

[145] W. Shi, J. Casas, M. Venkataramasubramani, L. Tang, *ISRN Nanomater.* **2012**, *2012*, 1.

[146] T. K. Sau, C. J. Murphy, *Langmuir* **2004**, *20*, 6414.

[147] Z. Tang, D. Geng, G. Lu, *J. Colloid Interface Sci.* **2005**, *287*, 159.

[148] S. M. Bilankohi, **2015**.

[149] P. S. Jensen, C. Engelbrekt, K. H. Sorensen, J. Zhang, Q. Chi, J. Ulstrup, *J. Mater. Chem.* **2012**, *22*, 13877.

[150] C. Engelbrekt, N. Šešelj, R. Poreddy, A. Riisager, J. Ulstrup, J. Zhang, *J. Mater. Chem. A* **2016**, *4*, 3278.

[151] Y. Xu, Y. Dong, J. Shi, M. Xu, Z. Zhang, X. Yang, *Catal. Commun.* **2011**, *13*, 54.

[152] A. Henglein, *J. Phys. Chem. B* **2000**, *104*, 2201.

[153] J. Shang, L. Ma, J. Li, W. Ai, T. Yu, G. G. Gurzadyan, *Sci. Rep.* **2012**, *2*, 792.

[154] F. Bonaccorso, Z. Sun, T. Hasan, A. C. Ferrari, *Nat. Photonics* **2010**, *4*, 611.

[155] S. R. Sahu, M. M. Devi, P. Mukherjee, P. Sen, K. Biswas, **2013**, *2013*.

[156] Q. H. Wei, K. H. Su, S. Durant, X. Zhang, *Nano Lett.* **2004**, *4*, 1067.

[157] H. Yao, L. Jin, H.-J. Sue, Y. Sumi, R. Nishimura, *J. Mater. Chem. A* **2013**, *1*, 10783.

[158] P. R. Griffiths, J. A. de Haseth, in *Fourier Transform Infrared Spectrom.*, John Wiley & Sons, Inc., **2007**, pp. 19–55.

[159] B. H. Stuart, *Infrared Spectroscopy: Fundamentals and Applications*, **2004**.

[160] N. Kumar, S. Das, C. Bernhard, G. D. Varma, *Supercond. Sci. Technol.* **2013**, *26*, 95008.

[161] L. M. Ombaka, P. G. Ndungu, V. O. Nyamori, *RSC Adv.* **2015**, *5*, 109.

[162] P. Tingaut, R. Hauert, T. Zimmermann, *J. Mater. Chem.* **2011**, *21*, 16066.

[163] I. V. Pavlidis, M. Patila, U. T. Bornscheuer, D. Gournis, H. Stamatis, *Trends Biotechnol.* **2014**, *32*, 312.

[164] C. V. Pham, M. Eck, M. Krueger, *Chem. Eng. J.* **2013**, *231*, 146.

[165] S. Kurien, **2005**, *1595*, 64.

[166] K. Siegbahn, *Rev. Mod. Phys.* **1982**, *217*, 709.

[167] P. van der Heide, in *X-Ray Photoelectron Spectrosc.*, John Wiley & Sons, Inc., **2011**, pp. 27–60.

[168] F. Taube, R. Ylmén, A. Shchukarev, S. Nietzsche, J. G. Norén, *J. Dent.* **2010**, *38*, 72.

[169] S. Hofmann, *Auger- and X-Ray Photoelectron Spectroscopy in Materials Science: A User-Oriented Guide*, **2013**.

[170] J. Heath, *Essent. Knowl. Briefings* **2015**, *Second Edi*, 32.

[171] G. Kothleitner, M. J. Neish, N. R. Lugg, S. D. Findlay, W. Grogger, F. Hofer, L. J. Allen, *Phys. Rev. Lett.* **2014**, *112*, 1.

[172] Y. Zhu, H. Inada, K. Nakamura, J. Wall, *Nat Mater* **2009**, *8*, 808.

[173] R. Erni, M. D. Rossell, C. Kisielowski, U. Dahmen, *Phys. Rev. Lett.* **2009**, *102*, 96101.

[174] F. L. Deepak, A. Mayoral, R. Arenal, *Advanced Transmission Electron Microscopy: Applications to Nanomaterials*, **2015**.

[175] S.K. Chapman., *Maintaining and Monitoring the Transmission Electron Microscope*, Oxford University Press, Oxford, **1986**.

[176] M. A. S. Rodriguez, *Textbook of Nanoscience and Nanotechnology*, **2013**.

[177] S. J. Pennycook, *Scanning Transmission Electron Microscopy*, Springer-Verlag New York, **2011**.

[178] M. Haider, S. Uhlemann, E. Schwan, H. Rose, B. Kabius, K. Urban, *Nature* **1998**, *392*, 768.

[179] D. Li, M. H. M. H. Nielsen, J. R. I. J. R. I. Lee, C. Frandsen, J. F. Banfield, J. J. De Yoreo, *Science (80-.).* **2012**, *336*, 1014.

[180] C. Gong, A. W. Robertson, K. He, G. Lee, E. Yoon, C. S. Allen, A. I. Kirkland, J. H. Warner, **2015**, 3.

[181] P. D. Nellist, *The Principles and Interpretation of Annular Dark-Field Z-Contrast Imaging*, **2008**.

[182] K. Takayanagi, S. Kim, S. Lee, Y. Oshima, T. Tanaka, Y. Tanishiro, H. Sawada, F. Hosokawa, T. Tomita, T. Kaneyama, Y. Kondo, *J. Electron Microsc. (Tokyo).* **2011**, *60*, 239.

[183] C. L. Johnson, E. Snoeck, M. Ezcurdia, B. Rodriguez-Gonzalez, I. Pastoriza-Santos, L. M. Liz-Marzan, M. J. Hytch, *Nat Mater* **2008**, *7*, 120.

[184] P. Zanello, *Inorganic Electrochemistry*, The Royal Society Of Chemistry, **2003**.

[185] A. J. Bard, L. R. Faulkner, *Electrochemical Methods. Fundamentals and Applications*, Wiley, New York, **2001**.

[186] I. Pilatowsky, R. J. Romero, C. A. Isaza, S. A. Gamboa, P. J. Sebastian, W. Rivera, in

Cogener. Fuel Cell-Sorption Air Cond. Syst., Springer London, London, **2011**, pp. 25–36.

[187] C. Kunusch, P. Puleston, M. Mayosky, in *Sliding-Mode Control PEM Fuel Cells*, Springer London, London, **2012**, pp. 13–33.

[188] M. Shao, A. Peles, K. Shoemaker, *Nano Lett.* **2011**, *11*, 3714.

[189] V. Tripković, I. Cerri, T. Bligaard, J. Rossmeisl, *Catal. Letters* **2014**, *144*, 380.

[190] T. L. Tan, L.-L. Wang, J. Zhang, D. D. Johnson, K. Bai, *ACS Catal.* **2015**, *5*, 2376.

[191] Y. Yu, H. L. Xin, R. Hovden, D. Wang, E. D. Rus, J. A. Mundy, D. A. Muller, H. D. Abruña, *Nano Lett.* **2012**, *12*, 4417.

[192] T. W. Hansen, A. T. DeLaRiva, S. R. Challa, A. K. Datye, *Acc. Chem. Res.* **2013**, *46*, 1720.

[193] Y. Shao-Horn, W. C. Sheng, S. Chen, P. J. Ferreira, E. F. Holby, D. Morgan, *Top. Catal.* **2007**, *46*, 285.

[194] A. Cao, R. Lu, G. Veser, *Phys. Chem. Chem. Phys.* **2010**, *12*, 13499.

[195] T. A. Pham, B. C. Choi, K. T. Lim, Y. T. Jeong, *Appl. Surf. Sci.* **2011**, *257*, 3350.

[196] J. Lu, B. Fu, M. C. Kung, G. Xiao, J. W. Elam, H. H. Kung, P. C. Stair, *Science (80-.).* **2012**, *335*, 1205 LP.

[197] E. Antolini, *Energy Environ. Sci.* **2009**, *2*, 915.

[198] S. Sharma, B. G. Pollet, *J. Power Sources* **2012**, *208*, 96.

[199] N. Seselj, C. Engelbrekt, J. Zhang, *Sci. Bull.* **2015**, *60*, 864.

[200] L. Xin, F. Yang, S. Rasouli, Y. Qiu, Z. F. Li, A. Uzunoglu, C. J. Sun, Y. Liu, P. Ferreira, W. Li, Y. Ren, L. A. Stanciu, J. Xie, *ACS Catal.* **2016**, *6*, 2642.

[201] B. P. Vinayan, S. Ramaprabhu, *Nanoscale* **2013**, *5*, 5109.

[202] C. Venkateswara Rao, C. R. Cabrera, Y. Ishikawa, *J. Phys. Chem. C* **2011**, *115*, 21963.

[203] T. Palaniselvam, V. Kashyap, S. N. Bhange, J. B. Baek, S. Kurungot, *Adv. Funct. Mater.* **2016**, 2150.

[204] M. J. E. Fischer, in *Surf. Plasmon Reson. Methods Protoc.* (Eds.: N.J. Mol, M.J.E. Fischer), Humana Press, Totowa, NJ, **2010**, pp. 55–73.

[205] A. Halder, M. Zhang, Q. Chi, *Biosens. Bioelectron.* **2017**, *87*, 764.

[206] J. C. Love, L. A. Estroff, J. K. Kriebel, R. G. Nuzzo, G. M. Whitesides, *Chem. Rev.* **2005**, *105*, 1103.

[207] C. Zhang, L. Fu, N. Liu, M. Liu, Y. Wang, Z. Liu, *Adv. Mater.* **2011**, *23*, 1020.

[208] J. H. Lee, N. Park, B. G. Kim, D. S. Jung, K. Im, J. Hur, J. W. Choi, *ACS Nano* **2013**, *7*, 9366.

[209] T. R. Ralph, G. A. Hards, J. E. Keating, S. A. Campbell, D. P. Wilkinson, M. Davis, J. St-Pierre, M. C. Johnson, *J. Electrochem. Soc.* **1997**, *144*, 3845.

[210] Z. Al Amri, M. P. Mercer, N. Vasiljevic, *Electrochim. Acta* **2016**, *210*, 520.

[211] B. C. Ong, S. K. Kamarudin, M. S. Masdar, U. A. Hasran, *Int. J. Hydrogen Energy*

2016.

[212] D. A. Dikin, S. Stankovich, E. J. Zimney, R. D. Piner, G. H. B. Dommett, G. Evmenenko, S. T. Nguyen, R. S. Ruoff, *Nature* **2007**, *448*, 457.

[213] L. Coyne, R. Mariner, A. Rice, *Langmuir* **1991**, *7*, 1660.

[214] R. Zhou, Y. Zheng, M. Jaroniec, S.-Z. Qiao, *ACS Catal.* **2016**, *6*, 4720.

[215] F. J. Vidal-Iglesias, J. Solla-Gullón, V. Montiel, A. Aldaz, *Electrochem. commun.* **2012**, *15*, 42.

[216] J. Zhang, *PEM Fuel Cell Electrocatalysts and Catalyst Layers: Fundamentals and Applications*, **2008**.

[217] H. Okamoto, W. Kon, Y. Mukouyama, *J. Phys. Chem. B* **2005**, *109*, 15659.

[218] S. Brimaud, J. Solla-Gullón, I. Weber, J. M. Feliu, R. J. Behm, *ChemElectroChem* **2014**, *1*, 1075.

[219] Y.-C. Bai, W.-D. Zhang, C.-H. Chen, J.-Q. Zhang, *J. Alloys Compd.* **2011**, *509*, 1029.

[220] N. M. Marković, P. N. Ross, *Surf. Sci. Rep.* **2002**, *45*, 117.

[221] J. Zhang, K. Sasaki, E. Sutter, R. R. Adzic, *Science (80-.).* **2007**, *315*, 220.

[222] M. C. Daniel, D. Astruc, *Chem. Rev.* **2004**, *104*, 293.

[223] Z. X. Liang, T. S. Zhao, J. B. Xu, *J. Power Sources* **2008**, *185*, 166.

[224] D. F. Yancey, E. V. Carino, R. M. Crooks, *J. Am. Chem. Soc.* **2010**, *132*, 10988.

[225] B. N. Wanjala, J. Luo, R. Loukrakpam, B. Fang, D. Mott, P. N. Njoki, M. Engelhard, H. R. Naslund, J. K. Wu, L. Wang, O. Malis, C. J. Zhong, *Chem. Mater.* **2010**, *22*, 4282.

[226] J. Luo, L. Wang, D. Mott, P. N. Njoki, Y. Lin, T. He, Z. Xu, B. N. Wanjana, I. I. S. Lim, C. J. Zhong, *Adv. Mater.* **2008**, *20*, 4342.

[227] C. J. Serpell, J. Cookson, D. Ozkaya, P. D. Beer, *Nat. Chem.* **2011**, *3*, 478.

[228] M. Min, C. Kim, H. Lee, *J. Mol. Catal. A Chem.* **2010**, *333*, 6.

[229] S. G. Jang, A. Khan, M. D. Dimitriou, B. J. Kim, N. A. Lynd, E. J. Kramer, C. J. Hawker, *Soft Matter* **2011**, *7*, 6255.

[230] R. K. Biroju, B. Choudhury, P. K. Giri, *Catal. Sci. Technol.* **2016**, *6*, 7101.

[231] V. Amendola, *Phys. Chem. Chem. Phys.* **2016**, *18*, 2230.

[232] A. P. Letters, Y. L. Samsung, Y. Lee, **2015**, DOI 10.1063/1.3683534.

[233] K. Balasubramanian, L. Zuccaro, K. Kern, *Adv. Funct. Mater.* **2014**, *24*, DOI 10.1002/adfm.201401796.

[234] Q. Chi, J. Zhang, J. E. T. Andersen, J. Ulstrup, *J. Phys. Chem. B* **2001**, *105*, 4669.

[235] W. Liu, D. Sun, J. Fu, R. Yuan, Z. Li, *RSC Adv.* **2014**, *4*, 11003.

[236] R. Brito, V. A. Rodríguez, J. Figueroa, C. R. Cabrera, *J. Electroanal. Chem.* **2002**, *520*, 47.

[237] J. Huang, J. C. Hemminger, *J. Am. Chem. Soc.* **1993**, *115*, 3342.

[238] D. Y. Petrovykh, H. Kimura-Suda, A. Opdahl, L. J. Richter, M. J. Tarlov, L. J. Whitman, *Langmuir* **2006**, *22*, 2578.

[239] J. W. Lee, W. Jung, *J. Ind. Eng. Chem.* **2014**, *20*, 2883.

[240] G. M. Veith, A. R. Lupini, L. Baggetto, J. F. Browning, J. K. Keum, A. Villa, L. Prati, A. B. Papandrew, G. A. Goenaga, D. R. Mullins, S. E. Bullock, N. J. Dudney, *Chem. Mater.* **2013**, *25*, 4936.

[241] P.-P. Zuo, H.-F. Feng, Z.-Z. Xu, L.-F. Zhang, Y.-L. Zhang, W. Xia, W.-Q. Zhang, *Chem. Cent. J.* **2013**, *7*, 39.

[242] B. Hammer, J. K. Nørskov, *Adv. Catal.* **2000**, *45*, 71.

[243] N. Kristian, Y. Yu, P. Gunawan, R. Xu, W. Deng, X. Liu, X. Wang, *Electrochim. Acta* **2009**, *54*, 4916.

[244] M. D. Obradović, J. R. Rogan, B. M. Babić, A. V Tripković, A. R. S. Gautam, V. R. Radmilović, S. L. Gojković, *J. Power Sources* **2012**, *197*, 72.

[245] H. Kita, H. Nakajima, K. Hayashi, *J. Electroanal. Chem. Interfacial Electrochem.* **1985**, *190*, 141.

[246] E. Herrero, Q.-S. Chen, J. Hernandez, S.-G. Sun, J. M. Feliu, *Phys. Chem. Chem. Phys.* **2011**, *13*, 16762.

[247] X. Zhou, J. Qiao, L. Yang, J. Zhang, *Adv. Energy Mater.* **2014**, *4*, 1301523.

[248] M. del Cueto, P. Ocón, J. M. L. Poyato, *J. Phys. Chem. C* **2015**, *119*, 2004.

[249] H. Meng, N. Larouche, M. Lefèvre, F. Jaouen, B. Stansfield, J.-P. Dodelet, *Electrochim. Acta* **2010**, *55*, 6450.

[250] C. Xu, Q. Hao, H. Duan, *J. Mater. Chem. A* **2014**, *2*, 8875.

[251] Z. Guo, X. Zhang, H. Sun, X. Dai, Y. Yang, X. Li, T. Meng, *Electrochim. Acta* **2014**, *134*, 411.

[252] S. Wang, X. Wang, S. P. Jiang, *Phys. Chem. Chem. Phys.* **2011**, *13*, 6883.

[253] W. Huang, H. Wang, J. Zhou, J. Wang, P. N. Duchesne, D. Muir, P. Zhang, N. Han, F. Zhao, M. Zeng, J. Zhong, C. Jin, Y. Li, S.-T. Lee, H. Dai, *Nat. Commun.* **2015**, *6*, 10035.

[254] H.-J. Qiu, X. Shen, J. Q. Wang, A. Hirata, T. Fujita, Y. Wang, M. W. Chen, *ACS Catal.* **2015**, *5*, 3779.

[255] S. B. Brummer, A. C. Makrides, *J. Phys. Chem.* **1964**, *68*, 1448.

[256] N. Markovic, P. N. Ross, *J. Phys. Chem.* **1993**, *97*, 9771.

[257] S. C. S. Lai, N. P. Lebedeva, T. H. M. Housmans, M. T. M. Koper, *Top. Catal.* **2007**, *46*, 320.

[258] A. Bach Delpeuch, M. Jacquot, M. Chatenet, C. Cremers, *Phys. Chem. Chem. Phys.* **2016**, *18*, 25169.

[259] N. Zhu, S. Han, S. Gan, J. Ulstrup, Q. Chi, *Adv. Funct. Mater.* **2013**, *23*, 5297.

[260] M. A. F. Akhairi, S. K. Kamarudin, *Int. J. Hydrogen Energy* **2016**, *41*, 4214.

[261] Y. Li, L. Han, B. An, Y. Wang, L. Wang, X. Yin, J. Lu, *J. Mater. Sci. Mater. Electron.* **2016**, *27*, 6208.

[262] A. De, J. Datta, I. Haldar, M. Biswas, *ACS Appl. Mater. Interfaces* **2016**, *8*, 28574.

[263] Y. Wang, A. Tabet-Aoul, M. Mohamedi, *J. Electrochem. Soc.* **2016**, *163*, F1272.

[264] W. R. Grove, *Philos. Mag. Ser. 3* **1838**, *13*, 430.

[265] X.-Z. Yuan, H. Wang, in *PEM Fuel Cell Electrocatal. Catal. Layers Fundam. Appl.* (Ed.: J. Zhang), Springer London, London, **2008**, pp. 1–87.

[266] B. Seger, P. V Kamat, *J. Phys. Chem. C* **2009**, *113*, 7990.

[267] R. I. Jafri, T. Arockiados, N. Rajalakshmi, S. Ramaprabhu, *J. Electrochem. Soc.* **2010**, *157*, B874.

[268] Y. Shao, S. Zhang, C. Wang, Z. Nie, J. Liu, Y. Wang, Y. Lin, *J. Power Sources* **2010**, *195*, 4600.

[269] K. Zhang, Q. Yue, G. Chen, Y. Zhai, L. Wang, H. Wang, J. Zhao, J. Liu, J. Jia, H. Li, *J. Phys. Chem. C* **2011**, *115*, 379.

[270] S. S. Jyothirmayee Aravind, R. Imran Jafri, N. Rajalakshmi, S. Ramaprabhu, *J. Mater. Chem.* **2011**, *21*, 18199.

[271] B. P. Vinayan, R. Nagar, S. Ramaprabhu, *J. Mater. Chem.* **2012**, *22*, 25325.

[272] D. He, K. Cheng, T. Peng, X. Sun, M. Pan, S. Mu, *J. Mater. Chem.* **2012**, *22*, 21298.

[273] D. Geng, Y. Hu, Y. Li, R. Li, X. Sun, *Electrochem. commun.* **2012**, *22*, 65.

[274] D. He, K. Cheng, H. Li, T. Peng, F. Xu, S. Mu, M. Pan, *Langmuir* **2012**, *28*, 3979.

[275] K.-W. Nam, J. Song, K.-H. Oh, M.-J. Choo, H. Park, J.-K. Park, J. W. Choi, *Carbon N. Y.* **2012**, *50*, 3739.

[276] Y. Li, Y. Li, E. Zhu, T. McLouth, C.-Y. Chiu, X. Huang, Y. Huang, *J. Am. Chem. Soc.* **2012**, *134*, 12326.

[277] B. P. Vinayan, S. Ramaprabhu, *Nanoscale* **2013**, *5*, 5109.

[278] H.-W. Ha, I. Y. Kim, S.-J. Hwang, R. S. Ruoff, *Electrochem. Solid State Lett.* **2011**, *14*, B70.

[279] Y. Xin, J. Liu, Y. Zhou, W. Liu, J. Gao, Y. Xie, Y. Yin, Z. Zou, *J. Power Sources* **2011**, *196*, 1012.

[280] M. S. Wietecha, J. Zhu, G. Gao, N. Wang, H. Feng, M. L. Gorring, M. L. Kasner, S. Hou, *J. Power Sources* **2012**, *198*, 30.

[281] H. Zhang, X. Xu, P. Gu, C. Li, P. Wu, C. Cai, *Electrochim. Acta* **2011**, *56*, 7064.

[282] S. H. Lee, N. Kakati, S. H. Jee, J. Maiti, Y.-S. Yoon, *Mater. Lett.* **2011**, *65*, 3281.

[283] C. Venkateswara Rao, C. R. Cabrera, Y. Ishikawa, *J. Phys. Chem. C* **2011**, *115*, 21963.

[284] P. Mani, R. Srivastava, P. Strasser, *J. Phys. Chem. C* **2008**, *112*, 2770.

[285] B. C. Beard, P. N. Ross, *J. Electrochem. Soc.* **1990**, *137*, 3368.

[286] M. Min, J. Cho, K. Cho, H. Kim, *Electrochim. Acta* **2000**, *45*, 4211.

[287] M. Ammam, E. B. Easton, *J. Power Sources* **2013**, *236*, 311.

[288] A. K. Shukla, M. Neergat, P. Bera, V. Jayaram, M. S. Hegde, *J. Electroanal. Chem.* **2001**, *504*, 111.

[289] L. Wang, Y. Yamauchi, *Chem. Mater.* **2011**, *23*, 2457.

[290] Y. Qiao, C. M. Li, *J. Mater. Chem.* **2011**, *21*, 4027.

[291] M. Umeda, H. Ojima, M. Mohamedi, I. Uchida, *J. Power Sources* **2004**, *136*, 10.

[292] T. Kawaguchi, Y. Rachi, W. Sugimoto, Y. Murakami, Y. Takasu, *J. Appl. Electrochem.* **2006**, *36*, 1117.

[293] S. G. da Silva, M. H. M. T. Assumpção, R. F. B. de Souza, G. S. Buzzo, E. V Spinacé, A. O. Neto, J. C. M. Silva, *Electrocatalysis* **2014**, *5*, 438.

[294] Z.-B. Wang, G.-P. Yin, Y.-G. Lin, *J. Power Sources* **2007**, *170*, 242.

[295] P. Waszczuk, T. M. Barnard, C. Rice, R. I. Masel, A. Wieckowski, *Electrochem. commun.* **2002**, *4*, 599.

[296] V. R. Stamenkovic, B. Fowler, B. S. Mun, G. Wang, P. N. Ross, C. A. Lucas, N. M. Marković, *Science (80-.).* **2007**, *315*, 493.

[297] J.-H. Choi, K.-W. Park, I.-S. Park, W.-H. Nam, Y.-E. Sung, *Electrochim. Acta* **2004**, *50*, 787.

[298] C. Xu, L. Cheng, P. Shen, Y. Liu, *Electrochem. commun.* **2007**, *9*, 997.

[299] H. A. Gasteiger, N. Markovic, P. N. Ross, E. J. Cairns, *J. Phys. Chem.* **1993**, *97*, 12020.

[300] C. Rice, S. Ha, R. I. Masel, A. Wieckowski, *J. Power Sources* **2003**, *115*, 229.

[301] D. Sebastián, V. Baglio, A. S. Aricò, A. Serov, P. Atanassov, *Appl. Catal. B Environ.* **2016**, *182*, 297.

[302] J.-S. Kim, J. S. Choi, M. J. Lee, B. H. Park, D. Bukhvalov, Y.-W. Son, D. Yoon, H. Cheong, J.-N. Yun, Y. Jung, J. Y. Park, M. Salmeron, *Sci. Rep.* **2013**, *3*, 2309.

[303] M. Ma, G. Tocci, A. Michaelides, G. Aeppli, *Nat Mater* **2016**, *15*, 66.

[304] S. Liang, *Quantum Tunneling and Field Electron Emission Theories*, World Scientific Publishing Co. Pte. Ltd., **2014**.

[305] B. D. H. D. A. Bonnell, *Scanning Probe Microscopy and Spectroscopy*, Wiley-VCH, New York, **2001**.

[306] E. Meyer, H. J. Hug, R. Bennewitz, *Scanning Probe Microscopy - The Lab on a Tip*, Springer-Verlag, Berlin, Germany, **2004**.

[307] W. S. J. a. Kaiser, in *Scanning Tunneling Microsc. I*, Springer-Verlag, Berlin, Germany, **1993**, pp. 9–24.

[308] C. J. Chen, *Introduction to Scanning Tunneling Microscopy*, Oxford University Press, New York, USA, **1993**.

[309] A. M. Kuznetsov, J. Ulstrup, *Electron Transfer in Chemistry and Biology: An Introduction to the Theory*, John Wiley And Sons Ltd, Chichester, UK and New York, USA, **1999**.

[310] L. Rodríguez-Pérez, Y. Coppel, I. Favier, E. Teuma, P. Serp, M. Gómez, *Dalton Trans.* **2010**, *39*, 7565.

[311] C.-J. Zhong, M. D. Porter, *J. Am. Chem. Soc.* **1994**, *116*, 11616.

Appendix

Contributions made during the Ph.D. project are included.

International Journals:

1. N. Seselj, C. Engelbrekt, J. Zhang, "Graphene-supported Platinum Catalysts for Fuel Cells", ***Science Bulletin***, 60 (2014), 864-876
2. C. Engelbrekt, N. Seselj, R. Poreddy, A. Riisager, J. Ulstrup, J. Zhang, "Atomically thin Pt shells on Au nanoparticle cores: facile synthesis and efficient synergetic catalysis" , ***J. Mater. Chem. A***, 4 (2016), 3278-3286
3. N. Seselj, C. Engelbrekt, Y. Ding, H. A. Hjuler, J. Ulstrup, J. Zhang, "Tailored electron transfer pathways in Au_{core}/Pt_{shell}–graphene nanocatalysts for fuel cells" , submitted to ***Advanced Energy Materials*** (May, 2017)
4. M. U.-B. Christiansen, N. Seselj, C. Engelbrekt, M. Wagner, F. N. Stappen, J. Zhang "Chemically controlled interfacial nanoparticle self-assembly into nanoporous gold films for electrochemical applications" (in preparation)

Poster presentations at national and international conferences:

5. M. U.-B. Christiansen, N. Seselj, C. Engelbrekt, M. Wagner, F. N. Stappen, J. Zhang, "Chemical Synthesis and Electrochemical Characterization of Nanoporous Gold films" *4th EuCheMS Inorganic Chemistry Conference (EICC-4)*, **2017**, Copenhagen, Denmark
6. N. Seselj, J. Ulstrup, J. Zhang, "Graphene Supported Au-Pt Core-Shell Catalyst: Electrocatalysis of Formic Acid Oxidation" (poster) *67th Annual Meeting of the International Society of Electrochemistry (ISE)*, **2016**, The Hague, Netherlands
7. N. Seselj, C. Engelbrekt, J. Zhang, "Development of graphene-supported Pt catalysts for fuel cells" (poster), *6th Symposium on Carbon and Related Nanomaterials - Carbonhagen*, **2015**, Copenhagen, Denmark
8. C. Engelbrekt, N. Seselj, J. Ulstrup, J. Zhang, "Facile synthesis of starch-scaffolded bimetallic Au-Pt nanostructure and electrocatalysis", *The 66th Annual Meeting of the International Society of Electrochemistry (ISE)*, **2015**, Taipei, Taiwan

9. C. Engelbrekt, N. Seselj, J. Ulstrup, J. Zhang, "The SAMENS Method for Gold Nanostructure Syntheses: Green Synthesis and Electrocatalysis", *15th International Symposium on Electroanalytical Chemistry*, **2015**, Changchun, China

10. C. Engelbrekt, N. Seselj, J. Ulstrup, J. Zhang, "Dynamics study of green AuNP formation and their basis for Au-Pt core-shell nanostructure synthesis" (poster), *Nanocrystals Conference*, **2014,** Punta Cana, Dominican Republic

11. N. Seselj, C. Engelbrekt, Jens Ulstrup, Jingdong Zhang, "Chemical production of graphene catalysts for electrochemical energy conversion" (poster), "*Chalmers Soft Matter Graduate School on Molecular Electronics and Molecular Switches*, **2014**, Nösunds, Sweden

Attended workshops or seminars:

12. *NOVA 2.0*, Metrohm seminar, **2015**, Glostrup, Denmark

13. *XVII Annual Linz Winter Workshop*, workshop, **2015**, Johannes Kepler University, Linz, Austria

14. *Asia Energy Conference*, conference/workshop, **2014**, Copenhagen, Denmark

15. *Nanosight User Meeting*, seminar, **2014**, Greve, Denmark

16. *Chalmers Soft Matter Graduate School on Molecular Electronics and Molecular Switches*, Summer school, **2014**, Nösunds, Sweden